Plasma Rotation and Momentum Transport Studies in the TCV Tokamak Based on Charge Exchange Spectroscopy Measurements

THÈSE N^{O} 4569 (2009)

PRÉSENTÉE LE 18 DÉCEMBRE 2009

À LA FACULTÉ DES SCIENCES DE BASE

CRPP ASSOCIATION EURATOM

PROGRAMME DOCTORAL EN PHYSIQUE

ÉCOLE POLYTECHNIQUE FÉDÉRALE DE LAUSANNE

POUR L'OBTENTION DU GRADE DE DOCTEUR ÈS SCIENCES

PAR

Alessandro Bortolon

acceptée sur proposition du jury:

Prof. O. Schneider, président du jury
Dr B. Duval, directeur de thèse
Dr P. de Vries, rapporteur
Dr J. Rice, rapporteur
Dr O. Sauter, rapporteur

ÉCOLE POLYTECHNIQUE
FÉDÉRALE DE LAUSANNE

Suisse
2009

document revised on Monday 14$^{\text{th}}$ December, 2009

Made with pdfLaTeX

Abstract

Thermonuclear controlled fusion research is a highly active branch of plasma physics. The main goal is the production of energy from the fusion reaction of hydrogen isotope nuclei, the same reaction that powers stars. The most promising present approach are *Tokamaks*, toroidal devices where high temperature plasmas are confined by means of magnetic fields. This thesis is devoted to a detailed and systematic study of plasma rotation in the *Tokamak à Configuration Variable* (TCV), at the *Centre de Recherches en Physique des Plasmas* (CRPP) in Lausanne, Switzerland.

In a tokamak, confinement is limited by particle and energy transport from the hot core to the cold edge and by macroscopic perturbations of magnetic equilibrium. Recently, plasma rotation has been demonstrated to beneficially affect both confinement and stability, explaining the great recent interest in plasma rotation studies.

Relatively little is understood about plasma rotation physics and, in particular, the so called "intrinsic" rotation that will constitute the main component of plasma rotation in next generation machines. That is why a great theoretical and experimental effort is being deployed in studying intrinsic rotation and this work is part of this context.

In TCV, plasma rotation is measured by the Charge eXchange Recombination Spectroscopy diagnostic (CXRS). The spectroscopic signal comes from the perpendicular observation of a low power Diagnostic Neutral Beam Injector (DNBI), which applies a negligible torque to the plasma. Hence, the DNBI/CXRS pair is an effective tool for the experimental study of intrinsic tokamak plasma rotation.

During this work, the pre existing toroidal observation view was complemented with two new systems, permitting the measurement of toroidal rotation, on inboard plasma radius, and poloidal rotation in the plasma periphery. The implementation of an automated wavelength calibration procedure, based on reference Neon spectra, permitted the first viable (toroidal and poloidal) rotation measurements of TCV, with uncertainties down to 1 km/s.

Using upgraded light collection optics and fiber optic transmission lines, simultaneous measurement of core and edge plasma was achieved, with a doubling of the radial resolution of the toroidal rotation measurement. The measurable range of plasma parameters was also extended to higher densities by the installation of back illuminated CCD detectors.

In the present configuration (CXRS09), the diagnostic is capable of routinely measuring toroidal and poloidal plasma rotations with a radial resolution of $\lesssim 1$ cm and a sample frequency of $10 \div 20$ Hz, for plasma densities of $0.8 \lesssim n_{\mathrm{e,av}} \lesssim 8 \times 10^{19}\,\mathrm{m}^{-3}$.

The basic scenario of Ohmically heated discharges in limiter L-mode configuration was initially addressed. A large core toroidal rotation up to $u_\phi \approx 50$ km/s in the counter current direction is measured, reversing nearly exactly upon reversal of plasma current I_p. The toroidal rotation profile may be schematically divided into a core, a peripheral and an intermediate region. For $q_e \approx 3$ (magnetic safety factor at the plasma edge) the core region velocity is relatively flat or slightly "bulged" in the co current direction inside the sawtooth inversion radius. In the peripheral region, the toroidal rotation is small with a monotonic intermediate region. The central rotation appears to be limited to approximately its value at the sawtooth inversion radius.

Poloidal rotation $u_\theta \lesssim 3$ km/s, measured in Ohmic discharges, is only weakly dependent on plasma parameters but reverses with reversed magnetic field, with values and direction coherent

with neoclassical predictions. Combining u_ϕ and u_θ measurements, the profile of the radial electric field E_r was estimated through the radial force balance equation. E_r down to 8 kVm (inward directed) is found in the plasma bulk, and close to zero at the plasma edge.

A spontaneous reversal of the toroidal rotation profile is observed when the average density exceeds $n_{\mathrm{e,av}} \approx 4{\times}10^{19}\,\mathrm{m}^{-3}$ at low $q_e \approx 3$, with the plasma now rotating in the co current direction. The transition between the co and counter rotation regimes is studied dynamically using n_e and I_p ramps and with the application of Electro Cyclotron Heating (ECH). The rotation reversal is weakly sensitive to impurity concentration and positive plasma triangularity appears to be a key ingredient. Whilst a physical explanation has not been identified yet, dynamic u_ϕ reversal observations indicate that it results from a changed balance of radial non-diffusive fluxes of toroidal momentum.

The study was extended to the divertor magnetic configuration in which the plasma column rotates in the co current direction at low n_e, and u_ϕ reverses at high n_e, opposite from the limited configuration. The rotation profile may again be divided into three regions, although the rotation at the plasma periphery does not always remain close to zero but evolves with the plasma parameters. In particular, independently on the core rotation regime, peripheral u_ϕ decreases with n_e and I_p and is strongly sensitive to the ion $\vec{B} \times \nabla B$ direction, suggesting a link with parallel fluxes in the Scrape-Off Layer (SOL). Combined measurements of CXRS and Mach probe indicate that in the plasma edge toroidal rotation matches the toroidal component of SOL flows.

From the analysis of toroidal rotation in stationary and transient phases, a characterization of the momentum transport is presented. The resulting radial momentum diffusivity, of the order of $\chi_\phi \sim 0.1 - 0.3\ \mathrm{m}^2/\mathrm{s}$, exceeds by 2 orders of magnitude the neoclassical estimation. A remarkable result is the existence of a "residual stress" component, which sustains a substantial stationary rotation gradient for null background rotation. Conversely, the analysis suggests a minor role for the convective (*pinch*) component, that is preliminarily confirmed by gyro-kinetic simulations including turbulent Coriolis convective pinch. Neoclassical predictions are in quantitative and qualitative disagreement with the experimental observations.

The effect of the sawtooth instability on the core rotation was addressed in a specific experimental scenario where the inter crash evolution of the core u_ϕ could be measured. The measurement required the development of a fast CXRS acquisition scheme based on a trigger constructed in real time from a Soft X-ray measurement. At the sawtooth crash the plasma core undergoes a strong acceleration in the co current direction ($\Delta u_\phi \approx 9$ km/s in the experimental scenario), possibly related to a strong transient toroidal electric field.

The systematic and varied observations reported in this work extend the experimental knowledge of bulk plasma rotation in low confinement regimes. In particular, the rotation reversal phenomena constitute an important test for momentum transport models of tokamak plasmas.

Keywords: plasma physics, nuclear fusion, tokamak, TCV, plasma rotation, intrinsic rotation, toroidal rotation, poloidal rotation, rotation reversal, momentum transport, plasma diagnostic, charge exchange, CXRS.

Sinossi

La ricerca per la fusione termonucleare controllata è un campo tra i più attivi nella fisica dei plasmi, e ha per obiettivo la produzione di energia tramite reazioni di fusione tra nuclei di isotopi dell'idrogeno, le stesse reazioni che alimentano le stelle. Attualmente una via promettente è rappresentata dai *Tokamak*, macchine toroidali nelle quali plasmi ad alte temperature vengono confinati da campi magnetici. Questa tesi è dedicata allo studio della rotazione del plasma all'interno del *Tokamak à Configuration Variable* (TCV) presso il *Centre de Recherches en Physique des Plasmas* di Losanna, in Svizzera.

Nei tokamak il confinamento è limitato dal trasporto di energia e particelle dal centro verso il bordo e da perturbazioni macroscopiche dell'equilibrio magnetico. Recentemente ci si è resi conto degli effetti benefici che la rotazione ha sulla stabilità e il confinamento del plasma. Tuttavia la fisica che sta alla base della rotazione, ed in particolare della rotazione intrinseca del plasma, è ancora per certi versi poco nota. Ciò spiega il grande sforzo teorico e sperimentale impiegato in questo campo di ricerca, nel quadro del quale si inserisce anche questo lavoro.

In TCV, la rotazione del plasma viene misurata dalla diagnostica di spettroscopia di scambio carica (CXRS). Il segnale viene fornito dall'osservazione perpendicolare di un fascio di atomi neutri iniettato nel plasma dall'iniettore DNBI. La bassa potenza del DNBI non perturba lo stato di rotazione del plasma, permettendo una misura della rotazione intrinseca.

Durante questa tesi, al preesisteente sistema di osservazione toroidale, sono stati affiancati due sistemi per la misura della rotazione toroidale nella parte interna del toro a della rotazione poloidale nella parte esterna. La misura della rotazione con una precisione di 1 km/s è stata resa possibile da una procedura automatica di calibrazione basata su spettri di Neon noti. Durante la tesi l'intera diagnostica è stata modificata, per potenziarne la risoluzione spaziale e la sensibilità, ampliandone al contempo il campo visivo.

Attualmente la diagnostica (CXRS09) misura le rotazioni toroidale e poloidale del plasma con una risoluzione radiale di 1 cm, a frequenze di $10 \div 20$ Hz, per plasmi di densità elettonica $0.8 \lesssim n_e \lesssim 8 \times 10^{19}\,\mathrm{m}^{-3}$.

Il lavoro sperimentale si è dapprima concentrato sullo scenario base di plasmi confinati in configurazione *limiter* con riscaldamento Ohmico. In questa configurazione, il plasma ruota in direzione contraria alla corrente di plasma con velocità che raggiungono i 50 km/s. Il profilo di rotazione toroidale può essere diviso in una zona interna in cui è piatto o concavo in direzione della corrente, una zona intermedia in cui la rotazione diminuisce col raggio e una zona esterna in cui la rotazione èvicina allo zero. La rotazione poloidale misurata è dell'ordine di $2 \div 3$ km/s, in accordo con le previsioni della teoria del trasporto neoclassico, sia per ampiezza che per direzione.

La rotazione toroidale inverte spontaneamente direzione a densità $n_\mathrm{e} > 4 \times 10^{19}\,\mathrm{m}^{-3}$ e $q_e \approx 3$ e questo fenomeno è stato al centro degli studi di questa tesi. Si è studiato in sequenze di plasmi stazionari e in plasmi in cui i parametri venivano variati dinamicamente. Nonostante le numerose osservazioni sperimentali correlate (effetto delle impurezze, effetto della forma, ecc.), il meccanismo fisico alla radice della transizione non e' ancora stato individuato.

Lo studio successivo dei plasma confinati in configurazione magnetica *diverted* ha messo in luce un'estrema variabilità della velocità del plasma nella regione periferica, non osservata nei plasmi *limiter*. Dal confronto con misure di diagnostiche di bordo è emerso lo stretto legame tra la velocità toroidale e i flussi di particelle presenti nella zona che circonda il plasma confinato (Scrape-Off Layer).

Lo studio del trasporto di momento angolare, sulla base delle osservazioni raccolte, ha evidenziato che la viscosità del plasma è di due ordini di grandezza maggiore delle previsioni della teoria neoclassica, indicando che fenomeni turbolenti sono alla base degli elevati valori di trasporto osservati sperimentalmtente. Simulazioni preliminari della componente turbolenta del trasporto di momento, eseguite col codice girocinetico GKW, indicano la presenza di una componente convettiva, tuttavia insufficiente a spiegare le velocità intrinseche osservate in TCV.

Attuando una strategia sperimentale specifica si è potuta misurare l'evoluzione della rotazione toroidale nell'intervallo compreso tra i collassi periodici del centro del plasma, associati all'intabilità "dente di sega". La misura ha richiesto lo sviluppo di un nuovo sistema di acquisizione per la diagnostica CXRS, basato su un segnale di trigger esterno, a sua volta costruito sulla base di misure in tempo reale di emissione di raggi X. I risultati indicano che, per effetto del dente di sega, la rotazione centrale del plasma subisce un aumento sostanziale (9 km/s nel caso in studio). Questo comportamento può essere legato al campo elettrico toroidale che si sviluppa durante il fenomeno di collasso.

Le osservazioni sistematiche raccolte durante questo lavoro di tesi estendono la conoscenza sperimentale della rotazione intrinseca del plasma. In particolare, i fenomeni di inversione spontanea della rotazione del plasma, costituiscono una solida base sperimentale per testare i modelli teorici di tresporto di momento angolare.

Parole chiave: fisica dei plasmi, fusione nucleare, tokamak, TCV, rotazione del plasma, rotazione intrinseca, rotazione toroidale, rotazione poloidale, inversione di rotazione, trasporto di momento, diagnostica del plasma, scambio carica, CXRS.

Contents

Chapter 1

Introduction

1.1 Context: fusion and tokamak

In the present day, much effort is being expended in the attempt to tackle the problem of the rising energy demand. Among the energy sources that are being developed, controlled thermonuclear fusion presents many advantages, such as safe large-scale energy production, abundant and geographically distributed fuel, no production of greenhouse gasses, little waste requiring long term storage. These advantages also present difficult scientific and technological challenges, principally related to the fact that fusion reactions take place only when the kinetic energy of reacting nuclei overcomes the electrostatic repulsion. For example, cross section of the primary reaction (fusion between deuterium and tritium) is significant only if the collision energy is larger than 10 keV. For a reaction rate relevant for large scale energy production, this energy, corresponding to a temperature exceeding 100 million degrees, must be transmitted to a large number of particles during a sufficiently long time. At the required temperature and density, deuterium and tritium are totally ionized and form a gas of ions and electrons called a plasma. Being this constituted by charged particles, a plasma can be confined by magnetic fields. Several concepts of magnetic confinement devices have been proposed and studied to date, among which the tokamak and stellarator have attained the best performance.

After half a century of progress in the research on plasma physics and magnetic confinement, a large international project is being finally undertaken: the construction of the International Thermonuclear Experimental Reactor (ITER) [1]. ITER will be the first prototype of fusion reactor, based on the tokamak magnetic confinement concept, capable of producing up to 0.5 GW of thermal power, continuously for 500 s. ITER is the result of negotiation between China, South Korea, United States, Europe (including Switzerland), India, Japan and Russia, and its mission is the scientific demonstration of the feasibility of a nuclear fusion power plant.

In parallel with the ITER project, whose construction is planned for 2018, research institutes are continuing in their effort to extend the scientific and technologic knowledge required for the energy production from thermonuclear fusion. In this context, the research work presented in this thesis was carried out on the *Tokamak à configuration Variable* (TCV) at the *Centre de Recherches en Physique des Plasmas* in Lausanne, Switzerland.

1.2 Plasma confinement: the *tokamak* configuration

In this chapter we will introduce some basic concepts that will be useful in the understanding of this thesis. Nevertheless, we will not go into great detail about magnetic plasma confinement's principles, which have been described many times elsewhere [2–4]. For a detailed description of

the tokamak configuration, see [5].

In a tokamak, plasma is contained in a toroidal vacuum vessel in which a strong confinement magnetic field B_ϕ is generated by external magnetic coils (Fig. 1.1). A toroidal plasma current I_p is induced by a solenoid passing through the torus center, acting as the primary circuit of a transformer, whose secondary is represented by the plasma ring. Plasma current has a two folded role: it constitutes the basic plasma heating mean, by ohmic heating, and provides a poloidal magnetic field B_θ that compensates for particle drifts that otherwise will make the configuration unstable [5]. A small vertical field (B_z) created with external coils is also required to avoid the radial expansion of the plasma ring as the pressure increases.

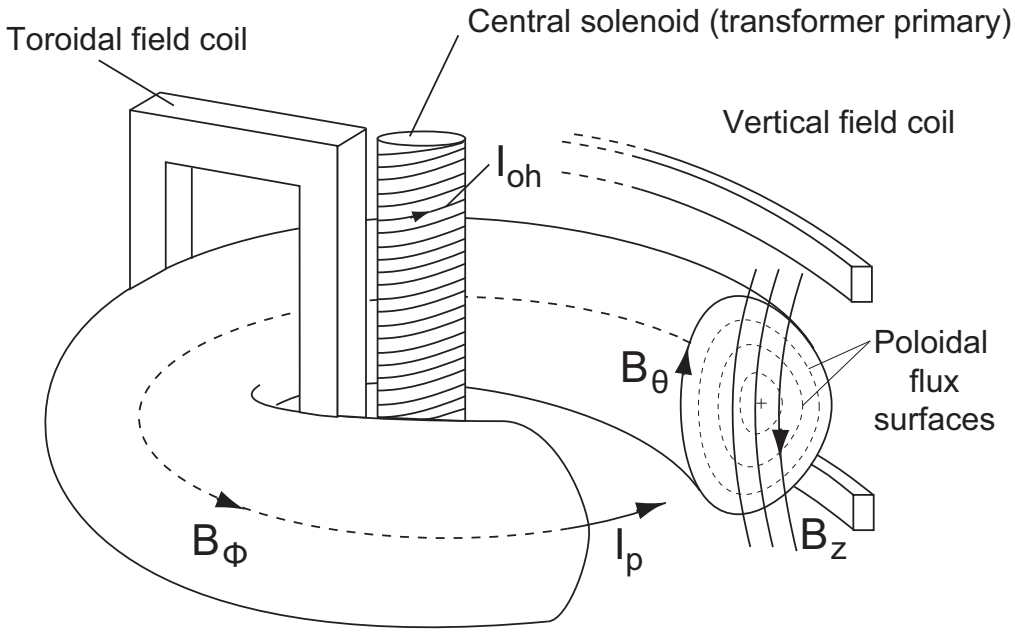

Figure 1.1: Schematic representation of the tokamak device.

The three components $B_\phi > B_\theta > B_v$ combine to produce a resultant helical magnetic field. The field lines lie on nested surfaces centered on the magnetic axis. These surfaces correspond to the locus of constant poloidal magnetic field flux ψ.

In this axisymmetric configuration, heat and particles are transported much faster along magnetic field lines than across the field. Therefore, to first approximation, temperature and density are uniform on magnetic surfaces and may thus be described as function of a radial coordinate, that labels the flux surfaces. In this work we adopt the common convention by which the radial coordinate is the normalized poloidal flux, defined as:

$$\rho_\psi = \sqrt{\frac{\psi - \psi_0}{\psi_a - \psi_0}} \tag{1.2.1}$$

where $\psi_{0,a}$ are the poloidal flux at magnetic axis and the plasma boundary.

For any field line, the number of toroidal turns required to complete one poloidal turn is indicated by q, termed the safety factor for its implications for plasma stability. In cylindrical large aspect ratio approximation, the safety factor may be written as:

$$q = \frac{rB_\phi}{R_0 B_\theta} \tag{1.2.2}$$

where r is the plasma minor radius, R_0 is the plasma major radius. Each flux surface is characterized by a specific value of the safety factor. Surfaces corresponding to rational values of $q = m/n$,

also called rational surfaces, play an important role in plasma stability. On rational surfaces field lines close on themselves after m poloidal loops and n toroidal loops, facilitating the development of resonant magnetic perturbations and the onset of various type of instabilities [2].

The plasma boundary is defined by the Last Closed Flux Surface (LCFS). On one side of the LCFS lies the confined plasma on closed flux surfaces. On the other side the magnetic field lines are open and terminate on material structures. The latter region is called Scrape Off Layer (SOL) and constitutes the interface between the confined plasma and the first wall. Its study is of primary importance for fusion, especially for erosion and redeposition issues [6].

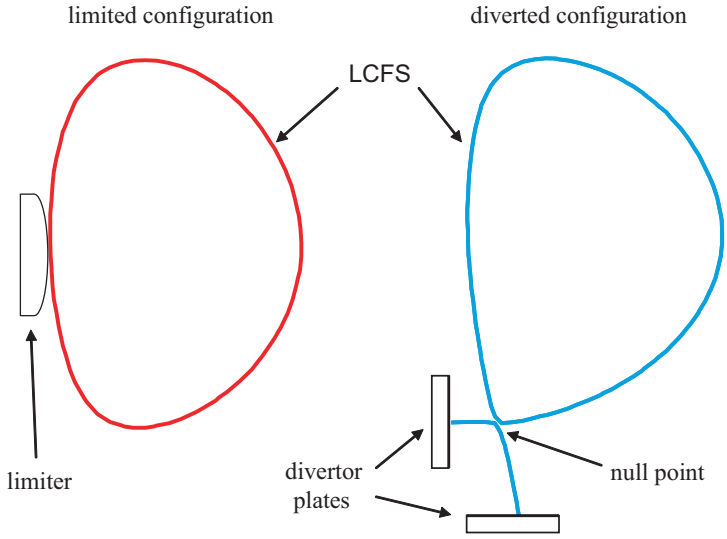

Figure 1.2: Schematic representation of the limited (left) and diverted (right) configurations.

The way in which the LCFS is created distinguishes between *limited* or *diverted* magnetic configurations (Fig. 1.2). In the first case, the LCFS is determined by the presence of a limiter, i.e. a solid element in direct contact with the plasma. In this configuration, any impurity released by plasma-surface interaction on the limits can enter the main plasma. In diverted configurations a null point of poloidal field (also called X-point) is created by means of externally applied poloidal fields, that divert the open field lines and localize the plasma-surface interaction in a specific device, called divertor. Moreover, open field lines in the vicinity of the X-point, where the poloidal magnetic field is null, are extremely long before intercepting the machine structure. Hence in diverted configuration, cooling of exhausted plasma by radiation and neutralization is largely facilitated, with beneficial effects for heat load and impurity release at the divertor targets.

1.3 The TCV tokamak

The *Tokamak à Configuration Variable* (TCV) [7] is a medium size tokamak, explicitly designed to study how stability and confinement of the plasma are influenced by the shape of poloidal cross section. A schematic representation of TCV is presented in Fig. 1.3. The stainless steel vacuum vessel (C) has an elongated cross section designed to house plasmas with extremely variable shape. The plasma shaping capability is ensured by 16, independently power supplied, toroidal coils (D). The vertical stability, particularly critical for elongated plasmas, is ensured by two set of in-vessel toroidal coils (F). The toroidal magnetic field is provided by means of 16 poloidal coils (B). A set of 9 ohmic coils located around the central column constitute the primary circuit of the transformer and are used to induce the toroidal plasma current (A).

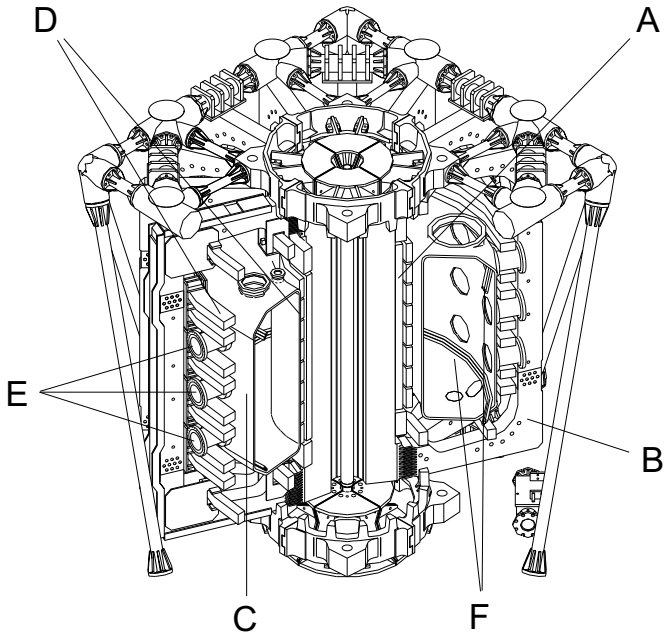

Figure 1.3: Schematic representation of the TCV tokamak. The main elements are indicated: vacuum vessel (C), shaping coils (D), poloidal coils that produce the toroidal magnetic field (B), toroidal coils used to stabilize elongated plasmas (F), ohmic coils used to induce the plasma current (A), access windows to the vacuum vessel (E) and the mechanical structure.

A summery of the technical specifications of the TCV tokamak, together with a sketch of the typical plasma parameters obtained are found in table 1.1 and 1.2.

A selection of plasma cross sections obtained in TCV is showed in Fig. 1.4. From magnetic reconstruction (see section 1.5.2) the plasma shape may be described by two parameters: elongation k and triangularity δ, that correspond to the first and second moment of the poloidal cross section. Their definition is explained in Fig. 1.5 and they are defined for all magnetic surfaces.

1.4 Electron Cyclotron heating system

In TCV, ohmic heating is provided by the plasma current by Joule effect and permits the plasma to attain electron temperatures up to 2 keV. An auxiliary heating system is also available that exploits the resonant interaction between microwave beams and plasma electrons along the gyration across the magnetic field lines. The microwave energy is transmitted to electrons whose gyration frequency is a multiple of the wave frequency. This localizes the heat deposition along an approximately vertical resonance layer determined by the magnetic field.

In TCV, a total of 4.5 MW of Electron Cyclotron (EC) power can be injected in the plasma for a total duration of 2 s. This power is provided by 9 gyrotrons of nominal power of 0.5 MW, 6 of which at the 82.7 GHz frequency and the remaining 3 at 118 GHz. For the typical magnetic fields of TCV these two frequencies correspond at the 2nd and 3rd harmonic of the EC frequency. For optimal power coupling, the EC waves are usually polarized in extraordinary mode (X mode), i.e. with the oscillating electric field orthogonal to the confinement magnetic field. 30 m long wave guides lead the beams generated by gyrotrons to launcher elements installed on TCV ports. The placement of the launchers is depicted in Fig. 1.6.

The second harmonic launchers (X2) are located on 6 lateral ports, and are equipped with a

Parameter	Symbol	Value
Major radius	R_0	0.88 m
Minor radius	a	0.255 m
Internal height of vessel	h	1.5 m
Aspect ration	$\epsilon = R_0/a$	$2.9 \div 3.8$ m
Vessel elongation	κ_{TCV}	3
Vessel time constant	τ_{vessel}	6.7 ms
Toroidal magnetic field on axis	B_ϕ	± 1.44 T
Loop voltage	V_{loop}	$1 \div 2$ V
Plasma current	I_p	≤ 1 MA
Ohmic heating power	P_{OH}	≤ 1 MW
X2 RF heating power	$P_{ECH}X2$	2.8 MW
X3 RF heating power	$P_{ECH}X3$	1.4 MW
Vessel base vacuum		$< 10^{-7}$ mbar

Table 1.1: Main technical specifications of the TCV device.

Parameter	Symbol	Value
Main plasma species		D (He, H)
Plasma width	w	≤ 0.48 m
Plasma height	h	≤ 1.44 m
Edge plasma elongation	κ_a	$0.9 \div 1.8$
Edge plasma triangularity	δ_a	$-0.8 \div 1$
Electron density	n_e	$\leq 10{\times}10^{19}\,\mathrm{m}^{-3}$
Electron temperature (OH)	T_e	≤ 1 keV
Electron temperature (ECH)	T_e	≤ 15 keV
Ion temperature	T_i	$\leq 0.1 \div 1$ keV
Electron plasma frequency	f_{pe}	$28 \div 120$ Ghz
Electron cyclotron frequency	f_{ce}	41 Ghz
Ion plasma frequency	f_{ci}	11 Ghz
Electron Larmor radius	ρ_e	$70 \div 250$ μm
Ion Larmor radius	ρ_i	$2.5 \div 4$ mm

Table 1.2: Main parameters of the TCV plasmas.

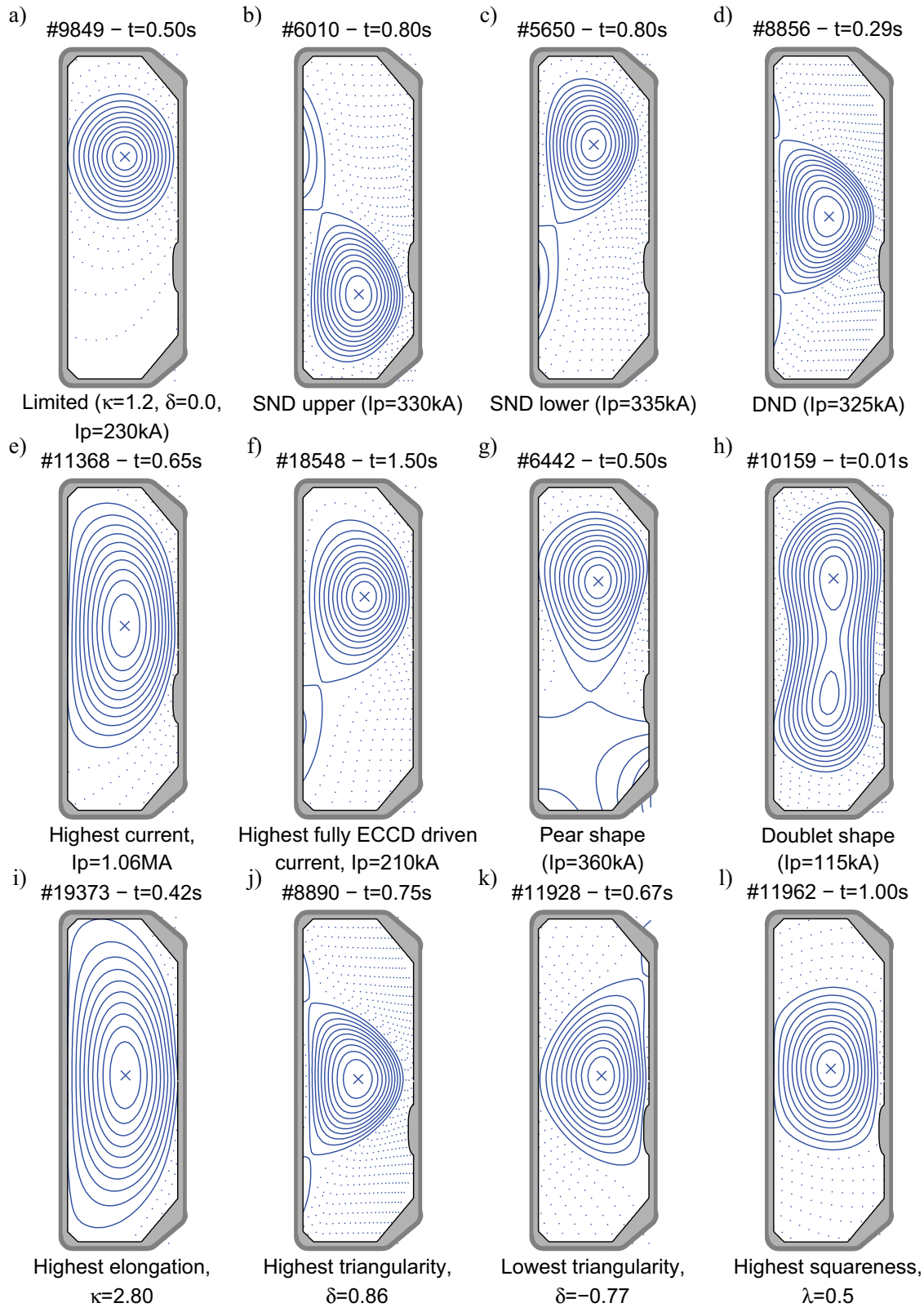

Figure 1.4: Selection of plasma cross sections that have been achieved in several years of TCV operation. The plasma shape is obtained from the magnetic equilibrium reconstruction LIUQE (see section 1.5.2).

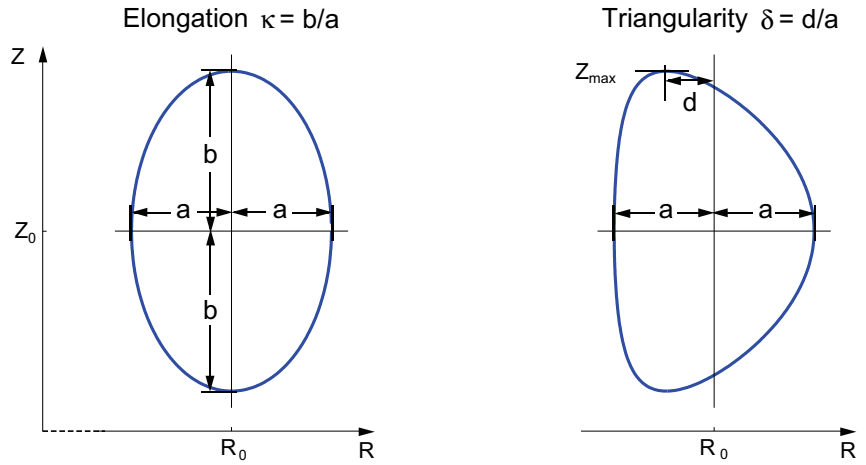

Figure 1.5: Definition of the plasma shape parameters k (elongation) and δ (triangularity).

mirror system allowing injection at different poloidal and toroidal angles. The variation of poloidal angle together with the variation of B_ϕ allow an extremely localized power deposition across all the plasma cross section. Injection with a non null toroidal angles can result in a net toroidal current contribution.

Plasma heating by mean of X2 waves is restricted to electron densities lower that the cut-off density $n_e = 4.25 \times 10^{19}\,\mathrm{m}^{-3}$. The X3 heating systems, characterized by a cut-off density of $n_e = 11.5 \times 10^{19}\,\mathrm{m}^{-3}$, overcomes this limit. Here, the beams are launched vertically from the top of the TCV vessel in order to maximize the path along the resonance layer and enhance the otherwise weak absorption. The power deposition is less localized compared to X2.

In all, the EC constitutes a flexible system, capable of heating the great variety of TCV plasmas, attaining electron temperatures of 18 keV. Furthermore, a plasma discharge can be fully sustained by exclusive use of EC driven current [8].

No high power auxiliary ion heating system is available on TCV. Since ohmic heating predominantly heats the electrons, the ion temperature is determined by the friction with electrons. As the collisional coupling between the two species decreases with the temperature differences between ions and electrons, in strongly EC heated discharges T_i is much lower than T_e.

1.5 TCV diagnostics

TCV benefits from a rich and versatile set of diagnostics that permits measurements of the most important plasma parameters, and this for the extraordinary variety of shapes and positioning that TCV allows for. The following paragraphs will describe briefly the diagnostics that were most relevant for this thesis.

1.5.1 Mirnov coils

Poloidal magnetic field fluctuations are measured by means of ten arrays of Mirnov probes located inside the vacuum vessel, protected behind first wall graphite tiles. Probe arrays consist of 38 individual pick-up coils.

Four of these arrays are arranged in poloidal rings separated by 90° in toroidal direction. Three other pairs of toroidal arrays are located at different vertical positions ($z = -0.35$, 0, $+0.35$ m on the equatorial plane). Each pair is composed of one array of 8 probes located at the inboard

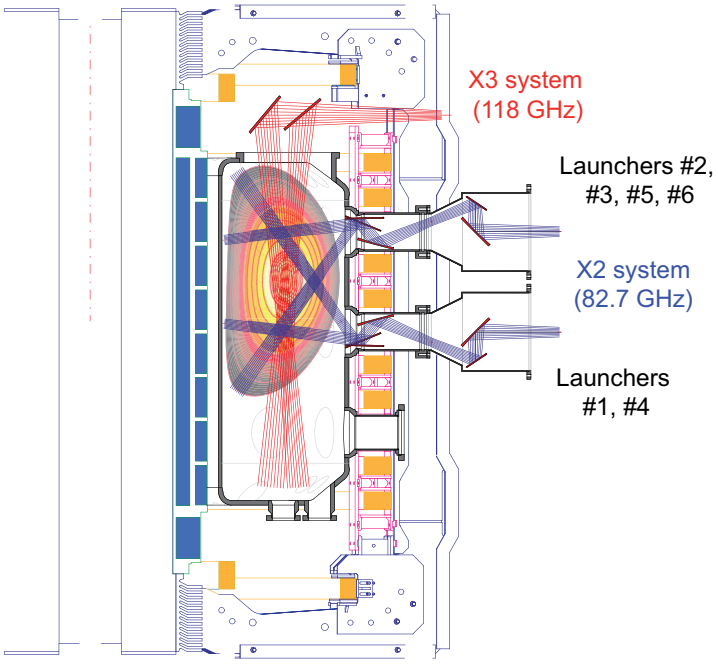

Figure 1.6: Schematic of the flexibility of ECH beam injection.

wall and one of 16 probes located at the outboard wall with all probes toroidally equispaced. The Low Field Side (LFS) arrays are complemented by a 17th probe, which serves to increase resolve structures of high toroidal periodicity.

Mirnov probes measurements are used for the magnetic equilibrium reconstruction as well as to characterize the Magneto Hydro Dynamic (MHD) activity. Acquisition frequencies up to 1 MHz are possible. Frequency between $50 \div 125$ kHz is although sufficient to measure MHD activity observed in most of the experiments presented in this work.

1.5.2 Magnetic equilibrium reconstruction

The plasma magnetic equilibrium is computed by the LIUQE code [9], using measurements of poloidal magnetic flux provided by the probes located inside and outside the vacuum vessel [10]. The code iteratively solves the Grad-Shafranov equation in order to obtain a poloidal flux description with the closest match to magnetic probe measurements. In order to improve the quality of this reconstruction, in particular in the central plasma region, additional constraints may be imposed, such as the plasma pressure profile (from Thomson scattering diagnostic), the description of the sawtooth inversion radius surface (from tomographic inversion of XTOMO diagnostic measurements), or the total energy, measured by a diamagnetic coil. The latter has been systematically applied for all experiments reported here.

1.5.3 Electron diagnostics

1.5.3.1 Thomson scattering

The Thomson scattering diagnostic provides local measurements of both electron temperature and density [11]. Temperature is evaluated through spectral analysis of the light of a laser beam, after it has been scattered by plasma electrons. The intensity of the scattered light is a measure of the electron density.

The TCV Thomson scattering diagnostic [12] employs three Nd-Yag lasers, at the wavelength of 1.064 μm, capable of 1 J pulses at a repetition rate of 20 kHz. The beam path of the lasers overlap, so that they can be used either simultaneously to increase the experimental signal to noise ratio, or temporally displaced in order to increase the sample rate of the measurement.

Temperature and density are measured for 25 plasma volumes, vertically separated by around 4.5 cm (Fig. 1.7a). The radial profiles are calculated by mapping the measurements to the reconstructed equilibrium. The Thomson scattering is the main diagnostic for electron temperature measurement, combining good spatial resolution with low systematic errors (less that 5%). Density measurement are prone to absolute calibration drifts. The absolute value of the electron density is adjusted to the FIR diagnostic.

1.5.3.2 FIR

The Far Infra Red (FIR) interferometer evaluates the electron density from the change in phase of a laser beam acquired as it passes across the plasma. The change of phase, detected by comparison with a reference laser beam, is proportional to the integral of the electron density along the beam path inside the plasma [11]. The TCV FIR diagnostic measures the integral density along 14 vertical chords, shown in Fig. 1.7b, with a typical precision of 1%. Normally, the acquisition rate is 20 kHz, but can be increased to 750 kHz. The dashed view line in the figure is used for feedback control of the gas value and thus the density. From the equilibrium reconstruction, the line average density along each chord is calculated. Moreover, by means of an Abel tomographic inversion of integral data, the radial density profile can be reconstructed. The method usually employed uses the Singular Value Decomposition technique with base functions from the Thomson scattering profiles.

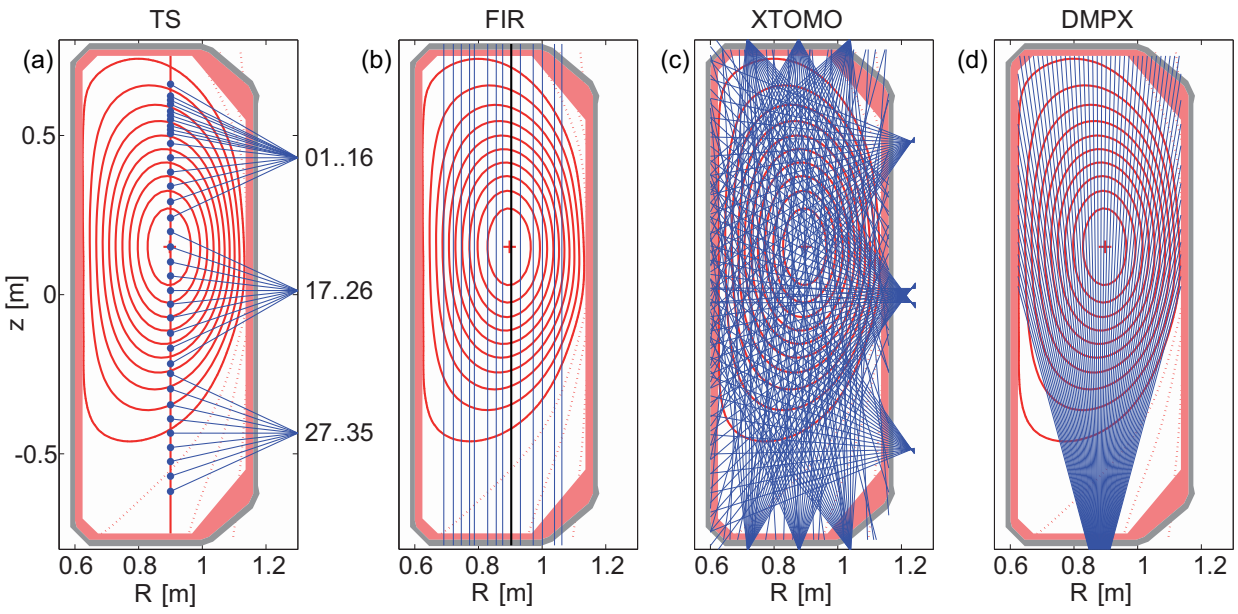

Figure 1.7: Measurement volumes of Thomson scattering along the laser path (a); viewing chords of the FIR (b), XTOMO (c) and DMPX (d) diagnostics. The measurement of highlighted central chord of FIR is used as reference for Thomson scattering cross calibration.

1.5.4 Soft X rays diagnostics

In tokamak plasmas the Soft X Ray radiation spectrum (X-ray radiation with energy <15 keV) is composed of bremsstrahlung radiation, line radiation from heavy impurities and electron ion recombination [13]. Several diagnostics are available on TCV to detect SXR, with particular emphasis on temporal and spatial resolution and spectral coverage. We will only describe here the two systems that have been particulary important for this work: XTOMO and DMPX. They provide information on MHD instabilities, in particular their poloidal mode structure of helical magnetic perturbations and of the sawtooth inversion radius and characteristics.

1.5.4.1 DMPX

The Duplex Multiwire Proportional X-ray counter (DMPX) [14] is housed in a helium filled camera located at the bottom of the TCV vessel. It observes the plasma through two beryllium windows (total thickness of 100 μm) in the energy range between 1 and 30 keV. Beryllium filters remove photons with energies below 1 keV, and additional aluminium foils can be used to observe higher energy photons (exceeding 15 keV). 64 chords span the plasma cross section, with an effective radial resolution of about 1 cm (see Fig. 1.7d). From the line integrated measurements, calibrated against a known source, the emissivity profile can be calculated through Abel inversion. However, this procedure assumes the iso emissivity on flux surfaces and poloidal symmetry.

1.5.4.2 XTOMO

The SXR tomographic system XTOMO [15] consists in ten linear detector arrays equipped with strips of 20 silicon diodes. With a 47 μm thick beryllium absorption foils in front of each array, the measured energy range covers 1-15 keV. The arrays are distributed on 9 poloidal ports on the same toroidal sector (Fig. 1.7c). 200 chords provide full poloidal coverage and are used to perform a tomographic reconstruction of the 2D emissivity, which is possible for virtually all plasma configurations, with a spatial resolution of 3-4 cm and an acquisition rate of 80 kHz. Thanks to its dense coverage of the plasma cross section, XTOMO has the precious capability of resolving the poloidal structure of the SXR emission.

1.5.5 Ion diagnostics

1.5.5.1 CXRS

The Charge eXchange Recombination Spectroscopy (CXRS) diagnostic provides local measurements of ion temperature and impurity density, as well as toroidal and poloidal rotation, through the analysis of spectral moments of an impurity line radiation, typically CVI 529.1 nm. In TCV, the line is populated by charge exchange (CX) reactions between intrinsic impurity (carbon) and a diagnostic neutral beam, which is weak enough to not perturb the plasma significantly. This permits CX measurements in the absence of auxiliary ion heating and external input torque. The development and maintenance of this diagnostic represented part of present work. This diagnostic will be described in detail in chapter 2.

1.5.5.2 Neutral particles analyzers

Even if most of the particles of a tokamak plasma are ionized, a non vanishing neutral density exists in the plasma core: it results from successive charge exchange reactions with neutrals atoms that, initially, come from the neutral gas surrounding the plasma.

A certain number of hot core ions that are neutralized by CX may escape the plasma without any further interaction. From the energy spectrum of such particles, a Neutral Particles Analyzer (NPA) can recover the parameters of the ion distribution function. TCV features two complementary diagnostic of this kind:

- the Vertical Neutral Particle Analyzer (VNPA), which collects neutrals along a vertical chord. The five detection channels, combined with an energy sweeping analyzer, allow an ion energy coverage of 0.6-8 keV, with a time resolution from 0.05 to 2 ms. However, hydrogen (H) and deuterium (D) ions are not resolved.

- the Compact Neutral Particle Analyzer (CNPA), that houses two arrays of 11+17 channels. These permit the separate measurement of the two mass species, D and H, with the energy range of 0.5-50 keV. The observation chord lies on the midplane, and can be set to either perpendicular or tangential direction (45°), in order to study properties of the perpendicular or parallel distribution function. During this thesis, the perpendicular configuration was adopted.

The VNPA and CNPA provide complementary measurements of the ion energy distribution function [16] and may be compared to the CXRS measurements. A ion temperature estimate can be obtained from the lower part of the energy spectrum from the NPA, while the high energy tail measurement eludes the CXRS observation (thermal energy).

NPAs' are inherently line integrated measurements. Nevertheless, through interpretative codes that predict the neutral spectrum as function of main plasma parameters' profiles [16, 17], some localization can be recovered. In particular, this can lead to an estimate of the neutral density profile, which is important to this work, for its role in the emission background of charge exchange light and particle friction forces.

1.5.6 Reciprocating Mach probe (RCP)

Parallel particle flows in the Scrape-Off Layer (SOF) have been measured using a fast reciprocating system [18], which inserts a 5 pin Langmuir probe head into the SOL plasma via a port located on the LFS vacuum vessel midplane. Fig. 1.8 illustrates the probe trajectory into a standard Lower Single Null (LSN) diverted equilibrium. Although the RCP position on the torus is fixed, the shape flexibility offered by TCV allows for vertically displacements of the plasma, so that different locations on the poloidal contour can be probed. This flexibility requires different probe heads, arranged in such a way that the pins match the poloidal contour of the magnetic equilibrium.

The pins labeled 1 and 2 in the photographic insets of Fig. 1.8 are the field aligned Mach probe pairs, from which the parallel flow Mach number is derived as the ratio of ion saturation currents: $M_{||} = u_{||}/c_s \approx 0.4 \ln(I_{sat,1}/I_{sat,2})$, where c_s is the ion sound speed. The poloidal array of 3 pins set in the central bar separating the Mach probe sensors provides SOL profiles of T_e and n_e, as well as pin floating potential, used to estimate the plasma potential [18].

Typically two probe reciprocations are made into each plasma discharge. Each scan provides the radial profiles of all quantities over a 2 cm slice of SOL plasma. From the combined measurement of pressure $p_e = n_\mathrm{e} T_\mathrm{e}$ and flows, the radial electric field can be deduced using the radial momentum balance equation.

Notice that, since the RCP measurement relies on current measurements, it does not distinguish between different ion species. In other words, the RCP measures a single fluid plasma velocity. In most cases, for the typical impurity contamination of TCV discharges, this corresponds, to a good approximation, to the main ion flow.

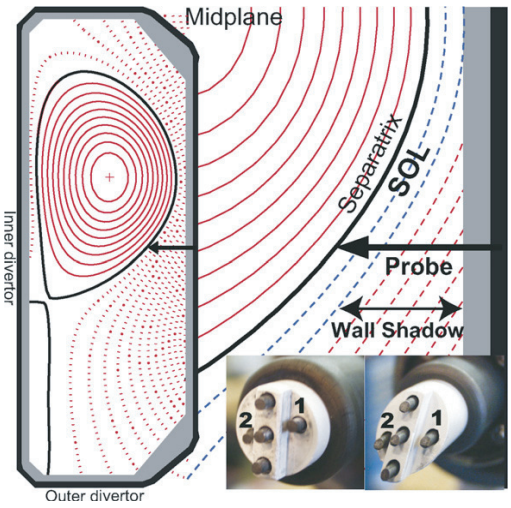

Figure 1.8: Schematic illustration of the probe insertion location for a typical Lower Single Null configuration. In the bottom insets are represented two Mach probe heads adapted for different plasma positions.

1.6 Thesis object and outline

In a tokamak, the plasma confinement is limited by the radial transport of energy and particles from the hot dense core to the cold plasma edge. A large fraction of radial transport is driven by turbulence related to small scale instabilities, whose origin is only partially understood.

Other important detrimental effects derive from macroscopic instabilities, the Magneto Hydro Dynamic (MHD) modes, that may alter the tokamak magnetic equilibrium, with consequences on both plasma confinement and stability.

Plasma rotation has been experimentally demonstrated to have beneficial effects on both confinement and stability. In toroidal devices, the radial shear of plasma flows can lead to turbulence decorrelation or even suppression, as observed when the plasma configuration transits from low (L-mode) to high confinement regime (H-mode), or at the formation of Internal Transport Barriers (ITB). At the same time, a sufficiently high plasma flow is observed to stabilize Resistive Wall Modes (RWM), which are MHD instabilities partially stabilized by the proximity of a conducting wall. These are particularly relevant for advanced reactor test experiments such as ITER.

In many present day fusion devices, plasma momentum is applied externally by the tangential injection of heating neutral beams. The presence of a substantial intrinsic toroidal rotation has also been observed in plasmas with no externally applied torque. This so called "spontaneous rotation" is important in next step devices, where the toroidal momentum driven by auxiliary heating systems may not dominate that generated by the plasma itself [19]. To date, the physical mechanisms generating the angular momentum, within the plasma, remain an open issue.

From an experimental point of view, a phenomenological description of intrinsic plasma rotation permits the formulation of scalings laws [20, 21], summarizing the dependencies of plasma flow on main discharge parameters. Such scaling laws may then be used to extrapolate the rotation to largest devices and are useful to validate or discard theoretical models.

The objective of this thesis is to characterize the intrinsic rotation of the TCV tokamak plasma, highlighting the role of main plasma parameters, and to identify the physical mechanisms that are best suited to explain the radial transport of momentum across the plasma.

In particular, the physics questions that this work addresses are:

- What are the intrinsic rotation's orders of magnitude, direction and profile?

- How does plasma rotation react to changes of main plasma parameters such as density, temperature and magnetic configuration?
- How fast and by which means does the plasma self accelerate or lose its momentum?
- What are the physical mechanisms best suited to account for the experimental observations?
- How do the present observations extrapolate to larger size devices as ITER?

This study is based on the first plasma rotation measurements in TCV, performed using the CXRS diagnostic. Setup and maintenance of this diagnostic constituted therefore a major part of this work. The diagnostic was required to provide local measurements of both toroidal and poloidal rotation. A diagnostic upgrade was completed, improving by a factor of two the radial resolution of toroidal rotation measurements and extending the coverage to the key region of the plasma edge.

The thesis is structured as follows:

- Chapter 2 is devoted to the CXRS diagnostic. First the measurement principles will be presented. Then CXRS diagnostic is described in detail, in particular its upgraded configuration (CXRS09), together with the analysis techniques employed.
- Chapter 3 presents a summary of concepts about plasma rotation and momentum transport in a tokamak device that will be useful in the following of the work.
- Chapter 4 describes the main features of intrinsic rotation in the basic configuration of limited L-mode, Ohmically heated.
- Chapter 5 reports the observations of spontaneous toroidal rotation reversals in limited L-mode, with a detailed description of the experimental scenario and the effect of main plasma parameters.
- Chapter 6 addresses the plasma rotation observations in diverted L-mode configuration, with emphasis on the relation between edge rotation and parallel particle fluxes present in the Scape-Off Layer.
- Chapter 7 collects studies that characterize the momentum transport in different plasma regimes, addressing the relative importance of different types of momentum transport/internal sources.
- Chapter 8 illustrates the methodology, the hardware setup and the results of experiments dedicated to explore the effect of sawtooth instabilities on core rotation profile, by means of fast time resolved measurements.
- Chapter 9 concludes this thesis summarizing the principal achievements and providing a brief outlook on the future investigation routes.

Chapter 2

CXRS diagnostic in TCV

The study of intrinsic plasma rotation and momentum transport requires high accuracy measurements of plasma rotation, with good spatial and temporal resolutions. In most present day tokamak devices such measurements are based on Charge eXchange Recombination Spectroscopy (CXRS), that permits the local measurement of ion temperature, velocity and density, from the observation of Doppler shift and line broadening of impurity line emission. The charge exchange emission required for the measurement is typically provided by the interaction of auxiliary heating neutral beams with the background plasma. However, while neutral beam injectors ensure abundant emission all along the plasma cross section, their effect on the background plasma is strong, not only in terms of heating but also in terms of externally applied torque.

In TCV, where no auxiliary ion heating is available, the CXRS diagnostic is performed with a specialized Diagnostic Neutral Beam Injector, that provides the line radiation from the hot plasma core without perturbing the plasma. Hence, the CXRS-DNBI tandem allows measurements of the so called intrinsic rotation of the plasma.

In the first part of this chapter, the principles of charge exchange spectroscopy will be introduced, with particular emphasis on effects that may affect the measurement of small plasma rotations, and their relevance to TCV.

In the second part the different technical aspects of the CXRS diagnostic, in its upgraded state at the end of this thesis, are presented. The spectral analysis methodology is discussed and, in particular, the absolute wavelength calibration technique developed to obtain the required accuracy is described.

The final section describes the DNBI and considers the perturbations that it may engender, to determine to what degree the measurements really correspond to spontaneous or intrinsic plasma rotation.

2.1 Measurement principle

The charge exchange recombination reaction between a plasma ion and a neutral atom results in the transfer of an electron from the neutral to an excited state of the target ion, characterized by principal quantum number n and orbital quantum number l. The reaction tends to populate high n energy and angular momentum levels, and the probability is maximized for approximately $n_{max} = Z^{3/4}$ [22]. A CX reaction which is often used for plasma diagnostic involves hydrogen neutrals and the fully ionized carbon impurity ions:

$$\mathrm{H}^0 + C^{6+} \rightarrow H^+ + C^{5+}(n,l) \tag{2.1.1}$$

The most probable populated state is $n = 4$, with the probability remaining non-negligible for larger n.

In typical tokamak plasmas, ionization times are longer than relaxation times, so the CX excited state decays to the ground state $n = 1$, through a cascade of transitions $(n, l) \rightarrow (n-1, l-1)$. This process is accompanied by the emission of multiple characteristic lines.

The structure of the CX cascade spectra depends on the probability of occupation and transition of the populated states, which depends on the plasma parameters. Typically, the emission covers the X-ray, Vacuum Ultra Violet and visible spectral regions. For diagnostic purposes, observation is often concentrated on visible spectral features where high resolution spectrometers and high quantum efficiency detectors are readily available.

From the spectral analysis of specific charge exchange lines the evolution of temperature, velocity and density of the recombining ion population is measured. In TCV, the CX measurement is optimized for the observation of transition of the CVI($n = 8 \rightarrow 7$) line at 529.1 nm spectral feature. With the near full graphite tiled vessel walls, carbon concentrations of 1% or higher are commonly found in TCV.[1] Fully stripped carbon is present with substantial density across the full plasma radius, and even in the edge region (SOL), due to radial transport from the hot plasma core [23, 24].

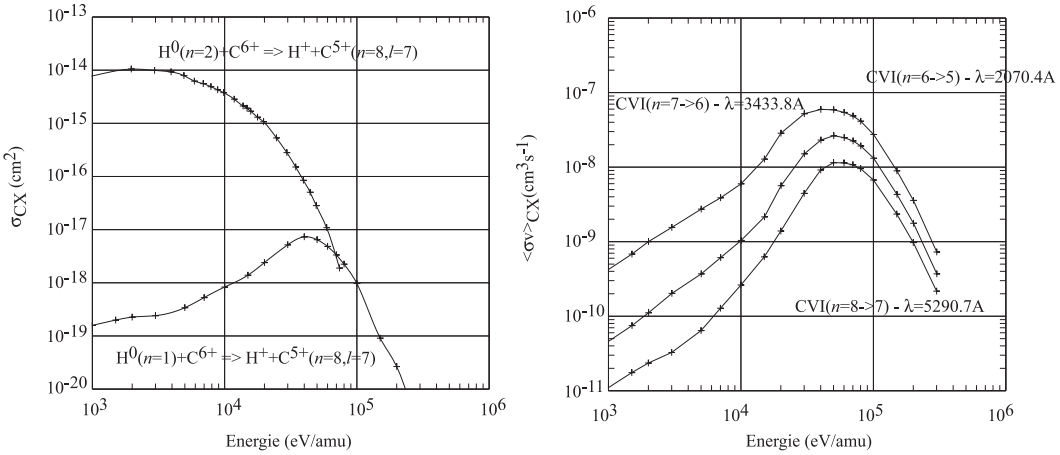

Figure 2.1: Left: cross section of the charge exchange capture from a donor for the reaction CVI($n = 8 \rightarrow 7$) . The cross section for excited n=2 donors is much higher at low energies. Right: effective cross section of the same reaction averaged over a Maxwellian distribution of carbon ions, as a function of the beam energy.

Neutral donor particles in the core region are typically provided by auxiliary heating neutral beams. These, however, strongly influence the background plasma, injecting energy and momentum into the plasma. On TCV, a Diagnostic Neutral Beam Injector is used (DNBI), whose low power, high energy and low injection angle obtain sufficient CX radiation, without perturbing significantly the plasma parameters.

As in many diagnostic systems, the neutral beam responsible for the charge exchange reactions in the plasma core is observed transversally (Fig. 2.6), so that ion parameters are measured locally, in the sense that they refer to the ions from the emitting volume defined by the intersection of view lines and neutral beam.

The CXRS diagnostic on TCV measures the carbon species density, temperature and velocity. It is important to examine to what degree these impurity based measurements are related to the behavior of the main plasma ions. Given the energy relaxation and heating times, carbon and main plasma ions (deuterium) are in thermal equilibrium on timescales that are faster than the

[1] This can be not the case after boronisation procedures. In this case the carbon content remains low and CXRS measurements are difficult for several days of TCV operation.

equipartition times of the CXRS diagnostic. Thus, to a good approximation, CXRS measures the main ion temperature (confirmed in Schlatter's Thesis [16] with measurements of ion temperature with Neutral Particle Analyzers).

With respect to plasma rotation, the question is more delicate since from neoclassical theory main ions and impurities are expected to rotate at different velocities (see chapter 3). Part of this thesis was dedicated to the verification of this issue in plasma discharges dominated by the intrinsic plasma rotation. In chapter 4 it will be shown that again, to a good approximation, carbon and hydrogen toroidal rotation are similar, whilst their poloidal rotation velocities may differ significantly.

2.2 Spectral profile

The lines observed by CXRS diagnostics are characterized by different broadening effects:

- Natural broadening, due to the finite lifetime of the excited state.
- Pressure broadening, due to the reduction of lifetime of the excited state in the presence of collisions with other particles.
- Doppler broadening, due to the Doppler shift averaged over the velocity distribution. For the case of a thermalized plasma the Maxwellian distribution results in a gaussian spectral profile.
- Fine structure of energy sub-levels of $(n \rightarrow n-1)$ transition, which means that observed line is, in reality, composed by a multiplet of different transitions. If the wavelength separation of the multiplet is small compared to e.g. Doppler broadening, this appears as line broadening.
- Zeeman and Stark effect that changes the sub level separation, which may result in further apparent broadening of the spectral line.

For the temperature and density of TCV plasmas, the spectral profile of the CVI line is dominated by the Doppler broadening. Furthermore, the ions in TCV are generally heated only by collisions with electrons, so that the ion distribution function is Maxwellian to a good approximation.[(2)]

For a small volume in which the plasma parameters do not vary significantly, the ion population (we consider carbon here) is described by a shifted maxwellian:

$$g(\mathbf{x},\mathbf{v}) = n_C \left(\frac{m_C}{2\pi T_C}\right)^{\frac{3}{2}} \exp\left[-\frac{1}{2}\frac{(\mathbf{v}-\mathbf{u})^2}{v_{th,C}^2}\right] \tag{2.2.1}$$

where $v_{th,C} = \sqrt{T_C/m_C}$ is the carbon thermal velocity, $\mathbf{u}$ is the average velocity and n_C the carbon density. The spectrum emitted in the direction of observation $\mathbf{e}_l$ assumes the form:

$$f(\lambda) = I \ \exp\left[-\frac{1}{2}\frac{(\lambda-\lambda_0)^2}{\Delta\lambda^2}\right] \tag{2.2.2}$$

(2) Substantial deviation from the Maxwellian are observed in TCV during Electron Cyclotron Current Drive (ECCD), when a suprathermal queue is measured. These features are not seen by the CXRS diagnostic which, for these cases, provides a measurement of the bulk population.

where I, λ_0 and $\Delta\lambda$ are the first three moments of the spectral profile $f(\lambda)$, related to the carbon density, velocity and temperature. Indicating with λ_{ref} the wavelength of the line free from motional Doppler shift we obtain:

$$\lambda_0 = \lambda_{ref}\left(1 + \frac{\mathbf{u}\cdot\mathbf{e}_l}{c}\right) \qquad \Delta\lambda = \lambda_{ref}\frac{v_{th,C}}{c} \tag{2.2.3}$$

The ion temperature and the ion velocity can be derived from:

$$T_\mathrm{i}[\mathrm{eV}] = \frac{m_C c^2}{e}\left(\frac{\Delta\lambda}{\lambda_0}\right)^2 \qquad\qquad \mathbf{u}\cdot\mathbf{e}_l = \frac{\lambda_0 - \lambda_{ref}}{\lambda_0} \tag{2.2.4}$$

In Fig. 2.2 these relations are illustrated for the case of CVI($n = 8 \rightarrow 7$) line: to discriminate velocities lower than 5 km/s the diagnostic must resolve line shifts of $\Delta\lambda \lesssim 0.1$ Å.

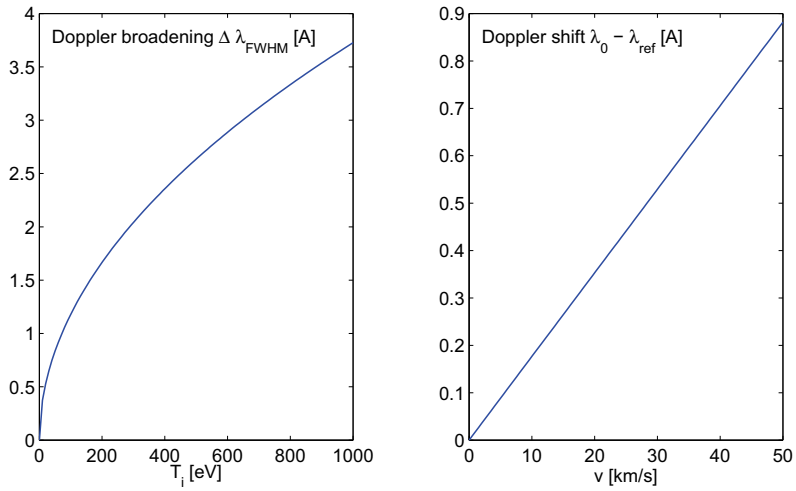

Figure 2.2: Relation between the ion temperature and velocity and line broadening and shift for the CVI($n = 8 \rightarrow 7$) carbon line.

The intensity I is function of the density of recombining ion and neutral donors in the emitting volume:

$$I[\mathrm{m^{-3}s^{-1}}] = \frac{1}{4\pi}\sum_i n_Z(x) n_{b,i} \langle\sigma v\rangle_{\lambda,i}(T_\mathrm{e}, n_\mathrm{e}) \tag{2.2.5}$$

where $n_Z(x)$ is the ion density of the considered impurity, $n_{b,i}$ is the neutral density of beam particles with energy E_i, i index indicates the DNBI component and $\langle\sigma v\rangle_{\lambda,i}$ is the effective cross section for charge exchange recombination of the considered transition as a function of the neutral energy, density and temperature of the plasma. Using the local density of the neutrals of all beam's energy fractions, together with the cross sections, the impurity density can be calculated from the measured line intensity. This measurement requires an absolute calibration of the diagnostic (see section 2.6.2), knowledge of cascade corrected effective CX emission cross sections $\langle\sigma v\rangle$, and the beam neutral density across the plasma obtained from a beam attenuation code [16, 23].

Experimentally, the measured charge exchange spectrum is the sum of the local contributions along the diagnostic line of sight. The orthogonal observation of neutral beam provides strong localization of the CX emission that is thus a local measurement. CX reactions with the thermal neutral population present close to the plasma edge may, however, engender a passive contribution to the spectrum.

When the active CX is produced by a *pencil* DNBI as in TCV, the passive CX component is comparable or more intense than the active component. To recover the measurement's localization the passive component must be subtracted from the total observed CX radiation. In TCV, this is performed modulating the DNBI current, which imposes some limits on the time resolution of the diagnostic.

2.3 Additional effects

In the previous section we saw how from the Doppler shift and broadening of a CX spectral feature the properties of the receiver impurity species can be deduced. This simple view does not account for effects resulting from the atomic physics, that, if not compensated, may introduce errors in the measurement. In the following paragraphs, the non thermal effects, that appear as additional broadening, and the energy dependence of the CX cross section are discussed. Both are able to cause apparent temperature and velocity contributions.

2.3.1 Multiplet structure

The fine structure of energy levels $(n = 8, l = -7, ..., 7)$ and $(n = 7, l = -6, ..., 6)$ means that the CVI$(n = 8 \rightarrow 7)$ line consists in a complex multiplet, i.e. the sum of light emission of each of the 37 allowed inter-multiplet transitions.

The multiplet structure depends on the population of each sub level (n, l) and their relative transition probabilities. As the sub populations are influenced by the emitting atom's environment (ion and electron impact excitations) a full collisional radiative model is, in principle, necessary to model the total spectrum.

For given plasma conditions, collisions may result in partial or complete mixing of atomic fine structure levels, such that the levels are now populated by their statistical weight. In [22] a criterium for establishing complete mixing for a given atomic energy level is reported (see Fig. 2.3). For typical TCV plasmas, $n > 5$ may be considered completely mixed. This implies that all permitted transition between $n = 8 \rightarrow 7$ are present, so that the observed line will be composed of a multiplet with an intrinsic apparent spectral width. In compensation, the calculation of the emission of each transition is simplified, as the population of each level is known from the relatively simple one electron atomic structure.

Under conditions of complete mixing, the atomic and spectroscopic database ADAS [25] can provide the relative emission for each of the 37 transitions for given plasma conditions. Fig. 2.4 shows the multiplet intensity calculated using ADAS for a set of plasma parameters. The structure of the multiplet, that is the strength of each line component, depends on the background plasma, so that the average wavelength $\lambda_{0,mix}$ and the intrinsic broadening $\Delta\lambda_{mix}$ of the line also depend on the plasma parameters. Unless the plasma conditions are known and relatively uniform within the observation volume, this effect may interfere in the determination of plasma velocity and temperature.

In [22], correction factors for T_i were estimated. In [26], starting from analytic approximations of the CX cross sections, formulae to estimate the corrections for T_i and u_ϕ were proposed. For the TCV data analysis, we utilize atomic data provided by the ADAS database, that provides the multiplet structure of a given $(n' \rightarrow n)$ transition accounting for the splitting and populating mechanisms.

The multiplet broadening and average wavelength can be calculated as the first and second

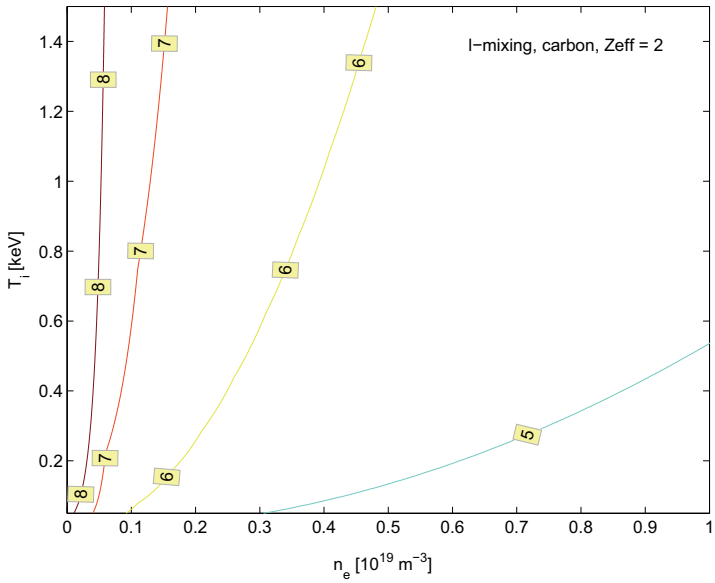

Figure 2.3: Criterium for complete l-mixing of a given level of C^{6+}. n-th level is completely mixed for plasma in the area under the n-th curve.

order momenta of the line distributions:

$$\lambda_M = \frac{1}{I}\sum_i \lambda_i I_i \qquad \Delta\lambda_M^2 = \frac{1}{I}\sum_i (\lambda_i - \lambda_0)^2 I_i \tag{2.3.1}$$

With this definition, the multiplet average wavelength and spectral width were calculated for a relevant set of plasma parameters ($T_\mathrm{i} = 0 \div 1$ keV, $n_\mathrm{e} = 0.2 \div 8 \times 10^{19}\,\mathrm{m}^{-3}$, $B_\phi = 1.4$ T, $Z_\mathrm{eff} = 2$). From this, apparent plasma velocity and temperature were derived as a function of plasma density and ion temperature (Fig. 2.5)

In the window of considered parameters, $5290.54 < \lambda_M < 5290.61$ Å and $0.6 < \Delta\lambda_M < 1.2$ Å. It can be seen that the multiplet structure alone may induce a variation of $\approx \pm 0.02$ Å in the average wavelength and ≈ 1 Å in $\Delta\lambda_M$. Considering a reference wavelength of $\lambda_0 = 5290.58$ Å (see section 2.6.1), this translates to apparent velocities of ± 1 km/s and temperatures of ≈ 60 eV, depending upon the plasma conditions. While the correction for rotation is small and of the order of other error sources for CXRS diagnostic (see section 2.5.3), for ion temperature the effect may not be neglected and must always be accounted for in the analysis.

2.3.2 Zeeman and Stark broadening

In strong magnetic and electric fields further splitting of the multiplet lines occurs, due to the Zeeman and Stark effects, which removes the degeneracies of sub levels.

For the Zeeman effect (magnetic field), an estimate of the symmetrical maximum wavelength displacement is given in [27]:

$$\Delta\lambda_{Zeeman} = 4.7 \times 10^{-9} \lambda_0^2 B\ [T] \tag{2.3.2}$$

where $\Delta\lambda_{Zeeman}$ and λ_0 are expressed in Å. For TCV, with $B \approx 1.4$ T and for CVI($n = 8 \rightarrow 7$) , we obtain $\Delta\lambda_{Zeeman} \approx 0.2$ Å.

For the Stark effect (electric field), analytic expressions to evaluate the ratio of the additional splitting to the natural separation of the fine structure levels are provided in [22]. For TCV relevant

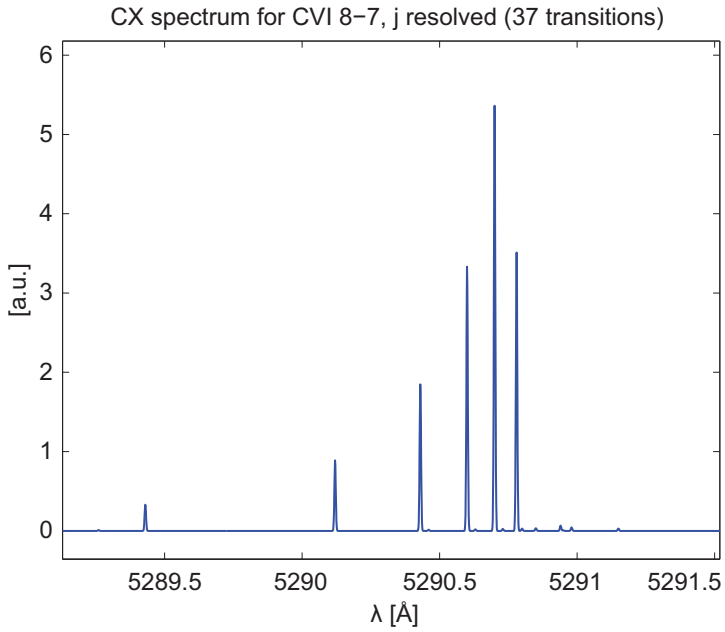

Figure 2.4: Multiplet spectrum for the CVI($n = 8 \rightarrow 7$) transition calculated by ADAS [25] for $B_\phi = 1.4$ T, $n_e = 1 \times 10^{19}\,\mathrm{m}^{-3}$, $T_i = 300$ eV, $Z_{\mathrm{eff}} = 2$.

conditions, with a C^{+5} ion at 500 eV in a magnetic field of ≈ 1.5 T, the maximal broadening of the CVI($n = 8 \rightarrow 7$) line is lower than 0.1 Å [23, 28].

In order to compare these effects with Doppler broadening, we consider the case of $T_i = 50$ eV, so that $\Delta\lambda_{Doppler} = 0.83$ Å. The cumulative effect of Doppler, Zeeman and Stark broadening can be written as:

$$\Delta\lambda \lesssim \sqrt{\Delta\lambda^2_{Doppler} + \Delta\lambda^2_{Zeeman} + \Delta\lambda^2_{Stark}} = 0.86 \text{ Å} \tag{2.3.3}$$

showing an effect of 4%. For larger temperatures, the effect is lower. Hence, in the analysis of spectra data, the contributions of these two effects will be neglected.

2.3.3 Energy dependence of cross section

The dependence of the capture cross sections of charge exchange on the impact energy may cause apparent line shifts and broadening that affect the velocity and temperature measurements [22, 26, 29]. Ions that are moving towards the neutral beam experience a collision energy higher than those that are moving away from the beam. If the cross section varies significantly in the range of collision energies, then one class of particles is more likely to undergo charge exchange recombination. This results in an enhancement of one side of the spectral line compared to the other, which appears as a shift of the line position and a distorted line width.

This mechanism principally perturbs the velocity measurement along lines of sight with a component parallel to the neutral beam. However, the ion gyro-motion in magnetic field projects this effect to lines of sight perpendicular to the magnetic field. If the lifetime of the excited state is smaller that one gyro period, the recombined ion, which is still charged, can precess around the magnetic field line before the emission [29, 30]. In TCV's 1.4 T magnetic field, with the typical $\tau \sim 1$ ns, a C^{5+} recombined ion makes less than 0.1 tours, so that, in principle, measurements of poloidal rotation could be affected.

In reality, on TCV the impact is minor. First of all the angle between CXRS chords and DNBI is $< 20°$. Secondly, this effect is important for ion temperatures of several keV, so that a

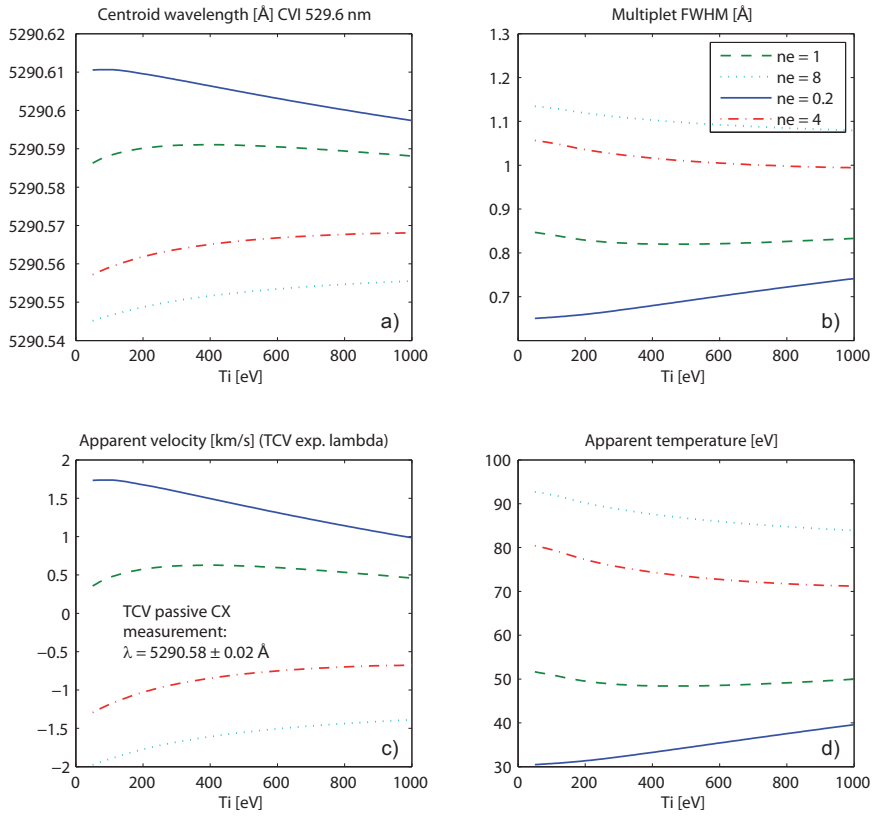

Figure 2.5: Average multiplet wavelength λ_M (a) and spectral width $\Delta\lambda_M$ (b) calculated from ADAS database, as a function of T_i and n_e. In bottom plots (c,d) the apparent velocity (assuming $\lambda_0 = 5290.58$ Å) and temperature are shown.

substantial range of collision energies contributes to the effective cross section; in TCV, T_i<1 keV and the DNBI full energy component cross section is close to the maximum of effective cross section. Thus, $\langle\sigma v\rangle$ varies by only $\approx 1\%$ for the full energy component, that is responsible for 95% of the CX recombination (see section 2.7). A rough estimate of the impact of cross section dependence on energy for TCV typical cases yields $\delta\lambda \lesssim 0.001$ Å, corresponding to $\delta u_i \lesssim 0.1$km/s that is one order of magnitude smaller compared to other error sources and will also be neglected in further analysis.

2.4 CXRS diagnostic systems

During this thesis, in particular during the TCV opening of 2006-2007, the original design of the CXRS diagnostic was completed and upgraded. The initial status was the result of the thesis work of Bosshard [23], and has been operational, with some modifications, for the period 2004-2006. Following chronological labeling, we will refer to the arrangements as CXRS04 and CXRS09, that are used to identify the diagnostic in its initial and present forms.

The CXRS09 diagnostic comprises three optical observation systems whose main elements are depicted in Fig. 2.6:

- a collection optical system, constituted by periscope mirrors and a focalizing lens, that collects the light emitted by interaction of DNBI with carbon;

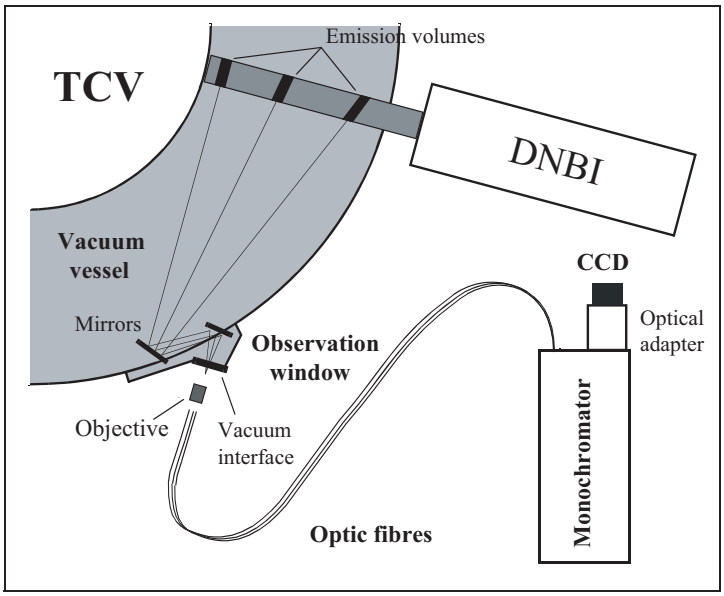

Figure 2.6: Schematic of the main elements of the CXRS diagnostic of TCV.

- a bundle of optic fibers that transport the collected light to the measurement instruments;
- monochromators that resolve the spectral features of the observed line;
- multi-channel detection systems, constituted by a CCD (Charged Coupled Device) camera.

At the beginning of this thesis the diagnostic featured a fully operational Low Field Side (LFS) view and the High Field Side (HFS) view was being commissioned. During the first part of this work, the HFS and Vertical (VER) systems were fully commissioned. Later on, both HFS and LFS views were upgraded by modification of their optical and detection systems. In the following sections we will report some important aspects of the different elements, with particular emphasis on the upgrade. A schematic comparison of the two configurations is presented in Table 2.1 and a detailed description of the CXRS04 configuration can be found in Bosshard thesis [23].

Motivated by initial rotation observations done at the beginning of this thesis, an upgrade of the CXRS diagnostic was undertaken, in order to increase the spatial resolution, the radial coverage and the sampling frequency of the diagnostic. The aim was to attain a precise evaluation of the toroidal rotation gradient across the full plasma cross section and to improve observation of the region close to the plasma edge.

To achieve these goals the following changes were made:

- Increase of the number of measurement volumes (chords) of each system from 16 to 40.
- Double entrance slit configuration on the spectrometers to house all 40 chords.
- Back illuminated, water cooled, EEV 57-10 detectors, mounted on Xcam cameras.
- 3 lenses optical system to efficiently couple the spectrometer output to the CCD.

	CXRS 04	CXRS 09
Observation views	LFS, HFS (commissioning)	LFS, HFS, VER
Chords	16×2	40×3
fiber core diameter (μm)	600 (core 600)	636
fiber N.A.	0.16	0.12
CCD	Wrigth FI (298x576)	e2V 57-10 BI (512x512)
Spatial resolution	2 cm	1 cm
Integration time	30 ms	30 ms
	DNBI 2004	DNBI 2009
Plasma source	RF	Arc
Energy fractions	60,30,8,2	85,10,3,2
Neutral equivalent current [A]	$2.4 \div 2.84$	$2.5 \div 3.0$
Energy [keV]	48	48
Beam divergence	0.7	0.5

Table 2.1: Comparison of CXRS and DNBI diagnostics in 2004 and 2009 configurations.

2.4.1 Monochromator

To resolve the wavelength shifts and broadening of impurity lines of TCV plasmas the use of high spectral dispersion spectrometers is required. The LFS and VER systems are equipped with Czerny-Turner spectrometer SPEX750Mi (focal length 0.75 m, aperture f/7.5 at first order, f/6 at zero-th order). HFS system is equipped with a Czerny-Turner spectrometer ACTON AM-506 of larger aperture (focal length 0.66 m, aperture f/5.5 at first order, f/4.7 at zero-th order), to help compensate for the weaker signal due to the beam attenuation. Unfortunately, the HFS spectrometer is affected by a strong coma aberration for optical paths far from the optical axis. To reduce this coma to a usable value, a partial opaque mask was installed on the first mirror, with a consequent 30% loss of aperture. The effective throughput of all CXRS systems is thus similar.

All systems are equipped with holographic grating of 2400 l/mm, so that the dispersion at 530 nm is 4.67 Å/mm for LFS and VER and 5.49 Å/mm for HFS. The spectrometers are used as monochromators, with fixed grating angles. A relatively small spectral interval is imaged on the detector (≈ 20 Å).

At the entrance of each spectrometer the optic fibers are aligned vertically. The light dispersed from the fibers is imaged at the spectrometer exit as a vertical series of spectra. With this arrangement the evolution of the same spectral line can be detected for multiple measurement volumes simultaneously.

Light losses in the fiber/spectrometer coupling were minimized by using no entrance optics [23]. Furthermore, the standard variable entrance slit was replaced by a 0.01 mm plate with a thin vertical cut of fixed width: the plate is attached to the bundle head in almost direct contact with the fiber ends and acts as the spectrometer's entrance slit. Several plates are available, acting as entrance slits of fixed width (100, 200 μm).

At the spectrometer's entrance, two bundles of fibers are combined and arranged in two vertical arrays, located in such a way that the plate slits are positioned at the entrance plane of the spectrometer. The 40 channels are then imaged though the spectrometer as two separate slits. Each raw spectrum on the CCD detector is the superposition of two spectra, displaced by a wavelength difference that depends on the slit spacing and the spectrometer dispersion. The superposition

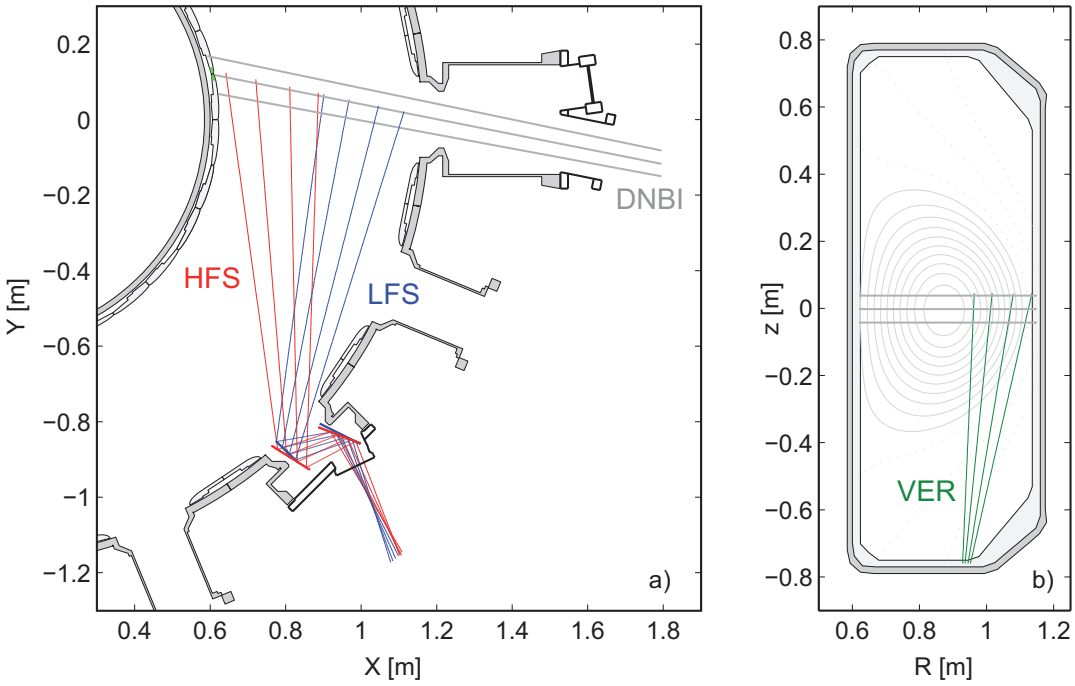

Figure 2.7: Global geometry view lines of the three CXRS systems. Each system features 40 separate chords (for ease of observation only 4 are shown). On the left, horizontal Low Field Side (blue) and High Field Side (red) observation systems measure the toroidal rotation. The Vertical observation system, on the right, measures the poloidal rotation.

could be removed with bandpass filters, which will also affect the quantity of transmitted light and reduce the sensitivity. However, no filter is used here as the background subtraction based on DNBI modulation (see section 2.5.1) provides an active spectrum virtually without background, so that the active lines appear well distinct.

From the analysis point of view, the double slit arrangement requires that two sets of instrumental functions must be considered and that pairs of spectra imaged on the CCD must be fitted together.

All spectrometers are equipped with an optical coupling system at the exit slit that reduces the size of the image to fit onto the detector. In the reducer, a combination of three lenses provides a magnification factor of ≈ 0.5. The position of lenses and the support of the camera can be adjusted separately for accurate focusing. Optically reducing the image size by a factor of 2 implies that a double resolution is required to measure the same line shifts and broadening. On the other hand, this is compensated by the $4\times$ enhancement in photon per unit of surface, with the further beneficial effect on the Signal to Noise Ratio (SNR) at the detector readout.

2.4.2 CCD detectors

For the measurement of spectra the three systems are equipped with a camera provided by Xcam Ltd, equipped with a CCD detector from e2V. The CCDs (model e2v CCD57-10) are back illuminated, so that quantum efficiency[(3)] up to 85% at our operational wavelength is available.

The CCDs are of the frame transfer architecture: the upper section of the detector (512x512 pixels) is used to acquire the image and the bottom section is used to store the image. After the

(3) The quantum efficiency of a CCD detector is the ratio of the number of incident photons to the number of electron-hole pairs created, often measured in electrons per photon (dimensionless).

exposure charges accumulated in the upper part are transferred to the bottom by a series of 512 synchronized vertical transfers. While the upper part is continually exposed for the next image, the charges in the bottom part are transferred via a read out register to the output amplifier and then to the data acquisition.

The time of frame transfer is 340 μs, which is much lower than the typical exposition times of ≈ 30 ms, so that no mechanical shutter is used. Smearing issues, where light is registered during the vertical transfer process, may arise in fast read out mode (see chapter 8), when the exposition time becomes comparable to the frame transfer time.

The read out of a full frame (512×512 pixels) is of the order of ≈ 0.35 s, but at the typical settings the detector is divided in 20 horizontal Regions Of Interest (ROI), one per pair of fibers. Before read out, the signal of each track is integrated (on chip binning), so that one spectrum per pair of fibers is acquired. Data tracks are separated by vertical bands that are not acquired (dead tracks). In this read out mode, 20 spectra 512 pixel wide (≈ 60 Å) are acquired in less than 10 ms.

The e2v detector features two read out nodes. Double node read out configuration can be used to halve the read out time where the left and right sides of the detector are read simultaneously and the complete image is reconstructed later. This way the 20 channels can be acquired in ≈ 5 ms.

The CCD detector are cooled by a Peltier stack, to an operational temperature of $-30°$ C. The heat is evacuated from the camera by a water cooling system. These temperatures were found to be necessary to minimize the read out noise and, in particular, to reduce a non gaussian feature due to quantum efficiency variation on the CCD (pattern noise).

2.4.3 Optic transmission line

The 2009 optic transmission line taking the collected light from the tokamak to the spectrometers consists of two bundles of 20 optic fibers (Model UV636 T, by CeramOptec GmbH, Germany). The silica core has a diameter of 636 μm and the total diameter of each fiber is 1000 μm. The fibers' Numerical Aperture is N.A.=0.12, slightly smaller than the former fibers', but it does not limit the étendue of the system (the limiting element is the monochromator). The fiber ends are arranged in arrays with minimal space between them, so that the fiber cores are spaced by the 400 μm of the fiber cladding. At the tokamak, two bundle ends are bound together to constitute a double array collection head. The two arrays can be aligned, so as to sample the same position in the plasma, or out of step, so as to nearly double the spatial resolution. The *coupled* or *extended* configurations are shown in Fig. 2.8 for the LFS system, are also available for HFS and VER systems.

For the VER system the coupled measurement points must be aligned with the magnetic field, to ensure the double sampling of the same flux surface.

2.5 Data analysis

After acquisition, the raw spectra are analyzed numerically to calculate the ion parameters, according to the following sequence of steps, some of which will be reported in greater detail:

- CCD offset subtraction.
- Determination of the passive CX spectra during the DNBI pulses.
- Calculation of the active spectra.

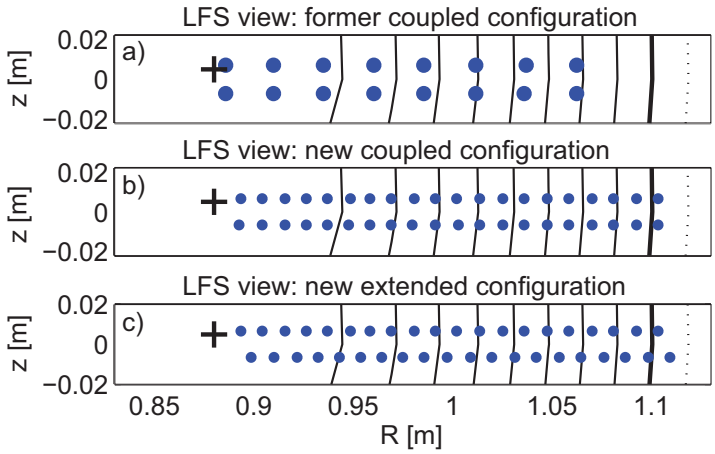

Figure 2.8: The location of collection volumes of the LFS CXRS system is shown for three diagnostic configurations: before the upgrade (top) 16 coupled measurements were available. After the upgrade 40 chords are available, that may be configured in coupled (middle) of alternate (bottom) configuration, to maximize the radial resolution. In the background, the magnetic flux surfaces of a reconstructed equilibrium with $z_{axis} = 0$ are shown for reference.

- Gaussian fit on the spectral active signal, accounting for the instrumental function.
- Calculation of local measurement of ion parameters from fit parameters.
- Calculation of the radial location mapping the 3D points into the reconstruction of magnetic equilibrium (see chapter 1).

2.5.1 Determination of active spectrum

The passive spectra (P) during the DNBI pulses are determined by interpolation of passive spectra before and after a beam pulse. The active spectra (A) are then calculated by subtracting the passive component from the spectra acquired during the DNBI pulses (A+P). This method relies on there being little variation of the passive signal during the DNBI pulse. If the background varies, errors can arise due to pollution of the active portion from the passive portion. This effect is partially compensated by interpolating the passive signal across DNBI pulses with a cubic spline curve. The passive contribution is then calculated by averaging the passive spectra closest to the DNBI pulse, normalizing the amplitude to match the intensity interpolation. This method proved to be robust and to compensate well for slow variations of the plasma parameters (see Fig. 2.9).

2.5.2 Fit of active spectrum

The detected spectral line profile results from the convolution of the real spectrum by the spectroscopic Instrumental Function (IF). The IF accounts for the distortion (symmetric or asymmetric broadening, displacement) of the spectral profile induced by the optic elements and its width is determined by the entrance slit aperture. If the IF and the real line width are comparable, a deconvolution is necessary. The problem is especially critical if one wants to resolve spectral features (Doppler shifts) smaller than the spectral width of IF.

The instrumental function of the system is measured from the spectrum of monochromatic radiation, typically provided by a laser source or a *cold* spectral line (see next section). As the deconvolution is an ill formulated problem (the solution depends strongly on the noisy portion of the convoluted spectra), here we will follow another procedure: the active experimental spectra

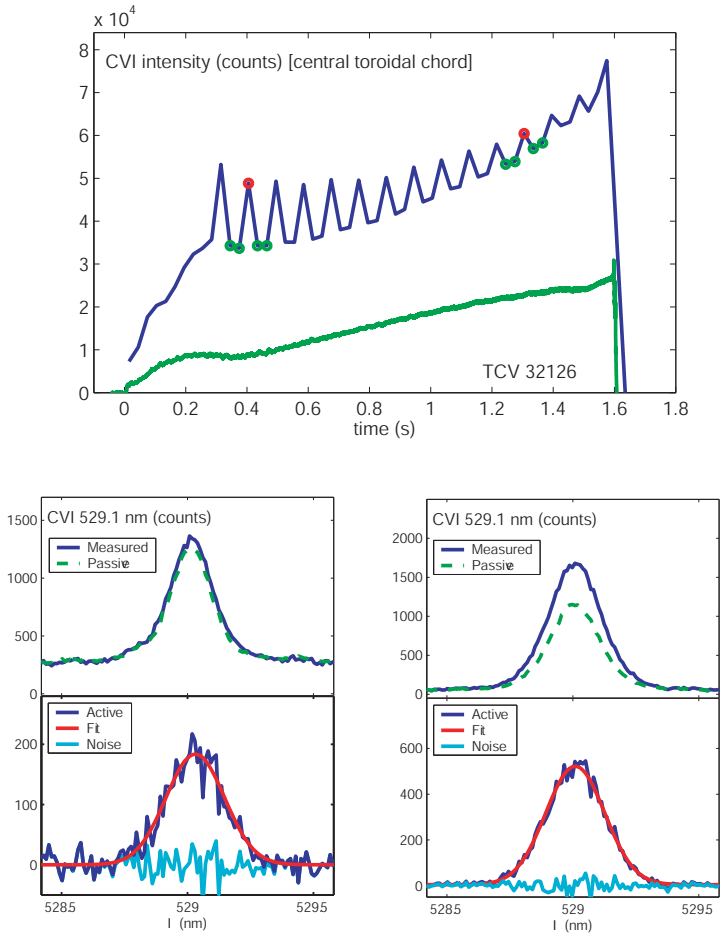

Figure 2.9: Example of analysis on a plasma discharge where the electron density was ramped from $n_{e,av} \approx 2.5$ to $7.2 \times 10^{19}\,\mathrm{m}^{-3}$. Top graph shows the intensity trace of a central CXRS chord, with the DNBI pulses visible as periodical spikes. The line integrated density from a FIR diagnostic chord is also shown as reference. The red circular markers indicate two time frames that correspond to bottom graphs columns (left $n_{e,av} = 7.0 \times 10^{19}\,\mathrm{m}^{-3}$, right $n_{e,av} = 2.5 \times 10^{19}\,\mathrm{m}^{-3}$), which illustrate the raw spectra, passive interpolated spectrum, active spectra and the result of the spectral fit.

are fitted with the convolution of a Gaussian spectral profile and the instrumental function. The fit correspond to a minimization of a χ^2 cost function. From the parameters of the gaussian best fit (position and width) the Doppler shift and the Doppler broadening are calculated and, in turn, the velocity and temperature. Put simply, an artificial curve is generated, convolved with the measured IF and the result is compared to the experimental measurement.

The coupled analysis of multiple channel observing the same flux surface can be performed with a multiple spectral fit with each spectral line constrained to have the same position and Full Width Half Maximum (FWHM). This also in case of double entrance slit, with the addition of accounting for two instrumental functions in the deconvolution of the respective lines imaged on the detector. This is particularly important when the active signal is low, where radial resolution can be sacrificed to obtain averaged measurements.

2.5.3 Error sources

There several possible error sources. The most relevant, in particular for the rotation measurements, are:

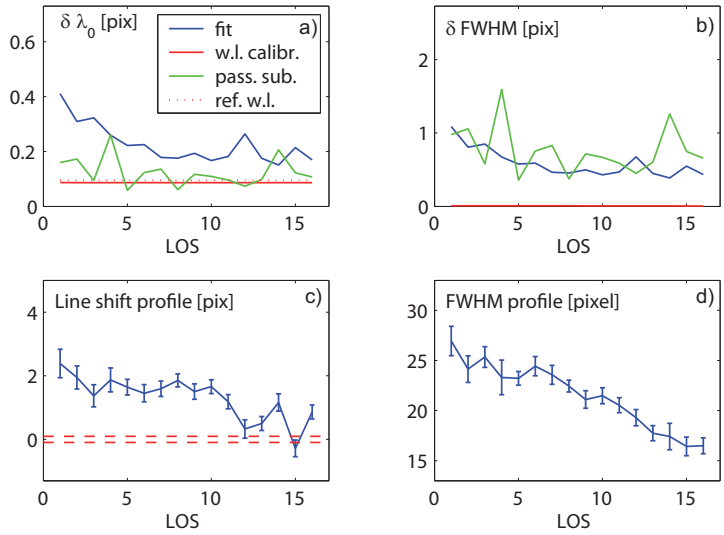

Figure 2.10: Comparison of different error sources, for the high density time frame ($n_{e,av} \approx 7 \times 10^{19}\,m^{-3}$) of Fig. 2.9. On x axis the Line Of Sight (LOS) numerical label increases moving from plasma core to the plasma periphery. The beam attenuation at high density results in a fit error that is higher for inner channels. In bottom graphs, the resulting profiles of Doppler shift (left) and broadening (right). The uncertainty due to the reference wavelength is indicated by a dashed horizontal band.

- The uncertainty in the spectral fit parameters. As already pointed out for the CXRS04 diagnostic [23], the noise is essentially constituted by the statistical fluctuations related to the photon signal detection. The effect on the fit parameters is evaluated *a posteriori* considering the Hessian matrix of the minimization function.

- Passive background subtraction. Especially in cases of non stationary plasmas, the passive component of the spectrum may be interpolated properly. In turn, the active signal will be polluted by a passive component, generating errors in the final result which are very difficult to evaluate. A method to estimate this effect was developed based on the pollution of the active spectrum by a fraction of the passive spectrum. The magnitude of the spurious component is estimated from the temporal evolution of the interpolated line intensity.

- An inaccurate wavelength calibration, which may induce a systematic overestimation or underestimation of the measured Doppler shifts.

- An error in the rest reference line position, that could affect systematically and equally all measurements.

- Uncertainties in the equilibrium reconstruction, when mapping the measurement of a flux surface label coordinate, such as ρ_ψ.

In Fig. 2.10 the contributions of the different error sources are shown, in the case of a 30 ms acquisition of an high density plasma ($n_{e,av} \approx 7 \times 10^{19}\,m^{-3}$). In this case, all the error sources considered affect similarly the Doppler shift measurement. The line broadening, and hence the temperature measurement, is much less sensitive to wavelength calibration uncertainties.

Furthermore, for the impurity density measurement, uncertainties in the CX reaction cross section and on the beam attenuation will result in systematic errors.

Depending on the plasma conditions and, in particular, the CVI CX line yield, the weighting of each contribution may change. In practice, for conditions of good count rates (SNR=10) and using

a suitable instrumental function, the position of the spectral line can be deduced to an accuracy of 0.1 pixel, which correspond to ≈ 0.4 km/s. For SNR ≈ 3 the uncertainty increases to 5 km/s.

Intrinsic uncertainties may also come from effects neglected in the analysis, like halo and plume neutrals that surround the beam, crosstalk between channels, perturbations from the DNBI, parameter dependence of multiplet features, etc. In general, the impact of such effects is always estimated less that 10% for the absolute values and often considerably less for relative changes.

2.6 Wavelength calibration

The measurement of plasma rotation with resolution of the order of ≈ 1 km/s requires not only excellent spectroscopic detection but also an extremely precise wavelength calibration. As it is common for CXRS diagnostics observing the CVI($n = 8 \rightarrow 7$) line, in TCV the wavelength calibration of all of the CXRS systems is based on the observation of a Neon reference spectrum from a discharge lamp, that, in the spectral range covered by the CCD detector (≈ 6 nm), provides four lines of known wavelength.

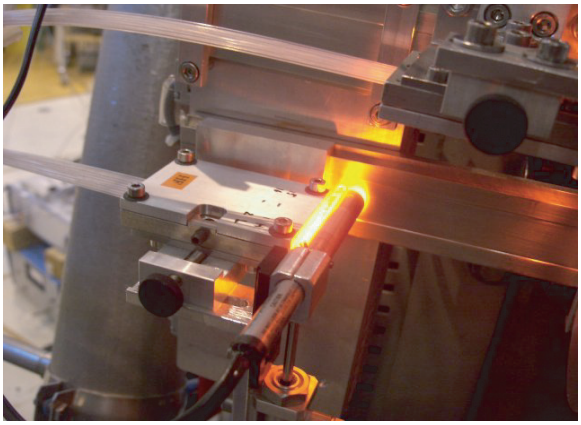

Figure 2.11: Collection head of HFS system, during a wavelength calibration. The Neon Pen Ray lamps are translated vertically in front of the fiber ends by the piston visible at the bottom of the figure.

The wavelength calibration source consists of a calibration lamp (Pen-Ray), installed in the proximity of the fiber bundle head, at the tokamak side. A pneumatic system that is remotely controllable is used to place the calibration lamp in front of the fiber head (see Fig. 2.11). A correct calibration requires the calibration source to lie on the optical axis of the system so as to fill the optical acceptance of the fibers, otherwise a displaced reference spectrum will be imaged on the CCD. To reduce the effect of lamp positioning errors, a glass diffuser is installed between the fibers and the lamp, so as to ensure a uniform fiber illumination [(4)]. Stability and robustness of the system were verified by repeated full calibration cycles.

By monitoring the wavelength range covered by the CCD over several hours, the spectroscopic system was found to suffer from mechanical drifts or rapid movements of tens of μm at the position of the detector. If not accounted for, this drifts would engender errors up to 5 km/s in the final velocity measurement, i.e. comparable with the velocity measured. A calibration spectrum was acquired in the 60 seconds following every TCV discharge to provide a wavelength reference for each experiment. The spectrum is acquired in full frame mode that also provides a monitor of the quality of the overall diagnostic performance.

[(4)] Optic fibers are expected to act as mixing element over input angle. However, a residual effect of the lamp position was found that caused displacements of the calibration spectra of up to 1 pixel

For the spectroscopic system the dispersion relation $\lambda(x_{CCD})$ is linear to an high degree of approximation, so wavelength is calculated by linear regression between the nominal wavelengths of the reference lines, and their position on the CCD's horizonal axis.

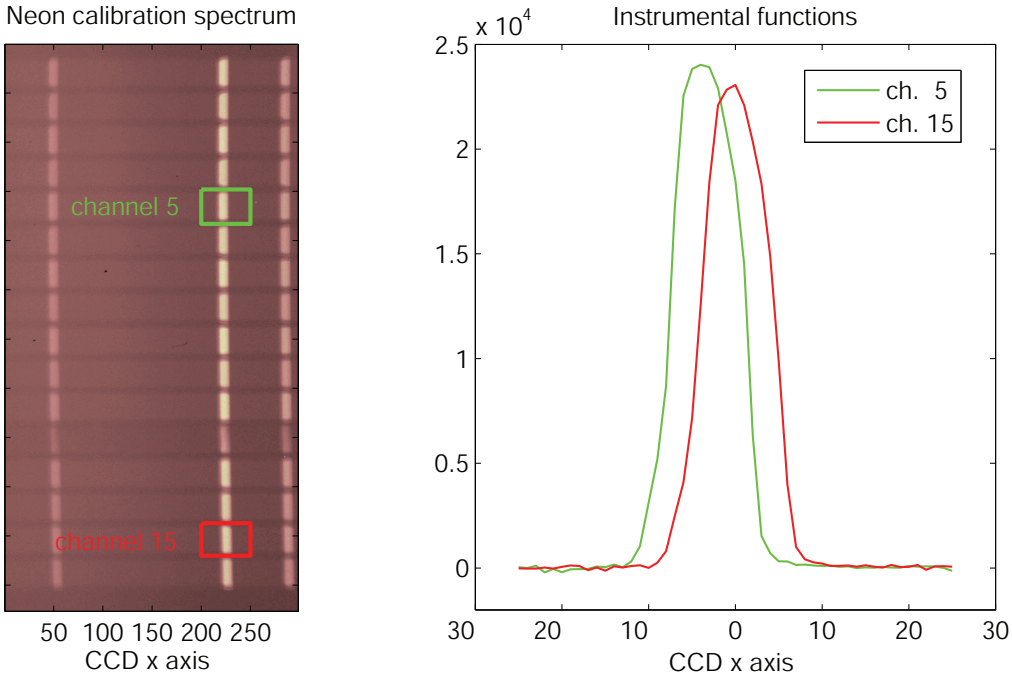

Figure 2.12: Examples of distortion of spectral line profile, due to large entrance slit and Czerny-Turner monochromator setup, are visible in a full frame calibration spectrum acquired with the Wright detector of LFS system (a). The profile of instrumental functions for two selected channels (b) is asymmetrical and, although corresponding to the same Neon line, the peaks are not vertically aligned.

To maximize the light collection the spectrometer entrance slit is kept at values of $100 \div 200$ μm which is comparable with the diameter of the fiber glass core. The fiber core circular section is thus imaged on the detector. The dispersion of the spectrometer results in a vertical bend of the slit image at the spectrometer output plane, sometimes accompanied by further small distortions from the optical reducer (visible in Fig. 2.12a). After on-chip binning, these effects are summed and can result in a strongly asymmetric line spectral profiles and apparent line displacements.

Dealing with these issues is not trivial as they may cause some ambiguity in the analysis of the experimental data, for example about the proper definition of 'line position', or the existence of a unique wavelength calibration across the whole CCD surface.

An elegant method to account for these aspects was developed and implemented at the beginning of this thesis. It is based on the choice of the instrumental function used for the analysis of both calibration and experimental spectra. Very commonly, the IF of an optic system is taken by approximating a 'cold' spectral line ($\Delta\lambda_{FWHM} \ll \Delta\lambda_{IF}$) with an analytical fitting expression, e.g. Gaussian, Lorentz, Voigt or a multiple combination of them. For TCV CXRS, each channel's instrumental function is separately defined from a selected range of the calibration spectrum around a well sampled calibration line (Fig. 2.12b). The selected spectrum is then normalized, so that its integral is equal to one. This choice has two beneficial consequences:

- There is no resort to analytical fits, which by definition, especially for high instrumental function asymmetry, are likely to introduce spurious features that lead to systematical errors in the measurement (e.g. the overestimation of a lateral wing).

- The position of the deconvoluted calibration line used for the instrumental function definition is assigned by definition to the middle of the selected interval, independently from the actual spectral line features, e.g. the centroid position.

The last point is particularly relevant as, in practice, the position of this line in known to sufficient accuracy so that, the accuracy of the constant term in the relation $\lambda(x_{CCD}) = \lambda(0) + \frac{d\lambda}{dx}x_{CCD}$ is determined by the uncertainty in the nominal wavelength of the Neon calibration line (10^{-5} nm). The choice of the same horizontal range for all channels guarantees the same calibrated lambda axis for all channels, correcting for the vertical distortion due to the spectrometers' optics: in other words, after deconvolution by the instrumental functions, the experimental spectra will be vertically aligned to the same wavelength reference. While it is not a crucial point for the measurement correctness, it is very helpful in the analysis.[5]

The method is efficient only if the instrumental function, i.e. the selected line of the calibration spectrum, is sampled with sufficient quality. To achieve this, the calibration spectrum is averaged over repeated acquisitions of Neon spectra with integration times up to 10 s. Another important requisite is that the IF must be constant over the horizontal lambda axis, i.e. the spectral lines at different wavelengths should differ only in intensity and position but all share the same spectral shape. This condition was well verified for all of the TCV CXRS systems.[6]

2.6.1 Experimental determination of the rest reference wavelength

As it will be shown in next chapters, typical rotation velocities of TCV plasmas range from zero to few tens of km/s and around few km/s for u_θ. To get an accuracy of 1 km/s or less, a precise value of the rest reference wavelength in necessary, with an uncertainty of 0.02 Å. This represents a problem in large tokamak devices such as JET and DIII-D, where the heating NBI driven rotation can be as large as 100 km/s. In smaller devices (NTSX, Alcator) the problem is overcome with the simultaneous measurement of the emitting volume with two opposing line of sights, deducing plasma velocity from a differential Doppler shift. Given the technical difficulty in obtaining a crossed view on TCV, the rotation measurements in TCV relies on the precise knowledge of the reference wavelength.

On the other hand, as already anticipated in section 2.3.1, the fine structure of the multiplet emission depends on the plasma parameters making questionable the choice of a unique rest reference wavelength suitable for the measurement in all plasma conditions. Given the uncertainties that still affect the calculations of the atomic physics parameters, an experimental approach was chosen on TCV, where an effective experimental value of rest wavelength, for TCV relevant plasma conditions, was obtained from spectral analysis of the CX passive emission.

To perform this measurement, a plasma discharge with $z_{axis} = 0$ cm, was observed by 9 horizontal lines of sight, along the device major radius, i.e. perpendicular to the plasma, in a toroidal sector that was not close to the DNBI. No optical adapter was used. This setup, shown in Fig. 2.13 (left), minimizes poloidal rotation effects. Fig. 2.13 (right) also shows an example of measured spectrum, integrated over a 300 ms time window. The C^{5+} line at 529.1 nm is accompanied by other spectral features. Each average spectrum was modeled by a combination of 4 gaussian line profiles, convoluted by the appropriate instrumental functions (red curve). This somehow simplified analysis does not account for more complex spectral features, but the method is adapted to the level of accuracy required. No systematic differences emerged in fit results

[5] In other implementations of CXRS diagnostics the vertical bend at the detector is compensated by curved entrance slits. The TCV solution provides more flexibility as the bending radius depends on the wavelength.

[6] An eventual variation of the IF with λ will mostly affect the $\frac{d\lambda}{dx}$ term and, provided that the IF line is in proximity of the CX line, will have negligible consequences for the Doppler shift measurement.

amongst the 9 observation chords. Tab 2.2 summarizes the results, indicating, for each fitted line, the central wavelength, the line width and the corresponding apparent ion temperature (not corrected for multiplet broadening).

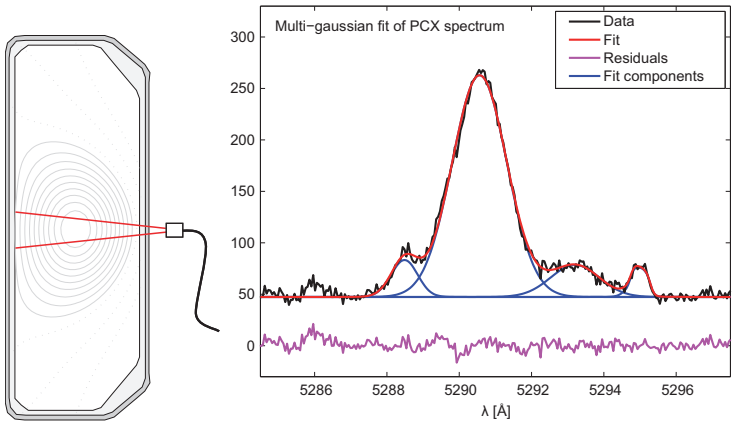

Figure 2.13: Left: schematic of the arrangement for the experimental determination of the reference wavelength from the orthogonal observation of passive CVI($n = 8 \rightarrow 7$) emission. Right: the spectrum acquired by one CXRS chord is modeled with multi gaussian fit accounting for deconvolution of instrumental function (TCV 27113).

λ_0 (Å)	$\Delta\lambda_{\mathrm{FWHM}}$ (Å)	T_i (eV)
5290.58 ± 0.02	0.8	52
5288.01 ± 0.02	0.3	8
5293.03 ± 0.02	0.7	40
5295.01 ± 0.02	0.05	0.5

Table 2.2: Fit of passive CX line results.

The value of λ_0 found T_i is to be considered as an average estimate, as the spectrum is actually line integrated, an therefore includes contributions from different plasma regions, with different plasma parameters. The $T_\mathrm{i} \approx 50$ eV suggests that the passive emission is more localized to the plasma edge where $T_\mathrm{i} \lesssim 100$ eV and $n_\mathrm{e} \approx 0.1 \times 10^{19}\,\mathrm{m}^{-3}$. Nevertheless, the estimation appears in rough agreement with the theoretical scans performed in section 2.3.1 indicating that the estimated correction factors (for rotation and temperature) are applicable.

One *a posteriori* verification of the correctness of the value comes from the poloidal rotation measurements in reversed field configurations. If the plasma poloidal cross section is up-down symmetrical, reversal of the total magnetic field corresponds to turning the tokamak upside down. In such conditions, the plasma flow would be expected to reverse whilst maintaining its profile for a given plasma configuration. Fig. 4.4 in chapter 4 compares the poloidal rotation profiles in plasma discharges up-down symmetrical with opposite directions of B_ϕ and I_p, but otherwise identical. The remarkable symmetry of the profiles, with respect to zero rotation (within 0.5 km/s), stems for the correctness of the reference wavelength and justifies an estimated uncertainty of $\delta\lambda_0 \approx 0.02$ Å.

2.6.2 Intensity calibration

The absolute calibration of the CXRS diagnostic was measured using homogeneous light source (integrating spherical light source by Labsphere Ltd, Model US-060-SF), whose radiance is known as a function of wavelength. The calibration procedure consists in acquiring the signal of the integrating lamp positioned in the vessel, along the CXRS chords, filling the observation chord's numerical aperture. The complete optical path is thus calibrated, accounting for all losses from elements (mirrors, lenses, fibers, entrance slit, monochromator) and the detector efficiency.

This procedure requires the TCV vessel to be open and was performed only twice during this thesis. No major drift in calibration was measured for the carbon impurity profiles. A drift in the transmission of the view lines could only come from the damage and deposition on the in vessel mirrors. From visual inspection, it may be estimated in less of 5% in the last full year of operation.

2.6.3 Diagnostic chords alignment

A precise alignment of the view lines of the three CXRS systems is required to obtain a globally coherent measurement of the ion parameters. If the DNBI beam waist is minimized to obtain the highest photon yield, it is important that the CXRS chords are correctly aligned to it. It is of primary importance in the calculation of the radial electric field from the radial force balance equation, that requires both the poloidal and toroidal rotation profiles. As shown in chapter 4, the small scale edge features observed in toroidal and poloidal rotation measurements need a very precise alignment, with radial uncertainty below 0.5 cm.

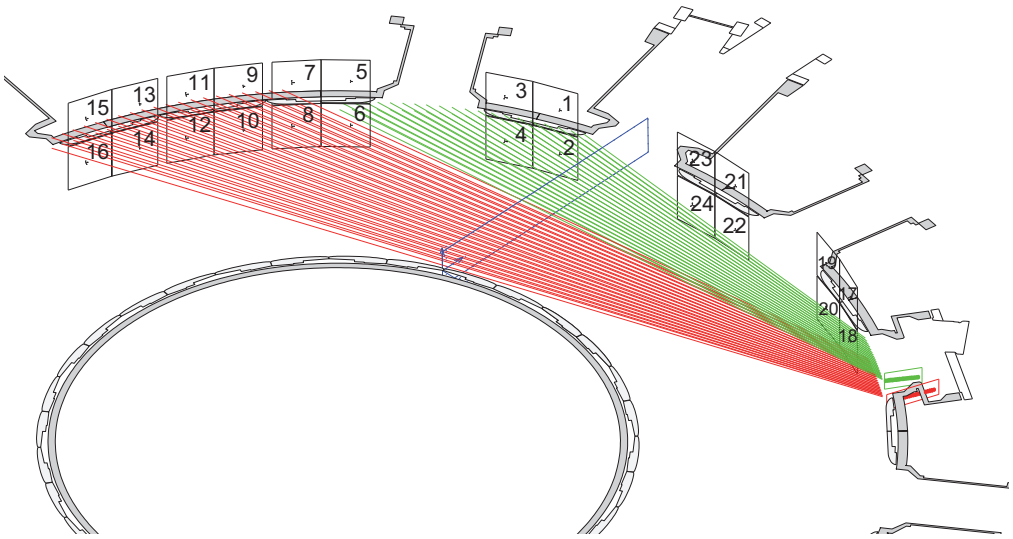

Figure 2.14: Example of 3D reconstruction of the diagnostic chords alignment.

Several complementary strategies were used to obtain the required accuracy.

- A beam target is introduced in the vessel and positioned along the beam path. By retro illuminating the optic fibers the collection volumes are identified and eventually adjusted on the base of ideal position previously marked on the target's surface. The location of the points on the target is acquired with digital pictures, that are later on analyzed numerically. The relatively small size of TCV vessel facilitates the introduction of alignment targets, but

at the same time the positioning of the target inside the vessel suffers from uncertainties (≈ 5 mm).

- Fibers are retro illuminated, in absence of the alignment target, so that the luminous spots are projected on first wall tiles.

- A small (point) light source is introduced from an lateral port next to the DNBI injection port, radially spanning the measurement region. The resulting intensity is measured channel per channel by the LFS and VER systems as a function of the source position in three dimensional space, providing a strong cross check constraint for the alignment of the two systems.

An alignment reconstruction tool was used to integrate all the available information with the alignment resulting from the best match to the different constraining data. In the adopted procedure, the positions of the view points on the target are fixed. The 3D position of the target is optimized to match the measured retro-illuminated spots on the tiles (Fig. 2.14). The six degrees of freedom are strongly constrained by the information from the HFS and LFS distribution of points on tiles plus the punctual light source measurements.

Following this procedure, the 3D position of the measurements volumes was measured with an uncertainty of less than 5 mm, which is comparable with the diameter of the cylindrical emitting volumes and lower than the effective radial resolution of the diagnostic.

A cross check, although not absolute, of the quality of the alignment is possible from experimental results, by comparing the ion temperature profiles from the different diagnostics (see Fig. 5.21) or the intensity of pairs of channels that observe the same radial region at the same time. The DNBI vertical injection angle can be modified to compensate any alignment drifts emerging from these observations.

2.6.4 Radial resolution

The capability to distinguish small features on the radial profiles of the measured quantities defines the diagnostic radial resolution. In CXRS09, the 20 vertical observation points are radially separated by ≈ 1.2 cm. The radial resolution is limited by the radial extension of the emitting volumes. In fact, because of the finite width of the DNBI and the observation geometry, each emitting volume spans a finite range radii.

For the horizontal LFS and HFS views, the radial resolution is highest at the plasma center, where the diagnostic chords intersect the beam nearly parallel to the flux surfaces (here the limit is the diameter of the local observation cone ≈ 7 mm), degrading towards the edge (≈ 25 mm).

For VER system, this observation geometry must be accounted for. Fig. 2.15 shows the calculated radial resolution accounting for the 3D beam structure in the plasma, reconstructed by the beam attenuation code, for a discharge with its magnetic axis on the horizonal midplane ($Z_{axis} = 0$ m). Plot b shows, for each VER line of sight (LOS), the flux surfaces intersected along the chord. The traces correspond to points of the LOS where the attenuation code gives neutral equivalent currents larger than 20% of the peak. The core chords collect signal form a large radial range, whilst the resolution is maximal at the edge. This is also clear from graph c where, for each chord, the average ρ_ψ and its uncertainty are calculated from the integral, weighted by the DNBI current. While the resolution is best in the edge region, it is not sufficient to avoid intersection of sampling regions, limiting the radial resolution. The effect is exemplified in graph d, where the measurement has been synthesized starting from a model profile featuring a sharp peak close to the

plasma edge.[7] The synthetic measurements, indicated by green circles, underestimate the peak amplitude by a factor of almost two. The case of a plasma vertically displaced at $Z_{axis} = 0.15$ cm is also presented (red triangles). Here the estimate is even worse: the loss of resolution is such that the peak is strongly smoothed out.

This effect is minimized when the chords are tangent to the flux surfaces: calculation shows that for a typical shape, with $\delta = 0.3$ and $\kappa = 1.4$, the magnetic axis at $Z_{axis} = 2$ cm guarantees the maximal radial resolution at the edge.

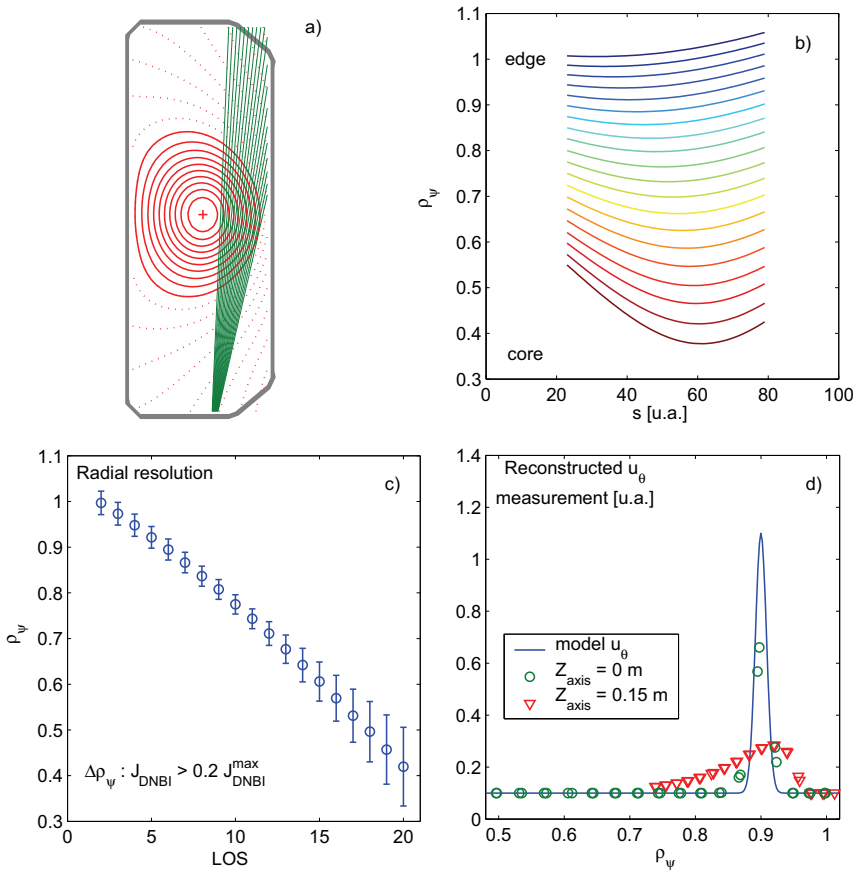

Figure 2.15: Schematic of the lines of sight (LOS) of the CXRS09 VER system (a) on a typical limited magnetic configuration discharge: each LOS crosses several flux surfaces, and collects light from different radial locations. In (b) the normalized radii ρ_ψ spanned by each chord crossing the DNBI volume (s parameterize the position along the LOS). For each LOS an average ρ_ψ is calculated considering the DNBI neutral current as a weight (c). The radial overlap of emitting volumes has the consequence to smooth the experimental profile. This effect is shown in (d) for test profile of u_θ considered for two vertical plasma positions. For a plasma with $Z_{axis} = 0$ the measurement would underestimate the u_θ peak amplitude by a factor of two.

2.6.5 Passive charge exchange emission

The charge exchange spectra on TCV are affected by a strong passive CX contribution, that in normal operation is twice as intense as the active contribution coming from the DNBI. The nature of the passive contribution of CX is not fully understood. The main channels that can contribute to the emission are:

[7] This situation is relevant for poloidal rotation measurements. See section 4.2.

- electronic excitation;
- free electron recombination;
- CX of thermal neutrals with radially diffused carbon nuclei.

Emission from electronic excitation is known to be negligible compared to charge exchange in the visible range [23].

Emission from recombination takes place over all the plasma volume. The cross section is small compared to that of charge exchange with neutrals ($Q_{ER} \approx 10^{-15}\text{cm}^{-3}$ for $T_\text{i} \approx 300\text{eV}$). Nevertheless, the core electron density can be 1000 times larger than the edge neutral density, so the contribution may be comparable in TCV.

Charge exchange with neutrals is, in many Tokamaks, identified as the main contribution to the passive signal. In TCV, simulations indicated that the signal is likely to come from interactions with excited $n = 2$ neutral population [23].

During this thesis, a spatial characterization of the passive CX emission was performed by reconstructing the integral measurement of horizontal and vertical views on the base of an input model for the radial emission profile, supposing that the passive emission is poloidally symmetrical.[8]

Figure 2.16 illustrates the results. The graph (a) shows the choices for the neutral radial profile, all monotonically increasing towards the edge, but with different degrees of penetration. In graphs (b) and (c), the intensity of passive light reconstructed is compared with the actual CXRS measurements, as function of channel number. The most satisfying agreement corresponds to an emission profile that extends finite in the core of the plasma. In particular the ansatz of a profile strongly peaked at the edge is in contrast with the measurement of LFS view.

From this exercise one can conclude that the passive emission is possibly the result of multiple mechanisms. A more specific study should include a detailed reconstruction of the neutral density profile, and in particular of the excited population. To date, a combination of electron recombination and thermal neutral CXRS is likely to account of the observations.

The fact that the passive CX signal is not limited to a thin boundary shell, implies that it may also mirror the core plasma parameters. The interpretation will then be more complicated, as the spectrum is composite and the result of a line integral. During this thesis the apparent rotation of deduced from the passive CX emission will be used as parametric of the plasma parameter dynamics.

2.7 DNBI

The CX radiation from the core of the plasma is provided by the Diagnostic Neutral Beam Injector. The DNBI was installed on TCV in 2000, and since that date two major upgrades were performed, first in 2002-2003 [31] and then in 2006-2008 [32]. Here we describe the system in its present day configuration.

Figure 2.17 illustrates the various components of the device. A cold cathode arc-discharge source (1) creates a plasma from which hydrogen ions and charged molecules are extracted. An ion optical grid system then focalizes and accelerates all charged particles to the beam energy. In the neutralizer tube (2) molecules are dissociated and neutralized by interaction with a low pressure gas. The neutralization fraction is of the order of 50% for hydrogen ions, and larger for

[8] This assumption can be wrong, given that strong asymmetries in the distribution of neutrals in the vessel are possible, especially in proximity of the limiter element or the null point in diverted configuration.

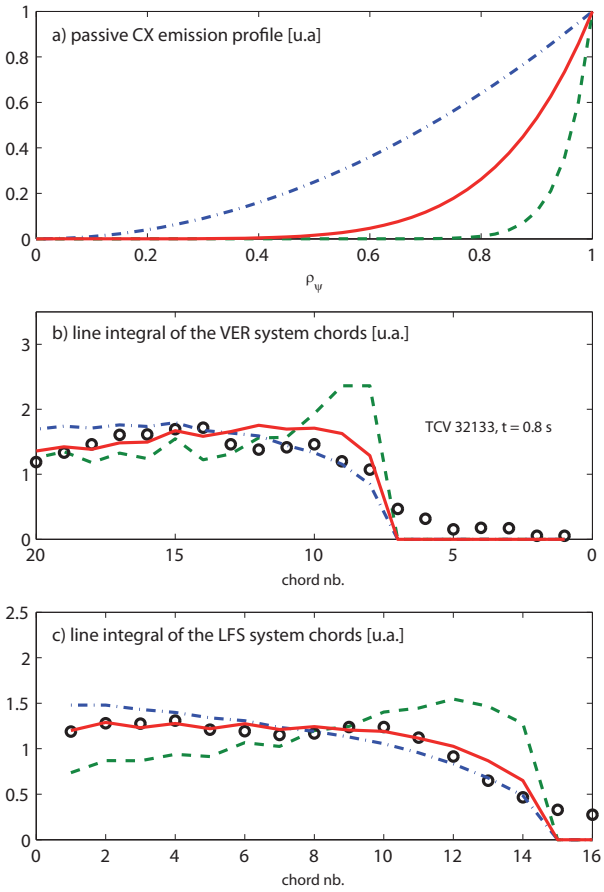

Figure 2.16: Three test radial profiles for the passive CX emission of CVI 529.1 are mapped to the magnetic equilibrium to obtain the line integrated intensity for the VER and LFS observations (solid curves). The comparison with the experimental measured intensities indicated that the passive emission is not only localized in a thin shell at the boundary of the plasma, but extends to the core and beyond.

other extracted particles. The residual charged population is deflected and removed by the beam by electric magnets (5). Through a short interfacing duct the neutral beam reaches the TCV chamber.

Usually the DNBI operates at neutral energies close to 50 kev/amu, to ensure a good beam penetration in intermediate and high density plasmas ($n_e > 5{\times}10^{19}\,\mathrm{m}^{-3}$) and to optimize the yield of the CVI($n = 8 \rightarrow 7$) carbon line that is close to its maximal value at this energy.

The DNBI is injected at the horizontal vessel midplane, almost perpendicular to the torus, to maximize the beam penetration whilst, incidentally, simultaneously minimizing the toroidally injected momentum. A small injection angle of 11.25° is retained to reduce particle trapping of the injected particles in the toroidal ripple of the magnetic field.

The beam has a gaussian shape and a small divergence of 0.5°. In order to reduce the beam width $1/e$ to ≈ 8 cm, the beam is focussed at the center of TCV vacuum vessel.

The DNBI is operated in pulsed mode, with typical injection phases of $10 \div 100$ ms and a duty cycle of 30% (ON:OFF = 1:2). The operation is synchronized with the acquisition of CXRS. The characteristic times of DNBI (typical current rise and fall times of 2 ms and $\approx 50\ \mu$s) are negligible compared with the typical exposition times of the CXRS ($15 \div 50$ ms). The modulation of the

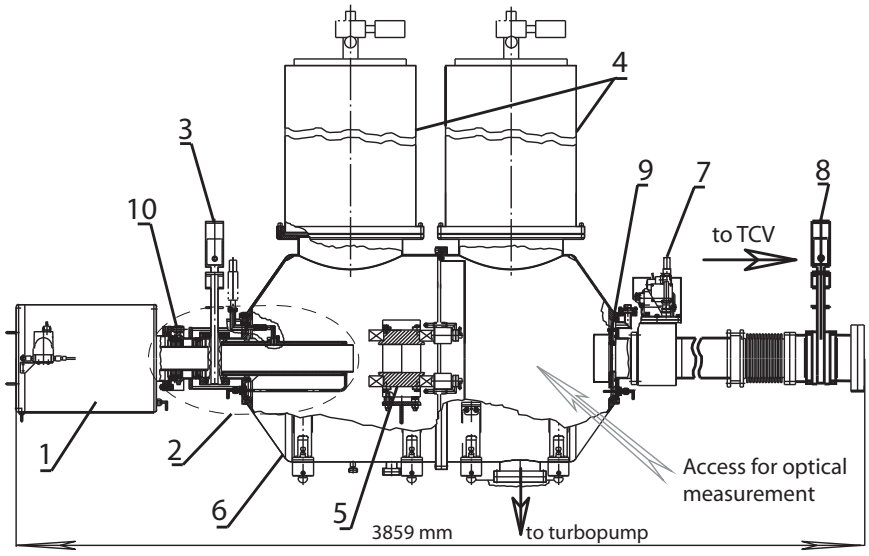

Figure 2.17: Side view of the DNBI. The labeled components are: 1) ion source, 2) neutralizer, 3) ion source valve, 4) cryogenic pumps, 5) magnetic separator with diaphragm, 6) vacuum tank, 7) retractable calorimeter, 8) TCV gate valve, 9) aiming target and 10) turning gear. The line view used for optical measurements of the beam fractions is indicated in the right bottom region.

DNBI helps in the extraction of the active spectral component of the measured emission.

2.7.1 Neutral beam energy spectrum

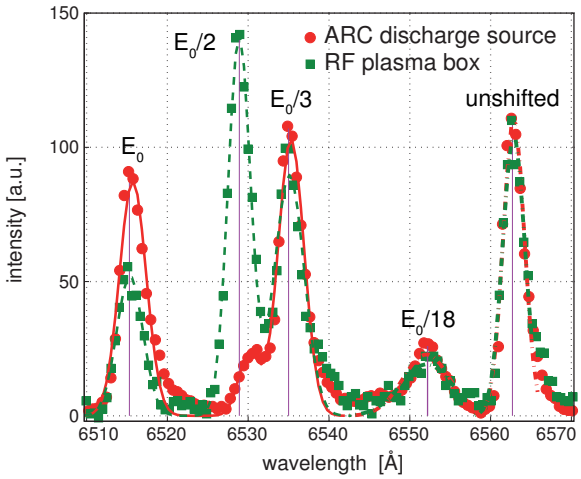

Figure 2.18: Neutral beam energy components are visible in the H_α emission, from observation at 45°, separated by the energy dependent Doppler shift. The graph compares the spectra acquired during beam pulsed generated with Radio Frequency and Arc Discharge sources.

Acceleration of H_2^+, H_3^+ and H_2O^+ present in the ion source, followed by dissociation and neutralization, results in the presence of 4 main energy particle components in the DNBI, of energy E_0, $E_0/2$, $E_0/3$, $E_0/18$. As the CX cross section is maximal around E_0, it is beneficial to maximize the full energy fraction where the beam penetration is also largest. The neutral beam composition is measured by observing the H_α emission at an angle of 45°: the different Doppler shifts separate the energy components. Fig 2.18 compares such spectra for the arc ion source and

the precedent plasma ion source. The full energy component has typically $\approx 85\%$ of the neutral density.

The contribution of the low energy components could, nevertheless, may be significant because the presence of neutrals in the excited $n = 2$ state (and above). The fraction of excited beam neutrals depends on plasma density, but is, in general, $\lesssim 0.5\%$ for TCV plasmas. However, the CX cross section at energies <30 keV is 3 to 5 orders of magnitude larger than that of ground state ($n = 1$), so the overall contribution may be substantial.

To obtain an estimation, we calculated the effective cross section for CVI($n = 8 \rightarrow 7$) from ADAS [25] for typical TCV conditions ($T_\mathrm{i} = 500$ eV, $n_i = 1 \times 10^{19}\,\mathrm{m}^{-3}$, $Z_\mathrm{eff} = 2$), considering 0.005 fraction of $n = 2$ neutrals. On this base, the relative contribution to the charge exchange recombination from low energy fractions has been evaluated for the DNBI sources (Arc and Radio Frequency) (see table 2.3).

DNBI source	Parameter	E_0	$E_0/2$	$E_0/3$	$E_0/18$
Radio frequency	Neutral fractions (%)	58	22	18	2
2004	Emission fractions (%)	82	9	8	1
Arc discharge	Neutral fractions (%)	88	4	7	1
2006	Emission fractions (%)	95	1	3	1

Table 2.3: Contribution of different energy components of the DNBI to the CX recombination, for the two source configurations.

The results indicate that the full energy component accounts for more than 85% of the CX recombinations. With the upgraded DNBI Arc source only 5% of the signal is due to lower energy fractions.

Each energy component is only approximately monochromatic. Due to plasma source ion temperature and broadening effects of neutralization, an energy spread of few tens of eV is present in each beam component. Furthermore, during beam pulse, the fluctuation of the acceleration voltage, possibly coupled with the fluctuation of beam current, translates into a broadening of the average energy spectrum that, following the DNBI configuration and operational state, can raise up to $\lesssim$ 1keV [33].

2.7.2 Perturbation induced by the DNBI

The DNBI may perturb the measurement in several ways, by polluting the measurement or affecting directly the plasma quantities that are to be measured, velocity and temperature. We devote this section to evaluate the impact of the DNBI in perturbing the measured quantities, i.e. carbon temperature and rotation.

2.7.2.1 Halo and plume

The H-like impurity ions, resulting from charge exchange with beam neutrals outside the observation volumes, may contribute to the collected active signal radiating by collisional excitation when crossing the lines of sight whilst moving along the magnetic field lines. This is the so called *plume* effect [22, 23], which mainly affects the impurity density measurement and decreases the spatial resolution. The effect of plume radiation is important for low Z ions, as they do not have to be excited to high principle quantum levels in order to emit visible light. For heavier impurities, the

contribution is weaker. In the case of CVI 529.1 nm, as it requires an electron impact excitation from ground state n=1 to n=8, the contribution is negligible [23].

Another indirect contribution to the active signal comes from the CX reactions with thermal neutrals (≈ 500 eV) produced by charge exchange recombination with the beam:

$$\mathrm{H}^0_{beam} + D^+_{plasma} \rightarrow H^+_{beam} + D^0_{plasma} \tag{2.7.1}$$

The effect of these *halo* neutrals is to enhance the CX emission. If not taken correctly into account this affects the measurement of the impurity density. If the halo density is significantly larger than the beam cross section it may also decrease the radial resolution. The halo produced by the TCV DNBI has been calculated [16] showing that, at the magnetic axis, the halo and fast neutral populations have comparable densities and a spatial distribution that is 30% of the beam profile. However, since effective cross sections decrease rapidly with the neutral donor energy (3 orders of magnitude for CVI 529.1 nm, from 50 keV and 500 eV) this effect should be small. Neglecting the halo contribution to the measured intensity leads to an overestimation of the impurity density of the order of 10% [23].

2.7.2.2 Heat deposition

For the nominal values of DNBI parameters, the injection power is upper bounded at 80 kW. Only a fraction of this power is finally adsorbed by the plasma. An evaluation of the energy losses of the beam in a maxwellian plasma (carbon, electrons and deuterium) shows that the power is absorbed preferably by the electrons [16, 23], with only 10% of the power absorbed by the ions. Furthermore, considering the duty cycle of 30%, the average power delivered by the DNBI on ions is of the order of 2 kW. This is from 10 to 100 times lower that the electron-ion equipartition power (i.e. the power exchanged between ions and electrons by collisions due to $T_\mathrm{e} \neq T_\mathrm{i}$) which, in TCV, is the main heat source for the ion species. Experimental verifications of this were provided by the NPA T_i measurements during beam operation, that showed an increase of the effective ion temperature due to the beam power deposition well below 10% of T_i [16].

2.7.2.3 Torque

The perturbation of the rotational state of the plasma may derive from two different main mechanisms:

- Neutral particles injected with a finite toroidal angle, when ionized in the plasma core, begin to circulate along magnetic field lines and distribute their angular momentum to the main plasma through collisions. This contribution is minimal for nearly perpendicular injection and is independent of the magnetic field configuration (e.g. $B_\phi \cdot I_\mathrm{p}$ direction). The effect of this torque is visible on timescales of the order of the ion-ion collision time τ_{ii}, $\tau_{ii} \approx 1 \div 2$ ms in TCV plasma core.

- A part of the fast neutrals of the beam, as they are ionizes in the plasma, may be in trapped ion orbits, that, because of their banana shaped orbital motion, origins an average radial ion current. This ion current is canceled by a radial current flowing in the background plasma, causing a $j \times B$ torque [34]. This affects promptly the plasma, and depends on the direction of I_p, giving in particular an inward radial current for co current beam injection and an outward one for counter current beam injection.

Concerning the collisional torque, an estimate of the acceleration induced during a DNBI pulse of length Δt, assumed smaller than the momentum confinement time, can be made with [23]:

$$\Delta u_\phi[\mathrm{m/s}] \approx \sqrt{\frac{m_p E_i[\mathrm{eV}](\varepsilon_i I_{b,i}[A])^2}{2e}} \frac{\sin\alpha}{M} \Delta t \tag{2.7.2}$$

where m_p and M are the proton mass and the total plasma mass in kg; E_i, $I_{b,i}$ and ε_i are the energy, the equivalent neutral current and its absorbed fraction of the i-th beam component; α is the beam injection angle. For two exemplary discharges of low and an high density this gives the results shown in Table 2.4. In these discharges only a fraction of the injected power is absorbed, ranging from 20% at $n_{\mathrm{e,av}} = 1{\times}10^{19}\,\mathrm{m}^{-3}$ to 80% at $n_{\mathrm{e,av}} = 6\times10^{19}\,\mathrm{m}^{-3}$. Considering a deuterium plasma with carbon impurity only, the estimated beam induced rotation is positive and of the order of the typical uncertainty of toroidal plasma rotation measurement ≈ 1 km/s. Notice that the beam attenuation scales roughly with the plasma density: the larger absorption at high density is compensated by a larger accelerated mass resulting in a rotation increment similar to the low density case. The lower energy beam fractions contribute significantly to the perturbation.

TCV	$n_{\mathrm{e,av}}$	E_0	$E_0/2$	$E_0/3$	$E_0/16$	Total
27182	$1{\times}10^{19}\,\mathrm{m}^{-3}$	0.28	0.18	0.21	0.03	0.70 km/s
27504	$6{\times}10^{19}\,\mathrm{m}^{-3}$	0.29	0.14	0.14	0.01	0.58 km/s

Table 2.4: Carbon velocity induced by the collisional torque for beam energy component and total. The values indicate the increment of velocity in km/s

To estimate the effect beam induced torques, it is useful to compare the rotation profile in discharges with opposite plasma direction, but otherwise similar. An example is represented by the two discharges in Fig. 2.19, obtained with the same plasma shape at the similar values of total current, plasma density and with similar electron density and temperature profiles. The toroidal rotation is found to invert with opposite current direction, with similar values in the region outside the sawtooth inversion radius, that in these discharges is located at $\rho_\psi \approx 0.35$. Discrepancies observed in the core region are related to a smaller inversion radius for the negative current discharge.

Another confirmation of negligible plasma velocity perturbation from the DNBI comes from the measurement of MHD modes frequency. For instance the frequency of sawtooth precursors can be considered parametric of core plasma rotation (see section 3.8). During beam pulses of 50 ms or shorter, no significant effect on sawtooth precursor frequencies was observed.

The effect of neutral beam injection on poloidal rotation has been estimated in [34], accounting for the neoclassical poloidal rotation damping. It was found that it is negligible compared with the effect on toroidal rotation for tokamak plasma configurations.

2.8 Conclusion

In this chapter the CXRS diagnostic on TCV has been described in its configuration after the upgrade performed during this thesis. For the horizontal views, the spatial resolution and radial coverage were successfully extended from 16 to 40 independent measurement volumes, with the new ability to perform measurements across the whole plasma diameter. A vertical view was

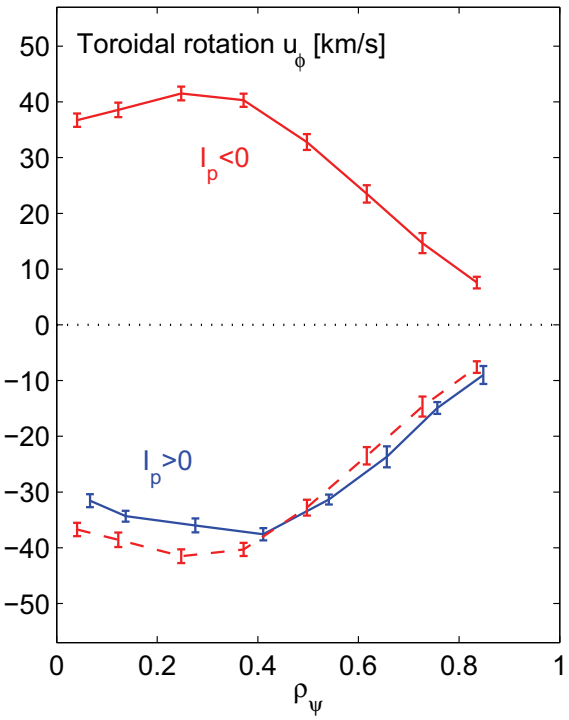

Figure 2.19: Toroidal rotation profile for positive I_p (blue-TCV 27098) and for negative I_p (red-TCV 27484). The toroidal rotation in TCV 27098, normalized in the co current direction, is also plotted in dotted blue.

successfully set up, in order to measure the poloidal rotation in the outboard midplane with another 40 measurement points.

Successively, the analysis method used to obtain active measurements has been described. A solid wavelength calibration is imperative to obtain the correct absolute rotation measurements. The shot by shot inline calibration methodology and the integration of the calibration data into the analysis code attained an accuracy for the wavelength position required to resolve Doppler shifts of 0.02 Å, corresponding to plasma velocities down to 1 km/s.

The DNBI is a key element of the diagnostic, that provides the signal from the core plasma and guarantees the localization of the measurement. It has then been described, with particular emphasis on its auxiliary effects such as plasma heating and applied torque. The estimation of these effects, combined with experimental results, show that the impact of the DNBI in CXRS measurement during ordinary operation is minimal and negligible compared to other error sources. This justifies one of the premises of this thesis, i.e. that the measurement of intrinsic rotation can be performed with the accuracy required for momentum transport studies.

Chapter 3

Plasma rotation

This chapter gives an overview of plasma rotation in tokamaks from a theoretical perspective, focusing on some of the fundamental aspects that are important in the interpretation of experimental observations.

For rotation, a tokamak plasma is a complex system as it has two coupled privileged directions: that parallel to the magnetic field and the toroidal direction. The first is the direction along which the charged plasma particles are constrained to flow, in absence of collisions or turbulence, and the second is a symmetry direction for the system which results in the concept of total toroidal momentum conservation.

The coupling between these two dynamics, through collisions (fast time scale) or instabilities (long time scale), is at the root of the physics determining the rotation state of the plasma: the first order flows, established on the fast timescale, will be determined by the parallel dynamic, while the toroidal effects are responsible for the slow cross field momentum transport and will determine the final stationary rotation profile.

3.1 Plasma velocity and momentum balance

From a statistical point of view, a plasma is a system constituted of a large collection of different species of interacting particles: ions, electrons and neutrals. The statistical behavior of a such a system is described by the Boltzmann equation, which prescribes the evolution of the distribution function $f_\alpha(\mathbf{x}, \mathbf{v}, t)$ of the species α particles:

$$\frac{\partial f_\alpha}{\partial t} + \mathbf{v} \cdot \nabla f_\alpha + \frac{\mathbf{F}}{m_\alpha} \cdot \nabla_v f_\alpha = \left(\frac{\partial f_\alpha}{\partial t} \right)_{collisions} \tag{3.1.1}$$

The distribution function changes as a result of forces $\mathbf{F}$ and collisions (right hand side). In a plasma, the main forces are the Lorentz forces $\mathbf{F} = q(\mathbf{E} + \mathbf{v} \times \mathbf{B})$. Collisions between particles, of same or different species, result in friction forces, viscosity and electrical resistivity. The full description of the plasma evolution requires a solution of the Boltzmann equation together with Maxwell equations for $\mathbf{E}$ and $\mathbf{B}$ fields, with an appropriate description of the collision term. This is a very complex problem and, for many applications, a fluid description can be, to a certain extent, a good approximation of the system. The multi fluid description is obtained evaluating the moments of the Boltzmann equation 3.1.1. From the first and second moment we obtain the mass and the momentum conservation equations for the species α:

$$\frac{dn_\alpha}{dt} + n_\alpha \nabla \cdot \mathbf{u}_\alpha = 0 \tag{3.1.2}$$

$$m_\alpha n_\alpha \frac{d\mathbf{u}_\alpha}{dt} = n_\alpha q_\alpha (\mathbf{E} + \mathbf{u}_\alpha \times \mathbf{B}) - \nabla \cdot \mathbf{P}_\alpha + \mathbf{R}_\alpha + \mathbf{S}_\alpha \tag{3.1.3}$$

where the total derivative is defined as $\frac{d}{dt} = \frac{\partial}{\partial} + \mathbf{u}_\alpha \cdot \nabla$ with the following definitions: $n_\alpha = \int f_\alpha dv$ is the number density; $\mathbf{u}_\alpha = \int v f_\alpha dv$ is the fluid velocity of the species α; $P_\alpha = n_\alpha m_\alpha (v - u_\alpha)(v - u_\alpha)$ is the pressure tensor; $\mathbf{R}_\alpha$ is the momentum transfer due to collisions between different plasma species (i.e. friction); $\mathbf{S}_\alpha$ is the momentum source and includes all torques externally applied to the plasma. This is Newton's law $m\frac{d\mathbf{u}}{dt} = F$, evaluated per unit volume.

A further level of simplification is obtained summing the equations over all of particle species in order to obtain a single fluid description. In this case, single fluid mass, particle density and fluid velocity are defined as:

$$m = \sum m_\alpha \qquad n = \frac{\sum m_\alpha n_\alpha}{\sum m_\alpha} \qquad \mathbf{u} = \frac{\sum_\alpha m_\alpha n_\alpha \mathbf{u}_\alpha}{\sum_\alpha m_\alpha n_\alpha} \tag{3.1.4}$$

Although in an impure plasma each species may flow with a different velocity, as we will see later on, in a plasma with low impurity density $n_i \gg n_\alpha, \alpha \neq i$, given that $m_e \ll m_i$, the single fluid velocity will substantially coincide with the main ion species $\mathbf{u} \approx \mathbf{u}_i$.

If we consider the stationary situation ($\frac{\mathrm{d}}{\mathrm{d}t} = 0$) with subsonic velocities, neglecting friction between other species and considering an isotropic pressure ($\mathbf{P} \approx p\mathbf{I}$, with $\mathbf{I}$ the identity matrix), these equations reduce to [2]:

$$n_\alpha \nabla \cdot \mathbf{u} = 0 \tag{3.1.5}$$

$$\nabla p_\alpha = q_\alpha n_\alpha (\mathbf{E} + u \times \mathbf{B}) \tag{3.1.6}$$

The second equation is known as the force balance equation and states that, to lowest order, the Lorentz force is balanced by the pressure force. Taking the cross product of Eq. 3.1.6 with $\mathbf{B}$, a perpendicular velocity is found:

$$\mathbf{u}_\alpha^\perp = \mathbf{u}_{E\times B} + \mathbf{u}_\alpha^* \tag{3.1.7}$$

$$\mathbf{u}_{E\times B} = \frac{\mathbf{E} \times \mathbf{B}}{B^2} \tag{3.1.8}$$

$$\mathbf{u}_\alpha^* = -\frac{1}{q_\alpha n_\alpha} \frac{\nabla p_\alpha \times \mathbf{B}}{B^2} \tag{3.1.9}$$

$\mathbf{u}_\alpha^\perp$ is determined by drift velocities due to the forces $q_\alpha n_\alpha \mathbf{E}$ and $-\nabla p$. The first is the $E \times B$ drift and affects in the same way all particle species and the second is the diamagnetic drift, which depends on the particles' charge and, importantly, is of opposite direction for ions and electrons. It can be shown [2], that the diamagnetic drift in the fluid model accounts for the single particle drifts provoked by the gradient and the curvature of magnetic field, inherent in the tokamak configuration.

The perpendicular velocity $\mathbf{u}^\perp$ is the lowest order solution of the momentum balance equation and demonstrates that electrical fields and pressure gradients constitute the primary drives for plasma velocity. The equilibrium, stated in the force balance equation, is established in Alfvènic timescales (μs), which is the propagation timescale of magnetic perturbations. On longer timescales, the plasma flow and magnetic and electric fields can evolve to very different values, through intermediate states for which, to first order, the force balance equation is satisfied [35,36].

3.2 Plasma rotation in a toroidally axisymmetric equilibrium

In a tokamak equilibrium described in the reference frame (r, θ, ϕ), the fluid plasma velocity $\mathbf{u}_\alpha$ may be decomposed into a toroidal component u_ϕ and a component in the poloidal plane. The

latter can be decomposed into two components: tangential and perpendicular to the magnetic surface, respectively u_θ and u_r. Note that u_θ coincides with the θ and r component of u only for circular, concentric, flux surfaces. The radial component, perpendicular to magnetic flux surfaces, describes the radial particle flux $\Gamma = m_\alpha n_\alpha u_{\alpha,r}$. In this thesis we will refer to plasma rotation as part of fluid velocity lying on a magnetic flux surface. The toroidal and poloidal components of plasma rotation are often represented in terms of angular velocity: $\omega_\phi = u_\phi/R$, $\omega_\theta = u_\theta/r$, expressed in radians/s. The plasma rotation may also be decomposed into components parallel and perpendicular to the magnetic field.

Given that $B_\phi \gg B_\theta$, toroidal and parallel rotations are similar in magnitude and often considered the same. Nevertheless, the distinction plays a crucial role in evaluating theoretically the toroidal momentum transport that determines the rotation profile.

It is important to note that the first order flows, in a tokamak plasma, lie entirely on a magnetic surface. This may be seen by taking the perpendicular component of the momentum balance equation and observing that the leading orders of ∇p, ∇T and $\mathbf{E} = -\nabla\Phi$ are perpendicular to the magnetic surface.

It is accepted [37, 38], that the first order flows are incompressible and can be expressed in the general forms:

$$\mathbf{u} = \omega(\psi) R \mathbf{e}_\phi + U_\theta(\psi)\mathbf{B} \tag{3.2.1}$$

$$u_\phi = \omega(\psi) R + u_\theta \frac{B_\phi}{B_\theta} \tag{3.2.2}$$

$$u_\theta = U_\theta(\psi) B_\theta \tag{3.2.3}$$

where ω and U_θ are functions of the poloidal flux ψ, hence constant on a flux surface.

Thus, in general, neither the poloidal nor toroidal rotation are flux functions. In particular, poloidal rotation varies with θ, following the poloidal variation of B_θ. The "rigid rotor" toroidal rotation $\omega(\psi)$ is corrected by a term that varies poloidally, following the variation of B_ϕ.[(1)] The relevance of this correction is still an open issue, from the experimental point of view, mostly due to the difficulty in measuring the inboard plasma rotation. It is common to assume that this correction is small compared to the rigid body rotation as the U_θ term is generally strongly damped by parallel viscosity. This is indeed a good approximation when dealing with plasmas accelerated toroidally by NBI and where the poloidal rotation still remains close to neoclassical predictions, so that $\omega(\psi)R \gg u_\theta B_\phi/B_\theta$. For intrinsic rotation, the contribution may not be as negligible as in the externally driven case. A first experimental answer to this issue will be provided in chapter 4.

3.3 Momentum transport: sinks, sources, fluxes

In this section we will formulate the problem of determining the rotation state of a plasma as a problem of momentum transport. Let us consider equations 3.1.2 and 3.1.3. Assuming stationary density, we take the mass continuity equation $\nabla \cdot (m_\alpha n_\alpha \mathbf{u}_\alpha) = 0$ to reformulate the momentum balance equation in the form:

$$m_\alpha n_\alpha \frac{\partial \mathbf{u}_\alpha}{\partial t} + \nabla \cdot (m_\alpha n_\alpha \mathbf{u}_\alpha \mathbf{u}_\alpha) + \nabla \cdot \mathbf{\Pi} = n_\alpha q_\alpha (\mathbf{E} + \mathbf{u}_\alpha \times \mathbf{B}) - \nabla p_\alpha + \mathbf{R}_\alpha + \mathbf{S}_\alpha \tag{3.3.1}$$

which now looks like a continuity equation for the momentum, stating that the variation of momentum in a volume element is determined by the exchange of momentum from the neighbors plus the forces acting on the volume element itself.

(1) Note that, in general, $\langle u_\theta B_\phi \rangle \neq 0$ (average over the flux surface).

The left hand side of the equation contains the divergence of two tensors that describe the inertia ($m_\alpha n_\alpha \mathbf{u}_\alpha \mathbf{u}_\alpha$) and the viscosity ($\mathbf{\Pi}$). Entering formally the equation as fluxes, they account for momentum transport.[2] In particular, $\mathbf{\Pi}$ contains elements depending on the plasma velocity gradient, characteristic of diffusive processes. The physical mechanisms that combine to result in momentum transport are numerous: neoclassical, turbulent, MHD. The right hand side contains the forces that can act as sources or sinks of momentum. In general, Lorentz forces, pressure and friction forces represent direct momentum sources for single species momentum balance. There are also the external contributions due to externally applied forces.

Taking the toroidal projection of the previous equation ($\mathbf{e}_\phi \cdot$) and summing over all the ion species with flux averaging (indicated by $\langle \cdot \rangle$), we obtain the following equations:

$$mn\frac{\partial \langle u_\phi \rangle}{\partial t} + \langle \nabla \cdot \mathbf{\Gamma}_\phi \rangle = \langle \mathbf{S} \rangle \tag{3.3.2}$$

$$\mathbf{\Gamma}_\phi = (mn\mathbf{uu})_\phi + \mathbf{\Pi}_\phi \tag{3.3.3}$$

where quantities $(\mathbf{u}, n, m)$ refer now to a single fluid plasma, Eq. 3.1.4.

$\mathbf{\Gamma}_\phi$ is a vector expressing the flux of toroidal momentum. For a tokamak topology of nested surfaces, the problem can be reduced to a one dimensional problem. If ρ is a monotonic function of the poloidal flux labeling the magnetic surfaces, $V(\rho)$ the volume enclosed by a flux surface, and $V' = \frac{\partial V}{\partial \rho}$, the flux surface average of a vectorial field $\mathbf{A}$ becomes:

$$\langle \nabla \cdot \mathbf{A} \rangle = \frac{1}{V'}\frac{\partial}{\partial \rho}\langle V' \mathbf{A} \cdot \nabla \rho \rangle \tag{3.3.4}$$

Indicating with $\Gamma_{\phi r} = \langle \mathbf{\Gamma} \cdot \nabla \rho \rangle$ the radial (perpendicular to magnetic surfaces) flux of toroidal momentum, then Eq. 3.3.2 becomes:

$$mn\frac{\partial u_\phi}{\partial t} + \frac{1}{V'}\frac{\partial}{\partial \rho}\left(V' \Gamma_{\phi r}\right) = S \tag{3.3.5}$$

for which all quantities are averaged on a flux surface. This equation simply states that the variation of the angular momentum carried by a plasma shell results from momentum exchange with neighboring shells plus any external source or momentum sink.

The radial momentum flux $\Gamma_{\phi r}$ contains all the physical mechanisms that contribute to differential acceleration of flux shells (neoclassical, turbulent, MHD). All these contributions are often recast in a practical expression following an explicit dependence on u_ϕ and its radial gradient:

$$\Gamma_{\phi r} = -\chi_\phi \frac{\partial u_\phi}{\partial \rho} + V_\phi u_\phi + v_{th} C_\phi \tag{3.3.6}$$

The term proportional to $\frac{\partial u_\phi}{\partial \rho}$ is the radial diffusive transport (cross-field viscosity); the term proportional to u_ϕ includes all convective contributions to momentum transport; the last term sums up the contributions that do not depend linearly on u_ϕ nor its gradient and is normalized to plasma thermal velocity. The proportionality coefficients χ_ϕ[m^2/s], V_ϕ[m/s] and C_ϕ[m/s] are evaluated along the radial profile, and their knowledge allows a complete description, at least phenomenologically, of the evolution of the toroidal velocity profile.

It can be shown that the first term in Eq. 3.3.6 comes from the leading term of the viscous stress tensors. The third contribution arises from higher order contributions to the viscous stress [39, 40]

[2] Strictly speaking they are tensors that assume the form and the dimension of a flux only after projection along a given direction.

and from the turbulent Reynolds stress contained in the inertial term [41]. For this it is often referred to as "residual Reynolds stress". It is important to note that such a term is formally equivalent to an external source of momentum as it may be included in the right hand side of Eq. 3.3.5 simply by applying a radial derivative. This indicates its importance for fusion reactors since it provides a mechanism to drive intrinsic rotation. Conversely the convective term may cause acceleration only in the presence of a non null background rotation profile.

The stationary rotation profile, in absence of external sources, is determined by the condition $\Gamma_{\phi r} = 0$, which is a first order differential equation for the real variable u_ϕ, complimented by an adequate boundary condition (e.g. prescribing u_ϕ at the plasma edge, eventually taken from the experiment):

$$\frac{\partial u_\phi}{\partial \rho} = -\frac{V_\phi}{\chi_\phi} u_\phi + v_{th} \frac{C_\phi}{\chi_\phi} \tag{3.3.7}$$

$$u_\phi(a) = u_{\phi a} \tag{3.3.8}$$

The last equation shows that, even in absence of external sources of momentum, a tokamak plasma can self sustain a finite rotation gradient.

The S term in Eq. 3.3.5 includes all external contributions to momentum as a function of the minor radius. These contributions represent momentum *sources* that tend to accelerate the plasma or *sinks* that tend to brake the plasma to a given rotation value.

Examples of the momentum sources are the Neutral Beam Injectors (NBI) [34], while momentum sinks are naturally represented by friction forces, for example, the loss of momentum due to interaction with neutral particles [42] or MHD structures as magnetic islands or resonant field errors [36, 43].

3.4 Neoclassical rotation

The problem of momentum transport has been addressed in the frame of neoclassical theory. This describes transport of particles, momentum and energy in a plasma confined by an inhomogeneous toroidal magnetic field, accounting for collisions. It does not account for effects of turbulent fluctuations.

In the absence of external sources, the toroidal and poloidal rotation profiles can be deduced from the parallel momentum balance (projecting Eq. 3.1.3 on $\mathbf{B}/B$) and calculating the parallel and perpendicular first order flows. This was addressed within the so called *moments approach* and a solution was reported by Hirschmann and Sigmar [35]. The results were summarized and explicitly provided for the case of ions and one or more impurity species in Kim and Diamond [38], where, neglecting friction with electrons, explicit expressions were proposed for toroidal and poloidal rotations in all collisional regimes:

$$u^i_{\phi,neo} = \frac{E_r}{B_\theta} - \frac{T_\mathrm{i}}{eB_\theta}\left[K_n(\nu_{*i},\epsilon)\frac{1}{n_i}\frac{dn_i}{dr} + K_T(\nu_{*i},\epsilon)\frac{1}{T_\mathrm{i}}\frac{dT_\mathrm{i}}{dr}\right] \tag{3.4.1}$$

$$u^i_{\theta,neo} = \frac{T_\mathrm{i}}{eB_\theta}\left(K_1\frac{1}{T_\mathrm{i}}\frac{dT_\mathrm{i}}{dr}\right)\frac{BB_\phi}{\langle B^2\rangle} \tag{3.4.2}$$

where n_i and T_i are the main ion density and temperature and the coefficients K_x depend on the ion collisionality ν_{*i} and inverse aspect ratio ϵ. Impurity and main ions may develop different poloidal

and toroidal rotations. In the low collisionality banana regime, differential rotation profiles are expressed by (superscript i and I designate ion and impurity species):

$$\Delta u_\theta^i = u_\theta^i - u_\theta^I \approx \frac{1}{2eB_\phi}\frac{dT_\mathrm{i}}{dr}\left[-3K_2 + 2\frac{L_{T,i}}{L_{p,i}}\left(1 - \frac{Z_i L_{pi}}{Z_I L_{pI}}\right)\right] \tag{3.4.3}$$

$$\Delta u_\phi^i = u_\phi^i - u_\phi^I \approx -K_2\frac{3}{2eB_\theta}\frac{dT_\mathrm{i}}{dr} \tag{3.4.4}$$

These results were extended by Testa [44] where simple analytical formulae are proposed to obtain neoclassical coefficients for all collisionality regimes, including effect of orbit squeezing. Within the same work, the correctness of the model predictions was confirmed by obtaining the same radial electric field profile for different rotations of carbon and deuterium species.

Kim's formulae are derived for $x = v_{th,I}/v_{th,i} \ll 1$, whereas for TCV carbon impurity, $v_{th,I}/v_{th,i} \approx 0.4$. The problem must, thus, be solved considering the complete form of the friction matrices, instead of the simplified form in [38]. As will be shown in greater detail, Kim's formulae's predictions (described for TCV discharges in [45]) tend to overestimate Δu_ϕ, that, in reality, rarely exceeds 3 km/s.

Within this treatment, the radial electric field E_r is undetermined. This degree of freedom relates to the axial symmetry of the problem, which is not resolved to the first order. A practical consequence is that, to obtain quantitative theoretical predictions, an experimental profile is always needed. Typically, the u_ϕ profile of a measured impurity is supplied to obtain predictions for the main ions' or other impurities' poloidal and toroidal rotations and the radial electric field profile [44].

A full self-consistent prediction of plasma rotation requires an independent theoretical prediction for E_r, which is typically the result of momentum transport on timescales longer that the ion collisional time. The stationary radial electric field profile can be determined by setting to zero the radial momentum flux and accounting for higher order terms, notably the inertia and viscous stress tensors.

In the frame of neoclassical theory, such calculations began decades ago and continue to the present day, demonstrating the importance of the topic and, incidentally, the complexity of the problem. Several authors propose predictions for the rotation gradient, within fluid [39] and kinetic treatments [40, 46] for different collisional regimes. The debate is still on-going. We will limit the discussion here to a summary of some recent predictions for the toroidal rotation gradient that in the second part of the thesis will be compared with experimental observations.

The following expression for the radial gradient of u_ϕ, suitable for all collisionality regimes, was proposed by Wong [46]:

$$\frac{du_\phi}{dr} = 3.7\frac{1}{eB_\theta\sqrt{\epsilon}}\left\{\frac{dT}{dr}\left[\frac{1}{2r} + \frac{2dq}{qdr} + \frac{2dn}{ndr} - \frac{dT}{2Tdr}\right] + \frac{d^2T}{dr^2}\right\} \tag{3.4.5}$$

where e is the electric charge and q the local safety factor.

Classen [39] proposed a formula from a two fluid treatment with ions and electrons in circular geometry:

$$\frac{du_\phi}{dr} = 0.107K_2q^2\frac{T_\mathrm{i}}{eB_\theta}\left(\frac{d\ln T_\mathrm{i}}{dr}\right)^2 \tag{3.4.6}$$

which was confirmed by more recent work [47, 48]. This formula is strictly valid for high collisionality Pfirsch-Schlüter regime where $K_2 = -1.83$. Nevertheless, in the same work, this formula is considered with $K_2 = 1.17$ in the low collisionality banana regime, suggesting a reversal of

the peaking direction of the u_ϕ profile as the ion collisionality increases. Although this extension was not explicitly justified, there are indications that kinetic treatments may support this procedure [48].

Leaving comparison with experimental observations for the present, we anticipate the general trend of experimental and theory comparison is of a mismatch in direction and in magnitude. For instance, in the region close to the plasma edge, where collisional models are best suited, a finite positive gradient is predicted whereas zero or negative gradient is observed. This could suggest that the stationary (long timescale) radial electric field is likely to be related to turbulent transport.

3.4.1 Inductive electric field

The role of the inductive toroidal electric field on stationary rotation was considered by Kim in [38]. Since quasi-neutrality is enforced by the plasma, it does not introduce a net momentum in the plasma. It can, however, produce a differential rotation between different ion species, with the impurity (carbon) ions accelerated in the counter current direction. This effect was evaluated [49], and concluded a counter current contribution, depending on Z_{eff}, that only accounts for a small or negligible contribution to the observed toroidal rotation.

These results are valid in stationary conditions, i.e. on timescales longer than the frictional timescales (ion-ion collision time). For faster timescales, an electric field can effectively accelerate ions that, for certain conditions, may also acquire enough energy to escape the confined plasma. Runaway ions have been observed under strong transient parallel electric fields developed during a sawtooth crash. A possible transient effect on background plasma velocity will be considered for TCV in chapter 8.

3.4.2 Poloidal flow damping

An important result of neoclassical theory is the prediction of strong damping that limits the magnitude of poloidal rotation. This relies on the toroidal magnetic equilibrium in which B_ϕ is larger for the inboard plasma and weaker outboard. A poloidally rotating plasma volume sees a time varying magnetic field by which it is periodically pinched (HFS) and stretched (LFS). Through the mechanism of magnetic pumping [50] the energy of this time varying field is transferred to the plasma, in the form of kinetic energy i.e. heat. Ultimately, under the action of magnetic pumping any externally induced poloidal rotation should decay towards the value predicted by the neoclassical theory u_θ^{neo}.

Poloidal flow damping is accounted for in the poloidal projection of the force balance equation, where the viscous tensor appears as:

$$\langle (\nabla \cdot \mathbf{\Pi})_\theta \rangle = \alpha (u_\theta - u_\theta^{neo}) \tag{3.4.7}$$

This term's effect is to damp the poloidal velocity to the neoclassical value u_θ^{neo} on a timescale that is expressed by the factor α, which depends on plasma parameters and notably on the collisionality regime (banana, plateau or Pfirsch-Schlüter) [50]. In general, the process occurs on timescales of the order of the ion-ion collision (≈ 1 ms in TCV).

Since Eq. 3.4.7 depends only on the local velocity and not, for example, on its radial gradient as for u_ϕ, the poloidal force balance equation is radially decoupled. In other words, the evolution of u_θ in one radial position is weakly dependent on the value of u_θ elsewhere. Hence, the effect of a localized poloidal torque remains localized at the position where it is applied. Moreover, strong gradients in u_θ (if $u_\theta \approx u_\theta^{neo}$ is satisfied as well) may survive up to the longer transport time scales (≈ 100 ms in TCV) and be measurable.

3.5 Turbulence induced momentum transport

Recently, several mechanisms have been proposed that ascribe a radial momentum transport to the micro instabilities that are responsible for turbulent energy and particle transport. This *turbulent* contributions follows from the inertial tensor term $mn\mathbf{uu}$ in Eq. 3.3.2, when accounting for all of the possible coupling between density and velocity fluctuations. This mechanism appears when decomposing the quantities into their background and fluctuating parts $\mathbf{u} = \bar{\mathbf{u}} + \tilde{\mathbf{u}}$, $n = \bar{n} + \tilde{n}$. The fluctuating part goes to zero when averaged over the fluctuation spectrum, e.g. $\langle \tilde{n} \rangle = 0$. The (ϕ, r) component of the inertia tensor (expressing the radial flux of toroidal momentum) assumes then the form: $\Gamma_{\phi r} \approx m\bar{n}\bar{u}_r\bar{u}_\phi + m\langle \bar{u}_\phi \rangle \langle \tilde{n}\tilde{u}_r \rangle + m\langle \bar{n} \rangle \langle \tilde{u}_\phi \tilde{u}_r \rangle$. From the last two terms, coupling of velocity and density fluctuations may result in a net contribution to the momentum transport.

The first two terms $m\bar{n}\bar{u}_r\bar{u}_\phi$ and $\langle u_\phi \rangle \langle \tilde{n}\tilde{u}_r \rangle = \langle u_\phi \rangle \Gamma_n$ represent the neoclassical and turbulent components of the radial particle flux, which is a natural channel for momentum transport as particles that are transported radially carry their momentum. However, the sum of these two term vanishes in stationary conditions when the radial particle flux is zero along the density profile.

The second term is the (ϕ, r) component of the, so called, Reynolds stress and may engender a genuine, non diffusive, radial momentum transport. Since it may also be significant and appears when the background contribution $m\bar{n}\bar{u}_r\bar{u}_\phi$ is small, it is often referred to as "residual Reynolds stress".

In order that the turbulent mode produce a net radial momentum flux, a requisite is the breaking of parallel symmetry [41, 51] otherwise the two opposed toroidal components will, on average, cancel. A model should provide a physical mechanism to break the natural symmetry of the spectrum. Recently proposed theories differ on the nature of the symmetry breaking mechanism. A full assessment of this theoretical research field goes beyond the scope of this work, therefore we will only highlight some general features, relevant for a theory-experiment comparison.

3.5.1 Convective fluxes

A toroidal momentum flux proportional to $\partial_r T_\mathrm{i}$ was proposed by Coppi [52], where symmetry breaking was related to an effect of parallel velocity gradient on the Ion Temperature Gradient's (ITG) mode growth rate. This mechanism is relevant for scenarios with high ion temperature, for examples in H-modes.

More recently Hahm [53], starting from the quasi-linear derivation from the gyrokinetic equation, predicted a Turbulent Equipartition Pinch (TEP) and a curvature-driven thermoelectric pinch. The first is mode independent and arises from a poloidal variation of the amplitude fluctuations, due to the magnetic curvature and has, for the angular momentum density, the form $V_\phi = -3F/R\chi_\phi$, where $F \approx 1$ in case of ballooning structure modes. The second is mode dependent and has the form $V_\phi = -4G/R\chi_\phi$, where the sign of G depends on the mode propagation direction: $G < 0$ (inward pinch) for Trapped Electron Modes (TEM) and G>0 (outward) for ITG. It is expected to be small for ohmic or electron heated plasma. Both convective fluxes are independent of the B_ϕ and I_p directions.

Symmetry breaking due to the toroidicity has been also reported by Peeters [54], who found a convective velocity related to the Coriolis velocity drift experienced by the plasma in the co-moving frame. In a simplified fluid model the pinch velocity assumes the form $V_\phi = -4 - R/L_n$. Recently, in the frame of the gyrokinetic theory, the Coriolis pinch has been demonstrated to include both the TEP and thermoelectric convective contributions [51].

3.5.2 Intrinsic torques

The potential role of the shear of the $u_{E\times B}$ for generating an intrinsic torque was reported by Dominguez and Staebler [55]. In more recent works, detailed, fully consistent treatments were presented by Gürcan [56] and Casson [57]. This effect is expected to be relevant in regions where steep gradients of plasma pressure are present, for example in the presence of edge or internal transport barriers.

Camenen [58] has recently proposed that the up-down asymmetry of a plasma can provide a finite $\langle k_{||}\rangle$, when averaging on a flux surface. This results in a radial flux which is not convective nor diffusive and has specific dependencies on fields direction. This hypothesis is at present being tested experimentally on TCV.

McDevitt [59], reported a role of the polarization current that may, again, produce a residual stress type flux, which is estimated to be weaker than neoclassical in collisional regimes [39], but that could be more important for other scenarios.

3.6 Perpendicular viscosity

Perpendicular viscosity accounts for the part of toroidal momentum flux that is proportional to the radial gradient of toroidal velocity, i.e. the momentum radial diffusion. It corresponds to the first term of the Eq. 3.3.6 and has the effect of flattening the radial gradient of toroidal rotation.

Formally, perpendicular viscosity is contained in the $\Pi_{r,\phi}$ component of the viscous tensor. Neoclassical theory predicts $\chi_\phi^{\text{neo}} = 0.14\epsilon^2\nu_{ii}\rho_L^2$ [46, 60], where ϵ is the inverse aspect ratio, ν_{ii} the ion-ion collision frequency and ρ_L the ion Larmor radius. For TCV plasmas χ_ϕ^{neo} is typically of the order of 0.01 m^2/s or lower . Nevertheless, from an experimental point of view, much evidence has been accumulated, on different devices, to show that the diffusion rates are typically one or two order of magnitudes higher. In particular, recent experiments based on torque modulation in large tokamak devices, showed clearly that $\chi_\phi \sim \chi_i$, where χ_i is the ion heat diffusion coefficient [61–63], that is itself anomalous. The prediction for the anomalous part of the viscosity relies on the model for the underlying turbulent transport and the amplitude evaluation requires the use of simulations.

High anomalous diffusion strongly reduces the capability of neoclassical, non diffusive fluxes to sustain a rotation gradient. This is fairly obvious, as the flattening effect is exacerbated by the strong anomalous diffusion and can be evaluated dividing the transport coefficients into the neoclassical and the anomalous components, e.g. $V_\phi = V_\phi^n + V_\phi^a$. The stationary u_ϕ profile, in absence of sources or sinks, is determined by the condition of $\Gamma_{r\phi} = 0$, that may be written:

$$\frac{du_\phi}{dr} = \frac{(V_\phi^n + V_\phi^a)u_\phi + v_{th}(C_\phi^n + C_\phi^a)}{\chi_\phi^n + \chi_\phi^a} \tag{3.6.1}$$

If only neoclassical non diffusive fluxes would contribute significantly to the rotation peaking ($V_\phi^n \gg V_\phi^a$ and $C_\phi^n \gg C_\phi^a$) and in the presence of anomalous viscosity ($\chi_\phi^n \ll \chi_\phi^a$), the equation would becomes:

$$\frac{du_\phi}{dr} \approx \frac{V_\phi^n u_\phi + v_{th}C_\phi^n}{\chi_\phi^n + \chi_\phi^a} \approx \frac{du_\phi^n}{dr}\frac{\chi_\phi^n}{\chi_\phi^a} \tag{3.6.2}$$

This shows that the gradient, sustainable by neoclassical flows in presence of anomalous viscosity is smaller by a factor of $\chi_\phi^a/\chi_\phi^n \sim 10 - 100$, than to the "fully" neoclassical gradients illustrated in the previous paragraphs. Hence, care must be used when comparing the theoretical predictions for the rotation gradient with experimental observations.

3.7 Momentum sink from interaction with neutral atoms

Generally, in the peripheral region of a tokamak plasma, a finite density of neutral atoms is present. The extent of this region depends on plasma equilibrium profiles of density and temperature, as well as transport. Chapter 4 will provide some estimations of the neutral density in TCV: typically, at $T_e \approx 100$ eV and $n_e \sim 1 \times 10^{18}$ m^{-3}, neutral density of $n_n \sim 1 \times 10^{18}$ m^{-3} may be found. In this region, the charge exchange reactions between neutrals and fast rotating ions cause the loss of plasma ions that escape the plasma with their momentum. This effect represents a sink for momentum that can be expressed as:

$$\mathbf{S}_{n_0} = -nmn_0\langle\sigma u\rangle_{cx}\mathbf{u} \tag{3.7.1}$$

where n_0 is the neutral density and $\langle\sigma u\rangle_{cx}$ is the total effective cross section of CX reaction between a hot ion (deuterium) and a cold neutral. The sink effect is local and tends to zero when the plasma rotation becomes equal to the average velocity of neutral population. Under the effect of neutral sink, plasma rotation is damped (locally) to the neutral population velocity, on a timescale $\approx 1/(n_0\langle\sigma u\rangle_{cx})$. Neutral velocities in the plasma periphery are extremely difficult to measure and are often considered as at rest in the laboratory frame.

3.8 MHD rotation and torques

Under the heading Magnetic Hydro Dynamic instabilities, or MHD modes, fall macroscopic perturbations of the magnetic configuration that can be present in a plasma discharge, affecting the equilibrium and the confinement properties of the plasma. Under certain conditions, the magnetic topology of nested flux surfaces may break up and reconnect to give origin to magnetic islands. MHD modes occur at given flux surfaces characterized by rational $q = m/n$ and therefore have a given periodicity described by the poloidal and toroidal numbers m and n. Due to the enhanced radial transport, density and temperature profiles are flattened inside the magnetic island, so the magnetic perturbation is apparent in Electron Cyclotron (ECE) or Soft X-Ray (SXR) emission, or reflectometry measurements.

Magnetic perturbations can propagate through the plasma with a phase velocity u_{MHD}. Since these perturbations are field aligned, only propagation perpendicular to the magnetic field is allowed, so $\mathbf{u}_{MHD} \cdot \mathbf{B} = 0$. This simplifying assumption of magnetic field frozen in the electron fluid leads to a magnetic perturbation drifting with the electron diamagnetic velocity on the background plasma rotation:

$$\mathbf{u}_{MHD} = \mathbf{u} + \mathbf{u}_e^*. \tag{3.8.1}$$

Although this formulation, in some cases, suffices to account for the observations [64], the real situation is more complex and the phase velocity depends strongly on the properties of the plasma background and of the island itself [65, 66]. In general, the magnetic islands are embedded within the ion fluid and the electron fluid, with propagation velocity between. Following these approaches and the plasma conditions, different theoretical predictions are obtained so that this model is, to this day, strongly debated [67–69]. Recent results suggest that the island flows with the electron fluid, when it does not perturb the density and temperature gradients; conversely, if the flattening is strong, the island follows the ions. In these two limits the island velocity $\mathbf{u}_{MHD}$, evaluated in the reference frame moving with $\mathbf{u}_{E\times B}$, will approach respectively the electron or ion diamagnetic velocity [70].

What is experimentally measured are the frequencies of perturbations, observed, for instance, in the magnetic field, ECE or SXR traces. When the poloidal and toroidal mode numbers are

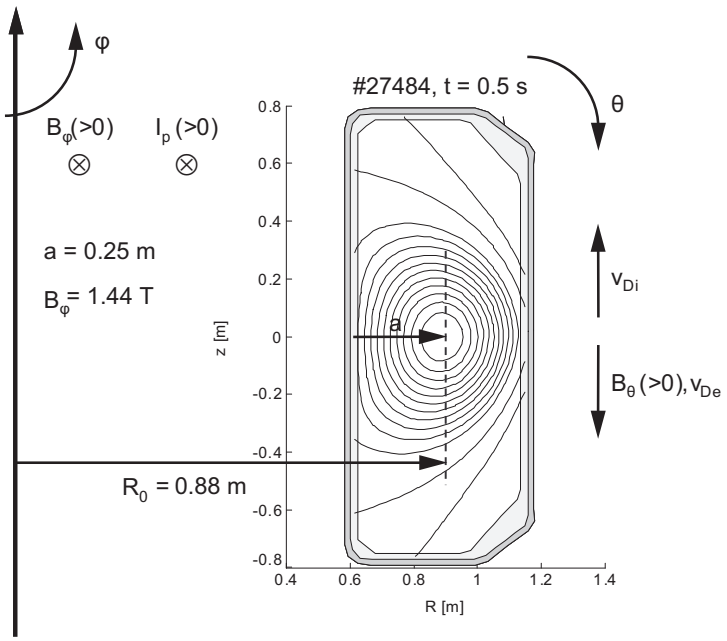

Figure 3.1: Schematic of the directions of plasma current, magnetic fields, ion and electron diamagnetic velocities, following the conventions used in TCV.

known, the relation between mode velocity and measured frequency f_{MHD} in kHz, follows from:

$$2\pi f_{MHD} = \omega_{MHD} = \mathbf{k} \cdot \mathbf{u}_{MHD} \tag{3.8.2}$$

where $\mathbf{k} = -\frac{m}{r}\mathbf{e}_\theta + \frac{n}{R}\mathbf{e}_\phi$ is the wave number of the mode, $k \cdot B = 0$ at the $q = rB_\phi/RB_\theta = m/n$ resonant flux surface. With this definition of k, the positive direction of propagation is the ion diamagnetic drift direction. The rotation fluid frequencies are similarly calculated for ions and electrons ($j = i, e$) as:

$$2\pi f_j = \omega_j = \mathbf{k} \cdot \mathbf{u}_j = \mathbf{k} \cdot (\mathbf{u}_{E\times B} + \mathbf{u}_j^*) = \omega_{\mathbf{u}_{E\times B}} + \omega_j^* \tag{3.8.3}$$

where $\mathbf{u}_{E\times B} = \frac{\mathbf{E}\times\mathbf{B}}{B^2}$ is the $E \times B$ drift velocity and $u_j^* = \frac{\mathbf{B}\times\nabla p}{q_j n_j}$ is the diamagnetic drift velocity ($q_j > 0$ for ions and $q < 0$ for electrons). It is important to compare the experimental MHD frequency with the ion or electron frequency. Results vary following the discharge scenario: at DIII-D, $f_{MHD} \approx f_i^*$ was measured [71], while at TEXTOR experimental observations are consistent with $f_{MHD} \approx f_e$ [64]. The situation of TCV L-mode has been preliminary addressed in [72] for the case of sawtooth precursor oscillations, indicating that mode velocities are compatible with the ion diamagnetic velocity.

In the case of $B_\phi \gg B_\theta$ the propagation direction becomes opposite to $\mathbf{e}_\theta$ and we obtain:

$$\omega_i = -\frac{m}{r}u_\theta + \frac{n}{R}u_\phi = \frac{n}{RB_\theta}(B_\theta u_\phi - B_\phi u_\theta) \tag{3.8.4}$$

$$\omega_e = \frac{n}{RB_\theta}E_r - \frac{n}{RB_\theta}\frac{\nabla p_e}{n_e q_e} \tag{3.8.5}$$

$$E_r = \frac{\nabla p_i}{n_i q_i Z_i} + (B_\theta u_\phi - B_\phi u_\theta) \tag{3.8.6}$$

with $q_e<0$ negative unitary charge.

In other tokamak devices, in the presence of the strong toroidal velocities induced by heating neutral beams, the diamagnetic and poloidal rotation terms are negligible in the radial force

balance, so that $u_\phi \approx E_r/B_\theta$ and therefore $\omega_{MHD} \approx nu_\phi/R$. On this basis the mode frequency can often be directly used as complementary measurement of toroidal rotation. In TCV, however, due to the relatively low value of spontaneous plasma rotation, poloidal velocity and diamagnetic drift can contribute an important fraction of the measured MHD frequency.

The comments reported here refer to MHD modes that may be considered isolated in the sense that they do not interact with the wall and do not perturb, significantly, the background plasma. In TCV, this situation is often found for sawtooth precursor modes or small peripheral modes. In different situations (as in presence of locked modes, or modes whose saturated width is a substantial fraction of the plasma minor radius) a strong coupling between MHD structures and background plasma is observed, that are typically manifested as MHD torques (plasma braking) or strongly enhanced viscosity (flattening of rotation profile) or a combination of both [64, 73]. Although rich experimental observations of this effect of MHD on momentum transport has been reported [72], in this thesis we will restrict the observations to cases where the impact is minor.

3.9 Parallel flows in the Scrape-Off Layer

Outside the Last Closed Flux Surface (LCFS), the magnetic field lines are open and connect to the vessel structure. The region outside the LCFS, where the decay of n_e and T_e profile is determined more by parallel losses than radial transport, is called Scrape-Off Layer (SOL). In the SOL, the plasma flows along the field lines towards the walls. SOL flows have been extensively studied experimentally and theoretically as they play an important role in erosion and redeposition issues that affect the operation of a fusion reactor.

The issue of coupling of u_ϕ rotation was addressed, e.g. by Chankin [74], to estimate the role of the toroidal momentum exchanged between the core plasma and the SOL to explain the asymmetries in divertor target loading.

Recent interest has grown in connection with plasma rotation issues. While the radial momentum transport can develop a stationary gradient of rotation, net acceleration will come through the transfer of momentum across the boundary, so it is important to consider the interaction between confined plasma rotation and open field line particle flows.

Parallel SOL flow is generated by an interplay of poloidal asymmetries of magnetic field, radial and parallel pressure gradients, poloidal and radial electric fields, anomalous particle transport, etc. In a simple picture, the plasma edge is mainly stagnant with strong near sonic flow developing, as solid targets (limiter or divertor tiles) are approached. In reality, particle drifts lead to strong poloidal fluxes which must be compensated by return parallel flows. These flows are described by the neoclassical Pfirsch-Schlüter (PS) flows. To account for experimental observation, an anomalous component of the fluxes was introduced, induced by strong outboard particle transport. The excess of particle flux entering the SOL in the outboard region would create a local pressure increase, which would be relieved by parallel flow along SOL flux tubes to the limiter or target plates. This two folded SOL flow picture was confirmed in TCV [75] and Alcator [76] with measurements of poloidally displaced in different magnetic configurations.

On TCV, measurements with a reciprocating Mach probe [75] characterized the dependence on poloidal position, ion species, density, current, magnetic configuration etc. The observed parallel flow was described as the sum of a dominating PS flow, and smaller components from ballooning and divertor sink. Expressing the plasma flow in terms of the parallel Mach number $M_{||} = u_{||}/c_s$, where $c_s = \sqrt{\frac{T_e+T_i}{m_i}}$ is the ion sound speed, this result is expressed by:

$$M_{||} = M_{||}^{PS} + M_{||}^{ball} + M_{||}^{sink} \tag{3.9.1}$$

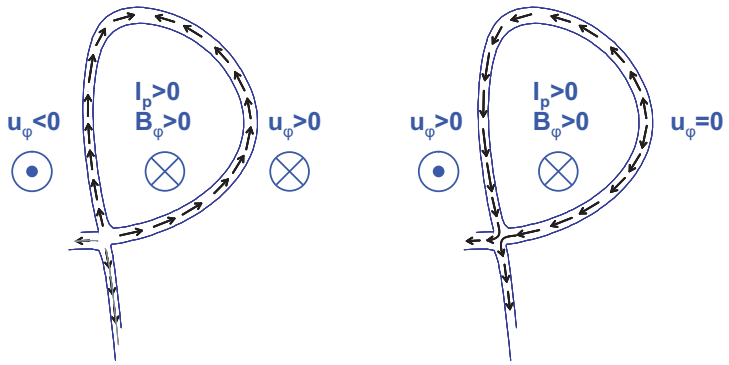

Figure 3.2: Schematic of the directions of Pfirsch-Schlüter (left) and anomalous ballooning (right) components of SOL flows, for a typical TCV Lower Single Null configuration.

where:

$$M_{||}^{PS} = \frac{2q_e \cos\theta}{c_s} \frac{\mathbf{B}}{B^2} \left(E_r - \frac{1}{en_e} \frac{dp_i}{dr} \right) \tag{3.9.2}$$

represents the Pfirsch-Schlüter component, which may reach values up to 0.6. This component has a cosine dependence on poloidal angle θ and, in particular, vanishes at the top and bottom of the plasma and is highest at the midplane with opposite direction in the inboard and outboard regions (see Fig. 3.2). The direction of its toroidal component depends on the B_ϕ and B_θ (I_p) directions. In TCV, which operates at positive field helicity ($B_\theta B_\phi > 0$), M_ϕ^{PS} is co current directed at the outboard midplane.

The second term describes the ballooning component:

$$M_{||}^{ball} = -0.2 \frac{z}{a} \left(\frac{n_{\mathrm{e,av}}}{10^{20}\ m^{-3}} \right)^{\frac{1}{2}} \tag{3.9.3}$$

expressed as a function of the average density and of the vertical distance from the midplane z, normalized to the plasma minor radius. $M_{||}^{ball}$ is of the order of 0.1. At the outboard plasma, it changes sign with z and vanishes at the midplane. This is in agreement with similar measurements performed on other tokamak devices, especially detailed in Alcator C-mod [76], that indicate a poloidal distribution of the anomalous flow, as in Fig. 3.2.

Finally, the third term, which gathers the effects of the solid target particle sink, is represented by a constant contribution, evaluated for each different magnetic configuration: $M_{||}^{sink} = +0.13, +0.07, -0.13$ for Upper Single Null (USN), Lower Single Null (LSN) and limiter configurations.

The coupling between SOL fluxes and confined plasma rotation results in an exchange of momentum between the two regions. In the confined plasma, u_θ is set to the neoclassical values and E_r and u_ϕ are linked. Conversely, in the SOL, E_r is robustly determined by parallel ambipolar fluxes towards the divertor plates or the limiter, so u_ϕ is linked to u_θ. This means that toroidal momentum transported across the LCFS results in toroidal *and* poloidal flows. Viceversa, the parallel fluxes that are generated in the SOL (PS fluxes, in presence of an E_r determined by open field parallel dynamics) may couple with the core rotation, affecting primarily u_ϕ and hence E_r.

It is interesting to notice that in [74], with a simple model that only retains the basic terms (plasma momentum transported only by radial particle diffusion) and neglecting viscous coupling, a linear dependence is derived between the pressure asymmetry at the divertor targets and u_ϕ at the LCFS. For TCV discharges limited on the central column and up-down symmetric, this would indicate $u_\phi \approx 0$ at the LCFS for main ions.

3.10 Conclusions

In this chapter, several different elements relevant to the study of flows of tokamak plasma were introduced. The way in which these elements contribute to determine the rotational state of the plasma depends on the timescales involved. To summarize with a simplified perspective, we can say that, primarily, the equilibrium between electric field and plasma rotation, stated in the force balance equation, is established on fast magnetic timescales ($\tau_A \sim 100$ μs). On longer collisional timescales ($\tau_{ii} \sim 1$ ms), collisional parallel dynamic is the leading process and determines, for example, the relative poloidal and toroidal velocities between main ions and impurities. The final relaxed velocities are ultimately determined by the electric field that evolves on the longest transport timescales ($\tau_\phi \sim 10$ ms), through processes that emerge only after considering the toroidal dynamic. These can be collisional or turbulent in nature and are contained in the toroidal components of the viscous and stress tensors.

From the theoretical point of view this means that small effects are important for the steady state plasma rotation and sophisticated high order developments are needed. From the experimental point of view, the long timescale evolutions, which are actually what is measured with today's diagnostics, give a direct insight on detailed aspects of physics of magnetically confined plasmas.

Chapter 4

Plasma rotation in limited L-mode configuration

After introducing the experimental equipment and the main theoretical aspects of plasma rotation in tokamak devices, we now move on to the results of the main physical subject of this thesis: the intrinsic rotation of tokamak plasmas.

Observations of intrinsic plasma rotation in different tokamak devices show a rich and complex phenomenology. Depending on plasma conditions (low or high confinement, limited or diverted configuration) and on heating scenario (Ohmic, Electron Cyclotron Resonant Heating or Ion Cyclotron Resonant Heating), the absolute value of toroidal rotation exhibits a wide range of values, from almost negligible to a significant fraction of the ion thermal energy [77, 78]. In Ohmic or ICRH heated High confinement (H-mode) discharges, plasma toroidal rotation is observed in the co current direction [79]. In Low confinement scenarios (L-mode), plasma is found to rotate toroidally in the counter current direction in many devices [45,80]. However, in some experiments, co current rotation has been observed [80], as well as a reversal of the core rotation [81], suggesting transitions in the underlying momentum transport properties.

Poloidal rotation is generally assumed to be damped close to neoclassical predictions, as confirmed by recent observations [82, 83]. Some qualitative and quantitative disagreement has nonetheless been reported [84], especially in presence of enhanced confinement regions, such as internal transport barriers [85].

In TCV, in order to assess intrinsic rotation, the scenario of L-mode confinement, Ohmic heated, in limited magnetic configuration, has been explored extensively. This basic scenario represents the initial step in the systematic exploration and characterization of plasma rotation in TCV plasmas.

We devote this chapter to address some general features of intrinsic rotation measured in TCV, for a wide range of plasma parameters. The toroidal and poloidal rotation profiles have been studied as a function of plasma parameters (n_e, I_p) in quasi stationary L-mode discharges. The relative simplicity of this scenario has permitted the identification of some important dependencies, such as the plasma current, the sawtooth instability, and the edge boundary conditions.

From a complete analysis of High Field Side (HFS) and Low Field Side (LFS) CXRS09 views, measuring toroidal rotation, as well as the Vertical (VER) CXRS09 system, for poloidal rotation, a comparison with the stationary first order parallel and perpendicular neoclassical particle fluxes has been possible.

Whilst at this stage the question of the mechanisms driving the intrinsic plasma rotation is not answered, these results constitute a basis for the following studies.

4.1 Stationary toroidal rotation profile: 3 regions

Plasma toroidal rotation was first studied by means of dedicated experiments. The measurement was performed in quasi stationary discharges with deuterium (D) as main ion and carbon (C) as the principal intrinsic impurity. The range of parameters of plasma discharges is shown in Table 4.1.

Parameter	Symbol	Value
Minor radius	a	0.25 m
Major radius	R_{axis}	0.88 m
Plasma current	I_p	$\pm(150 \div 320)$ kA
Toroidal magnetic field	B_ϕ	± 1.44 T
Edge safety factor	q_e	$2.4 \div 8.8$
Loop voltage	V_{loop}	$1 \div 2$ V
Central electron temperature	$T_{\mathrm{e}0}$	$600 \div 1200$ eV
Central ion temperature	$T_{\mathrm{i}0}$	$300 \div 700$ eV
Average electron density	$n_{\mathrm{e,av}}$	$0.8 \div 7{\times}10^{19}$ m^{-3}
Elongation	κ	$1.3 \div 1.7$
Triangularity	δ	$0.2 \div 0.6$
Effective charge	Z_eff	$1.2 \div 2$
Carbon toroidal rotation	u_ϕ	$10 \div 40$ km/s
Carbon poloidal rotation	u_θ	$1 \div 3$ km/s
Ion thermal velocity	$v_{th,i}$	$110 \div 240$ km/s
Ion diamagnetic drift	u_i^*	$4 \div 8$ km/s
Ion sound speed	c_s	$220 \div 450$ km/s

Table 4.1: Parameters of TCV discharges were explored to study the stationary rotation in limited L-mode configurations. The lower section contains some rotation relevant plasma quantities.

Although some MHD activity was present in these discharges, only discharges where activity was low were selected. Given the relatively low values of q_e for most of the cases, sawtooth oscillations were affecting the plasma core, i.e. relaxations with periods $\tau_\mathrm{ST} \approx 2 \div 6$ ms. With the typical charge exchange exposure time (>30 ms), CXRS measures the averaged value across many sawtooth events. Dedicated measurements were designed to resolve the dynamic in between sawtooth crashes, as described in chapter 8.

The characteristics of the toroidal rotation in limited L-mode have been reported in detail in [45], based on measurements performed with the CXRS04 diagnostic. Here we review the principal features, also summarized in Fig. 4.1:

- A large toroidal rotation is observed (up to 50 km/s) in the direction opposite to the plasma current (electron diamagnetic drift direction). The toroidal rotation profile reverses nearly symmetrically upon reversal of the plasma current direction.
- Inside the sawtooth inversion radius, the rotation profile is flat or, for high I_p ($q_e \lesssim 4$), hollow.
- Outside the inversion radius, the rotation profile decreases approximately linearly towards the edge.
- The edge rotation (measured by successive vertical plasma displacements [86]) is small and possibly in the direction of plasma current.

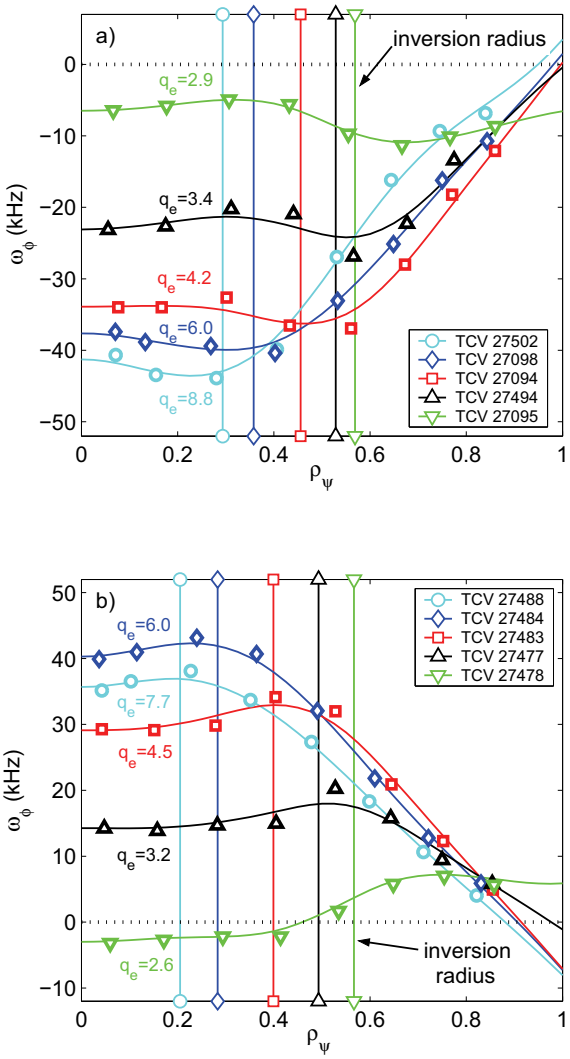

Figure 4.1: Toroidal angular velocity profiles for a sequence of limited discharges for (a) positive and (b) negative plasma currents (rotation always in the counter current direction). Solid curve is a cubic fit of the CXRS04 diagnostic measurement, extrapolating to the peripheral region $\rho_\psi > 0.85$. The maximum rotation is located approximately at the sawtooth inversion radius and decreases with plasma current.

Comparing the measured velocities with characteristic plasma velocities (see Table 4.1) rotation in TCV is found to be subsonic and of the order of the ion diamagnetic velocity. This situation is usually referred to as the small plasma rotation regime. Under these conditions, diamagnetic effects, i.e. related to pressure gradient, may provide a non negligible contribution in the momentum balance equation.

On the basis of these observations, a scaling law for the maximal rotation (often close to the inversion radius) was proposed [45], emphasizing the role of the ion energy content (through T_i) and the sawtooth effect (through I_p):

$$u_{\phi,\max}\ [\mathrm{km/s}] = -12.5 \cdot \frac{T_{i0}\ [\mathrm{km/s}]}{I_p\ [\mathrm{kA}]} \tag{4.1.1}$$

where $u_{\phi,\max}$ is the maximal toroidal rotation and T_{i0} is the central ion temperature (Fig. 4.2a). This scaling law was obtained using plasma discharges where $q_e > 3$. For higher plasma current the rotation gradient is drastically reduced outside the inversion radius. This effect is quantified in Fig. 4.2b, where an estimation of central rotation in absence of sawteeth $u_{\phi,0}$ (deduced by linear

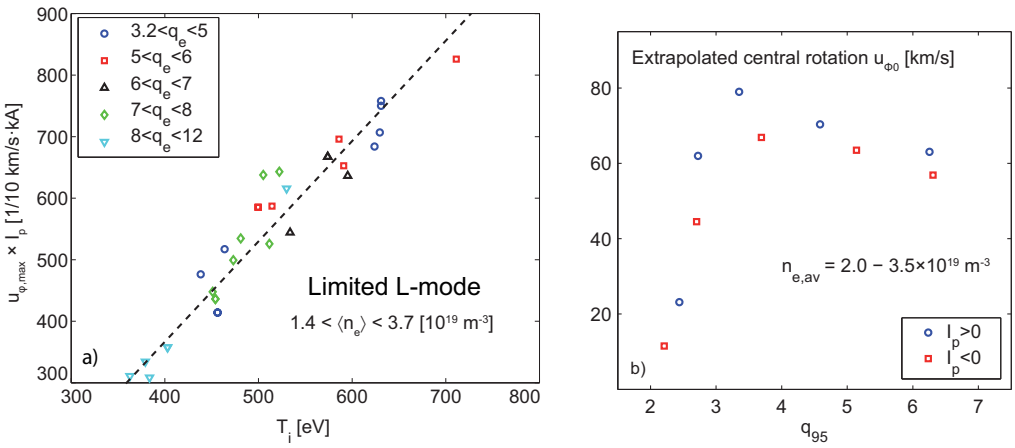

Figure 4.2: Left: dependence of the plasma current of normalized maximum toroidal velocity $u_{\phi,max} \cdot I_\mathrm{p}$ on the ion temperature. The database includes positive and negative plasma currents and a wide plasma density range. Discharges with $q_e < 3$ are not included. Right: deduced central toroidal rotation for the data in Fig. 4.1 (constant plasma density) linearly extrapolated from the toroidal profile gradient outside the sawtooth inversion radius. Most of the plasma current scaling is no longer present. For $q_{95} < 3$ rotation decreases rapidly.

extrapolation from the profile outside the inversion radius), is plotted against q_{95} for the profiles in Fig. 4.1. For $q_{95} < 3$ the extrapolated $u_{\phi,0}$, parametric of ∇u_ϕ, decreases abruptly with q_{95}. On the same graph, the weak variation of extrapolated u_ϕ for $q_{95} > 3$ indicates that I_p enters the scaling law mostly through the inversion radius position [87].

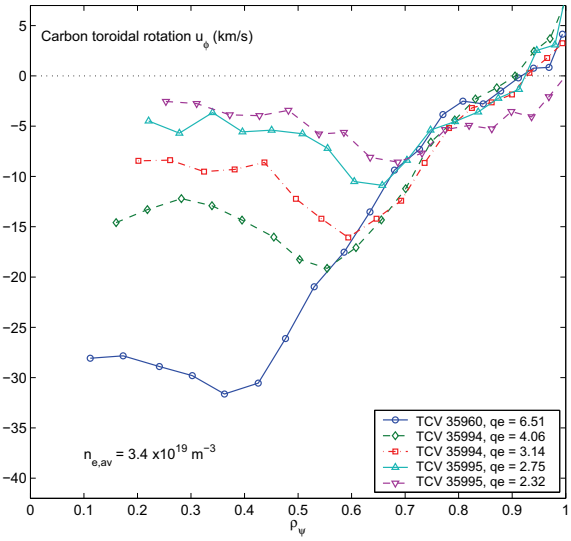

Figure 4.3: Toroidal angular velocity profiles measured with CXRS09 diagnostic for a sequence of limited discharges at positive plasma current $I_\mathrm{p} = 150 \div 330$ kA (rotation is always in the counter current direction). Measurements in the peripheral region $\rho_\psi \gtrsim 0.85$ indicate $u_\phi \approx +5$ km/s (co current) in the edge region and weakly dependent on plasma current.

These results were confirmed and refined by recent measurements performed with the CXRS09 diagnostic. Fig. 4.3 illustrates the result of a stationary I_p scan at constant plasma density. The higher spatial resolution and radial coverage permit more detailed u_ϕ profiles. In particular, three regions are clearly identified from their dependence on plasma parameters, where the predominant physics mechanism combination is likely to be different:

- **Sawtooth region**, that extends from the plasma core to the sawtooth inversion radius $\rho_{\rm inv}$. Here, the rotation profile is clearly hollow, producing a surface of maximum rotation located near the sawtooth inversion radius. The "rotation hole" in the core is deeper for higher plasma current, with values up to ≈ 5 km/s, a reasonable fraction of the maximal rotation. The sawtooth effect suggests that a co current directed torque of some kind is exerted in this region or an outward transfer of momentum from the plasma center takes place.

- **Intermediate region** or **gradient region**, from $\rho_{\rm inv}$ outwards to approximately $\rho_\psi = 0.85$. Here u_ϕ decreases roughly linearly to values close to zero. In this region the plasma rotation develops spontaneously a finite gradient of u_ϕ, which is the result of toroidal momentum transport. This gradient appears closely related to the ion temperature gradient [45].

- **Peripheral region**, from $\rho_\psi = 0.85$ to the plasma edge, i.e. $\rho_\psi = 1$. Here the plasma rotation is close to zero, with a low rotation gradient. There is an increase in the co current direction in the inner boundary layer $\rho_\psi = 0.95 \div 1$, reaching values of ≈ 5 km/s at the plasma edge. As can be seen in Fig. 4.1 and 4.3, the value of rotation in this region appears insensitive to plasma parameters ($I_{\rm p}$, $n_{\rm e,av}$). This behavior is often referred to the *no-slip* condition, and suggests some sort of friction or momentum sink, as for instance a strong interaction with the neutral particles background. The edge region is a complex region as the confined plasma interacts with the Scrape Off Layer in all energy, particle and momentum channels. The interaction between edge plasma rotation and SOL flows is likely to be an important ingredient in the story.

For the lowest accessible safety factors ($q_e = 2.4$) the sawtooth dominated region encompasses a major part of the plasma volume and both the intermediate and peripheral regions appear strongly perturbed. The mode associated with the sawtooth resonates at the surface $q = 1$, but its radial extension can spread across several centimeters.

4.2 Poloidal rotation and radial electric field

In this section we turn our attention to the plasma poloidal rotation u_θ. The measurement of u_θ is more challenging as the poloidal flow is generally small. u_θ is strongly damped by magnetic pumping and friction with trapped particles, so that values close to neoclassical predictions (1-2 km/s for TCV) are expected (see chapter 3).

The question as to whether poloidal rotation is close to neoclassical values or determined by other mechanisms, possibly linked to micro turbulence, is strongly debated at the time of writing. Poloidal rotation and its shear have been predicted and observed in presence of transport barriers [85,88], where they appear to play a crucial role. From the experimental point of view, poloidal rotation measurements are not yet conclusive, in part due to the difficulty in obtaining an accurate measurement that requires extremely good spectral signal and excellent quality wavelength calibration and that can be affected by many apparent contributions [29, 83, 84].

The measurements performed during this thesis demonstrated that in TCV plasmas in L-mode, u_θ is indeed much lower that u_ϕ, with values of the order of 1 km/s, of the order and in the direction of neoclassical predictions.

In figure 4.4, the u_θ profiles for two similar discharges in limited configuration with opposite values of $I_{\rm p}$ and B_ϕ are shown to illustrate the main features of u_θ. For these discharges the plasma parameters were well matched $n_{\rm e} = 4 \times 10^{19}\,{\rm m}^{-3}$, $|I_{\rm p}| = 300$ kA to 5% accuracy. For both discharges, the poloidal rotation is directed in the electron diamagnetic drift direction across the covered range. The sign of u_θ reverses direction upon reversal of B_ϕ sign, as expected from

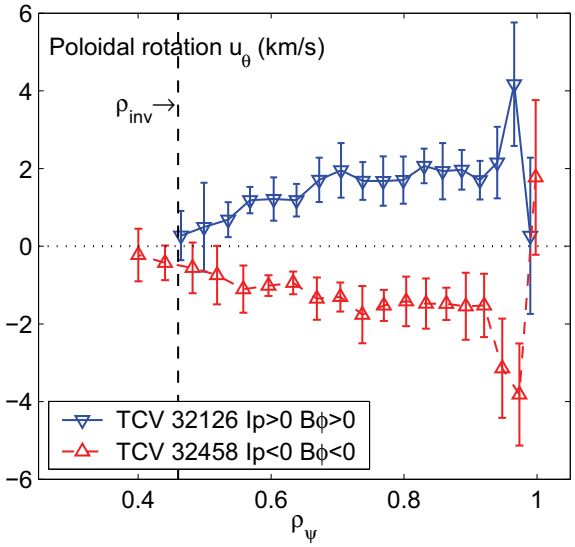

Figure 4.4: Poloidal velocity profiles of two discharges with identical target plasma parameters, except for the opposite direction of toroidal plasma current and magnetic field. $\rho_{\rm inv} \approx 0.5$ in these discharges.

the radial force balance equation solved for u_θ: $u_\theta = \frac{1}{B_\phi}(-E_r + ...)$. In the intermediate region, $u_\phi \approx 2$ km/s is observed, decreasing towards the core of the plasma. Although $u_\theta = 0$ at the magnetic axis is to be expected, a direct verification is, at present, not within the possibilities of the CXRS diagnostic: the radial coverage of the vertical CXRS09 view is limited to the outboard plasma radius, i.e. $\rho_\psi > 0.4$ for these magnetic configurations. Nevertheless, in the following, u_θ will be extrapolated to zero at the plasma center. An indirect confirmation of the validity of this assumption may be taken from a comparison of HFS and LFS measurements, as explained in the following sections.

In the peripheral region, a peak of u_θ in the electron diamagnetic drift direction is observed, localized at $\rho_\psi = 0.95$. At the plasma edge, in these two cases, u_θ is close to zero within the larger uncertainties resulting from the weak active signal obtained.

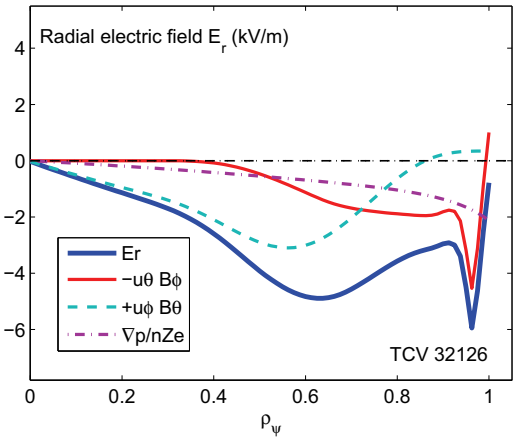

Figure 4.5: Radial electric field calculated from the radial force balance equation, from experimental profiles of u_ϕ, u_θ and $p_C = n_C T_C$ (TCV 32126).

The toroidal and poloidal rotation profiles can be used to deduce the radial electric field E_r from the radial part of the force balance equation. This calculation is shown in Fig. 4.5 for TCV 32126.

The radial electric field is negative with values of -4 kV/m at mid radius. This relatively high value results from the co-directed negative contributions of u_ϕ and u_θ. Notice that, as u_θ enters the radial force balance multiplied by B_ϕ, low values of u_θ contribute substantially to E_r. On the other hand, the diamagnetic term only becomes important in the peripheral region.

Similarly to what was observed in presence of edge transport barriers [88–91], the peak of u_θ directly translates in a peak of E_r. The vertical CXRS observation geometry would serve to smooth any radial feature by averaging over volumes spanning adjacent flux surfaces (see chapter 2). The actual peak may be more pronounced by up to a factor of 2. A radial static potential well is widely believed to be a key element for the turbulence suppression or decorrelation typical of H-mode transport barrier: nevertheless, in these TCV L-mode observations, no abrupt change in confinement appears nor there is any indication of pedestal formation.

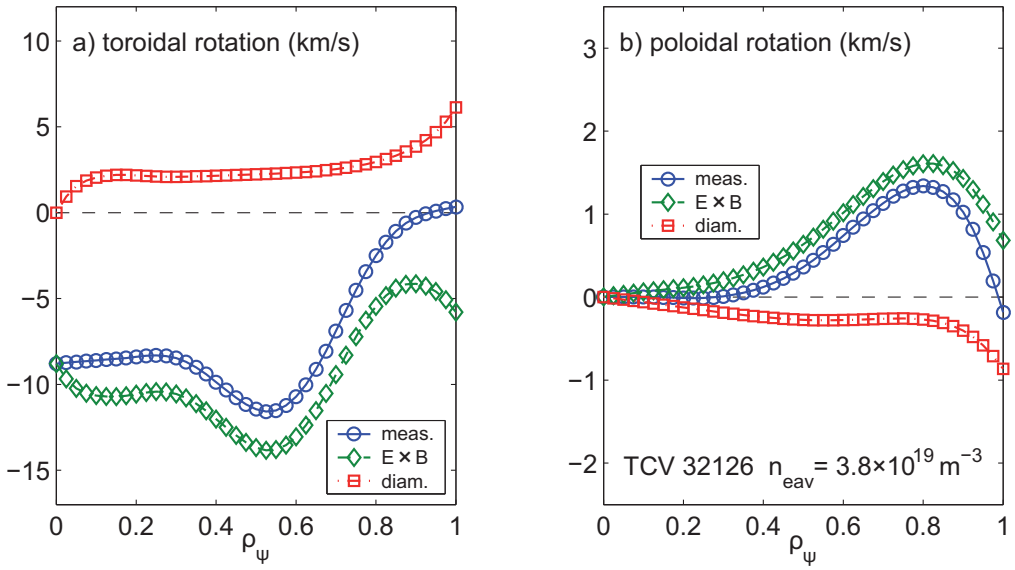

Figure 4.6: $\mathbf{u}_{E\times B}$ and diamagnetic velocities, contribution to the measured carbon rotation for TCV 32126. Experimental profiles are cubic fits to the CXRS measurements.

It is interesting to compare the toroidal and poloidal components of diamagnetic and $\mathbf{u}_{E\times B}$ velocities (Fig. 4.6). It is clear that the $\mathbf{u}_{E\times B}$ drift velocity represents the main drive, for both u_ϕ and u_θ, being larger than diamagnetic velocity by a factor of 5 in the plasma core. Nevertheless, in the peripheral region and near the edge, the diamagnetic velocity represents the main contribution of u_ϕ and contributes significantly to u_θ.

It remains an open question as to the mechanism that leads to this strong radial electric field or, equivalently, what drives the plasma rotation that produces such substantial E_r. In the absence of external drives, the answer is quite possibly to be found in the identification of a direct toroidal momentum transport mechanism.

4.3 Neoclassical first order flows

In this section we will compare the toroidal and poloidal rotations with the values of first order flows predicted by neoclassical theory. As introduced in chapter 3, first order toroidal and poloidal flows are determined by parallel friction and viscous forces once the radial electric field profile is provided. In other words, in presence of a given E_r the first order toroidal and poloidal rotations of ions and any impurity species are predicted by neoclassical theory from knowledge of density and temperature profiles and magnetic configuration.

Alternatively, the toroidal rotation profile of any species can be used to close the system and obtain the prediction of all other flows *and* the radial electric field. This approach has been applied for instance in [44], to estimate the poloidal rotation of impurities and main ions from the carbon toroidal rotation measured by CXRS. The radial electric field provides a tool to check the consistency of the calculation, as the force balance equation must hold for each ion species separately. To adopt this approach we note that, due to the high ratio $v_{th,i}/v_{th,C} \approx 0.4$, the approximations of the friction matrix proposed in [38] and adopted in [44] are not well suited for TCV. Hence, in our calculation, impurity-ion friction has been retained, using the general form of the viscous force matrix [35, 38].

The results are shown in figure 4.7 for two representative discharges whose main parameters are summarized in the following table:

TCV #	$n_{\mathrm{e,av}}$	$T_\mathrm{e}/T_\mathrm{i}$	I_p/B_ϕ	Z_eff	q
35963	1.5	0.4/0.3	-340/-1.42	1.4	6
32126	3.8	1/0.6	340/1.42	1.4	3.1

Let us highlight the general features :

- Deuterium and carbon rotations are similar within a difference of 2 km/s, that increases to 5 km/s for high current and density discharges. Notice that this differential rotation is smaller than the value obtained applying directly the formula 7.4.2 in [38] and presented e.g. in [45].
- In the intermediate region $0.5 < \rho_\psi < 0.95$, the carbon poloidal rotation compares well with the neoclassical predicted value, for both direction and amplitude. Towards the core, the neoclassical carbon rotation appears somewhat larger than experimental values. This may be related to the sawtooth activity that increases the radial transport of momentum and is not included properly in the model.
- Deuterium poloidal rotation is less than for carbon, strongly damped to values ≈ 1 km/s or smaller.
- The radial electric field profiles calculated from radial force balance using carbon (diamonds) and deuterium (circles) neoclassical velocities agree, supporting the correctness of the calculation. Furthermore, there is a good agreement between these neoclassical predictions and the E_r calculated using only experimental profiles (squares).

While in the core u_θ compares reasonably well with the neoclassical predictions, the edge peak feature, although a robust observation, is not yet understood. A phenomenon that may play a role is the friction with neutral particles that are present in the peripheral region. This has been reported to have an impact of enhancing poloidal rotation in the plasma edge in DIII-D [42]. Following the procedure applied there, the friction force was included in the parallel momentum balance. The results (not shown) indicate that the effect on poloidal rotation is too small to account for the sharp peak. Although this is not addressed in this thesis, we mention here another mechanism that could have a role, that of ion orbit losses in the plasma edge [92], whose impact on plasma flows was recently pointed out.

4.4 Poloidal angle dependence of toroidal plasma rotation

In this section we will use the comparison of CXRS measurements in the LFS and HFS midplane to address the question of the rigid rotor approximation, i.e. to which extent may the toroidal and

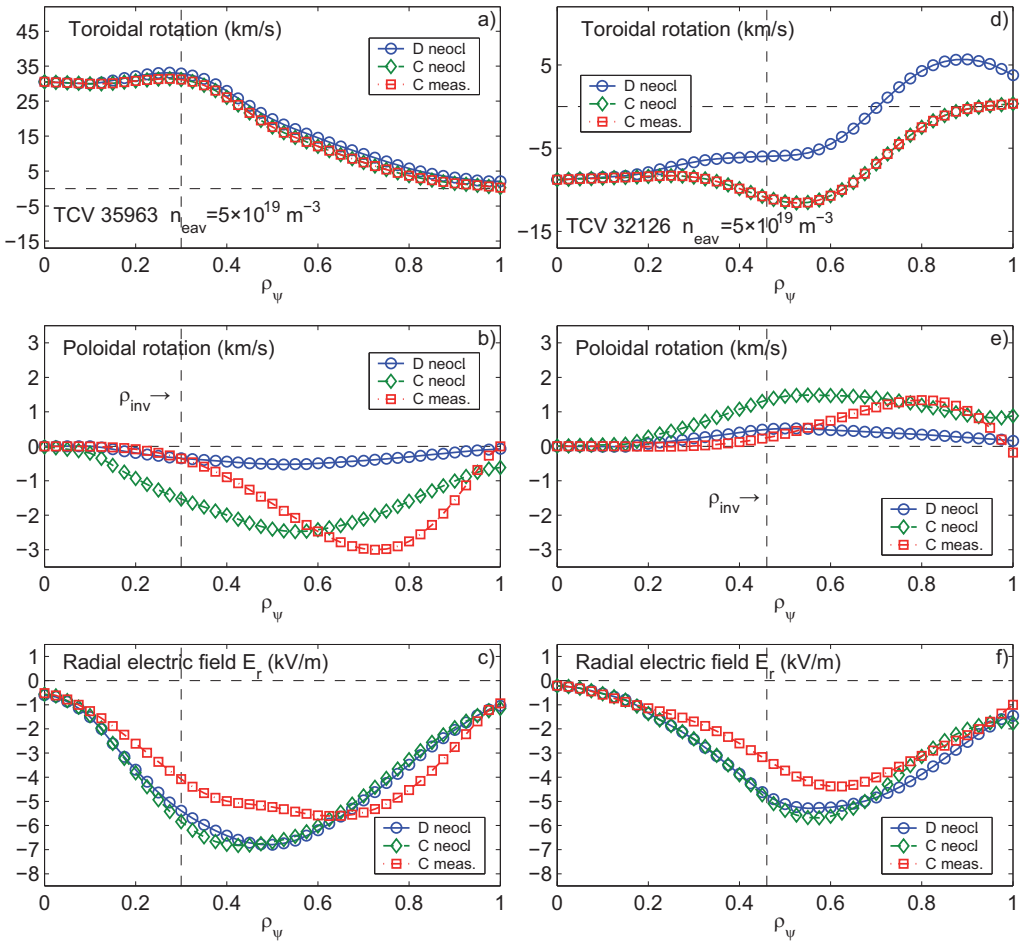

Figure 4.7: Neoclassical prediction for toroidal and poloidal rotations, for deuterium main ion (circles) and carbon impurity (diamonds), calculated from experimental profiles of two externally limited discharges: TCV 35963 ($I_p = -150$ kA, $n_{e,av} = 1.5 \times 10^{19}$ m^{-3}, left column) and TCV 32126 ($I_p = +320$ kA, $n_{e,av} = 3.8 \times 10^{19}$ m^{-3}, right column). Experimental profiles of carbon velocities, fitted on a 41 point radial grid, are plotted for comparison (squares). In the calculation, the carbon toroidal rotation is taken from experiment. Bottom graphs show the radial electric field, calculated from the radial force balance equation.

poloidal rotation be considered constant on a flux surface. As introduced in chapter 3, following the incompressible fluid approximation, a finite poloidal rotation provokes a poloidal asymmetry of u_ϕ. From the experimental point of view, there is little literature on this aspect [45,93], mainly because CX based diagnostics are typically designed to observe the outboard midplane region. In the presence of external momentum sources as heating NBI, u_ϕ exceeds u_θ (of the order of neoclassical values) by two orders of magnitude and the rigid body approximation is expected to hold. This may not be the case for plasmas with weak toroidal rotation, e.g. when the intrinsic rotation is dominant, as it is expected for ITER.

The TCV HFS view was designed to probe this question. Unfortunately, due to two major failures of the CCD detector of the HFS system, only sporadic HFS measurements have been performed during this thesis. In Fig. 4.8, the measurements of LFS and HFS CXRS views for three discharges in limited configuration are combined to obtain the rotation profile along the midplane diameter. For these discharges the HFS system was used in a "commissioning" configuration, providing only 9 out of 16 measurements, from magnetic axis to approximately $\rho_\psi = 0.7$ on the inboard side of the plasma. The three discharges illustrated have similar plasma parameters, but

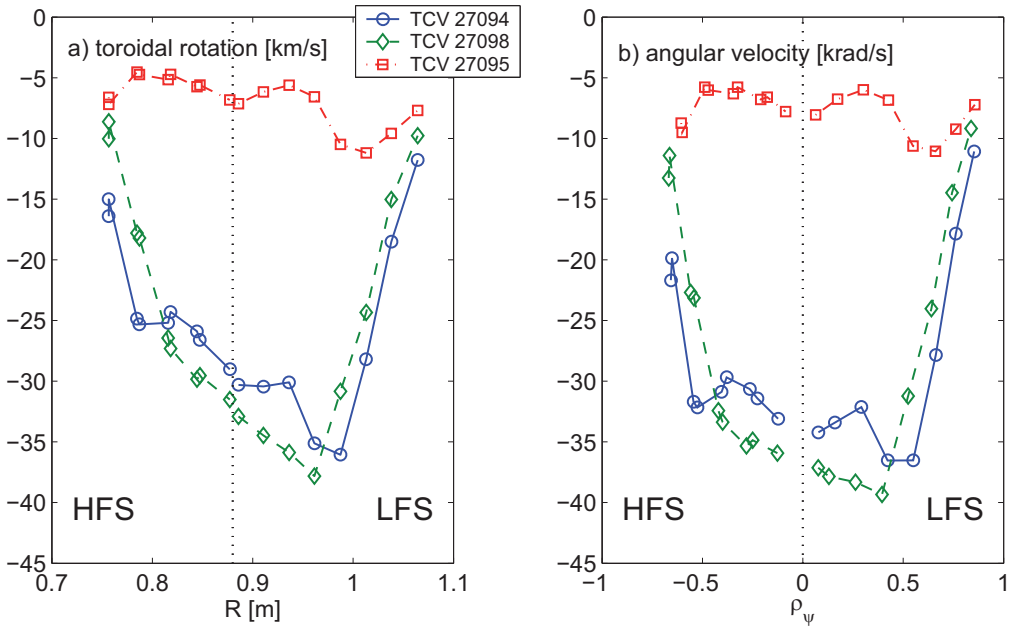

Figure 4.8: Toroidal rotation measured along the midplane diameter obtained by combining data from HFS and LFS horizontal views of CXRS diagnostic. Quasi stationary profiles are shown for three discharges (TCV 27094,27098,27095) with $I_p = 170, 200, 320$ kA. The magnetic axis lies at $R = 0.89$ m.

different plasma currents $I_p = 170, 200, 320$ kA ($q_e = 6, 4, 2.5$). Rotation profiles shown were measured in the quasi stationary phases.

The left plot shows the toroidal rotation u_ϕ as a function of the major radius. There is a good match in the central region between the LFS and HFS measurements. The region affected by the sawtooth activity, delimited by the inversion radius, is well defined for both the inboard and outboard measurements. A strong shear of u_ϕ is present in the central region indicating a strong asymmetry in the rotation. This asymmetry is reduced, but remains finite, when considering the angular velocity $\omega_\phi = u_\phi/R$ [krad/s] that, in the rigid body approximation, is constant on magnetic surfaces. In right plot, ω_ϕ is shown as a function of ρ_ψ ($\rho_\psi < 0$ indicates $R < R_{axis}$) and it appears clearly that the inboard plasma is rotating more slowly than the outboard, by an amount that at mid radius may reach 5 krad/s, that is 15-20% of ω_ϕ.

As shown in chapter 3, the inboard-outboard asymmetry of toroidal rotation arises naturally as an effect of the presence of a finite poloidal rotation. From the knowledge of u_ϕ and u_θ measured on the LFS midplane, Eq. 3.2.1 can be used to reconstruct, in the incompressible fluid approximation, the profiles of u_ϕ and u_θ in the HFS midplane, for comparison with experimental observations. Unfortunately, although the CXRS09 HFS system is ready for this, the possibility of obtaining reliable simultaneous measurements of both HFS u_ϕ and LFS u_θ has not yet arisen. As a first step, we can make an estimate on the base of u_θ predicted by neoclassical theory, which, as we saw, is of the same order of that measured.

In Fig. 4.9 we compare the u_ϕ and u_θ radial profiles for the LFS (blue, circles) and HFS (red, squares), plotted as function of the normalized poloidal flux, for discharge TCV 27098. Solid curves indicate the incompressible fluid model profiles. In this representation it appears that the asymmetry in ω_ϕ for this discharge increases from the center outwards, with values ≈ 8 krad/s at $\rho_\psi = 0.65$, which are well outside the uncertainty of both measurements (2 km/s). A smaller asymmetry is observed on u_θ, that on the LFS is assumed neoclassical. In the presence of such poloidal plasma flow, the HFS u_ϕ is predicted to be much slower than for the LFS. The neoclassical prediction for u_θ may be in excess, possibly due to an overestimation of Z_{eff} or dT_i/dr. As a test,

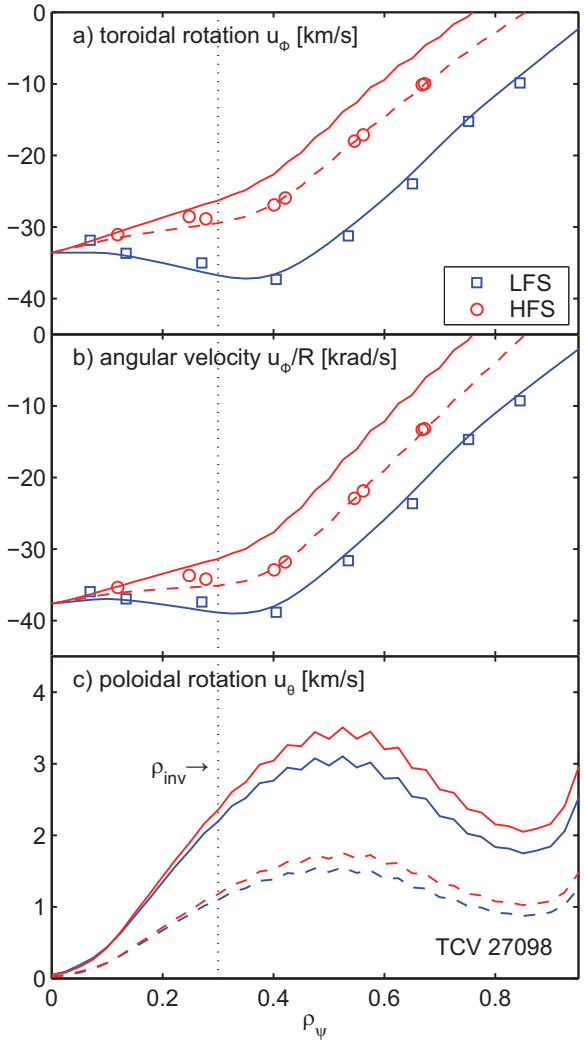

Figure 4.9: Comparison of toroidal rotation measured in the LFS and HFS midplane, with the predictions of incompressible fluid approximation, for discharge TCV 27098. Poloidal rotation is assumed neoclassical (solid curves) or, with better agreement, half of the neoclassical value (dashed curves). The mismatch in angular velocity can reach 8 krad/s, which is out of the uncertainty of the measurements, indicating that the rigid rotor is only rough approximation for carbon species.

we consider u_θ lower by a factor of two compared to neoclassical values (dashed curves): this *ad hoc* hypothesis permits to match the experimental observations.

Similar results are obtained for discharges with different I_p and n_e, suggesting that, in TCV Ohmic plasmas, the carbon poloidal rotation is close to neoclassical values but sufficiently high to engender poloidal asymmetries in the carbon angular velocity. Hence, the rigid rotor approximation is only valid within an accuracy of 20%, and varies depending on the plasma configuration and on plasma parameters.

It is important to stress that Eq. 3.2.1 applies for each given plasma species separately [38], hence different degrees of HFS/LFS asymmetry are expected for impurity and main ion species. Considering that typically, for TCV, according to neoclassical estimations $u_{\phi,D} \sim u_{\phi,C}$ and $u_{\theta,D} < u_{\theta,C}$ (see Fig. 4.7), a lower degree of asymmetry is expected for deuterium main ion ($<5\%$). In this sense, the rigid rotor approximation can be considered a good representation for the toroidal plasma flow.

4.5 No-slip condition and neutral particles momentum sink

The measurements of toroidal rotation close and across the plasma edge indicate that, for limited configurations, the rotation in the peripheral region of $\rho_\psi > 0.95$ is close to zero, regardless of the values of current and density. Even if a peaking u_ϕ profile builds up in the gradient region, a boundary condition appears to keep the plasma rotating close to zero km/s in proximity of the edge.

This effect, often referred as the *no-slip* boundary condition, has been related to the sink of toroidal momentum due to CX reactions with neutral particles present in this region. The neutral density could be especially important in the case of limited configuration, where the interaction with the limiter (the central column in TCV) favors the recycling of neutral atoms.

To evaluate this contribution, the spatial distribution of the neutral density (n_0) is required, a quantity that is extremely difficult to measure directly. In JET, n_0 has been estimated from the passive component of the charge exchange recombination of carbon [94]. In TCV, the neutral deuterium profile in the confined plasma is more reliably estimated by means of the DOUBLE-TCV code [16,17]. Given the experimental profiles of electrons and main ions, DOUBLE calculates the neutral emission spectrum accounting for the main atomic processes that affect the neutral transport across the plasma (atom-atom, atom-ion, electron-atom). In particular, it can be used as synthetic diagnostic for the CNPA and VNPA diagnostics. The neutral density profile is in this case calculated predictively, by optimizing the match with experimental energy spectra.

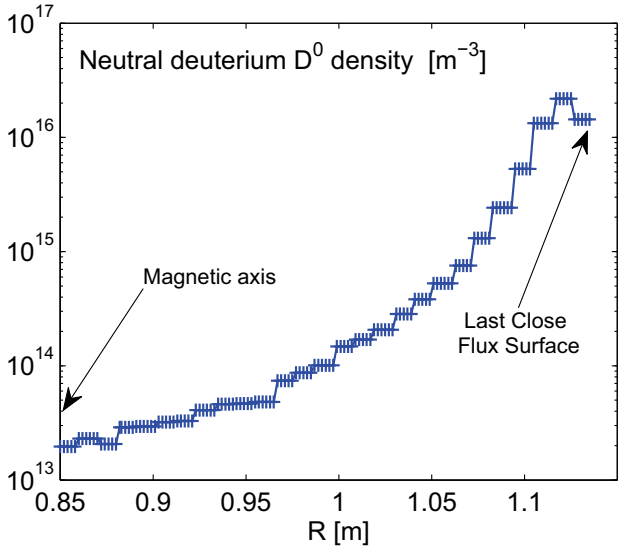

Figure 4.10: Radial profile, from magnetic axis to LCFS, of neutral deuterium density calculated by DOUBLE-TCV code, for the limited discharge TCV 36002, $n_{\mathrm{e,av}} \approx 4 \times 10^{19}\,\mathrm{m}^{-3}$, $I_\mathrm{p} = +340$ kA.

In Fig. 4.10 the density of neutral deuterium species, calculated by DOUBLE, is plotted as a function of the major radius. From the neutral density we can calculate a neutral friction force that expresses the loss of momentum due to CX with neutrals as $F_{cx} = -nmu\langle\sigma u\rangle_{cx} n_0$, where n_0 is the neutral density and all the other quantities refer to the main ion species, that is deuterium. To evaluate the magnitude of this force, one can also consider:

$$\tau_{cx} = \frac{nm\mathbf{u}}{F_{cx}} = \frac{1}{\langle\sigma u\rangle_{cx} n_0} \tag{4.5.1}$$

which represents the time employed to lose the initial momentum $nm\mathbf{u}$. Considering neutral energies of few eV, characteristic of the plasma boundary, and experimental plasma velocity, the

effective cross section is of the order of $\langle \sigma u \rangle_{cx} \sim 1 \times 10^{-14} \mathrm{m}^{-3}$ [25, 42]. Hence in the edge region, where $n_{D^0} \sim 1 \times 10^{16} \mathrm{m}^{-3}$, $\tau_{cx} \sim 10$ ms, which is of the order of the CXRS diagnostic time resolution and faster than the radial momentum diffusion time (~ 100 ms).

τ_{cx} also represents the timescale on which the total angular momentum of the plasma is conserved: for longer timescales, any redistribution of momentum, implying a change of rotation in the edge region, will eventually result in a global change of momentum, as illustrated in Fig. 4.11.

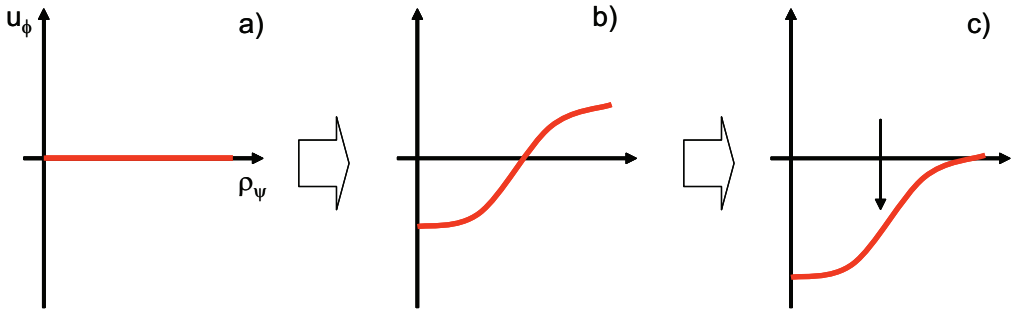

Figure 4.11: Schematic evolution of a plasma acquiring total angular momentum due to an edge sink. Starting point is a flat rotation profile (a). Turning on an outward radial momentum flux results in the acceleration of the central and peripheral regions in opposite directions: the total momentum remains zero on a fast timescale. On longer timescales, the edge recovers zero rotation from the effect of friction with edge neutrals. In the core, a gradient is sustained by momentum flux and the profile shifts rigidly. The final result is a net acceleration of the plasma column.

This scheme where the edge rotation is low and close to zero is true for limited configurations at low density and positive triangularity. Finite values of toroidal rotation in the peripheral region have been measured for plasma configurations with strong negative triangularity and, occasionally, high density and current discharges ($n_{\mathrm{e,av}} > 4 \times 10^{19}\,\mathrm{m}^{-3}$, $I_{\mathrm{p}} > 300\ kA$, with triangularity $\delta > 0.6$). These observations indicate that the neutral particle sink is one element of a more complex combination of effects.

4.6 Conclusions

In this chapter we reported the main features of the rotation in TCV in the basic configuration of limited, Ohmically heated, L-mode plasmas. Some aspects emerged from experiments in quasi stationary discharges with various combinations of plasma current and density.

In general, the plasma rotates toroidally in the counter current direction with velocities that are a fraction of the thermal deuterium velocity.

The toroidal rotation profile may be described as consisting of three regions: 1) a core plasma, inside the sawtooth inversion radius, which is dominated by the sawtooth activity, that flattens a u_ϕ profile otherwise peaking; 2) a peripheral region near the edge, where plasma rotation is close to zero, with a tendency to increase in the co current direction at the plasma boundary; 3) an intermediate region, in which a finite gradient of rotation is present, increasing approximately linearly with the ion temperature.

The peaking of the rotation profile in the presence of small edge velocity implies that the angular momentum cannot simply diffuse in the plasma interior from the edge, as observed in Alcator H-mode [80]. Instead, a non diffusive momentum transport mechanism is necessary to sustain the gradient against radial viscosity dissipation.

Poloidal rotation appears to be less sensitive to the plasma parameters. This is coherent with neoclassical theory predictions. The combination of toroidal and poloidal elements shows

that intrinsic rotation is dominated by the $E \times B$ drive, although the diamagnetic term can be important in the peripheral region.

The unique ability of TCV CXRS to measure toroidal rotation across the whole plasma diameter permitted to observe, for the first time to our knowledge, finite poloidal asymmetries of carbon rotation. Differences between LFS and HFS angular rotation up to 10 kHz are observed in the intermediate and peripheral region. These can be understood as effects of a small, but substantial, carbon poloidal rotation. Given that the deuterium poloidal rotation is predicted to be smaller than for carbon ($<$1 km/s), the "rigid rotor" approximation (ω_ϕ constant on flux surfaces) is expected to hold for the main ion and one fluid plasma rotation. On the other hand, as the asymmetries are of the same order of the measured velocities, the assumption of rigid rotor for impurities is in general not valid and must be verified.

The presence of a finite toroidal rotation in the absence of externally applied torque, requires a momentum transport inwards or outwards across the plasma edge. The role of neutrals as a momentum sink has been evaluated by reconstructing the neutral density profile on the base of NPA measurements. The estimation of a momentum loss time of $\tau_{cx} \approx 2$ ms appears to be coherent with dynamic observations, that will be reported in the following chapters.

For a wide range of plasma conditions, the plasma rotation varies continuously with the two parameters n_e and I_p. Abrupt changes in the toroidal rotation, that can be qualified as spontaneous transitions in momentum transport, have also been observed [81] for specific plasma conditions.

Chapter 5

Spontaneous rotation reversal in limited configuration

The previous chapter was devoted to the plasma rotation of Ohmic heated TCV discharges in limited magnetic configuration. For a wide range of the parameters (I_p, n_e), the plasma rotates in the counter current direction with edge rotation close to zero. The peaking of the toroidal rotation profile appears closely related to the ion temperature, with the maximal toroidal rotation set by the flattening effect of sawtooth oscillations in the plasma core [45]. In this chapter, we extend the parameter domain to high current ($I_\mathrm{p} \gtrsim 290$ kA, $q_e \lesssim 3$), where deviations from the reported trends are found [95].

A spontaneous reversal of the toroidal rotation profile was observed: for average plasma density over a given threshold $n_{\mathrm{e,av}} \approx 4 \times 10^{19}\,\mathrm{m}^{-3}$ the plasma core rotates in the opposite (co current) direction, with similar absolute values $u_{\phi,axis} \approx \pm 10$ km/s [81].

The dependence of the direction of intrinsic plasma rotation on plasma parameters, in particular density, was already documented on other Tokamak devices [80, 96]. Those observations were, in general, not supported by radially resolved measurements. TCV's CXRS diagnostic was used to show that opposite toroidal rotation also corresponds to an opposite direction of the rotation peaking. In fact, rotation reversals imply a change in the sign of the gradient of the rotation profile in the intermediate radial region that, in the absence of an external torque, suggests a radical change in the character of radial momentum transport.

Spontaneous reversals of toroidal rotation are particulary relevant in the study of momentum transport, as they provide a clear and reproducible phenomenon to compare with models. This chapter is dedicated to the experimental characterization of the rotation reversal phenomenology. During this thesis, the effect of various plasma parameters (n_e, I_p, δ) on reversal rotation was studied extensively, both dynamically, by means of density or current ramps and in sequences of stationary discharges. Despite the extraordinary robustness of the phenomenon and the large amount of data collected (effect of plasma current, shape, collisionality, core-edge dynamic, hysteresis), a univocal understanding of the mechanism responsible for the reversal has not been identified.

On the basis of the reported observations, a qualitative interpretation in terms of radial momentum transport will be sketched out in this chapter. Some candidate explanations, based on neoclassical or turbulent toroidal momentum transport, will be considered in closer detail in chapter 7, specifically devoted to momentum transport studies.

5.1 Rotation reversal in Ohmic density ramps

The first experimental demonstration of toroidal rotation reversal was observed in Ohmic plasma discharges in limiter configuration, at low q_e, where the density was ramped.

In Fig. 5.1 the main traces of a discharge at $I_p = 340$ kA, $\delta = 0.3$, $\kappa = 1.5$ are plotted. The current flat top starts at $t = 0.4$ s; from $t = 0.5$ s to $t = 1.5$ s the central electron density is ramped up from 3 to 7×10^{19} m^{-3}. With increasing density, central T_e decreases from 1 to 0.8 keV, with T_C increasing from 450 to 600 eV due to the increased collisional heat equilibration between electrons and carbon ions. At the start of the density ramp ($t = 0.5$ s), the central toroidal rotation is approximately zero. A counter current acceleration follows, as T_C increases. This behavior ceases at $t = 1.1$ s, when the plasma core velocity changes rapidly from -14 to +10 km/s, within 100 ms, to flow in the co current direction. After this transition, the toroidal velocity and T_C are maintained until the discharge termination, although the density ramp continues. The timescale for the transition ($\tau_{rev} \approx 100$ ms) is considerably faster than that of timescale of variation of other plasma parameters.

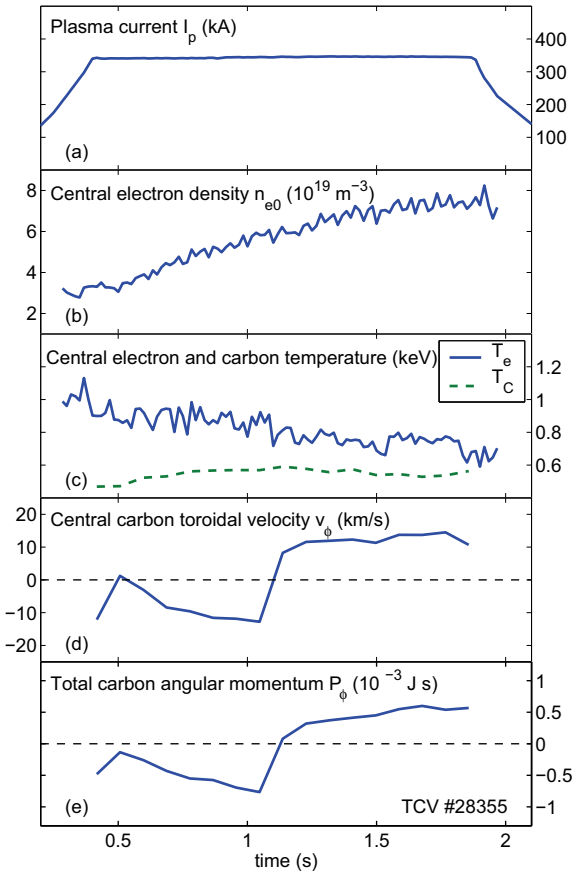

Figure 5.1: Summary of temporal evolution of the toroidal rotation velocity, together with some of the main TCV plasma parameters, across a rotation reversal during a plasma density ramp. Positive values indicate flows in the ion diamagnetic direction (co current).

The rotation reversal affects a large part of the plasma profile, as shown in Fig. 5.2, which compares the angular velocity profile before (solid, $t = 1$ s) and after (dashed, $t = 1.2$ s) the reversal. The plasma core rotates in the ion diamagnetic direction up to $\rho_\psi \approx 0.7$ with a flat or slightly centrally peaked profile, and a central velocity of $u_\phi \approx 12$ km/s. The outermost CXRS measurements indicate that the rotation in the plasma periphery is still counter current. The

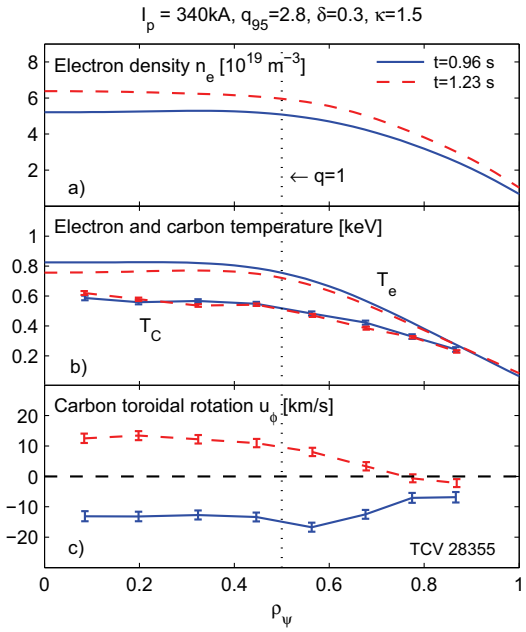

Figure 5.2: Comparison of the radial profiles of the plasma density and temperature together with the toroidal velocity profile across a toroidal velocity reversal during the plasma discharge in Fig. 5.1. The plasma edge rotation appears constrained to similar values and, interestingly, a co current bulge of the velocity profile inside the sawtooth inversion radius persists after the profile inversion.

core rotation reversal corresponds to a change in sign of the angular rotation gradient that, in the intermediate region ($\rho_\psi = 0.7$) passes, for discharge shown here, from $\nabla u_\phi / u_\phi$ -15 to 15. The two rotational states occur for similar temperature and density profiles (Fig. 5.2 a and b), that are both flat inside the sawtooth inversion radius. Across the reversal, in the core region n_e has increased from 5.2 to $6.4 \times 10^{19}\,\mathrm{m}^{-3}$ whereas T_e has only slightly decreased. In particular, the T_i profile is constant across the transition, within the measurement uncertainty.

The reversal was found to be robustly reproducible, occurring close to the same n_e threshold for plasmas with similar target parameters. This can be appreciated in Fig. 5.3, where the core rotation is plotted as a function of the line average density $n_{\mathrm{e,av}}$ for a selection of density ramp discharges with similar magnetic configuration ($\delta \approx 0.3$, $\kappa \approx 1.5$), and plasma current ($I_\mathrm{p} = 330 - 350$ kA) but different $n_{\mathrm{e,av}}$ waveforms. For all these discharges, the velocity traces reproduce the dynamic described above, with the reversal taking place at approximately the same density threshold. It is remarkable that these discharges were performed over a period of two years of TCV activity, during which TCV underwent multiple boronisation procedures. This is a clear demonstration that this phenomenon is not affected by the operational state of the device but has a plasma related origin. This also suggests a minor role of the impurity concentration. In fact, for the discharges in the graph, Z_eff varies from 1.4 to 2.2, corresponding to a carbon content different by almost a factor of 2.

The dynamic of u_ϕ reversal is also little influenced by the density ramp rate. Figure 5.4 compares the core rotation loci as function of time for four repetitions of the same plasma discharge, but with different n_e ramping rates. For all ramp rates the rotation reversal is triggered at the same electron density and the full reversal is always achieved in the same time interval of 200 ms with the same final rotation. This behavior reflects the fact that there was no clear evidence of continuous

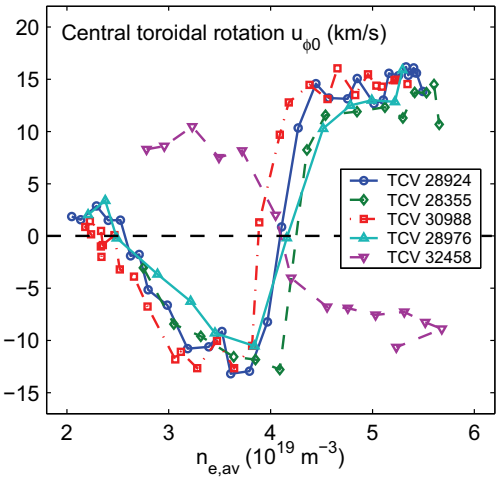

Figure 5.3: Central toroidal rotation as a function of the average plasma density for discharges with a density ramp. The central toroidal rotation of discharge TCV 32458, where the plasma current was reversed ($I_p < 0$), is also shown. The density ramp rates for these discharges were not the same. All discharges exhibit a counter to co current velocity reversal close to the same plasma density.

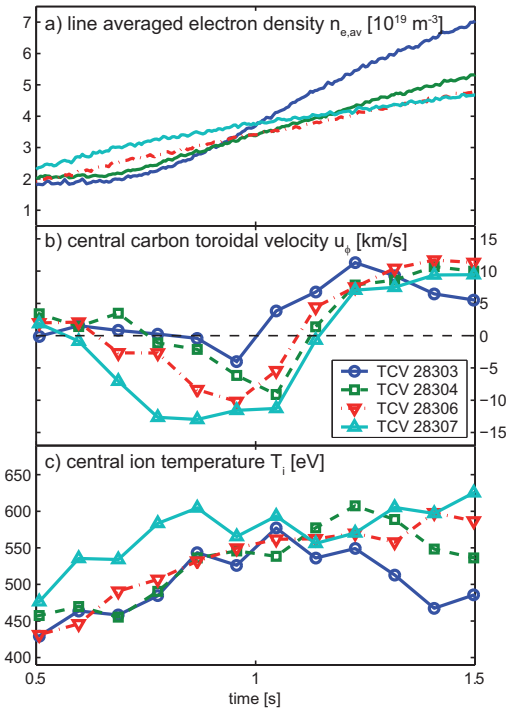

Figure 5.4: Temporal evolution of line averaged density, central toroidal rotation and ion temperature for four similar discharges at I_p =340 kA, with different density ramp rates.

dependence between rotation profile and electron density. This was confirmed in stationary fine scan of electron density, in stationary discharges with $I_p = 340$ kA and n_e close to $n_{e,thres}$, where the stationary profile always was measured peaking in one or the other direction (see Fig. 8.1). These observations suggest the existence of two distinct rotational regimes, characterized by opposite sign u_ϕ gradient in the intermediate radial region, with a transition between the two triggered by the density overcoming a threshold.

The transition was also found to be reversible. Figure 5.5a shows the time evolution of central

electron density and carbon toroidal rotation, for a discharge where the plasma density was first ramped over the threshold and then reduced by cutting the gas feed, on a timescale mainly determined by the wall recycling. At $t = 0.9$ s, the transition density threshold is reached ($n_{e0} \approx 6 \times 10^{19}\,\mathrm{m}^{-3}$) and the plasma rotation reverses direction. During the subsequent n_e decrease, u_ϕ decreases slowly (as does T_i, not shown) until the rotation reverses back to the counter current direction at $t = 1.55$ s, at a lower density of $n_{e0} = 4.4 \times 10^{19}\,\mathrm{m}^{-3}$. The locus of $u_{\phi 0}$ against n_{e0} (Fig. 5.5b) shows that the central rotation, following the back reversal, recovers its initial values for the same central density. Indeed, the whole rotation profile is recovered (Fig. 5.5c) so, from this time on, the plasma rotates in the counter current rotation regime. When representing the evolution u_ϕ against n_{e0} the hysteresis on the electron density is seen, suggesting a more complex dependence on plasma parameters than a single dependence on n_e.

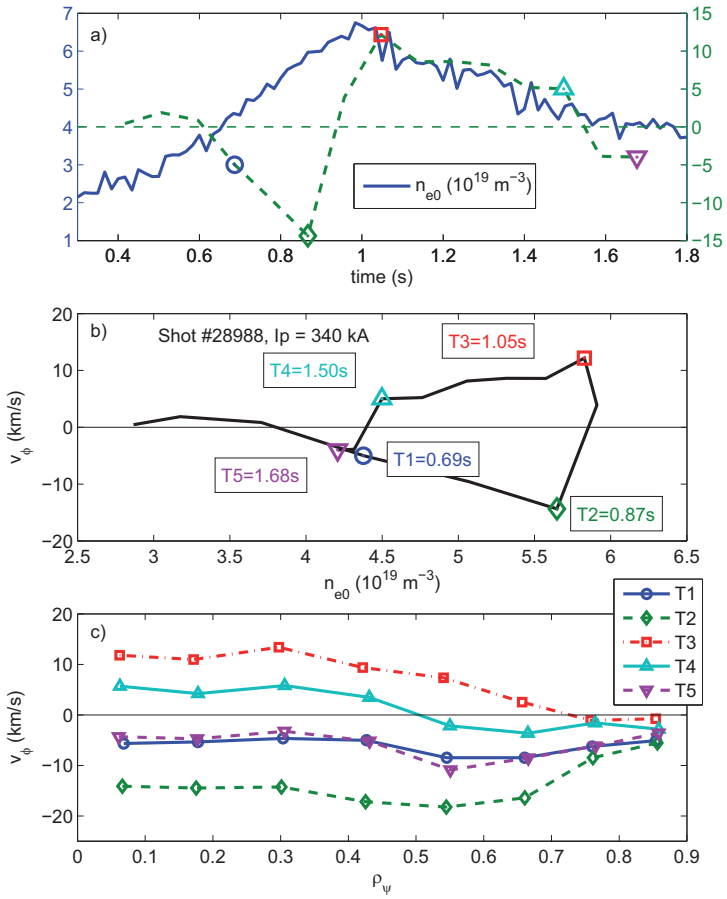

Figure 5.5: a) Time evolution of electron density (solid) and toroidal rotation (dashed) at the magnetic axis, for a discharge at $I_\mathrm{p} = +340$ kA featuring a density ramp up followed by a density ramp down. Color markers indicate five reference times, also labeled T1-T5. The locus of the core rotation as a function of the core plasma density through this discharge (b) indicates some hysteresis in the electron density parameter. c) The radial profiles corresponding to the reference times.

Experiments indicate that an edge safety factor $q_e \approx 3$ or lower is a key element in obtaining a rotation reversal. Fig. 5.6 summarizes the results of a series of four discharges performed at different plasma current ($q_e = 2.8 - 3.6$) for the same programmed density ramp and in the same magnetic configuration ($\delta = 0.35, \kappa = 1.4$). The reversal tends to occur at higher densities for higher q_e and a reversal is no longer observed for $q_e > 3.2$ ($I_\mathrm{p} < 290$ kA) for this magnetic configuration. In left graph the pre reversal rotation appears to scale strongly with I_p, which is interpreted as the effect of sawtooth inversion radius increase with I_p. Interestingly, the rotation in

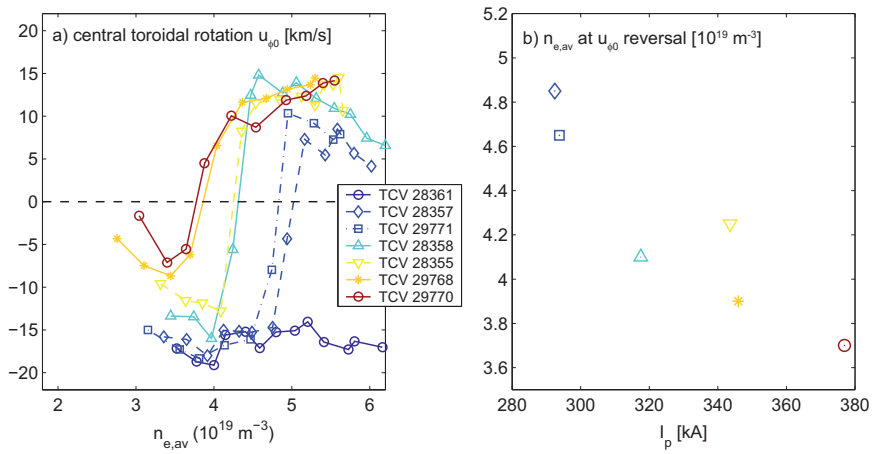

Figure 5.6: a) Temporal evolution of central toroidal rotation $u_{\phi 0}$ for a series of TCV discharges, repeating the same n_e ramp at different plasma current $I_p \approx 280 \div 380$ kA. b) The density at which the reversal of u_ϕ is observed decreases at higher current. At $I_p \approx 285$ kA u_ϕ remains in the counter current direction.

the co current, inverted, regime seems to show a weaker dependence (the roll over of core rotation for $n_{e,av} > 5 \times 10^{19}$ m^{-3} is more related to a decrease of T_i). To what extent this can be attributed to change in the effect of the sawtooth instability on the plasma rotation profile or a change in the transport between the two regimes, will be addressed below.

5.1.1 Rotation reversal dynamic

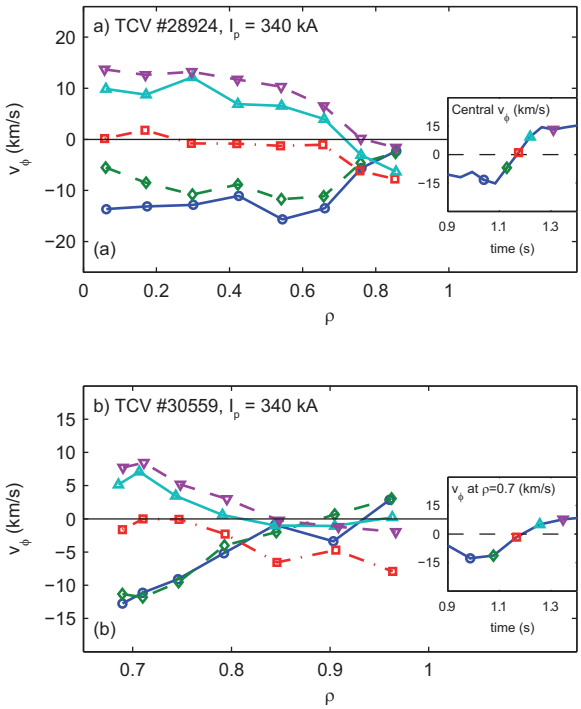

Figure 5.7: Temporal evolution of the core (a) and peripheral (b) angular velocity profiles across the rotation reversal. The acceleration of the plasma core is accompanied by a counter acceleration in the edge.

As described in previous paragraphs, the rotation reversal occurs on timescales of about

$\tau_{rev} \approx 100$ ms that are relatively independent on discharge parameters such as density ramp rate or impurity content. This timescale is similar to the typical relaxation times observed in L-mode, e.g. after minor disruptions [43]. Such timescales may be interpreted as the momentum redistribution times providing a coarse estimation of toroidal momentum transport in L-mode discharges: a reversal time scale of 100 ms corresponds to a diffusion coefficient of $\chi_\phi = a^2/\tau_{rev} \approx 0.5 \mathrm{m}^2/\mathrm{s}$, which is an order of magnitude larger than the neoclassical prediction of 0.01 m^2/s, indicating anomalous momentum transport. A more detailed characterization of the transport requires an evaluation of the dynamic evolution of the rotation profile. The u_ϕ reversal timescale is unfortunately comparable or faster than the CXRS temporal resolution, so that knowledge of the evolution of the rotation profile during a reversal is generally limited to few plasma discharges with particularly slow u_ϕ evolutions or where the active signal was large enough to permit a reduction of CXRS exposure to 15 ms.

Figure 5.7 shows the rotation profile evolution for a discharge where a slower transition ($\tau_{rev} \approx$ 200 ms) was observed with an increased CXRS sampling rate (20 Hz). Profiles corresponding to measurements before, during and after the reversal are shown. The change of the rotation profile first appears in the central part of the plasma column up to $\rho_\psi \approx 0.7$, whilst the edge rotation is unchanged, to measurement uncertainties. The next profile corresponds to the plasma core rotation crossing $u_\phi = 0$ km/s: the central plasma region, $\rho_\psi < 0.6$, appears to accelerate rigidly in the co current direction. During reversal, the outermost CXRS chord, $\rho_\psi = 0.85$, shows a transitory increased negative velocity of ≈ -7 km/s. This was studied by high spatial edge resolution measurements in discharges where the plasma axis was vertically displaced such that the CXRS diagnostic chords observed the plasma edge. Figure 5.7b shows the edge toroidal rotation profiles across a rotation reversal for a discharge with $I_p = 340$ kA: rotation reversal takes place at $t = 1.15$ s and affects the plasma up to $\rho_\psi \approx 0.8$; for more external radii, the rotation for the standard (counter) and inverted (co current) regimes is always ≈ 0 km/s. The plasma core deceleration > 10 m/s was accompanied by an increase (in the counter direction) of the plasma edge rotation of ≈ 5 km/s.

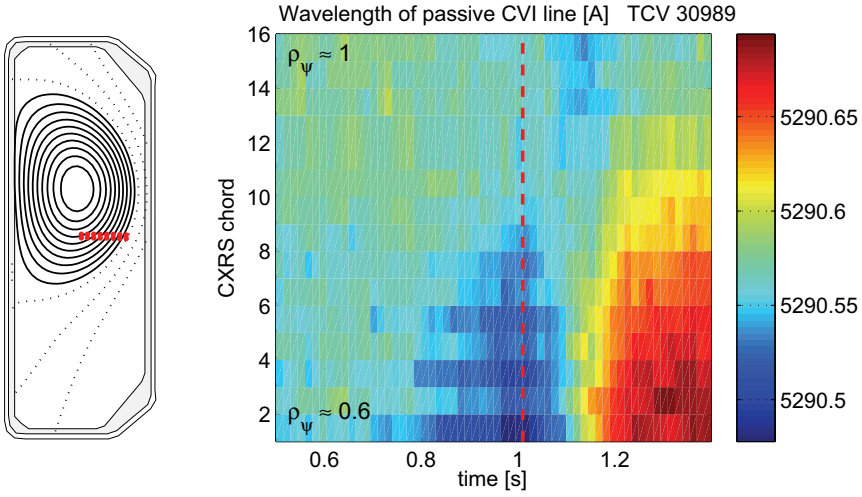

Figure 5.8: Temporal evolution of the wavelength of passive carbon CX line across the rotation reversal, for 16 chords of the LFS CXRS04 system. The vertical shift of the magnetic axis permits the observation of the plasma edge. The vertical dashed line indicates the beginning of the core u_ϕ acceleration.

An attempt to further correlate the dynamic of core and edge rotation across the reversal is based on an analysis of the passive CX signal, that is ordinarily sampled three times faster that the active measurement (see chapter 2). Figure 5.8 shows the average wavelength of the passive CX

line, which is parametric of the plasma rotation, as a function of time, with 16 channels acquired by the CXRS04 LFS system, for a density ramp discharge (TCV 30989) with a sample frequency of 30 ms. Rotation reversal in this discharge takes place between $t = 1.05 - 1.1$ s. At this time the increase of rotation in the plasma core (channels 1-4) corresponds to a decrease of the external channels (13-16). This counter acceleration of the edge lasts for ≈ 100 ms and at $t = 1.2$ s, when the u_ϕ profile has relaxed to its co current direction, the edge rotation appears to regain former values. The interpretation of these faster observations is complicated since the passive CX signal is integrated along the CXRS chord and follows the intensity distribution of passive emission (see chapter 2). Nevertheless the passive CX dynamic observations agree with and confirm the results of slow active CX measurements.

These observations are not consistent with a diffusive flux of angular momentum from the edge region due to plasma viscosity, but imply that the plasma has suffered a change in the balance of internally generated sources (non diffusive fluxes) of toroidal momentum. The transient edge acceleration in the opposite direction may be ascribed to partial conservation of total momentum, which is not maintained on timescales longer than ~ 50 ms, where the excess momentum is thought to have been dissipated on the vessel wall to within the resolution of the CXRS diagnostic. A quantitative characterization of the toroidal momentum transport, based on these observations is presented in chapter 7.

5.1.2 Poloidal rotation across toroidal rotation reversal

The sudden reversal of toroidal rotation is not accompanied by a substantial change in poloidal rotation u_θ. This is exemplified in Fig. 5.9, where carbon poloidal rotation profile before and after the toroidal rotation reversal are compared, in a density ramp discharge at $I_\mathrm{p} = 340$ kA (vertical lines in Fig. 5.9a indicate the reference times), where the toroidal rotation reversal occurs at $n_\mathrm{e,av} \approx 4 \times 10^{19}\,\mathrm{m}^{-3}$. In the intermediate region $0.6 < \rho_\psi < 0.9$ poloidal rotation has increased by 1 km/s after the u_ϕ reversal. This increase is also observed in the peak close to the plasma edge. However, this increase seems to follow the slow evolution of plasma density (Fig. 5.9b).

Using the ion force balance equation for the carbon impurity, radial profiles of carbon density, temperature and velocities provided by CXRS measurements can be combined to estimate the radial electric field E_r. For TCV 32126, E_r was evaluated before and after the reversal, at the times indicated by vertical lines in the graph a. Fig. 5.9 c and d show the contribution of each term together with the deduced E_r profiles. Because of the limited radial coverage of vertical and horizontal diagnostic systems, to derive E_r profile, u_θ has been extrapolated with values close to zero in the region $\rho_\psi < 0.5$ and n_C, T_C and u_ϕ have been linearly extrapolated for $\rho_\psi > 0.95$. Furthermore, all the quantities entering the force balance equation are all evaluated on the LFS midplane.

The core electric field, which is dominated by the strong toroidal rotation, changes sign with u_ϕ reversing from counter to co current (positive values correspond to outward directed E_r, confining electrons). Close to the edge, the negative contribution of poloidal rotation and diamagnetic term dominate and electric field always remains negative (inward, confining ions), with slightly larger values after velocity reversal.

It is interesting to notice here that the change in E_r, which corresponds to a change in the $u_{E\times B}$ direction (in the core) and shear (in the intermediate region), takes place without affecting substantially energy or particle confinement, as indicated by the unchanged peaking of T_e and n_e profiles. This suggest that the change of rotation and shear associated with spontaneous rotation profiles are far from a threshold for turbulence stabilization.

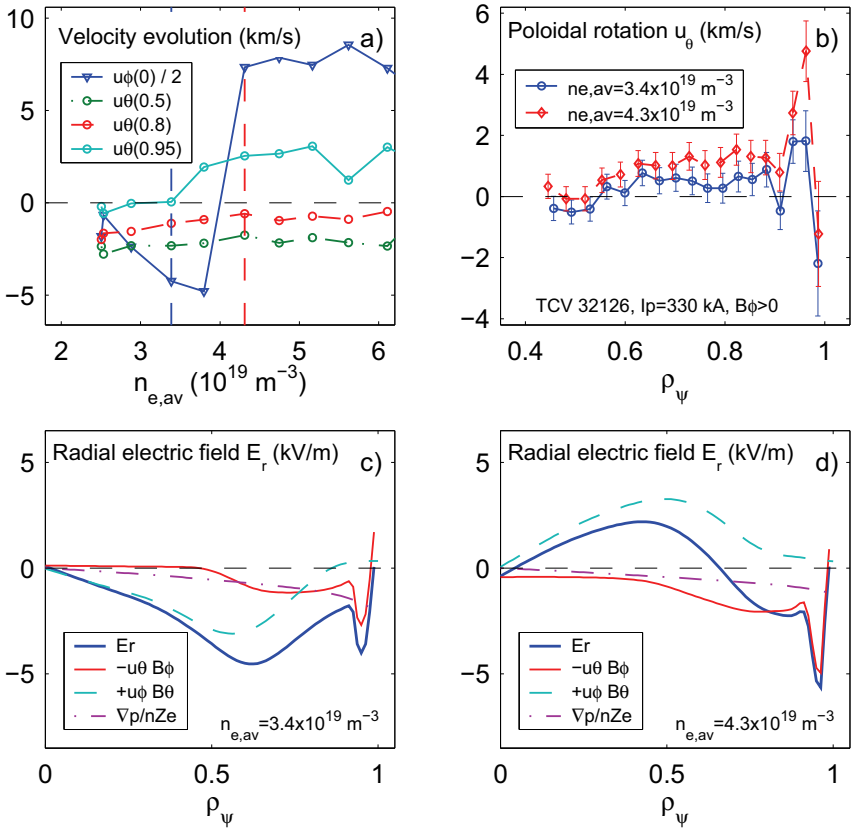

Figure 5.9: Poloidal rotation profile across a toroidal velocity inversion for a limited configuration. a) The poloidal rotation evolution with density at $\rho_\psi = 0.5, 0.8, 0.95$, together with a scaled plot of the toroidal velocity evolution all as a function of average plasma density. b) The poloidal rotation profiles before and after the inversion. In (c) and (d) the deduced electric field for the profiles in (b). The reversal of the toroidal rotation is associated with an inversion in the core radial electric field whereas the negative E_r feature in the plasma edge becomes stronger. For geometrical observation reasons, this feature may be narrower and deeper than estimated.

5.2 Current modulation experiments

To examine a possible role of safety factor profile, the rotation reversal was studied in stationary density discharges, where, to obtain the rotation reversal, the total plasma current I_p was modulated in ramps between a starting value of 270 kA, to a maximum value up to 380 kA. With this excursion in plasma current at approximately constant shape $\delta \approx 0.35$ and $\kappa \approx 1.4$), the safety factor is varied in the range $q_e = 3.1 - 5.3$ and sawtooth inversion radius $\rho_\mathrm{inv} = 0.4 - 0.5$.

Figure 5.10 summarizes the results of such experiments. Top left graph shows I_p time traces to be compared with the central u_ϕ evolution shown in the bottom left graph. Rotation reversal has been obtained for plasmas with sufficiently high density ($n_\mathrm{e,av} > 3.7 \times 10^{19}\,\mathrm{m}^{-3}$), always occurring on similar timescales. At lower density, the plasma always rotates in the counter current regime (e.g. TCV 30564, 30565). In contrast with the n_e ramp experiments (see Fig. 5.3), a precise I_p threshold for the transition, possibly a function of density, could not be identified. Instead, the transition appeared to be very sensitive to the time evolution of plasma parameters. This is highlighted by discharges TCV 30562, 30566, where the reversal from co to counter current rotation occurred late in the discharge at $t = 1.5$ s, during the ramp down phase. On the other hand experiments like TCV 30567 suggested that, to obtain the back reversal, a much lower current value was required.

This behavior was first ascribed to the rate of variation of the total current, which, in these discharges, was comparable to the current diffusion time ($\approx$ 200 ms), with the result of a poor control on the actual current profile (local q and magnetic shear s). These results motivated experiments where the total current was changed in steps, with quasi stationary phases long enough to permit a relaxation of the current profile.

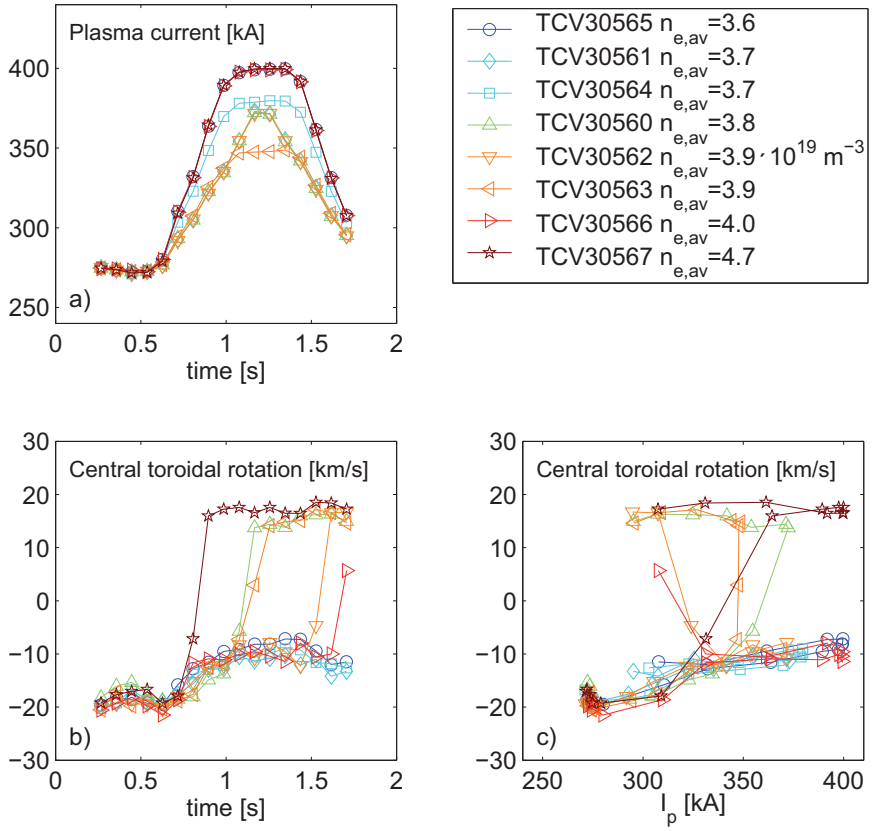

Figure 5.10: Temporal evolution of plasma current (a) and toroidal rotation (b) in a series of discharges in a range of plasma density $n_{e,av} = 3.6 \div 4.7 \times 10^{19}\,\mathrm{m}^{-3}$. Reversal of u_ϕ is found for high n_e and $I_p > 300$ kA. The locus of u_ϕ as function of I_p shows that for similar plasma parameters both co and counter rotation can be observed (e.g. TCV 30567).

In Fig. 5.11, I_p, n_e and average core u_ϕ traces are shown for two discharges with an initial flat top current of $I_p = 200$ and 280 kA respectively. In both discharges, at $t = 0.6$ s I_p was increased to 340 kA in 100 ms and then maintained for a 400 ms time interval; then, at $t = 1.0$, with a sharp ramp of 100 ms, the initial I_p value is recovered, for a final plateau phase of 200 ms. The requested target density $n_e = 4.64 \times 10^{19}\,\mathrm{m}^{-3}$ was reached at $t = 0.4$ s. The rapid jumps of total plasma current actually strongly perturb the plasma density, especially for TCV 30995. Nevertheless, n_e remains always substantially higher than $n_{e,av} = 4 \times 10^{19}\,\mathrm{m}^{-3}$, which is the density threshold for u_ϕ reversal in $I_p = 340$ kA discharges.

In both discharges the core rotation reverses from counter to co current direction at the $t = 0.6$ s when the current reaches the target value, passing from -30,-20 km/s to +15 km/s on similar timescales. The difference in initial I_p accounts for the different core rotation measured in the first phase $t = 0.4 - 0.6$ s, coherently with the scaling law Eq. 4.1.1. However, when at $t = 1.2$ s the initial current is recovered, only the lowest current discharge displays a back reversal. For TCV 30997, u_ϕ remains co current until the discharge termination. These experiments indicate an hysteresis in I_p, confirming that a back reversal requires I_p lower than that needed to access the co current regime. These results again demonstrate that the rotation regime is not strictly

a function of the plasma parameters. Following the discharge time history, both co or counter rotating regime may be obtained in stationary plasma phases (tens of energy confinement times) for the same combination of external plasma parameters (TCV 30997 in Fig. 5.11). In this sense this phenomenon may be qualified as a bifurcation.

This property could be used to compare two plasmas with similar target parameters (e.g. $n_{\mathrm{e,av}}$ and q_e) and opposite core rotation direction, and investigate possible effects of rotation on confinement (particle density and temperature gradients).

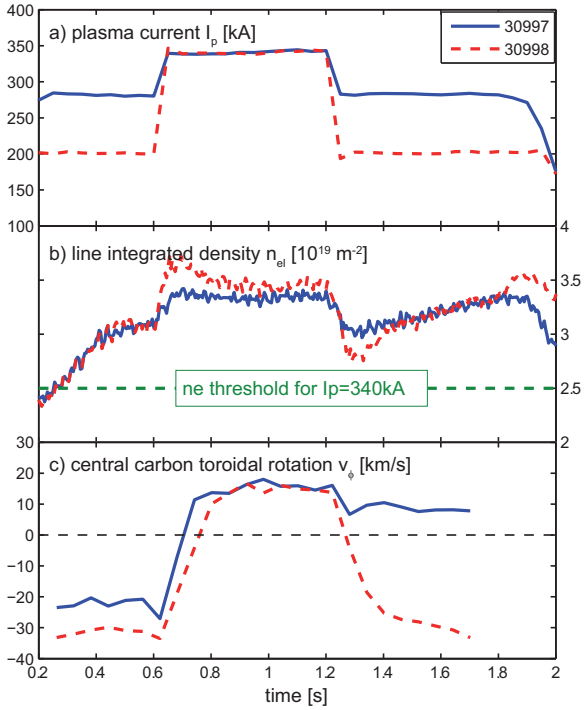

Figure 5.11: Temporal traces of plasma current, line integrated density and central toroidal rotation for two plasma discharges with I_{p} modulated in 3 plateaux. The electron density threshold for the u_ϕ reversal observed in discharges at $I_{\mathrm{p}} = 340$ kA is indicated.

5.2.1 Sawtooth and MHD activity

At low safety factor ($q_0 < 1, q_e < 4$) the plasma core is dominated by sawtooth activity that, for the typical plasma shapes addressed here, extends up to $\rho_{inv} \approx 0.5 - 0.6$ at plasma currents of $280 - 380$ kA. We devote this section to present the main phenomenology observed in discharges that undergo spontaneous rotation reversal.

No drastic variation of sawtooth period is observed across the rotation reversal. This is shown in Fig. 5.12a where the sawtooth period (calculated as the time interval between two subsequent crashes) is plotted as a function of the time for three representative density ramp discharges at $I_{\mathrm{p}} = 340$ kA and triangularity $\delta = -0.26, 0.36, 0.48$. The slow increase of τ_{ST} is related to a slow, but substantial, increase of n_{e} across the discharges. There is no abrupt change in τ_{ST} observed at the u_ϕ reversal, that for these discharges occurs at $t \approx 1.1$ s. For the same discharges, the sawtooth inversion radius position, determined from the Soft X-Rays emission profiles from XTOMO diagnostic, at the HFS and LFS midplane is also shown (Fig. 5.12b), apparently with no significant variation across the transition either, to within the uncertainty of the analysis technique, ≈ 2 cm.

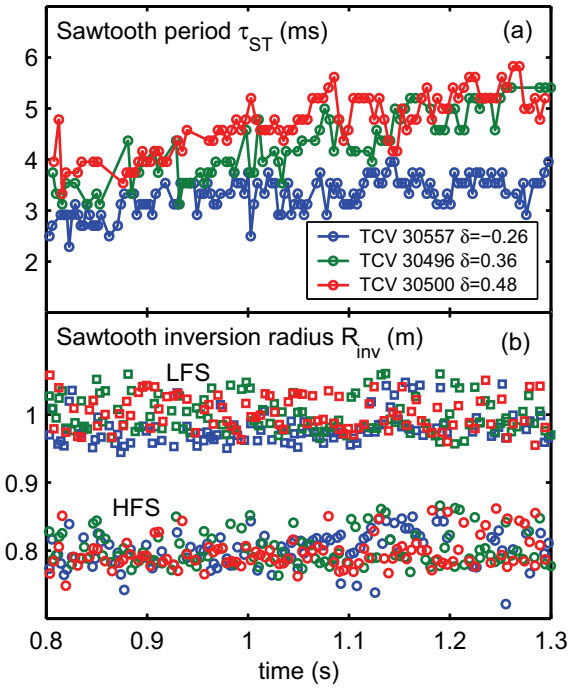

Figure 5.12: a) Sawteeth period as a function of time for three TCV discharges with a range of triangularity from -0.26 to 0.48. A density ramp takes all these discharges across the value associated with a toroidal velocity reversal at t=1.1 s. b) Low and high field side sawteeth inversion radii for these discharges over the same period. Although the position of the sawteeth radii is a function of triangularity, there is no evidence of a modification of the sawteeth period or inversion radius at the toroidal rotation reversal time. The values are deduced from SXR measurement from the XTOMO diagnostic.

A more detailed analysis of the data from the higher spatial resolution DMPX diagnostic led to detection of a measurable reduction of the sawtooth inversion radius and sawtooth period, occurring when the plasma rotation passes from the counter to co direction. Fig. 5.13 shows the spectrograms of four channels of the diagnostic observing the region $\rho_\psi \approx 0.5$ for TCV 32126, where the sawtooth was present with $\tau_{ST} \approx 4-5$ ms. An extended time window of 50 ms was used to calculate the Fourier spectrum and follow the sawtooth frequency, visible with its harmonics as red traces in the spectrogram. Since, at the inversion radius, the SXR emission is rather constant, the chord observing that region is typically characterized by the minimum signal at the sawtooth frequency. In this density ramp discharge (TCV 32126) the rotation reversal occurs at $t = 0.75$ s and, at this time, the minimum of signal passes from chord 42 to chord 43, indicating a reduction of ρ_{inv}. Chords observing the LFS plasma lead to the same conclusion. Precise quantification of the effect is challenging because the DMPX only provides line integrated measurements. Nevertheless, from the radial separation of the chords at the position where they are tangential to flux surfaces, the change is lower than 1 cm ($\Delta\rho_\psi \approx 0.03$). The observed variation of $\rho_{\rm inv}$ is close to the limit of the resolution of the diagnostic, however it takes place faster than the natural evolution of sawtooth amplitude and period following the ramping of $n_{\rm e}$ and was confirmed for several discharges and systematically correlated with the reversal of plasma rotation.

A signature of toroidal rotation reversal is also found in the characteristics of a so called "sawtooth precursor mode". A sawtooth crash may be preceded by the destabilization of a MHD mode resonant around the $q = 1$ surface, characterized by poloidal and toroidal mode numbers $n = 1$, $m = 1$. The sawtooth precursor may oscillate long enough to be detected. From of its localization, its frequency may be directly linked to plasma rotation and is often considered parametric of toroidal plasma rotation [64,97]. For the discharges presented here, the $q = 1$ surface

is well inside the plasma core ($\rho_\psi \approx 0.5$) so the precursor is well detected from the SXR emission data.

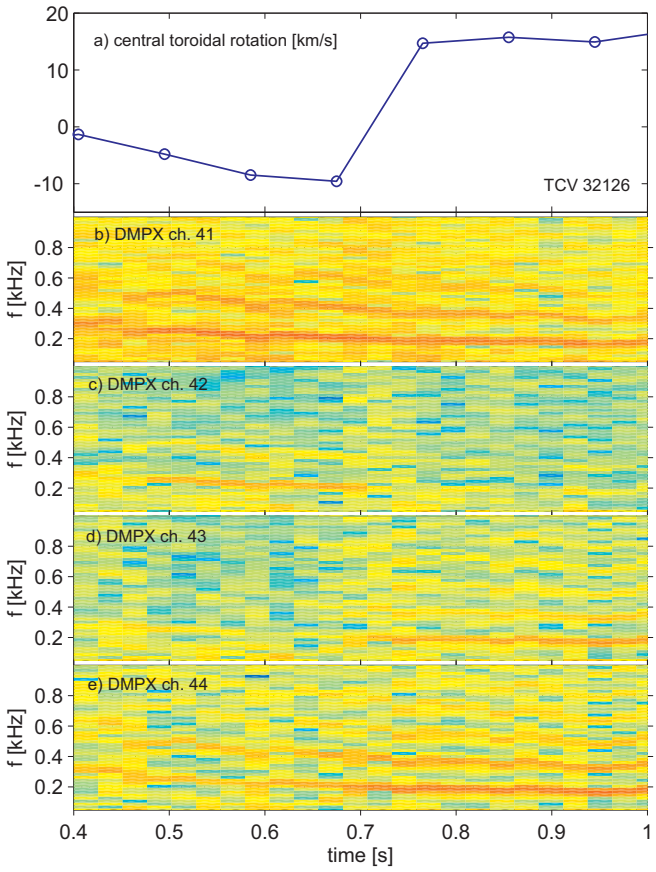

Figure 5.13: The temporal evolution of the core toroidal rotation (a) compared with the low frequency spectrograms (b-e) of four DMPX chords observing the region of HFS sawtooth inversion, in plasma discharge TCV 32126. The sawtooth frequency $f_{ST} \approx 200$ kHz is visible with its harmonics as red traces. The signal at $f = f_{ST}$ is minimal for the chord observing the inversion radius region, i.e for ch.43 for t<0.7 and for ch.42 for t>0.7.

Fig. 5.14a shows a spectrogram of the Soft X-Ray Signal measured by a chord of the DMPX diagnostic observing the region where the precursor mode is resonant ($\rho_\psi \approx \rho_{\text{inv}}$), for TCV 30998 discharge described in section 5.2. The carbon toroidal rotation by the CXRS04 diagnostic is also shown for comparison (Fig. 5.14b). In the first part of the discharge, when core u_ϕ is counter current, the precursor oscillations are clearly detected (Fig. 5.14c). Here a 60 μs time window used for Fourier analysis permitting a larger bandwidth and precursor oscillations become also visible as narrow vertical bands in the spectrogram. The temporal evolution of the precursor frequency agrees well with the CXRS measurements. In particular, for $t > 1.3$ s, the precursor frequency drops from 8.5 kHz to approximately 2 kHz, simultaneously with the rotation reversal, providing an independent evidence of a deceleration of the plasma column. Later in the discharge, during the co current rotation, the precursor is hardly detectable on the spectrogram, as it only lasts one or two oscillation cycles before the sawtooth crash (Fig. 5.14d). Approximating the period from the peak to peak time interval of the raw SXR trace d, an approximate frequency of 1.5 kHz is

observed for the full co current rotating phase $0.6 < t < 1.2$ s. The observed variation of frequency Δf_{MHD} is coherent with a Doppler effect related to the change of toroidal rotation at the radial location of the mode at $\rho_\psi = 0.4$, $R = 0.98$ m at LFS midplane. Neglecting possible variation of u_θ and ∇p across the reversal, one can estimate:

$$\frac{\Delta u_\phi(\rho_{\rm inv})}{2\pi R} \approx \frac{50{\rm km/s}}{6.2{\rm m}} \approx 8 \text{ kHz}$$

for comparison with the $\Delta f_{MHD} \approx 8.5 - 1.5 \approx 7$ kHz from the analysis of SXR measurements.

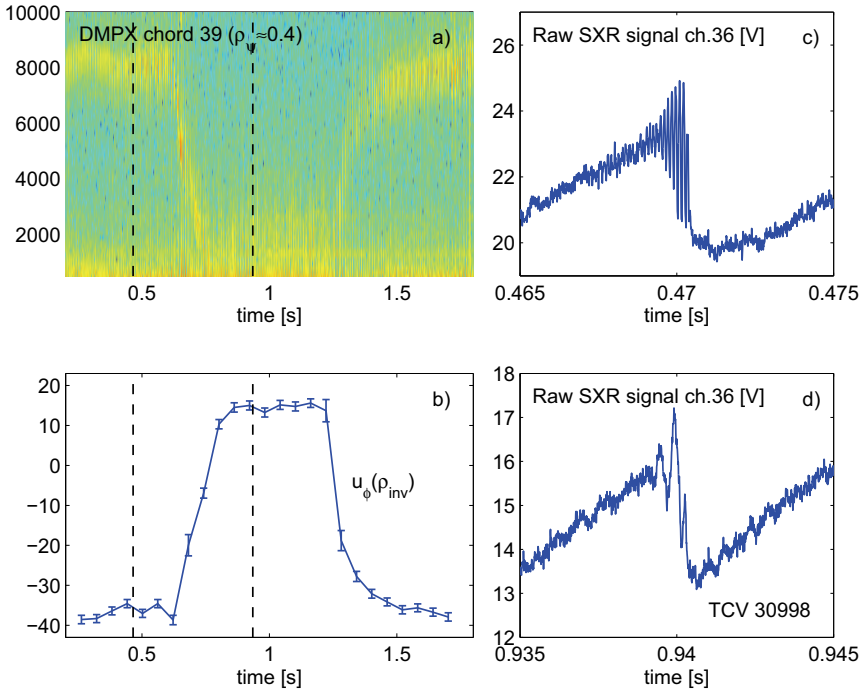

Figure 5.14: a) Spectrogram of the SXR signal measured by one chord of DMPX diagnostic, during plasma discharge with $I_{\rm p}$ modulation (TCV 30998 in Fig. 5.11). The selected chord observes the region where the sawtooth precursor is resonant ($\rho_\psi \approx 0.4$). The temporal evolution of mode frequency mimics that of u_ϕ at the same location (b). Graphs (c) and (d) show the raw SXR signal in two time windows indicated by vertical dashed lines in (a) and (b).

Magnetic measurement often showed the presence of a small amplitude $n = 1$, $m = 2$ mode in these discharges, characterized by frequencies $\approx 5 \div 7$ kHz and counter current phase velocity (Fig. 5.15). This mode is localized at the $q = 2$ flux surface, which in these discharges is located approximately at $\rho_\psi = 0.9$; here, the plasma toroidal rotation undergoes little change across the core's rotation reversal, remaining negative and close to zero. Consistently, no substantial change of this mode's frequency is observed and the toroidal component of phase velocity is always observed counter current in toroidal Mirnov probes array. This [2,1] mode, typically present throughout the discharge, is sometimes initiated at the rotation reversal. Its frequency may evolve during the discharge and there is often some sign of a discontinuity in the mode frequency and amplitude at the time of toroidal velocity reversal. In particular, as shown for instance in Fig 5.16, in the counter rotating regime (low density), the [2,1] peripheral mode ($f \approx 6$ kHz) appears to interact with the [1,1] sawtooth precursor ($f \approx 5$ kHz). This coupling, possibly enhanced by the proximity of the two mode frequencies when plasma flows counter current, strongly decreases after the reversal to co current rotation, when the precursor frequency and amplitude are reduced.

This somehow varied phenomenology, illustrated on few selected cases, is indeed common to the majority of the discharges that feature rotation reversal, and may be summarized in as follows:

- Counter current rotation (low density, $\nabla u_\phi(0.7) > 0$), clear precursor activity (frequency$\gtrsim$ 5 kHz) more strongly coupled with peripheral mode (when present), slightly larger ρ_{inv}.

- Co current rotation (high density, $\nabla u_\phi(0.7) < 0$), weak precursor activity (≈ 2 kHz) decoupled with peripheral mode, smaller ρ_{inv}.

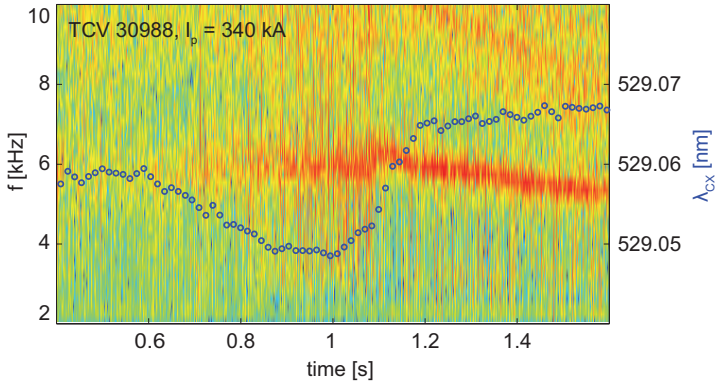

Figure 5.15: MHD spectrogram (Mirnov coil signal) during a limited discharge with a density ramp is shown together with the wavelength of the passive CVI light of the innermost CXRS observation chord, which is used as a parametric measurement of the core rotation.

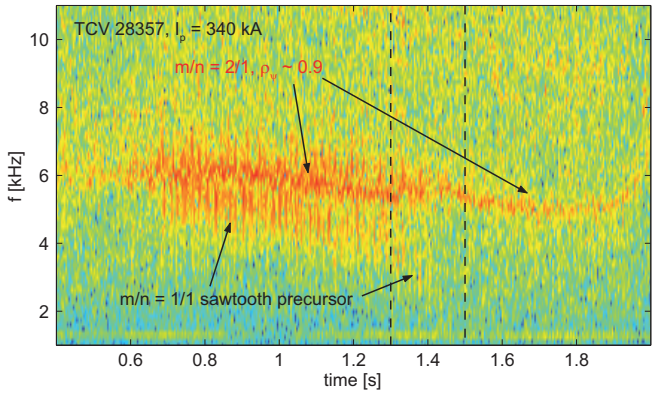

Figure 5.16: MHD spectrogram (Mirnov coil signal) during a limited discharge with a density ramp. Vertical dashed lines mark the time window for the reversal of u_ϕ from counter to co current direction. In the co current rotation phase the precursor activity persists at $f \approx 2$ kHz, but is much weaker and disappears from the spectrogram.

It would be tempting to associate directly the counter rotating regime to the coupling of sawtooth precursor and peripheral MHD modes. However, as shown in chapter 4, the counter rotation regime, characterized by a negative ∇u_ϕ in the intermediate region, is characteristic of a large range of plasma parameters, regardless of the presence of MHD or sawtooth activity, in particular in $I_{\text{p}} \lesssim 150$ kA discharges where $q_0 > 1$ and no sawtooth are present. On this basis, the phenomenology described in this paragraph, especially concerning the precursor mode activity, is likely to represent the signature of toroidal rotation reversal, rather than a mechanism that drives it, or, stated in otherwise, an effect of the plasma rotation on MHD structures and not viceversa.

5.3 Effect of collisionality by means of ECH

A set of experiments was dedicated to possible rotation reversal in ECH heated discharges. The initial motivation was to decouple the effect of density temperature and their gradients, and to investigate the possible role of combinations of these quantities, as e.g. the plasma collisionality. The relatively high density required for rotation reversal restricted the achievable heating schemes (see section 1.4). Therefore, ECH heating at the third harmonic (X3) was used to heat the central plasma, while second harmonic EC beams (X2) were employed for power deposition outside the core region.

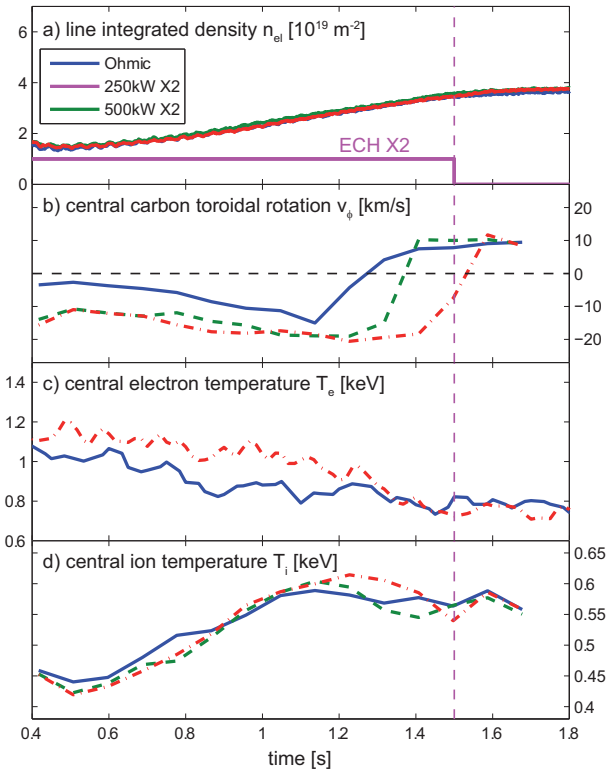

Figure 5.17: Main plasma parameters for three limited plasma discharges, with density ramps. With increasing ECH injected power the reversal of u_ϕ takes place at higher density. In these discharges the X2 power is adsorbed at $\rho_\psi \approx 0.7$.

In presence of ECH heating, the density threshold for the reversal increased with the injected power. This is summarized in Fig. 5.17 where the evolution of plasma parameters is shown, for three shots with increasing injected ECH power. The power deposition radius was located at $\rho_\psi \approx 0.7$, with the aim of increasing T_e (decrease collisionality) in the region where the gradient of rotation is seen to revert. However, following the reconstruction made with the ECH ray tracing code TORAY, only ≈ 100 kW were absorbed by the plasma, explaining the modest increase of central electron temperature. Nonetheless, the dynamic of rotation reversal was strongly affected, with the rotation reversal delayed in time, such that a higher density was required for reversal.

This result was confirmed by experiments where the rotation reversal was inhibited or triggered by an appropriate use of the ECH power, as shown in Fig. 5.18. Left column graphs refer to TCV 28987 discharge ($I_\mathrm{p} = 340$ kA), where the density was ramped to obtain the rotation reversal

and then allowed to decrease by cutting the gas feed. With the hysteresis in $n_{e,av}$, the plasma continues to rotate in the co current direction. However, the application of 500 kW of X2 power at $t = 1.2$ s induces a sudden and fast back reversal of core toroidal rotation.

Right column graphs show plasma discharge TCV 28939, starting with plasma density $n_{e,av} > 4 \times 10^{19}\,\mathrm{m}^{-3}$, i.e. over the reversal threshold for Ohmic plasmas at this current. However, an early application of 500 kW of X3 power prevents the rotation reversal with the plasma still rotating in counter current direction. At $t = 1.2$ s the X3 power is turned off and the plasma rotation promptly reverses rotation direction to co current.

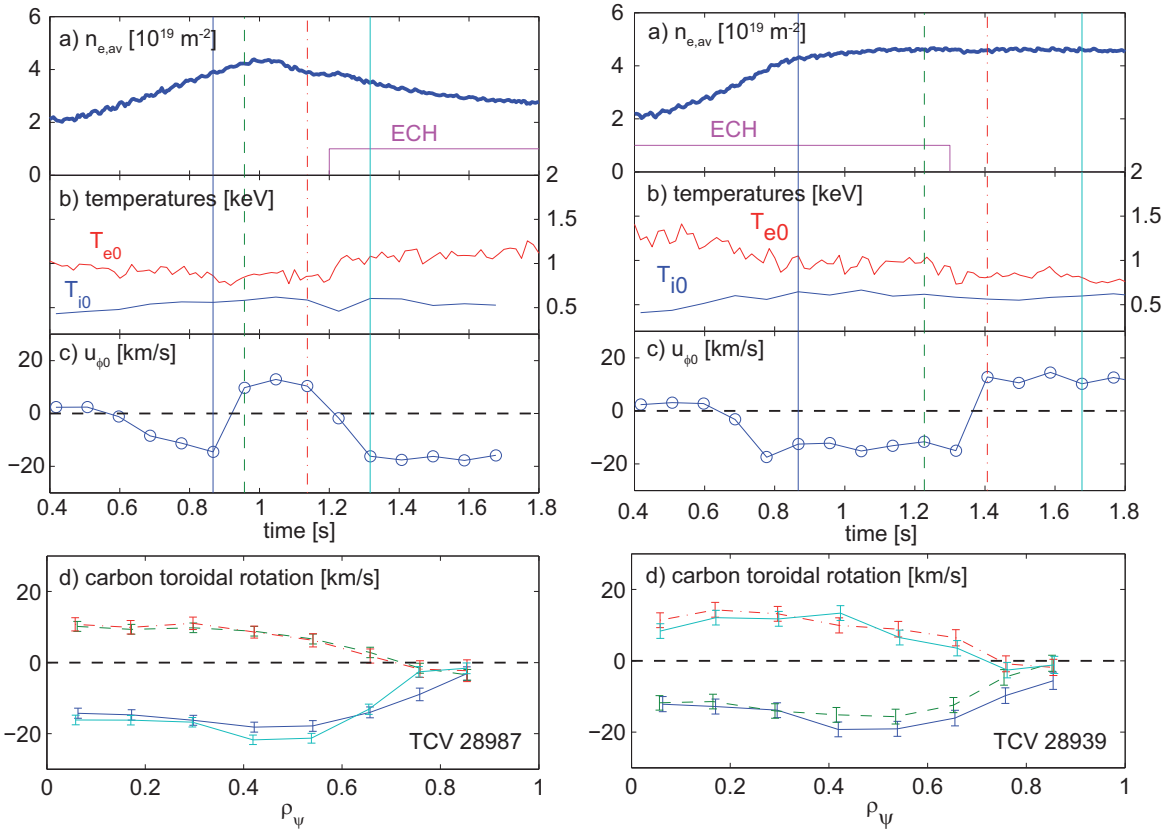

Figure 5.18: Temporal evolution of electron density, electron and ion temperature and central toroidal rotation, in two ECH heated discharges. Left column: TCV 28987 rotation reversal followed by back transition induced by X2 heating. Right column: TCV 28939, rotation reversal induced by cutting X3 heating. Bottom plots show the toroidal rotation profiles at the times indicated by the vertical lines.

Both experiments are consistent with the increase of the density threshold accompanying the ECH heating. Incidently, TCV 28939 is an example of using ECH to study the effect of rotation reversal decoupling the effect of different plasma parameters, at constant plasma density. Fig 5.19 shows the profiles of some transport related quantities, averaged over two time windows $t = 0.8 - 1.2$ s and $1.4 - 1.8$ s, corresponding to X3 heated co rotating plasma and Ohmic counter rotating plasma, respectively. The ECH deposition has the effect of increasing the electron temperature by 100 eV in the plasma core. Remarkably, the n_e profile remains practically unchanged after X3 is switched off, demonstrating that the electron density, even if successfully used as a tool parameter to induce the transition, is not the only determining parameter. In the bottom plots, the profile of effective collisionality $\nu_{\mathrm{eff}} = 0.10\ R\ Z_{\mathrm{eff}}\ n_e\ T_e^2$, where R in the major radius, n_e is $10^{19} m^{-3}$ and T_e is in keV [98] is shown for the two time windows (here ν_{eff} is calculated with Z_{eff} profile coming from CXRS absolute calibrated carbon density measurements, not shown). As we can see, the decrease in T_e reflects in an increase of 0.5 in ν_{eff} in the gradient region ($\nu_{\mathrm{eff}} = 1.5 - 2$ at $\rho_\psi = 0.7$).

This variation is not substantial but, examining other parameters such as the normalized gradients of T_e ir n_e, it may be sufficient to affect the character of the micro instabilities responsible for anomalous transport in this region.

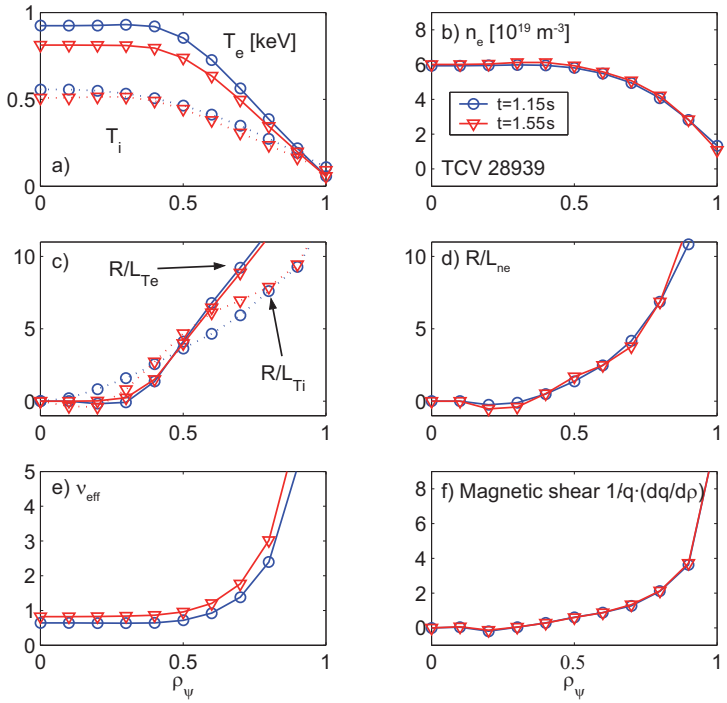

Figure 5.19: Radial profiles of some plasma parameters in two phases of TCV 28939 in Fig. 5.18: ECH heated, counter current toroidal rotation (blue circles) and and Ohmic co current rotation (red triangles). Magnetic shear is calculated from magnetic equilibrium reconstruction provided by LIUQE code.

5.4 Effect of shape

All plasma configurations described thus far have strong positive triangularity $\delta \approx 0.45$. Fig. 5.20a shows the evolution of the core toroidal rotation as a function of average plasma density for four discharges with triangularity in the range of $\delta = 0.48 - 0.0$. There is a strong decrease of the core rotation with decreasing δ and, although some discontinuity in the core rotation evolution may still be discerned at $n_e \approx 3.5 \times 10^{19}\,\mathrm{m}^{-3}$, this also reduces with decreasing triangularity. The effect on the radial profiles of the toroidal velocity (Fig. 5.20b) is even more marked. With lower triangularity, the core rotation remains close to zero with a strong rotation in the plasma edge region, a velocity profile reversal is not observed, with the transition appearing as a small increase of the core velocity (increase of gradient).

This trend continues for negative triangularity, shown in Fig. 5.20c for low and negative δ. The core rotation scales more in the counter current direction with decreasing δ. Fig. 5.20d plots the toroidal rotation profiles at $n_{e,av} = 4.5 \times 10^{19}\,\mathrm{m}^{-3}$. The whole rotation profile is increasingly in the counter current direction with decreasing triangularity although, here again, the profile saturates and rolls over when it reaches values -15 km/s, here in the $\rho_\psi \approx 0.8$ region.

Negative triangularity has previously been observed to result in a strong increase of the energy confinement time on TCV [99] with a corresponding increase in the electron and ion temperatures to which the toroidal rotation is sensitive. Fig. 5.21 shows the ion temperature and carbon content for a range of plasma triangularities (the ion temperature profile graph superimposes

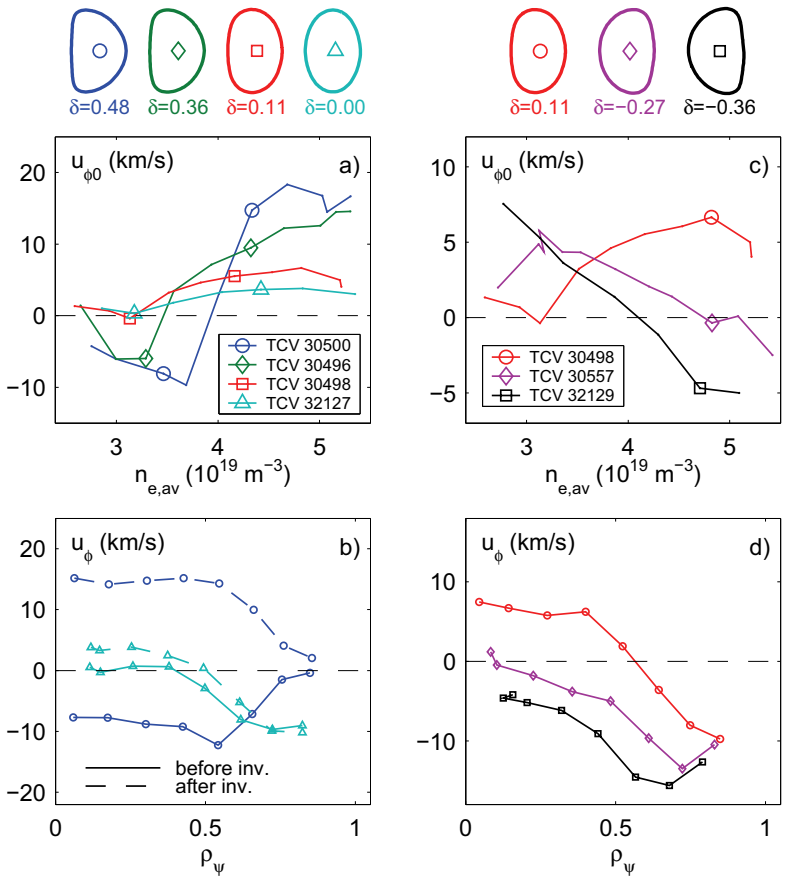

Figure 5.20: Toroidal rotation profiles as function of plasma triangularity in density ramp discharges. The core toroidal rotation (a) and the toroidal rotation profiles (c), are shown for $\delta > 0$ discharges. The toroidal velocity reversal phenomenon becomes less pronounced with decreasing δ. The profiles for $\delta = 0.48$ and 0 (elliptical shape) are shown for average plasma densities of 3.3 and $4.2 \times 10^{19}\,\mathrm{m}^{-3}$, i.e., across the density associated with a toroidal rotation reversal. At $\delta = 0$, the u_ϕ is small in the plasma core and there is a strong counter current rotation in the peripheral region at both densities. The trend with negative δ is summarized with data from discharges with a triangularity of $\delta = 0.11$, -0.27, and -0.36. In (c) the core u_ϕ as a function of plasma density and in (d) toroidal velocity profiles for $n_{\mathrm{e,av}} \approx 4.8 \times 10^{19}\,\mathrm{m}^{-3}$, i.e. above the density associated with the velocity reversal. The whole plasma rotates more strongly in the counter current direction with decreasing δ. At strongly negative δ in the peripheral region u_ϕ tends to saturate at values $u_\phi \approx -15$ km/ s.

measurements from the toroidal and poloidal observation chords). With decreasing triangularity, ion temperature and carbon content increase strongly: the carbon induced Z_{eff} varies from 1.2 for $\delta = 0.5$ to over 2.5 for $\delta = -0.5$.

From these experiments, it is difficult to derive a unique conclusion on the relation between rotation and triangularity. Although, for limited discharges, the toroidal rotation was found to depend little on the carbon content, there is a strong increase in the ion temperature, which in Ohmic discharges cannot be independently set. It is, of course, tempting to associate the apparent increased confinement with the increased rotation near the plasma edge, but the present data do not permit this conclusion unequivocally. On the other hand, measurements of vertical CXRS observation tends to exclude a role for poloidal rotation on the enhancement of confinement (Fig. 5.21c) at negative triangularity.

Plasma shape, especially triangularity, is known to affect plasma equilibrium, MHD stability and sawtooth character [**?**]. In these discharges, where δ was varied from $\delta = -0.3 \div 0.6$ at

constant plasma current, the edge safety factor varies in the range of $q_e = 2.4 \div 5$, with the sawteeth inversion radius varying from 0.2 to 0.3 m. The larger extent of the sawtooth dominated region could account for the strongly hollowed rotation profile in the core.

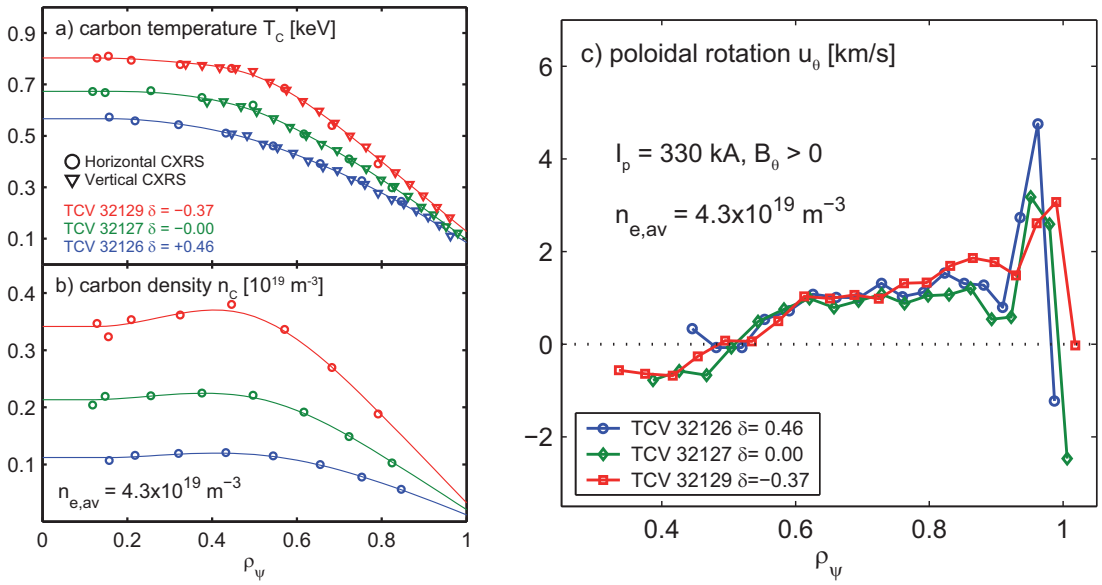

Figure 5.21: a) Ion temperature profiles shown for $\delta = 0.46$, 0, and -0.37 at $n_{e,av} \approx 4.5 \times 10^{19}\,\mathrm{m}^{-3}$. The excellent agreement between the poloidal and toroidal diagnostic T_i is a comforting demonstration of a good system alignment. With these Ohmically heated discharges, the ion temperature increases with decreasing δ from collisions with the increasing hot electrons resulting from a concurrent improvement in the energy confinement. b) The near linear increase in the carbon concentration for the same discharges, over this small shot range, may only be ascribed to a confinement improvement. c) Despite the strong change in the ion temperature with δ, the poloidal rotation profiles are remarkably similar

5.5 Conclusions

This chapter presented a detailed experimental study of the spontaneous toroidal rotation reversal, which takes place in high density, high current discharges in limited L-mode. An initial qualitative interpretation was attempted from the experimental results.

MHD activity, although present with rich phenomenology, appears to play a minor role in the process. The MHD modes present in these discharges generally are of small amplitude and appear with multiple and varied dynamics which are difficult to correlate with the simple and robust event of rotation reversal. In addition, no rapid change in the sawtooth period ($\tau_{ST} \sim 6 - 8$ ms), amplitude is observed across the transition. On the other hand, changes in the frequency of precursor modes is coherent with the variation of toroidal rotation at the reversal. Overall, the phenomenology suggests that, even if MHD modes can sometimes strongly influence the rotation profile [43], in rotation reversal discharges they appear to adapt passively to background rotation dynamics. In particular, the strongly reduced precursor activity, which characterizes the co current rotation regime, could be an indication of a possible stabilization effect of the plasma rotation or its gradient.

A possible link between the rotation reversal and the particle/energy transport comes from the force balance equation for the carbon impurity:

$$E_r = \frac{\nabla p_C}{n_C Z_C e} - (u_\phi B_\theta - u_\theta B_\phi) \tag{5.5.1}$$

where E_r is the radial electric field, $\nabla p_C/Z_C e$ the diamagnetic term, $p_C = n_C T_C$ the carbon pressure, B is the magnetic field, and u the plasma velocity (ϕ and θ indicate the toroidal and poloidal vectorial components). Experimentally, across the transition, the diamagnetic term and poloidal rotation u_θ vary slowly, so that the *sudden* reversal of toroidal rotation is directly reflected by a change in the E_r profile.

In tokamak plasmas, the radial electric field is often determined by the transport regime that may change during the performed density ramps. For example, with increasing density, the ion neoclassical transport rates, due to Coulomb collisions, become increasingly important and possibly comparable to the anomalous electron transport rates, as reported in [101]. An eventual transition of collisional regime (e.g. from banana regime to collisional Pfirsch-Schlüter) may also affect substantially the character of toroidal momentum transport [39]. At the same time, the type of turbulence responsible for anomalous transport may also depend on plasma parameters that vary during the density ramp: T_e, T_C ,n_e, etc. Experiments with EC heating indicated that the parameter driving the transition must, at least, contain terms depending on T_e and n_e. Collisionality was considered a possible important parameter, as it strongly influences the particle and energy transport, especially close to the transition from Trapped Electron Mode (TEM) to Ion Temperature Gradient (ITG) mode dominated turbulence [99,102,103]. This hypothesis, however, at present stage lacks any clear experimental vindication.

Recently, TCV observations, have been partly confirmed in Alcator C-mod, taking advantage of the recently installed diagnostic [104,105], that provides radially resolved u_ϕ measurements. In an experimental campaign in collaboration with TCV group, reversal of u_ϕ profile has been obtained by varying the n_e in Ohmic discharges at $q_e \approx 3$ ($B_\phi \approx 3$ T, $I_\mathrm{p} \approx 600$ kA, $n_\mathrm{e} \approx 8 \times 10^{19}\,\mathrm{m}^{-3}$). The analysis is presently on-going. The interpretation of the experimental results is complicated by the fact that, in these Alcator discharges, magnetic configuration was marginally close to a diverted configuration. However, the evolution of u_ϕ profile across the reversal, marked by the recoil of the plasma edge, was clearly observed in a way that is consistent with TCV's results (Fig. 5.7).

The rotation reversal phenomenon described in this chapter is highly reproducible, with a database of many discharges assembled in which the rotation reversal was obtained. The experimental evidence indicates that there is a rapid change in the balance of non diffusive fluxes of toroidal momentum in the core of the plasma. The reported phenomenology extends the experimental knowledge of bulk rotation in low confinement regimes and defines a unique test for momentum transport models of tokamak plasmas.

Chapter 6

Plasma rotation in diverted L-mode configuration

We devoted the previous chapters to the study of spontaneous rotation in plasmas in low confinement mode in limited magnetic configuration. We saw that the plasma column self accelerates to toroidal velocities that are an important fraction of the ion thermal velocity. Even if the typical rotation direction is opposite to the plasma current, varying main plasma parameters a different rotation regime can be acceded, with reversed toroidal rotation direction. On the other hand, the edge rotation was found to be close to zero for a wide range of plasma density and currents. The latter phenomenon was ascribed to the strong plasma-wall interaction at the limiter, with an important role of the neutral particles surrounding the plasma edge, which act as toroidal momentum sink.

The following step in the approach to the intrinsic plasma rotation question, is to address the diverted magnetic configuration. In diverted configuration case the Last Closed Magnetic Surface defining the plasma boundary is in contact with no solid element, and more complex dynamics at the Scrape-Off Layer are present. Even if the diverted configuration represents a key element to access the H-mode confinement regime, in this work Ohmically heated L-mode plasmas were addressed.

Compared to the limited, the diverted configuration shows a richer edge rotation phenomenology. Furthermore, and somehow surprisingly, also the core rotation appears to be affected by the topological change of the magnetic configuration: different rotation regimes are observed as function of plasma parameters, characterized by different peaking directions.

However, the dependence on plasma parameters is different compared to the limited case. The diverted configuration scenario is more complex and, in particular, the interaction of confined plasma rotation with the Scrape-Off Layer flows appears to be a key element to determine the stationary rotation profile of the plasma. As a result, a unique phenomenological description of the rotation profile is difficult. Instead, separate scaling laws for the rotation in different radial regions will be proposed.

6.1 Diverted configuration in TCV

As introduced in chapter 1, the TCV tokamak is not equipped with a complete divertor device. Nevertheless diverted plasma configurations can be obtained by using the shaping poloidal coils to create null points, or X-points (where total poloidal field is zero), inside the vacuum vessel. In this way Lower Single Null (LSN), Upper Single Null (USN) and Double Single Null (DSN) configuration can be obtained. Figure 6.1 shows some examples of equilibria obtained in TCV

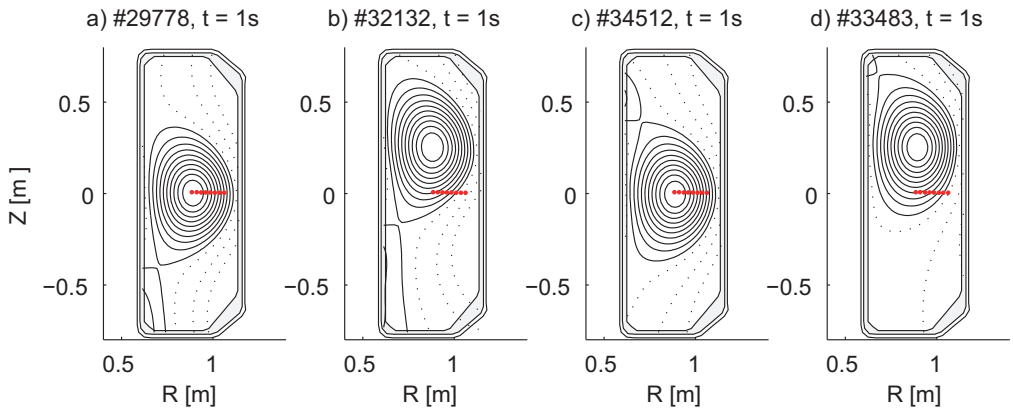

Figure 6.1: Examples of magnetic configurations obtained in TCV for the study of plasma rotation in diverted configuration discharges. From left to right: LSN, LSN at $Z_{mag} = 23$ cm, USN and USN at $Z_{mag} = 23$ cm. The measurement points of CXRS04 diagnostic are depicted as red spots.

δ	0.6
κ	1.6
a	0.21 m
I_p	$\pm 170 \div 290$ kA
q_{95}	$3.2 \div 6.5$
$n_{\mathrm{e,av}}$	$2 \div 6.5 \times 10^{19}\,\mathrm{m}^{-3}$

Table 6.1: Range of main plasma parameters covered in the experimental study of rotation in diverted discharges.

that have been used in present work. It is important to notice that the absence of a divertor may complicate the comparison with observations from other tokamak devices. For example, in TCV the outboard and inboard divertor legs are typically of different length, that corresponds to a substantially different plasma-wall connection length, a parameter that has a large impact on parallel fluxes in the Scrape Off Layer (SOL), and that strongly influences the recycling properties [18].

In the study of the diverted configuration, we considered plasmas with relatively fixed shape, within the uncertainty of the equilibrium reconstruction, with little variation of triangularity around $\delta = 0.6$ and elongation around $\kappa = 1.6$. The reference parameters for the discharges presented in this chapter are summarized in Table 6.1. The eventual shape effects in diverted configuration, that could be relevant for instance for $\delta < 0$ or H-mode experiments, have been left for the following studies.

As for diverted configuration, the poloidal component of magnetic field is zero at the null point, the safety factor q_e at $\rho_\psi = 1$ goes to infinity. In this case, in order to characterize the magnetic configuration, the value of the safety factor where the poloidal flux is at the 95% of its maximum is typically used, indicated in the following with q_{95}.

It is well established that the direction of the $\vec{B} \times \nabla B$ with respect to the null point position has a strong impact on the input power threshold to access the H-mode confinement regime. When the drift points towards the X-point the threshold is lower, and the configuration is said *favorable*. Viceversa when the $\vec{B} \times \nabla B$ drift points away from the X-point the configuration is said *unfavorable*.

Favorable or unfavorable configurations are determined by B direction and X-point position, and in TCV both can be, and has been, set independently, similarly to what was done in [76]. Furthermore, in analogy to what presented in previous chapters, the same configuration has been obtained at $Z_{mag} = 23$ cm (see Fig. 6.1), to obtain high resolution measurements of edge rotation

combined with edge SOL parallel fluxes away from the midplane.

To facilitate the comparison of observations obtained with both fields directions, **within this chapter positive and negative toroidal velocities will correspond respectively to co and counter current toroidal rotation.**

6.2 Toroidal rotation dependence on plasma density

The effect of plasma density on u_ϕ profile has been studied in shot by shot density scans, in stationary discharges. Here the plasma current was kept at $I_\mathrm{p} \approx 250$ kA ($q_{95} \approx 3.6$), while the target density was changed from $n_{\mathrm{e,av}} = 2$ to $8 \times 10^{19}\,\mathrm{m}^{-3}$.

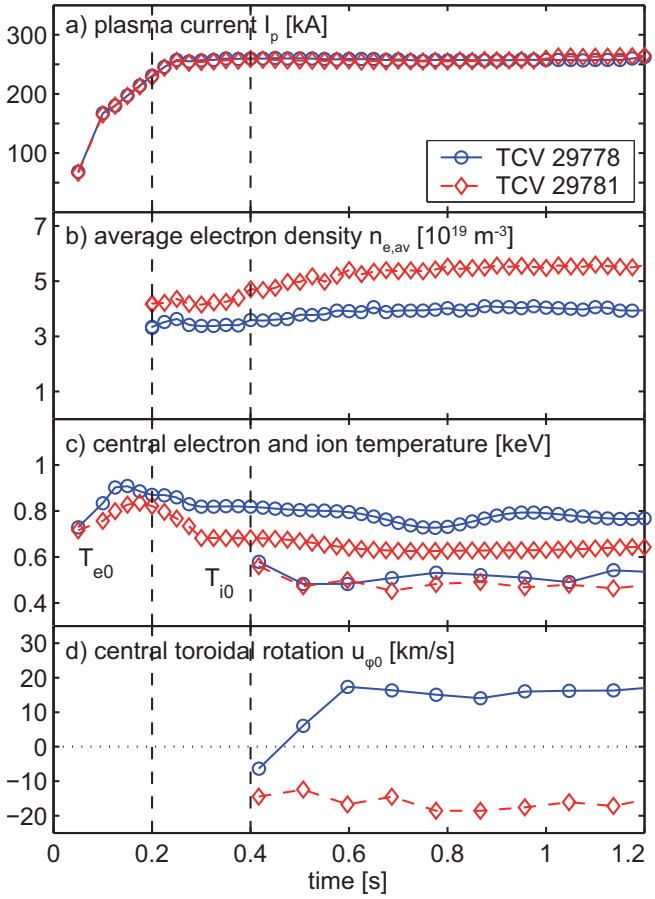

Figure 6.2: Main parameter traces of two LSN discharges at $I_\mathrm{p} = +260$ kA, $B_\phi = +1.42$ T, at different target densities ($n_{\mathrm{e,av}} = 4.0, 5.5 \times 10^{19}\,\mathrm{m}^{-3}$). The vertical dashed lined mark the time window for the divertor formation.In diverted configuration the stationary core rotation is positive (co current) for the lower n_e and negative (counter current) for higher n_e.

Let us start by describing the discharge evolution observed during the diverted discharges. In Fig. 6.2 the time traces of some plasma parameters for two discharges at $n_{\mathrm{e,av}} = 4$ and $5.5{\times}10^{19}\,\mathrm{m}^{-3}$ are shown. The divertor formation starts at $t = 0.2$ s (before the plasma boundary is limited on the central column) and the divertor is completely formed at $t = 0.4$ s. Electron density and temperature reach the target values at $t = 0.5$ s, that are then maintained during the I_p flat top. The CXRS measurement start at $t = 0.6$ s, with a sample period of 90 ms (integration time $\Delta t_{exp} = 30$ ms). At this time in both discharges plasma core is found to rotate in the counter

current direction (negative values). However, while for the higher density discharge the plasma maintains the rotation value all along the discharge, in the low density discharge the core u_ϕ evolves towards positive values, and a stationary rotation of 12 km/s in co current direction is reached at $t = 0.8$ s. This observations already illustrate the key role of density in determining the plasma rotation and the different phenomenology that characterize the diverted configuration compared to the limited.

During this thesis we addressed the issue of momentum transport from both dynamical and steady state analysis. Letting the first for the chapter 7, we devote this chapter to the results obtained by the study of the stationary rotation. In the following we will consider stationary u_ϕ profiles as profiles averaged on the relaxed phase, typically $300 \div 600$ ms, corresponding to 4-6 CXRS profiles.

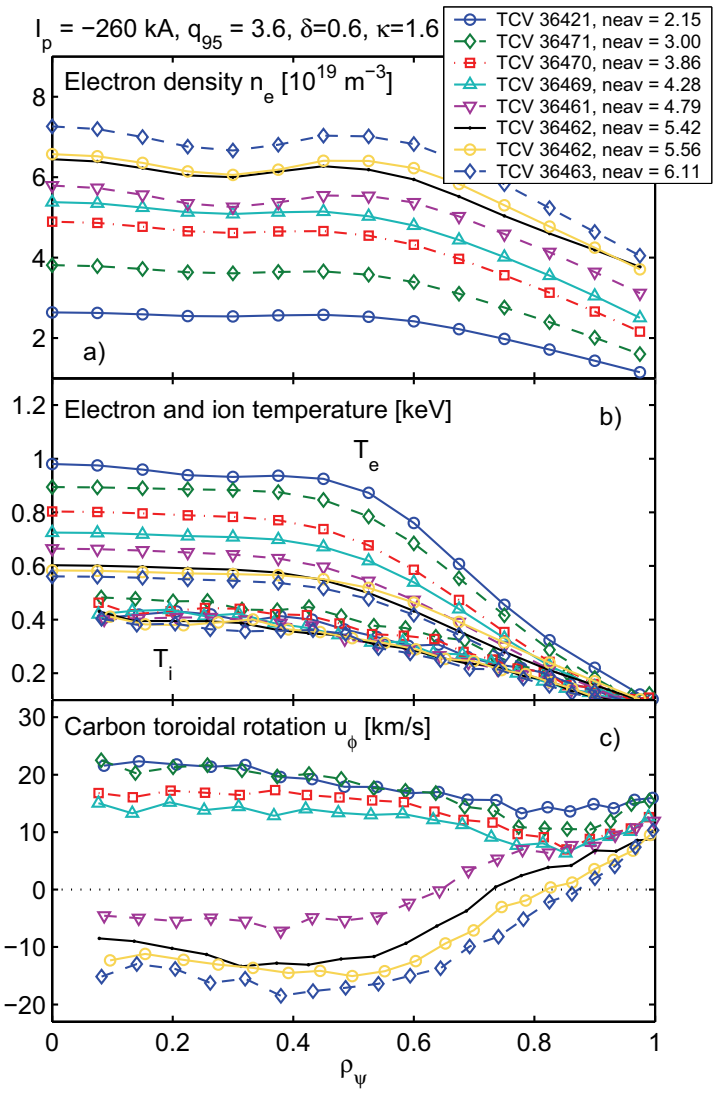

Figure 6.3: Radial profiles of electron density, electron and ion temperature and carbon toroidal rotation in stationary phases of LSN discharges. Electron and ion measurements from Thomson scattering and CXRS09 diagnostics respectively. Positive values indicate co current rotation.

Figure 6.3 shows the stationary density, temperature and rotation profiles for a series of plasma discharges with same target values $I_p = -260$ kA, $\delta = 0.6$, $\kappa = 1.6$, in LSN diverted configuration. In these graphs each profile corresponds to a profile averaged on a time window of $\Delta t = 150 \div 500$ms

where the plasma parameters showed no substantial evolution. Positive values of rotation indicate co current rotation. Experiments summarized here were performed with negative direction of B_ϕ and I_p which, for these LSN discharges, correspond to *favorable* $\vec{B} \times \nabla B$ configuration.

Toroidal plasma rotation was measured with the CXRS09 diagnostic. The low active signal due to the low impurity content inherent of diverted discharges was counteracted by binning couples of channels, so that 20 local measurements cover the LFS mid radius from $\rho_\psi \approx 0.1$ to the LCFS.

We first consider the lowest density discharge, $n_{\mathrm{e,av}} \approx 2{\times}10^{19}\,\mathrm{m}^{-3}$ (blue solid curves in Fig. 6.3): contrary to what was observed in limited configuration discharges with similar target parameters, we find that in stationary conditions the plasma rotates in the co current direction (positive values in the figure) in the whole region covered by the CXRS measurements. Rotation profile is peaking in the co current direction, with $u_\phi \approx 23$ km/s in the center, decreasing to its minimum value ≈ 15 km/s in the region of $\rho_\psi \approx 0.85$. Further out to the LCFS, u_ϕ profile appears flat or slightly increasing, with a positive edge rotation of 15 km/s.

At higher plasma densities ($n_{\mathrm{e,av}} \approx 3 \div 4 \times 10^{19}\,\mathrm{m}^{-3}$), plasma column rotates more slowly, with u_ϕ profile almost rigidly decreasing by ≈ 5 km/s, but maintaining a finite positive rotation gradient $\nabla u_\phi \approx 5$ km/s/m, in the intermediate region. Increasing furthermore n_e a reversal of core toroidal rotation profile is observed: in fact for TCV 36461 at $n_{\mathrm{e,av}} \approx 4.8 \times 10^{19}\,\mathrm{m}^{-3}$ the plasma center is now rotating at -5 km/s, in the counter current direction. This reversal involves the intermediate region $0.5 < \rho_\psi < 0.8$ where the gradient of rotation becomes positive with larger values of $\nabla u_\phi \approx 15$ km/s/m. Notice that the u_ϕ at $\rho_\psi \approx 1$ is still rotating in the co current direction, with values larger than 7 km/s. In the region where the u_ϕ profile crosses zero there is no clear indication of flattening or decreasing of rotation gradient. In the plasma core, the effect u_ϕ is strongly hollowed or bulged in the co current direction. According to the observations in limited discharges this is may be ascribed to the sawtooth activity (here $\tau_{ST} \approx 4 \div 5$ ms, $\rho_\mathrm{inv} \approx 0.4$). DMPX measurements locate the sawtooth inversion radius at $\rho_\psi = 0.5$.

It is useful to summarize the phenomenology just illustrated, following the three regions scheme used in the previous chapters for limited plasmas. The toroidal rotation profile u_ϕ, normalized to the current direction, can be described as (see Fig. 6.4):

Peripheral region, $\rho_\psi > 0.85$**.** Here the toroidal rotation is always co current $u_\phi > 0$, increasing towards the edge $\nabla u_\phi < 0$. Close to the edge u_ϕ decreases with plasma density, but remaining in co current direction even at highest densities.

Intermediate/gradient region, $\rho_\mathrm{inv} < \rho_\psi < 0.85$**.** Here a gradient of u_ϕ builds up, whose sign and amplitude depend on plasma conditions. In particular for $n_{\mathrm{e,av}} \lesssim 4.5{\times}10^{19}\,\mathrm{m}^{-3}$ negative ∇u_ϕ is found, u_ϕ peaks in co current direction. Conversely, for $n_{\mathrm{e,av}} \gtrsim 4.5{\times}10^{19}\,\mathrm{m}^{-3}$ ∇u_ϕ is positive and u_ϕ peaks in the opposite counter current direction, with larger absolute values.

Sawtooth region, $\rho_\psi < \rho_\mathrm{inv}$**.** Here the u_ϕ profile is determined by the sawtooth activity, that tends to bulge u_ϕ in the co current direction. At low and high density respectively, the core u_ϕ profile is hollow or slightly peaking by up to 5 km/s.

Some qualitative but important remarks come out from these first observations. First of all, in the peripheral region u_ϕ exhibits a strong dependence on density that is not observed in standard limited discharges, where u_ϕ appears to be constrained close to zero. This aspect is of primary importance in both transport modeling and extrapolation to fusion performance: in fact, in absence of external torques, for a given type of momentum transport (e.g. dominated by an inward momentum pinch), the absolute value of toroidal rotation, which is thought to be important for

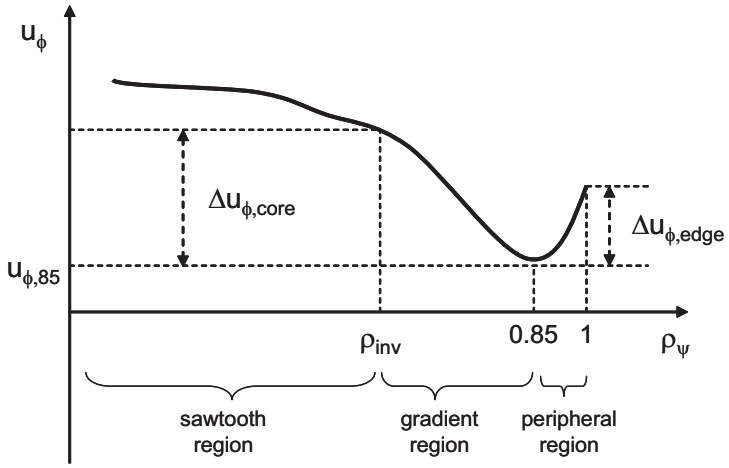

Figure 6.4: Schematic representation of the toroidal rotation profile in Ohmic L-mode plasmas in diverted configuration. Values increases in the co current direction co current rotation.

Resistive Wall Mode stabilization [100, 106, 107] and/or enhancement of energy confinement [108], is determined by the velocity at the plasma boundary.

Secondly, there is no evidence of a smooth transition between low and high density discharges: in fact, in stationary conditions, the gradient of toroidal rotation in the intermediate region ∇u_ϕ, which represent the peaking of the u_ϕ profile, is found either positive or negative. In this sense, we can talk of different rotation regimes, which are likely to be the result of a different combination of physics mechanisms. Furthermore, as it will be shown clearly in next sections, differently from what found in limited reversal discharges, a density threshold was not identified. Instead in a broad range density $2 \lesssim n_{\mathrm{e,av}} \lesssim 4 \times 10^{19}\,\mathrm{m}^{-3}$ both positive or negative peaking discharges were found (see e.g. Fig. 6.9).

As a consequence of the variability of u_ϕ in the peripheral region, edge rotation may be positive (co current rotation) while the core is rotation negative (counter current rotation) due to a positive ∇u_ϕ in the intermediate region. To avoid ambiguity, in the following we will refer to co/counter current rotation regime with reference to the u_ϕ peaking direction. With this convention the co current regime corresponds to $\nabla u_\phi < 0$, independently on the sign of u_ϕ.

6.3 Toroidal rotation dependence on plasma current

The effect of the plasma current has been addressed with a shot by shot current scan at the reference density of $n_{\mathrm{e,av}} \approx 3.5 \times 10^{19}\,\mathrm{m}^{-3}$. The current range that could be explored without incurring in strong MHD was relatively small, covering $I_\mathrm{p} = 200 - 290$ kA ($q_{95} = 6.5 \div 3.2$).

Figure 6.5 shows the rotation density and temperature profiles for a set of six Lower Single Null discharges performed at approximately the same density of $n_{\mathrm{e,av}} \approx 3.5{\times}10^{19}\,\mathrm{m}^{-3}$ but at different plasma currents $I_\mathrm{p} = 220, 260, 250, 290$ kA ($q_e = 6.3 \div 3.4$). Here I_p and B_ϕ were positive, that is *favorable* $\vec{B} \times \nabla B$ direction. These graphs combine data from both CXRS04 and CXRS09 diagnostic configurations: for older discharges, only 8 CXRS measurements were available, that did not cover the peripheral region.

A strong effect of I_p on u_ϕ profile is observed. At lowest I_p the plasma rotates counter current, with u_ϕ peaking in the counter current direction. With increasing I_p (decreasing q_{95}) u_ϕ profile appears to shift rigidly towards positive values, following the increase of rotation in the region $\rho_\psi \approx 0.8$, but maintaining a positive gradient in the intermediate region. u_ϕ in the core appears flattened by sawtooth activity, whose effect enlarges as ρ_{inv} increases, as visible in the figure, from

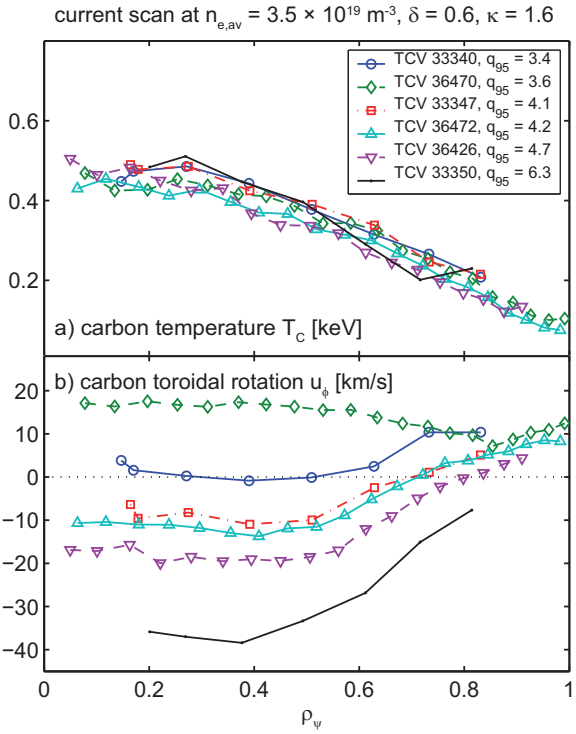

Figure 6.5: Stationary u_ϕ profiles for a group of plasma discharges at approximately the same density $n_{\mathrm{e,av}} \approx 4 \times 10^{19}\,\mathrm{m}^{-3}$, but at different currents $I_\mathrm{p} = 220, 260, 250, 290$ kA ($q_e = 6.3 \div 3.4$).

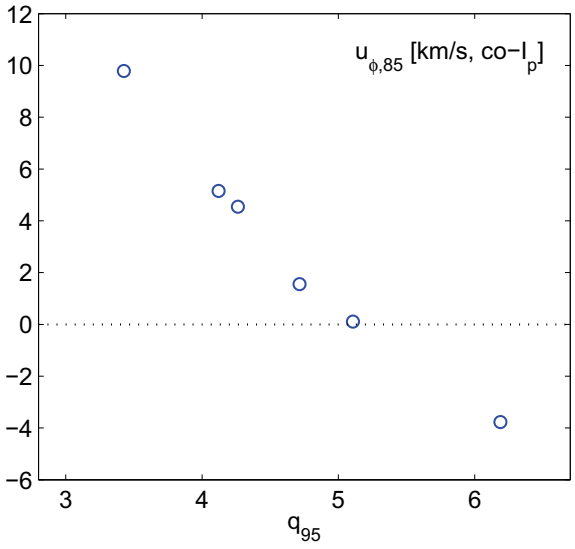

Figure 6.6: Toroidal rotation at $\rho_\psi = 0.85$ for the group of discharges in Fig. 6.5.

$\rho_{\mathrm{inv}} \approx 0.3$ (TCV 33350) to $\rho_{\mathrm{inv}} \approx 0.6$ (TCV 33340). It is remarkable that for the high edge rotation combined with large ρ_{inv}, resulting in a fully co rotating plasma, even u_ϕ peaking persists in counter I_p direction. This sequence of discharges and in particular TCV 33340 represent a strong evidence that the convective part of momentum transport (pinch) has a minor role in sustaining the plasma rotation gradient in TCV. If this was not the case, a substantial variation of ∇u_ϕ would be observed in the intermediate region as u_ϕ varies for positive and negative values.

At high I_p ($q_{95} = 3.6$) a reversal of u_ϕ peaking is observed (TCV 36470), with a negative ∇u_ϕ developed in the radial intermediate region, $\rho_\psi < 0.75$. Notice that for very similar plasma condi-

tions (TCV 33340) the same toroidal rotation is observed at $\rho_\psi \approx 0.75$. Furthermore measurements in the peripheral region, available with the upgraded CXRS09, shows that, for $\rho_\psi > 0.85$, u_ϕ increases with ρ_ψ similarly to lower I_p discharges (TCV 36472). This observations suggest a change in the balance of toroidal momentum drives localized in the core.

A remarkable result comparing with limited plasma configuration is that in diverted discharges the toroidal rotation in the peripheral region can vary following the plasma current. This is clearly visible in Fig. 6.6, where the toroidal rotation $u_{\phi,85}$ at $\rho_\psi = 0.85$ is plotted against q_{95}, pointing out an approximately linear trend.

6.4 MHD activity

Before entering into details of the analysis of the collected rotation database, we devote some attention at the MHD properties. These discharges often show some level of MHD activity, which is affected by the density change. Fig. 6.7 shows four spectrograms of a magnetic Mirnov coil for four repetitions of the same discharge at increasing target density. The core rotation regime is indicated in the label box. The corresponding toroidal rotation profiles are shown in Fig. 6.8 (right column).

At the lowest density, with u_ϕ peaking in the co current direction, low or negligible MHD activity is observed. An increasing activity is visible with increasing density. The spectral analysis indicates that, similarly to discharges in limited configuration, here again two modes are present, a [2,1] peripheral mode together with the [1,1] sawtooth precursor, at lower frequency. The increase of density corresponds to an increased frequency of *both* modes ($\Delta f_{MHD} \approx 2$ kHz increasing $n_{\mathrm{e,av}}$ from 2.1 to $4.2 \times 10^{19}\,\mathrm{m}^{-3}$). This is coherent with the increase, in counter current direction, of the entire rotation profile, that follows from the edge rotation scaling with density (Fig. 6.8).

Notice that, likely due to the relatively large Doppler contribution coming from the poloidal rotation, the MHD frequency is always observed positive, that is it does not goes to zero at the velocity reversal.

At this stage it is difficult to prove or discard a causality link between observations of MHD frequency and plasma rotation, in particular concerning the reversal of core rotation. However, it can be noticed that the appearance and increase of MHD activity at increasing density is a common observation in TCV, which is seen similarly in both limited and diverted discharges. Furthermore, in low density discharges, with little or negligible MHD activity, limited and diverted plasmas are observed to rotate in opposite directions, suggesting that an intrinsic drive exists, which, independently from the MHD, can generate both co and counter rotation in the core.

Notice that in TCV strong impact of MHD modes on the rotation profile is observed only in presence of modes of amplitude comparable with minor radius or locking modes, eventually preluding to disruption [49].

These remarks, together with the fact that MHD frequency appears to be coherent with a MHD perturbation transported by the background plasma, suggest that for the discharges considered in this work, the MHD modes may not perturb significantly the plasma rotation profile.

6.5 Magnetic configuration and edge rotation

A key feature of intrinsic toroidal rotation in diverted configuration is the strong dependence of u_ϕ on the peripheral region ($\rho_\psi \gtrsim 0.85$) on n_e and I_p. The question arises to identify the physics mechanisms responsible for this. From the experimental approach, first of all, we tried elucidate to which extent the toroidal rotation in the peripheral region is affected by the interaction with the strong particle flows present in the Scrape Off Layer region [75]. A coupling between SOL flows

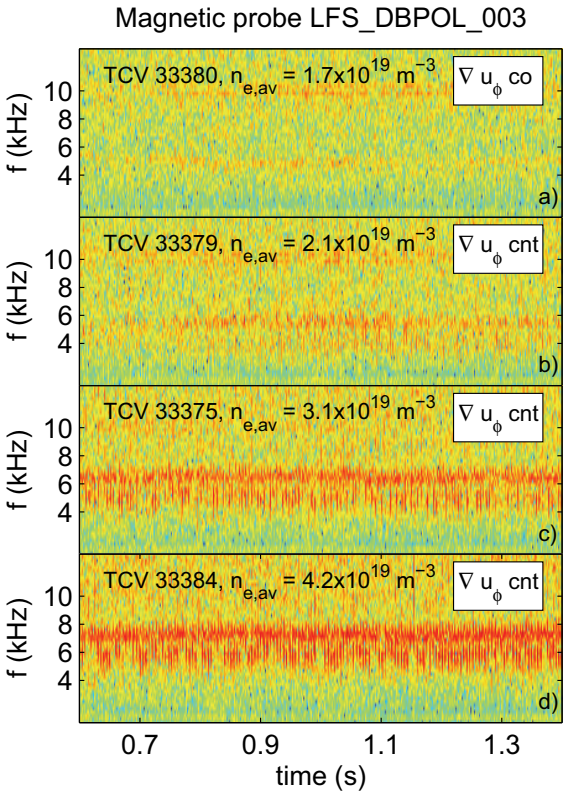

Figure 6.7: Spectrograms of the signal of a Mirnov coil, for four quasi stationary discharges with increasing plasma density. The toroidal rotation regime is indicated in the label box.

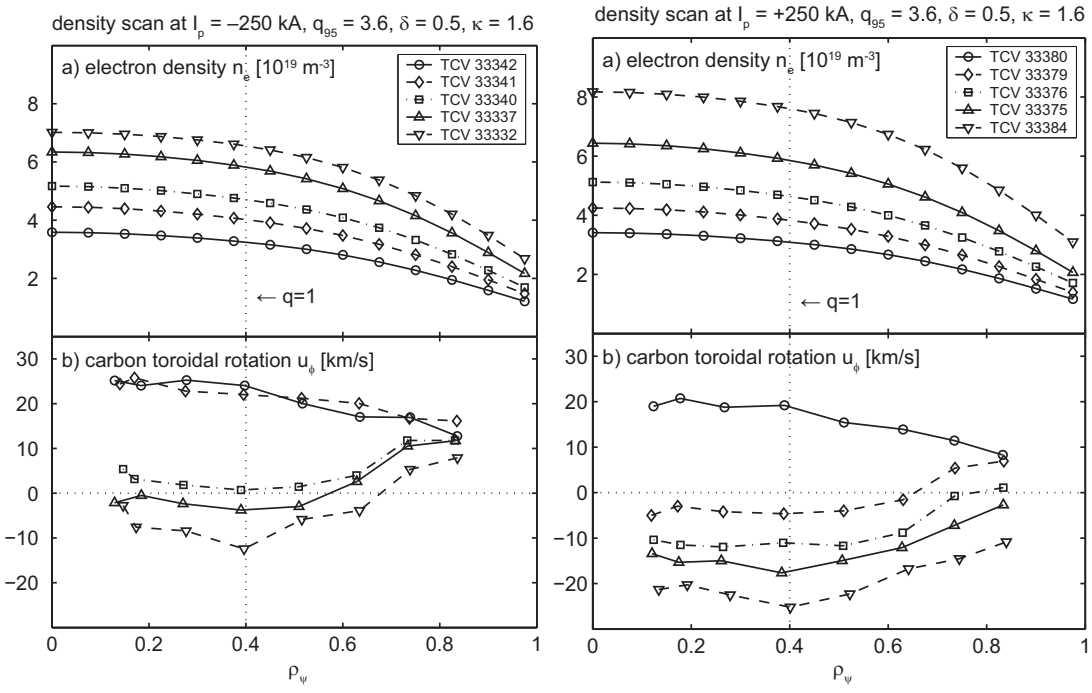

Figure 6.8: Stationary u_ϕ profiles from the CXRS04 diagnostic in two series of LSN discharges at different target $n_{\mathrm{e,av}}$. Discharges in left column were performed with I_p,B_ϕ<0 (favorable configuration). Discharges in right column were performed at I_p,B_ϕ>0 (unfavorable configuration).

and core rotation is somehow a natural expectation, and indeed signs of it have been observed in other tokamak devices, in particular in Alcator C-mod [76,109].

As SOL fluxes are sensitive to the magnetic configuration, and in particular to $\vec{B}\times\nabla B$ [80,110], we measured the toroidal rotation profile in TCV discharges in different configurations, varying the plasma current direction and null point position. The plasma vertical position has also been varied to obtain measurements in positions off from the LFS midplane. To illustrate the results we consider two series of LSN discharges, in favorable and unfavorable configurations, where n_e was varied keeping the other parameters fixed (Figure 6.8).

The main elements of the behavior depicted in previous paragraphs are visible. For both configurations two rotation regimes are found, with the rotation gradient peaking in the co current direction at low density and in the opposite direction at high density. Going from high to low density the edge rotation increases, and the rotation profile appears to follow rigidly, with a tendency to saturation for the negative current case. This peripheral rotation dependence on density is summarized in Fig. 6.9. In the graph, the value of u_ϕ at $\rho_\psi = 0.85$ for each discharge is plotted as a function of average plasma density $n_{e,av}$. The different markers distinguish favorable and unfavorable ion drift configurations (here only LSN discharges are included), color of data points distinguishes the rotation regime as co or counter core rotation.

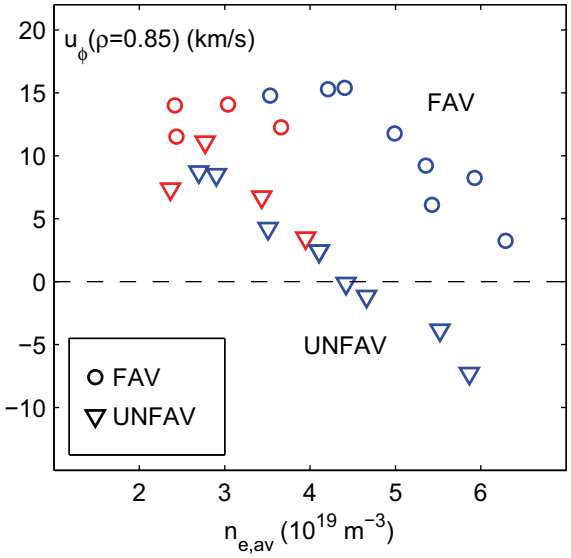

Figure 6.9: The outermost rotation values $\rho_\psi \approx 0.85$ are shown for the stationary rotation profiles of diverted discharges for both favorable (FAV, circles) and unfavorable (UNFAV, triangles) ion drift directions. At lower densities, the toroidal rotation at the center saturates at ≈ 15 km/s. Both rotation values decrease with plasma density with the favorable discharges rotating 10 km/s faster in the counter current direction than the unfavorable configurations, for a given plasma density.

Some important aspects emerge from these results:

- Edge rotation decreases with n_e almost linearly, for both configurations, with a tendency to saturate for the favorable configuration for $n_{e,av} < 3\times10^{19}\,\mathrm{m}^{-3}$ at $u_\phi \approx +15$ km/s.
- For $n_{e,av} > 3\times10^{19}\,\mathrm{m}^{-3}$, favorable and unfavorable configurations are characterized by edge rotation different by an off-set value of 10 km/s, with favorable configuration plasmas rotating faster.
- The value of the rotation in the peripheral region is weakly dependent on the rotation regime of the core. In fact, points in Fig. 6.9 align regardless of the peaking direction of u_ϕ, indicated

by the color. This suggests that the rotation in the peripheral region is determined by some local physic mechanism, possibly independently from the core rotation.

- Co and counter rotation regimes in the core may be obtained for the same values of $u_{\phi,85}$ in the edge (same density), indicating that the transition to co rotation in the core is not induced by a change in the boundary rotation.

Let us first address the decrease of rotation in counter direction with increasing n_e. This observation suggests some sort of coupling with parallel fluxes in the SOL which, in the very same discharges, have been measured by Mach probe at the LFS midplane. In fact, the measured ion fluxes are directed along the field lines in the co current direction, with values of the order of the ion sound speed $c_s = \sqrt{(T_i + T_e)/m_i}$. A strong density dependence is also observed with $M_\parallel = u_\parallel/c_s \approx 3$ at $n_{e,av} = 2{\times}10^{19}\,m^{-3}$, that decreases to values close to $n_{e,av} = 6{\times}10^{19}\,m^{-3}$ [18,75]. A direct comparison between SOL fluxes and the toroidal rotation measured by CXRS in the peripheral region is nevertheless not straightforward. First of all in these discharges, CXRS04 diagnostic and Mach probe measurements are radially separated by 2 cm. Secondly, the two measurements refer to different ion species (D and C) that may, in principle, have different fluxes: the difference is estimated by the neoclassical theory [38], and is proportional to the pressure gradient and scales with the inverse of n_e. Due to the relatively low plasma velocities measured on TCV, Δu_ϕ might be comparable with measured C velocity in the core plasma, where main ions are in banana regime. However, in the region close to plasma edge, where main ions are in the Pfirsch-Schlüter regime, the difference tends to vanish [38], as indicated by neoclassical estimates presented in chapter 4.

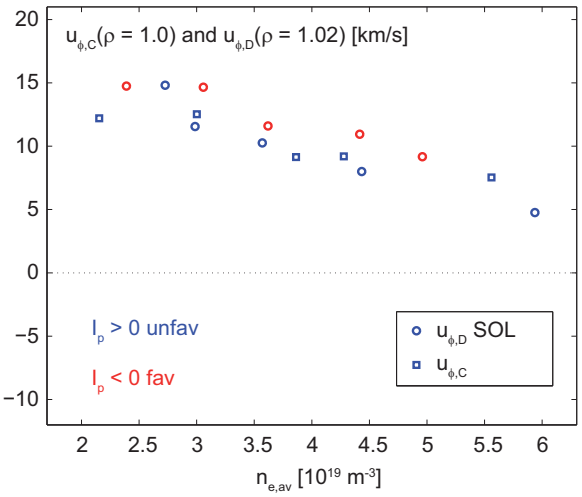

Figure 6.10: Edge carbon toroidal rotation compared with toroidal component of main ion SOL flows, both measured at LFS midplane, for two series of LSN discharges, as a function of average plasma density. Positive values indicate co current flow. CXR09 data are for $I_p < 0$ only.

Unfortunately, the combined measurement of SOL and CXRS09 (covering the edge region) was not possible during this thesis work as the reciprocating probe was dismounted before the CXRS upgrade. Nevertheless, measurements by the two diagnostics can be compared considering a series of similar discharges. The comparison needs some care. First of all, the plasma equilibrium and main parameters have to be as similar as possible. Second, the last radial measurement point for such discharges is at $\rho_\psi = 1$, but due to the geometry of chords and DNBI the measurement is actually spread over a radial range of ≈ 5 mm, across the LCFS. Hence we compare the outermost u_ϕ measurement with the flux in SOL averaged in the region $4 \div 7$ mm from the LCFS. To make

the comparison the fluid velocity must be derived from the Mach number, which is done assuming $T_\mathrm{i} = T_\mathrm{e}$ in the SOL, with the latter given by Mach probe. Finally, the toroidal projection of parallel flows must be taken. The resulting toroidal flows in the SOL are plotted as a function of $n_\mathrm{e,av}$ in Fig. 6.10, together with u_ϕ at $\rho_\psi = 1$ measured by CXRS.

A remarkable agreement is found between the two sets of measurements, which describe the same trend, with approximately the same absolute values of plasma density. It is also remarkable that in proximity of plasma edge, carbon and main ion toroidal velocities are similar ($\Delta u_\phi < 2$ km/s), within the uncertainty of the measurement. The core rotation profile appears to connect continuously with the SOL fluxes (at least at LFS midplane, where the measurements where taken), reinforcing the idea of a coupling between core and edge physics.

Notice that, while at the time of writing only negative current discharges where measured with the CXRS09 diagnostic, the SOL flows measurements considered here were performed at LFS midplane for both positive (blue) and negative (red) plasma current (in the same LSN magnetic configuration) with very similar results. The results in Fig. 6.10 suggest that also toroidal rotation at $\rho_\psi = 1$, at LFS midplane, is little sensitive to I_p direction (and/or $\vec{B} \times \nabla B$ direction). This hypothesis will be confirmed or discarded through planned TCV experiments, where the rotation in the peripheral region will be measured with the CXRS09 diagnostic for reversed direction of I_p and B_ϕ.

The u_ϕ decrease with density at $\rho_\psi = 1$ spans from 15 to 5 km/s, and cannot alone account for the trend observed at $\rho_\psi = 0.85$ (Fig. 6.9). This reflects the fact that in the $0.85 < \rho_\psi < 1$ region, a steep positive gradient of u_ϕ is present, independent on the rotation regime inside $\rho_\psi = 0.85$. This increase in the co current direction in the peripheral region can be characterized by the quantity $\Delta u_{\phi,85} = u_\phi(1) - u_\phi(0.85)$ (see Fig. 6.4), which is a coarse estimate of the u_ϕ gradient in the peripheral region. Figure 6.11 shows $\Delta u_{\phi,85}$ as a function on $n_\mathrm{e,av}$ for a series of plasma discharges in LSN favorable configuration (profiles in Fig. 6.3). For these diverted discharges, $\Delta u_{\phi,85}$ varies from zero (low density, flat u_ϕ near the edge) to 9 km/s at the largest densities explored, with a clear trend which is insensitive on core rotation regime.

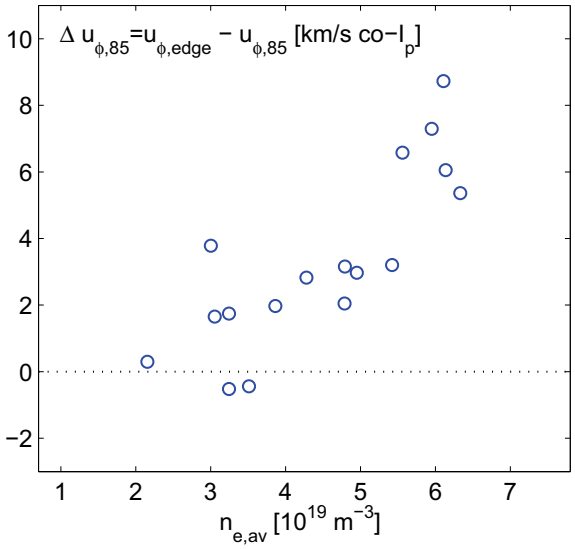

Figure 6.11: Differential toroidal rotation between $\rho_\psi = 1$ and $\rho_\psi = 0.85$, as a function of $n_\mathrm{e,av}$ for a group of discharges at $I_\mathrm{p} = -260$ kA. A strong gradient of u_ϕ develops in the peripheral region with increasing density.

To summarize, experimental evidence coming from the combined analysis of CXRS09 mea-

surement in the peripheral region and the Mach probe measurements of parallel flows in the SOL indicates that, at the midplane, the toroidal rotation close to the edge is linked to the SOL parallel fluxes. The value of u_ϕ at $\rho_\psi = 0.85$, results from the combination of SOL fluxes and rotation gradient in the peripheral region, both roughly linearly decreasing with plasma density.

6.5.1 A possible explanation for configuration off-set

The comparison between SOL fluxes and CXRS rotation measurements across the LCFS showed a strong coupling between SOL and edge flows at LFS midplane. At the same time, measurements suggest that the mechanism producing favorable/unfavorable toroidal rotation off-set at $\rho_\psi = 0.85$ (Fig. 6.9) is not related to the flows at the LFS midplane. Rather, its effect develops in the peripheral region $0.85 < \rho_\psi < 1$.

Among the mechanisms that could produce such an effect, we propose, as a first working hypothesis, a poloidal asymmetry in the toroidal rotation in the peripheral region, induced by the poloidal asymmetry of parallel fluxes in the Scape-Off Layer.

In TCV, the poloidal variation of SOL fluxes has been measured by Reciprocating Mach Probe (RCP) at the LFS [18, 75]: a ballooning component was identified, which becomes stronger away from the LFS midplane. In other experiments [76], SOL fluxes have also been measured with Mach probes at the HFS, finding a ballooning component which becomes dominant. Furthermore, the ballooning component changes direction (respect to I_p direction) passing from *favorable* to *unfavorable* configuration [76]. Assuming that u_ϕ at the edge strongly couples with SOL fluxes all around the plasma boundary, a poloidal asymmetry on u_ϕ is expected at the plasma edge ($\rho_\psi \approx 1$). In the plasma core, the asymmetry is smoothed out by the strong parallel viscosity, that make $\omega_\phi = u_\phi/R$ approximately constant on flux surfaces. Nevertheless, this poloidal asymmetry of edge rotation may penetrate into the peripheral plasma. The change of direction (respect to I_p) of ballooning component of SOL flows, present especially in HFS SOL, passing from favorable to unfavorable configuration, could then reflect on the toroidal rotation in the peripheral region, and engender the configuration off-set in $u_{\phi,85}$.

This working hypothesis was not tested experimentally during this thesis, because of lack of both SOL fluxes and CXRS measurements in the HFS plasma. Nevertheless we observe that:

- Assuming the parallel flows at the HFS to be of the same order of magnitude or larger than the fluxes at LFS midplane, and dominated by the turbulent part, the expected difference in core rotation would be coherent (direction and magnitude) with $u_{\phi,85}$ rotation measurements.

- In TCV, the ballooning component of fluxes roughly scales with $n_{\mathrm{e,av}}^{0.5}$ as indicated by RCP measurements out of the midplane ($Z_{mag} = \pm 23$ cm) [18]. This is consistent with the fact that the configuration off-set increases with density.

- For limited discharges the configuration off-set is not present, as it would be expected, since in that case plasmas are typically up-down symmetric and the effect of ballooning fluxes in the upper plasmas are compensated by fluxes in the lower plasma.

- Experimentally, measurements of SOL flows at LFS midplane, where ballooning component is minimal, found no difference for diverted and limited discharges.

Even if these qualitative arguments support the hypothesis of a role of HFS flows in determining the rotation profile in the peripheral region, at present stage this remains a speculation. An experimental test could come in the next TCV experimental campaigns, when HFS measurements with the CXRS09 diagnostic will complete the acquired data set.

6.6 Core rotation

After discussing the u_ϕ behavior in the peripheral region, we focus now on the intermediate and core region. Concerning the core region, we already observed that the effect of sawtooth instability dominates the rotation inside $\rho_{\rm inv}$. In fact from Fig. 6.8 it appears that, under the periodical activity of sawtooth crashes ($\tau_{\rm ST} \approx 4$ ms), u_ϕ profile develops a slight peaking in the co current direction inside $\rho_{\rm inv} \approx 0.4$. This feature is common to both diverted and limited discharges and is likely to be related to a general effect of magnetic reconnection physics, inducing an inward toroidal momentum flux or a co current torque of some kind. This subject will be addressed in detail in chapter 8.

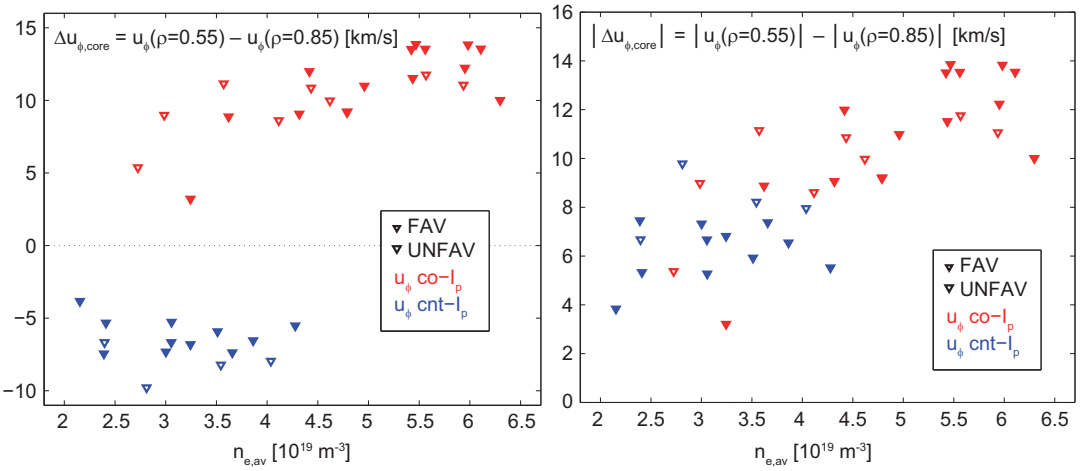

Figure 6.12: The quantity $\Delta u_{\phi,core} = u_\phi(0.55) - u_\phi(0.85)$ estimates the peaking of toroidal rotation profile in the *intermediate* region. Left graph shows $\Delta u_{\phi,core}$ as a function of $n_{\rm e,av}$. Right plot shows $|\Delta u_{\phi,core}|$. At low density co current and counter current peaking regimes are characterized by similar absolute values of peaking.

Considering the intermediate region, this is where the gradient of u_ϕ builds up. Both density and current scans revealed that different rotation regimes exist depending on plasma parameters, characterized by opposite sign of ∇u_ϕ in the intermediate region. Furthermore, as we will see, in diverted configuration the absolute value of the ∇u_ϕ has a clear dependence on plasma density, differently to what found in the analysis of limited discharges [45].

To illustrate properly these aspects, we consider an extended set of u_ϕ profiles, measured in quasi stationary discharges with $\pm I_{\rm p} \approx 260$ kA ($\rho_{\rm inv} \approx 0.4$) and other parameters as in Table 6.1. This selection collects u_ϕ measurements from CXRS04 and CXRS09 diagnostic configurations, with variable DNBI performance, and therefore variable data quality. To get a robust evaluation of the peaking of u_ϕ profile, we choose the quantity $\Delta u_{\phi,core} = u_\phi(0.55) - u_\phi(0.85)$, which quantifies the rotation increment from the peripheral region to the inner plasma, close to the inversion radius. $\Delta u_{\phi,core}$ is representative of the average ∇u_ϕ in the intermediate region being positive for co current peaking and negative for counter current peaking rotation profile.

Fig. 6.12 (left) shows $\Delta u_{\phi,core}$ for the considered set of discharges, as a function of $n_{\rm e,av}$. Full symbols indicate $I_{\rm p} < 0$, that for LSN means *favorable* $\vec{B} \times \nabla B$ drift; conversely, open symbols indicate $I_{\rm p} > 0$, i.e. *unfavorable* drift. Red and blue points indicate respectively co current and counter current peaking of u_ϕ. Some important aspects emerge:

- Favorable and unfavorable configuration points populate the graph homogeneously, indicating that the magnetic configuration and notably the $\vec{B} \times \nabla B$ direction, which strongly affect u_ϕ in the peripheral region, has weak effect in the intermediate region.

- Positive and negative $\Delta u_{\phi,core}$ are observed in a wide range of densities. Especially below $n_{\mathrm{e,av}} \approx 4 \times 10^{19}\,\mathrm{m}^{-3}$, both co and counter rotation regimes can be observed for very similar plasma discharges. This may be related to the discharge history, and in particular to the density evolution during the divertor formation.

- In counter current regime $\Delta u_{\phi,core}$ increases with $n_{\mathrm{e,av}}$, going from $\Delta u_{\phi,core} \approx 5$ to $\Delta u_{\phi,core} \approx 15$ km/s in the range of explored densities. This variation, even if relatively small in absolute value, corresponds to an increase of ∇u_ϕ of a factor of ≈ 3.

- In co current regime $\Delta u_{\phi,core}$ appears less influenced by $n_{\mathrm{e,av}}$, with $\Delta u_{\phi,core} \approx -7$ for $n_{\mathrm{e,av}} < 5{\times}10^{19}\,\mathrm{m}^{-3}$.

The absolute value of $\Delta u_{\phi,core}$ is presented in Fig. 6.12, right. At low density, from this database there is no clear evidence of a different dependence on $n_{\mathrm{e,av}}$ for the two rotation regimes. It must be considered that values of $\Delta u_{\phi,core} = 4$ km/s are calculated from the difference of two velocities, each with uncertainty of ± 2 km/s, somewhat higher for CXRS04 data.

6.7 Rotation inversion, poloidal rotation and electric field

Toroidal rotation in diverted discharges shows a strong dependence on plasma parameters, with rotation reversal in the core coupled with variable rotation in the peripheral region. Poloidal rotation appears not to be affected by this variability, remaining close to the neoclassical values. Fist of all, we observe here that u_θ measurements in diverted discharges are more challenging than in limited, as the diverted configuration permits a more efficient evacuation of impurities (carbon), resulting in a lower CX signal.

Figure 6.13a compares the poloidal rotation measured in two diverted discharges TCV 33380, 33384 with all plasma parameters similar except for plasma density. The u_θ profiles shown are averaged on time windows $\Delta t \approx 500$ ms. For this substantial change in plasma density ($n_{\mathrm{e,av}} = 2{-}6.5{\times}10^{19}\,\mathrm{m}^{-3}$), the poloidal rotation remains positive, in the electron diamagnetic drift direction (I_p, $B_\phi > 0$). The two profiles are very similar, with values of 2 km/s in the gradient region $0.5 < \rho_\psi < 0.6$, that are comparable to expectation from neoclassical theory. Notice that the u_θ peak observed in the region close to the edge in high density limited discharges, here is not seen. Instead u_θ appears to be close to zero for both high and low plasma density. Given that in neoclassical theory poloidal rotation is mainly driven by ∇T_i (see chapter 3), this could be related to the difference in ion temperature profile in the region across the LCFS, between limited and diverted configurations: in this case the diverted configuration will correspond to a smoother decrease of T_i across the plasma edge. This hypothesis, given the difficulties of measuring the ion temperature in this region, remains unverified.

The u_θ measurements have been combined with the pressure and u_ϕ measurements to provide an estimate of the radial electric field E_r, through the radial force balance equation. The results are illustrated in Fig. 6.13b and c for respectively the lowest and highest density discharges at $I_\mathrm{p} > 0$ in Fig. 6.8 (right column). At low density u_ϕ rotates co current in the core and $u_\phi(0.85)$ is positive, sustaining an E_r profile positive in the core and close to zero for $\rho_\psi > 0.7$, where the u_θ and u_ϕ contributions nearly compensate. In the high density discharge u_ϕ is counter rotating across all the minor radius, hence u_θ and u_ϕ contributions add up, producing a strong and negative E_r across all the minor radius. For these calculation the T_C, n_C, and u_ϕ profiles are extrapolated for $\rho_\psi > 0.85$, and $u_\theta \approx 0$ is assumed for $\rho_\psi < 0.4$.

It is interesting to notice that such a strong change in the radial electric field, in particular in the gradient region $0.5 < \rho_\psi < 0.8$, where the $E \times B$ velocity increases from 3 to 8 km/s, is

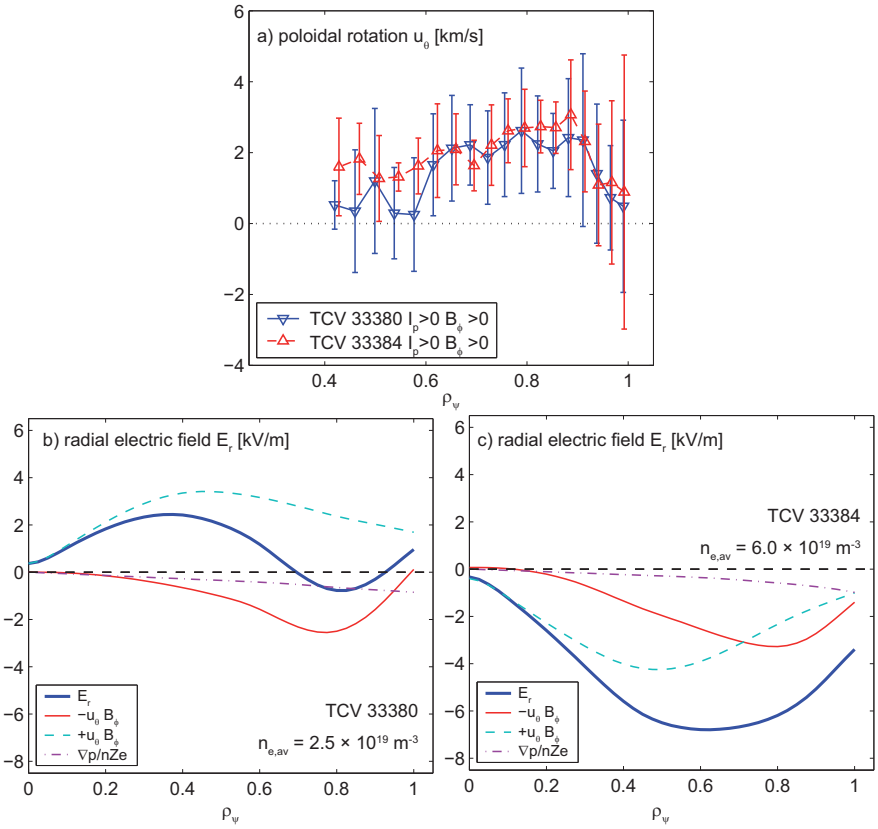

Figure 6.13: a) Poloidal rotation profiles for two diverted discharges at $n_{\mathrm{e,av}} = 2.5$ and $6 \times 10^{19}\,\mathrm{m}^{-3}$. For these discharges u_ϕ is shown in Fig. 6.8. Opposite sign of radial electric field E_r is found in the core in the low (b) and high (c) density, due to the u_ϕ reversal.

not accompanied by enhancement of energy or particle transport. This suggests that the intrinsic velocities of TCV L-mode plasmas, and especially their gradients are typically not sufficient to affect directly the micro turbulence responsible for anomalous transport.

6.8 Phenomenological scaling laws

It is important to provide a phenomenological description of the rotation profile as a function of plasma parameters, for the theory/experiment comparison and for extrapolation to future devices. An important result on this path is represented by the so called "Rice scaling" [20], for the intrinsic H-mode rotation. In [45] a scaling law for the maximal rotation in limited L-mode was proposed from the analysis of first TCV results. An effort was made to formulate a phenomenological law that summarizes the experimental observations for diverted configuration L-mode.

In order to evidence the role of main plasma parameters on core rotation profile, we consider a database of 46 LSN discharges, with positive and negative I_p, at $n_{\mathrm{e,av}} = 2-7 \times 10^{19}\,\mathrm{m}^{-3}$ and other parameters as in Table 6.1. Figure 6.14 summarizes the distribution of some relevant parameters, in order to characterize the coverage of the parameter space and to highlight intrinsic correlation between plasma parameters. To obtain a deeper insight on the underlying physics an extended study is required, to try and decouple physical quantities (e.g. n_e, T_e, T_i, ν_eff and their gradients) that in the present database are strongly correlated (see Fig 6.14).

Hence, our result will represent an *operational* scaling law, that describes the main features of rotation profiles on the basis of operational parameters (I_p, n_e). Of course, departs from the

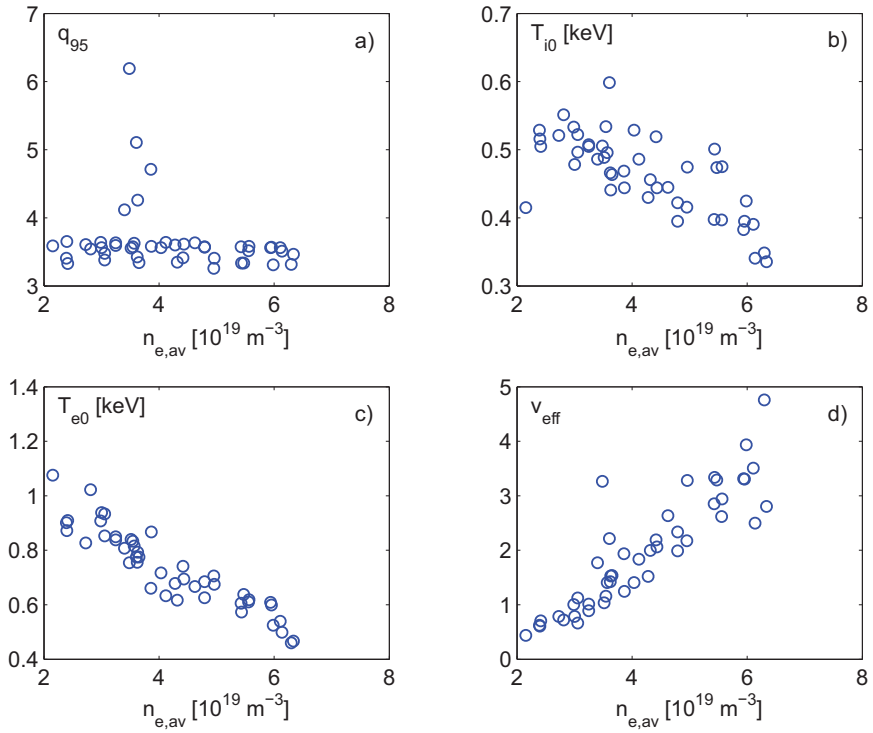

Figure 6.14: Parameters space for the database of stationary u_ϕ in diverted discharges.

law are expected in more complex scenarios as high I_p, high n_e, ECH, ECCD, extremely shaped plasmas.

A simple scaling law in the form proposed in [45] is not suitable for the diverted L-mode plasmas. The reported observations suggest that the different radial regions are characterized by different physics mechanisms, at least the dominating ones, so that a global picture may be drawn by addressing separately three specific regions: edge/SOL, peripheral and intermediate.

6.8.1 Plasma edge ($\rho_\psi \approx 1$)

The SOL flows are well described by the phenomenological law proposed in Horacek's thesis [18] and presented in section 3.9, that combines the different sources of parallel flows, and points out the role of Pfirsch-Schlüter flows at the LFS edge.

For reader convenience we report here the expression of the Pfirsch-Schlüter contribution, reformulated in terms of toroidal rotation, remembering that it may be considered valid for carbon impurity as well:

$$u_{\phi,edge} \approx u_{\phi,PS} = \frac{2q}{B}\mathrm{sign}(I_\mathrm{p}B_\phi)(E_r - \frac{1}{en_e}\frac{dp_i}{dr})[\mathrm{m/s}] \tag{6.8.1}$$

The last term in parenthesis has in the past been measured by the reciprocating probe, but in ordinarily operation is difficult to estimate experimentally. Nevertheless, from results summarized in Fig. 6.10, that is restricting the validity of the conclusions to $I_\mathrm{p} \approx \pm 250$ kA discharges, we can approximate the dependence of edge rotation on plasma density with the linear scaling law:

$$u_{\phi,edge}[\mathrm{km/s}] \approx 18 - 2 \cdot n_{\mathrm{e,av}}[10^{19}\mathrm{m}^{-3}]. \tag{6.8.2}$$

Model	α_0	$\alpha_{n_{\rm e,av}}$	α_{q95}	$\alpha_{T_{i0}}$	$\alpha_{\nu_{\rm eff}}$	RSME
M_1	40.6	-3.07	-5.12			0.22
M_2	2.9		-5.14	6.39		0.38
M_3	24.3		-5.24		0.76	0.25

Table 6.2: Table of the scaling parameters for $u_{\phi,85}$. Models M_1, M_2 and M_3 include different plasma parameters as regression variables.

6.8.2 Peripheral region ($\rho_\psi \approx 0.85$)

Here we formulate a scaling law for $u_{\phi,85}$= $u_\phi(0.85)$, which represents the boundary condition for the rotation profile in the inner plasma region. To be coherent with the linear parametric dependencies with density and current that emerged separately from reported observations, scaling law is searched with a multivariate regression in the form:

$$y = \alpha_0 + \alpha_1 x_1 + \alpha_2 x_2 \ldots \alpha_i x_i \ldots \tag{6.8.3}$$

where the x_i are the plasma variables and y is the estimated quantity.

In our case we have $y = u_{\phi,85}$. Different choices of regression variables are possible, more or less related to physics, possibly adimensional. An example of the procedure is found in [111]. The regression was performed on LSN discharges at $I_{\rm p} < 0$ (*favorable* configuration). Table 6.2 summarizes the results of regressions following models with different sets of regression variables, among $n_{\rm e,av}$,q_{95}, T_{i0} and $\nu_{\rm eff}$:

All the proposed models describe reasonably well the experimental data set. This is partially because the variables are strongly coupled, and it is impossible to point out the effect of single (or a combination of) variables with respect to the others. However, excluding q_{95} or $I_{\rm p}$ always leads to unsatisfactory regression. Figure 6.15 shows the results of the M_2 regression: data set is reasonably well reproduced, especially for what concerns the $I_{\rm p}$ dependence. When considering LSN plasmas in *unfavorable* configuration the trend in density is slightly different and we obtain $\alpha_{n_{\rm e,av}} = -3.9$. Finally, we can express the $u_{\phi,85}$ in the form:

$$u_{\phi,85}[\mathrm{km/s}] = 40.6 - (3.45 \pm 0.45)\ n_{\rm e,av}[10^{19}\mathrm{m}^{-3}] - 5.12\ q_{95} \tag{6.8.4}$$

where positive values indicate co current direction, and the plus or minus signs correspond respectively to favorable and unfavorable configuration.

6.8.3 Gradient region ($0.5<\rho_\psi<0.85$)

Considering the gradient region, we try and cast the observations in a scaling law for $|\Delta u_{\phi,core}|$. Differently from what we did for $u_{\phi,85}$ here the scaling is proposed in the power law form:

$$y = \beta_0 x_1^{\beta_1} x_2^{\beta_2} \ldots x_i^{\beta_i} \ldots \tag{6.8.5}$$

with $y = |\Delta u_{\phi,core}|$. Consequently a multivariate logarithmic regression will be applied. A choice of this type is suggested from the scaling law found in limited discharges [45], expressing the coupling between toroidal rotation and ion temperature, which is expected to be recovered in some form. Since for $\Delta u_{\phi,core}$ no relevant difference was observed with respect to magnetic configurations (see section 6.6), we include in our regression discharges from both favorable and unfavorable configurations.

Table 6.3 summarizes the results of regression using models with different sets of regression variables, labeled with model codes. First of all the M_1 model is calculated on a subset of

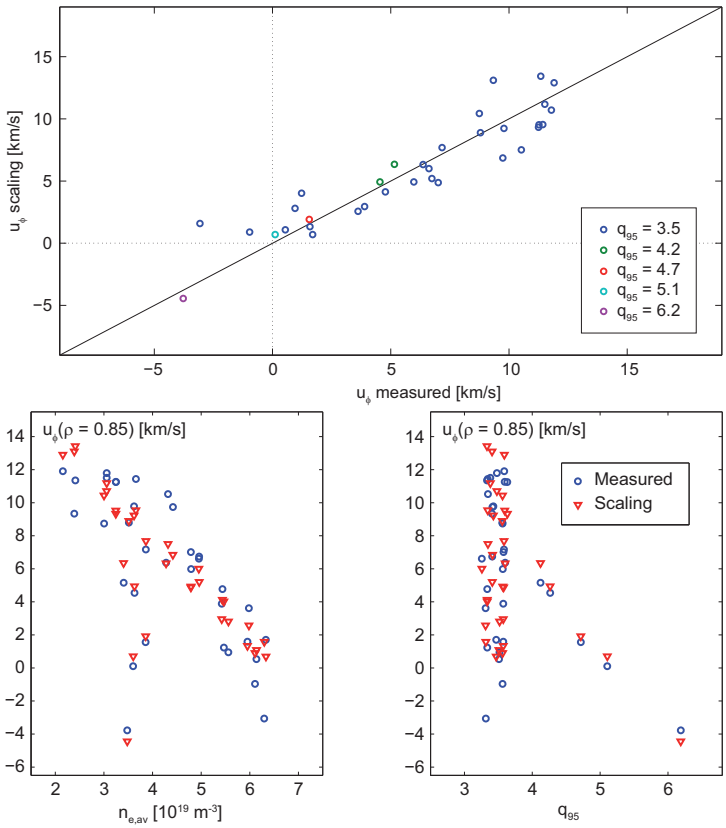

Figure 6.15: Comparaison of $u_{\phi,85}$ measured on the diverted discharge database with the prediction from the scaling law M_2 in Table 6.2. The two quantities are compared as function of $n_{\mathrm{e,av}}$ and q_{95} in the bottom plots.

discharges with constant $n_{\mathrm{e,av}}$ and varying current. The regression corresponds to the scaling for limited discharges, and similarly we found a dependence close to linear in T_{i} but an inverse dependence on I_{p}^2. Notice that this dependence is rather strong and, own to the fact that $\Delta u_{\phi,core}$ is defined outside the inversion radius, it indicates an actual effect on the gradient of u_ϕ. It is also important to notice that within this model with two variables, density variation is not reproducible at all. To obtain a global regression, we include explicitly $n_{\mathrm{e,av}}$ as a regression variable, and obtain the M_2 results (counter current rotation regime only), and M_3 (co and counter current rotation regimes). The dependence on T_{i} and q_{95} remains similar, but a clear dependence (linear or stronger) on plasma density is found, that did not emerged in the former work on limited Ohmic discharges [45].

In Fig. 6.16 the measured velocities are compared with those predicted from the scaling law, demonstrating the quality of the regression, especially accurate in matching the I_{p} scan data.

Model	$\log(\beta_0)$	$\beta_{n_{\mathrm{e,av}}}$	β_{q95}	$\beta_{T_{i0}}$	$\beta_{\nu_{\mathrm{eff}}}$	RMSE	Selection
M_1	12.8		2.1	0.83		0.013	$n_{\mathrm{e,av}} \approx 3.5 \times 10^{19}\,\mathrm{m}^{-3}$
M_2	-4.5	1.5	2.2	1.0		0.028	cnt I_{p}
M_3	-3.9	1.17	2.1	1.040		0.028	all
M_4	-1.4		1.4	0.8	0.55	0.038	all

Table 6.3: Table of the scaling parameters for $\Delta u_{\phi,core}$. Models M_1 to M_4 include different plasma parameters as regression variables.

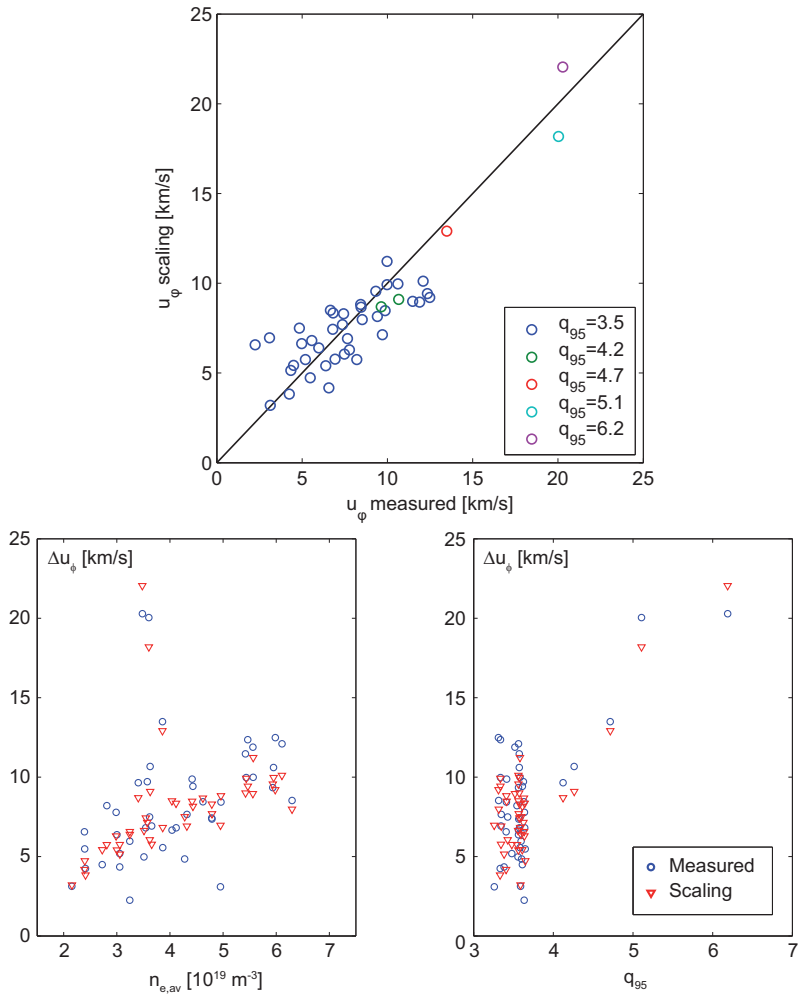

Figure 6.16: $\Delta u_{\phi,core}$ measured in the diverted database plotted against $\Delta u_{\phi,core}$ calculated from scaling law M_3 in Table 6.3. The two quantities are compared as function of $n_{\rm e,av}$ and q_{95} in the bottom plots.

Relatively good regressions can also be obtained with different choices of parameters (M_4 gives an example), but excluding q_{95} or $n_{\rm e,av}$ always leads to unsatisfactory results. We recall that from present database is difficult to extract a precise physics insight, as the regression variables were inevitably coupled (e.g. q_{95} and T_{i0}). On the spirit of providing an operational tool the following form (M_3) is proposed:

$$|\Delta u_{\phi,core}| = \exp(-3.9)\ n_{\rm e,av}^{1.2}\ T_{i0}\ q_{95}^{2.1} \tag{6.8.6}$$

where velocity is expressed in km/s, density in 10^{19}m^{-3} and temperature in eV.

Assuming $n_i \sim n_e$, this form highlights the role of kinetic ion stored energy $W_i = n_i T_i$, reinforcing the similarity with previous results of other devices [20, 112, 113].

6.9 Conclusions

In this chapter we illustrated the main features of stationary rotation in the experimental scenario of diverted discharges in L-mode. A very different phenomenology compared to the limiter case is observed.

First of all, near the plasma edge ($\rho_\psi \approx 1$) the plasma is found to rotate in the co current direction, with values of $5 \div 15$ km/s which vary with plasma parameters. Toroidal rotation

measurements in the peripheral radial region, recently permitted by the CXRS09 diagnostic, have been compared with Mach probe measurements in the LFS SOL: the results indicate a strong coupling between the SOL parallel fluxes and the toroidal rotation close to the edge, suggesting that SOL fluxes, determined by open field line dynamics, act as boundary condition for rotation profile of confined plasma.

In the peripheral region, extending from $\rho_\psi \approx 0.85$ to the plasma edge, the toroidal rotation appears strongly sensitive to the $\vec{B} \times \nabla B$ direction. In particular an off-set of approximately 10 km/s is observed in u_ϕ at $\rho_\psi \approx 0.85$, between discharges in *favorable* or *unfavorable* configuration, otherwise similar. The reason for this difference is not understood yet.

Surprisingly, a different behavior compared to limited plasma is also found in the inner plasma. In diverted configuration too, two rotation regimes are observed at different plasma density, characterized by opposite peaking direction of the toroidal rotation profile. However, at low density u_ϕ peaks in the co current direction, while at high density it peaks in the counter current (opposite behavior compared to limited configuration). The mechanism establishing the rotation regime has not been identified yet. Nevertheless, the observations indicate that the rotation in the peripheral region has no role.

The central part of the plasma is dominated by the sawtooth activity, that, similarly to what found in limited plasma, tends to *bulge* the toroidal rotation profile in the co current direction.

Operational scaling laws have been proposed to describe the observed trends in different radial regions separately. These scaling laws permit the prediction, to a certain degree of confidence, of the rotation profile in future discharges in Ohmic diverted L-mode. The reproducibility of u_ϕ profiles across the years, that emerged by comparing data from the CXRS04 and CXRS09 diagnostics, supports the usefulness of the proposed laws. A remarkable result is that the peaking of the rotation profile in the core plasma is approximately proportional to the product of $n_\mathrm{e} \cdot T_\mathrm{i}$, pointing out the role of ion energy content in the spontaneous acceleration of the plasma columns.

Chapter 7

Toroidal momentum transport

Previous chapters showed how, in TCV, a peaked toroidal rotation profile develops spontaneously in plasma discharges with negligible externally applied torque. In the absence of core momentum deposition or internal momentum sinks, this observation indicates the presence of a non diffusive transport of toroidal momentum from the peripheral region towards the plasma core.

This chapter is devoted to the experimental study of momentum transport, with the scope of characterizing, on the basis of the collected observations, the value of the diffusive and non diffusive momentum fluxes, to be compared to the ones predicted by theory.

The possible approaches to the problem, similar to the one used for energy and particle transport, will be introduced first. Then, the toroidal momentum transport will be addressed from the analysis of both stationary and dynamic experiments. In the final part the possible role of neoclassical and turbulent momentum transport will be discussed.

7.1 Experimental approaches

The temporal evolution of the toroidal rotation profile is described by the radial toroidal momentum transport equation, derived in chapter 3 (Eq. 3.3.5). For the studies presented in this chapter the following simplified form will be used, expressed in cylindrical approximation and neglecting the radial variation of plasma density (all quantities are radial functions averaged over a flux surface):

$$\frac{\partial u_\phi}{\partial t} = \frac{1}{r}\frac{\partial}{\partial r}\left(r\Gamma_\phi(r)\right) + S(r) \tag{7.1.1}$$

$$\Gamma_\phi(r) = -\chi_\phi \frac{\partial u_\phi}{\partial r} + V_\phi u_\phi + v_{th} C_\phi \tag{7.1.2}$$

where Γ_ϕ is the radial flux of toroidal momentum and S includes all the external sources of momentum. Equation 7.1.2 expresses the radial toroidal momentum flux as a sum of three contribution, distinguished on the basis of their dependence on u_ϕ. First term on right hand side accounts for radial diffusivity; second term represents the convective part of the momentum transport, also called "pinch" flux. The third term, where the ion thermal velocity appears for dimensional reasons, includes the flux components that do not depend explicitly on ∇u_ϕ nor u_ϕ. This latter component is specific of momentum transport, compared to particle and energy, and is formally re writable as a source, hence it has the potential to provide a plasma acceleration [56, 114]. One of the main results of this work is the fact that C_ϕ is necessary to account for TCV experimental observations of intrinsic rotation. In this chapter we will refer to this part of momentum flux as "residual stress", as it is commonly done, or "intrinsic torque".

7.1.1 Stationary rotation

In stationary plasma conditions and in absence of external sources, Eq. **??** reads (using the normalization on the thermal velocity $\tilde{u}_\phi = u_\phi/v_{th,i}$, $\tilde{u}'_\phi = \frac{1}{v_{th,i}}\frac{\partial u_\phi}{\partial r}$):

$$\tilde{u}'_\phi = \frac{V}{\chi_\phi}\tilde{u}_\phi + \frac{C_\phi}{\chi_\phi} \tag{7.1.3}$$

From the precise knowledge of the rotation profile, this expression provides a useful tool to characterize momentum transport. First of all, C_ϕ/χ_ϕ is directly estimated from the value of $\tilde{u}'_\phi$ measured in regions where $u_\phi = 0$. Furthermore, reconstructing experimentally the dependence of stationary u'_ϕ on u_ϕ allows to estimate the ratios V_ϕ/χ_ϕ and C_ϕ/χ_ϕ. In general from steady state profiles, it is not possible to decouple the viscous transport contribution χ_ϕ from the non diffusive part. To do so temporal dependent analysis have to be performed.

Where present, controllable external torques allow further possibilities to study momentum transport. For instance on NSTX, the high injected torques permitted to study fast rotating plasma and put in evidence the dominating pinch component [115]. In DIII-D a zero velocity profile was measured with an unbalanced injected momentum, hence providing a direct proof of the existence of C_ϕ/χ_ϕ and the undirect measurement of its profile [116]. An effective viscosity χ_ϕ^{eff} is often calculated from the knowledge of stationary u_ϕ profiles and the applied torque, assuming that $\Gamma_\phi = -\chi_\phi^{\text{eff}}\nabla_r u_\phi$ [115, 117]. This assumption may lead to underestimation of the actual viscosity, e.g. in case of substantial convective contribution to momentum flux. Indeed in other tokamak devices, the experimental evidence that $\chi_\phi^{\text{eff}} < \chi_i$ (ion thermal diffusivity), confronted to a theoretical prediction of equality of the two coefficients, was considered as an indication of the importance of non diffusive fluxes [62]. Notice that in absence of external torque, as in TCV, comparison of χ_ϕ and χ_i can only be carried out with real viscosity χ_ϕ, since a diffusion flux alone cannot sustain a stationary non null velocity gradient.

7.1.2 Analysis of transient

The temporal evolution of u_ϕ permits to determine the value of viscosity χ_ϕ. To do this one has to solve the time dependent Eq. 3.3.2 using the experimental u_ϕ profiles. This is typically done within a predictive, least mean square, approach: starting from an initial u_ϕ profile, the radial profiles of χ_ϕ, V_ϕ and C_ϕ are adjusted to match the experimental evolution of u_ϕ. This process may involve many free parameters, hence to obtain significant solutions, some ad hoc constraints are often included. This approach has been used extensively in particle and impurity transport studies. For momentum transport this approach has been appplied for example in Alcator C-mod, pointing out diffusive flux of momentum from the plasma edge at the onset of H-mode [79]. In TCV this type of analysis has been applied for the evolution of u_ϕ following the plasma brake by MHD [49, 72] pointing out the viscosity in excess of two orders of magnitude compared to the neoclassical prediction.

7.1.3 Modulation of torque - harmonic analysis

This technique has been used on JET [63, 118], NSTX [115], JT-60 [119] and DIII-D [116]. It consists in modulating the plasma rotation imposing a modulated torque, usually with auxiliary heating NBI or magnetic braking techniques. The advantage is that only the convective $V_\phi u_\phi$ flux is sensitive to the modulation of the velocity, so it can be determined independently from the intrinsic torque. In TCV, there are no auxiliary heating neutral beams, so a direct modulation is not applicable. One option would be to modulate the rotation by means the ECH or ECCD. As

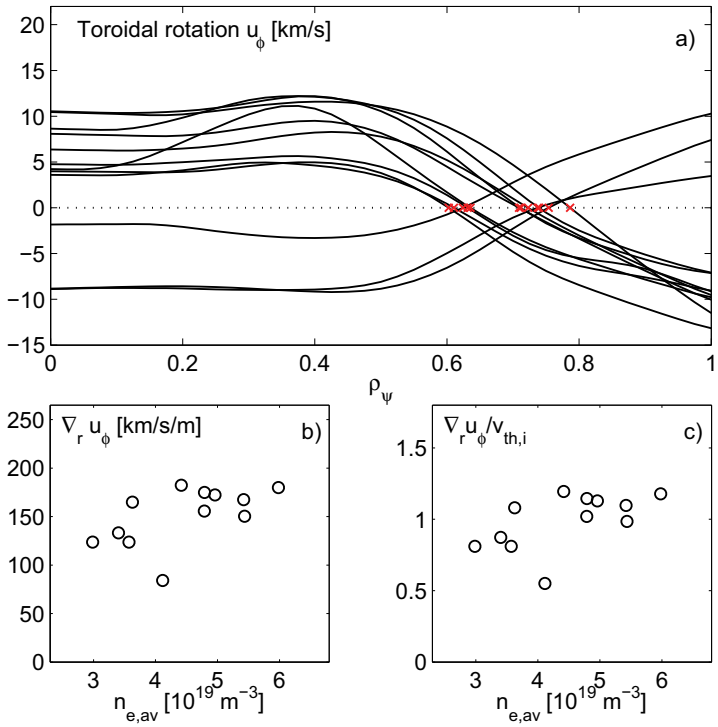

Figure 7.1: a) Selection of stationary rotation profiles in diverted L-mode, which cross zero at a $\rho_\psi$in [0.6, 0.85] (fitted profiles, not normalized, all counter current). Bottom graphs: toroidal rotation gradient at the position where u_ϕ=0 (b), in km/s/m and normalized to the main ion thermal velocity (c).

the latter are to perturb very much the plasma (electron temperature increases suddenly), this imply an integrated modeling of energy, particle and momentum transport.

A more applicable option, which has not been performed during this thesis for lack of time, is to induce perturbations of the u_ϕ profile, by switching periodically the magnetic configuration from Lower Single Null to Upper Single Null configurations. As presented in chapter 6, the u_ϕ in the peripheral region varies by ± 10 km/s at $n_{\mathrm{e,av}} > 4 \times 10^{19}\,\mathrm{m}^{-3}$. By modulating the boundary condition, the absolute value of rotation in the intermediate/gradient region is varied, with little direct effect on other plasma parameters in the same region.

7.2 Experimental characterization of non diffusive fluxes

7.2.1 Stationary rotation

In general, to characterize experimentally the non diffusive flux, in its convective and residual stress components, it is necessary to vary separately the plasma rotation u_ϕ and its gradient ∇u_ϕ, over a sufficiently large range values. In TCV, where no external torque is available, u_ϕ can only be varied by changing some plasma parameter. Limited discharges are not suitable to this type of analysis, since the rotation value is mostly determined by T_i, that in TCV is only indirectly determined by ion-electron equipartition, hence it is difficult to scan u_ϕ without perturbing strongly other discharge parameters. Instead, diverted discharges are characterized by a strong dependence of rotation in the peripheral region on n_e and I_p, together with weaker dependence of the core rotation on the same parameters. Therefore, under certain limitations, momentum transport analysis can be carried out.

First of all, we notice that the convective part of momentum transport is not dominating by the non diffusive fluxes. The simple and clear demonstration comes from the n_e and I_p scans reported in chapter 6, where, as the edge rotation varies responding to the increase of n_e or I_p the gradient of rotation remains finite and, eventually, u_ϕ profile crosses the axes $u_\phi = 0$ (Fig. 6.3 and 6.5).

From Eq. 7.1.3, we see that at the radial position where $u_\phi = 0$ the pinch flux is null and the gradient can only be sustained by the residual stress term C_ϕ.

In this section we will restrict the analysis to stationary diverted plasma discharges, with $I_p \approx \pm 250$ kA ($q_{95} \approx 3.6$), with variable plasma density $n_{e,av} \approx 3 \div 6 \times 10^{19}\,\mathrm{m}^{-3}$, in which the radial null velocity location was at $0.6 < \rho_\psi < 0.8$. Figure 7.1a shows the u_ϕ profiles interpolated with a cubic fit (experimental profiles measured by CXRS09 diagnostic are shown in Fig. 6.3).

Considering the quantity $\nabla_r u_\phi / v_{th,i} = C_\phi / \chi_\phi$ evaluated at the null velocity radius, we obtain the results in Fig. 7.1c. Each point in the graph corresponds to a stationary profile in (a) and represents a local measurement of the viscosity normalized residual stress C_ϕ/χ_ϕ. In the radial region $0.6 < \rho_\psi < 0.8$, $C_\phi/\chi_\phi \approx 0.5 \div 1.5$ m^{-1} is found. As for diverted discharges the rotation in the peripheral region is co current, the condition $u_\phi = 0$ is only fulfilled when plasma is in counter rotation regime. Notice that in this graph, taking into account the uncertainty on the gradient estimation and the fact that the radial location of the measurement is not fixed, the $n_{e,av}$ is to be considered as a label.

To obtain an estimate of the relative weight of V_ϕ and C_ϕ in the momentum transport, we can consider Fig. 7.2a, where, for each stationary rotation profile in the considered selection, ∇u_ϕ at $\rho_\psi \approx 0.65$ is plotted as a function of u_ϕ at the same position. Because the peripheral rotation

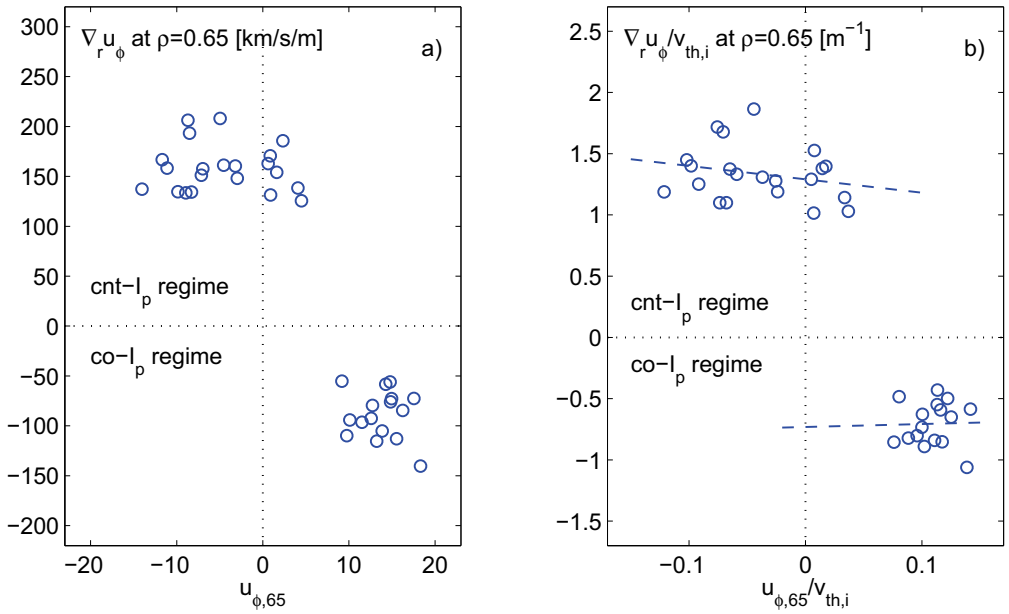

Figure 7.2: a) Gradient of u_ϕ at ρ_ψ=0.65 plotted versus u_ϕ at the same location, for plasma discharges in diverted configuration at $q_{95} \approx 3.6$. Values are normalized to current direction, so positive (negative) gradients represents profiles in counter (co) current regime. b) The same values normalized to thermal velocity. From linear interpolations C_ϕ/χ_ϕ and V_ϕ/χ_ϕ in counter current regime may be estimated.

in diverted discharges scales with the n_e, the range of $2 < n_{e,av} < 6{\times}10^{19}\,\mathrm{m}^{-3}$ covered in this graph translates in an extended range of toroidal rotation $u_\phi(0.65) \approx -15 \div 20$ km/s. Points with positive and negative toroidal rotation gradient, correspond to counter and co current rotation regime respectively. First of all, we notice that the two rotation regimes are clearly distinct, in the sense that a finite toroidal rotation gradient is always present in the intermediate region. Moreover,

the rotation gradient in the counter regime appears to be higher ($|\nabla u_\phi| \approx 120 \div 220$ km/s m^{-1}) than in the co current regime ($|\nabla u_\phi| \approx 50 \div 130$ km/s m^{-1}).

Fig. 7.2b shows the same data, but normalized on the local ion thermal velocity. Following Eq. 7.1.3, when a linear trend is present in this graph, the effect of transport coefficients can be distinguished. In particular, if data can be interpolated by a linear fit of the form $y = a + by$, the angular coefficient is $b = V_\phi/\chi_\phi$ and the offset $a = C_\phi/\chi_\phi$.

For the co current regime (bottom part of the graph) the range of u_ϕ available is too restricted to identify a clear trend. Considering only the counter current rotation regimes (top part of the graph), the data indicate a weak dependence of ∇u_ϕ on u_ϕ, suggesting a low effect of convection. The spread of the points does not show a clear linear relation between ∇u_ϕ on u_ϕ. However, if a linear fit is performed, the viscosity normalized values of $V_\phi/\chi_\phi \approx -1.1$ m^{-1} and $C_\phi/\chi_\phi \approx 1.3$ m^{-1} are obtained. If we assume for the momentum diffusivity, the typical values resulting from analysis of rotation dynamics (see next section) $\chi_\phi \approx 0.3$ m^2/s, then the pinch velocity of the order of $V_\phi \lesssim 0.3$ m/s and residual stress of the order of $C_\phi \approx 0.4$ m/s are obtained.

In reality, the relative weight of these convective and residual stress contributions to the radial momentum transport is evaluated by the ratio $(v_{th,i}C_\phi)/(V_\phi u_\phi)$. For the typical thermal velocities measured in these discharges at $\rho_\psi = 0.65$, $v_{th,i} \sim 120$ km/s, hence $(v_{th,i}C_\phi)/(V_\phi u_\phi) \gtrsim 10$. This result indicates that, at least in the counter current rotation regime of diverted Ohmic discharges, the non diffusive momentum flux is dominated by the non convective part.

Notice that, as in these experiments the spread of $u_\phi(0.65)$ was obtained varying the plasma density, the trends appearing in Fig. 7.2 could also result from a more complex dependence of transport coefficient on plasma parameters. For example, a direct dependence of C_ϕ on $n_{\mathrm{e,av}}$ would give the same result of a convective pinch contribution.

7.3 Rotation profile evolution

As anticipated, the diffusive transport component can be determined separately only from the analysis of dynamic evolution or modulation of u_ϕ profile. In general, the diffusive component determines the timescale of dynamical evolution of u_ϕ profile, while the ratio between the diffusive and non diffusive flux components determines the peaking of the stationary profiles (in absence of applied torques). In this section, we report some examples of analysis of transient u_ϕ profile during spontaneous evolutions that have been observed in TCV L-mode discharges in limited and diverted magnetic configuration, with the scope of estimating the transport coefficients, in particular the toroidal momentum diffusivity χ_ϕ.

For the limited discharge, a common observation of rotation evolution is the toroidal rotation reversal discussed in chapter 5. The timescale of the reversal might vary within $100 \div 200$ ms, faster than the variation of other plasma parameters. Typically only one or no profiles were measured across the reversal, with exception of few discharges where, thank to the high carbon content, the diagnostic sample frequency could be increased. Left column graphs of Fig. 7.3 show the main traces of a density ramp discharge at $I_\mathrm{p} \approx \pm 340$ kA (TCV 28924), where CXRS measurements were acquired at a sample period of 45 ms, and the evolution of the u_ϕ across the reversal could be measured.

An example of toroidal rotation profile evolution in a diverted L-mode comes from the early discharge phase. Right column graphs of Fig. 7.3 show the main traces of a diverted discharge at $I_\mathrm{p} \approx 260$ kA (TCV 29779), with programmed density of $n_{\mathrm{e,av}} = 4 \times 10^{19}$ m^{-3}. Until $t = 0.35$ s the plasma is limited on the central column. Then the divertor formation starts and the target diverted configuration is attained at $t = 0.5$ s. From this moment on, plasma parameters and configuration are maintained. The CXRS measurements starting at $t = 0.4$ s indicate that the core rotation is

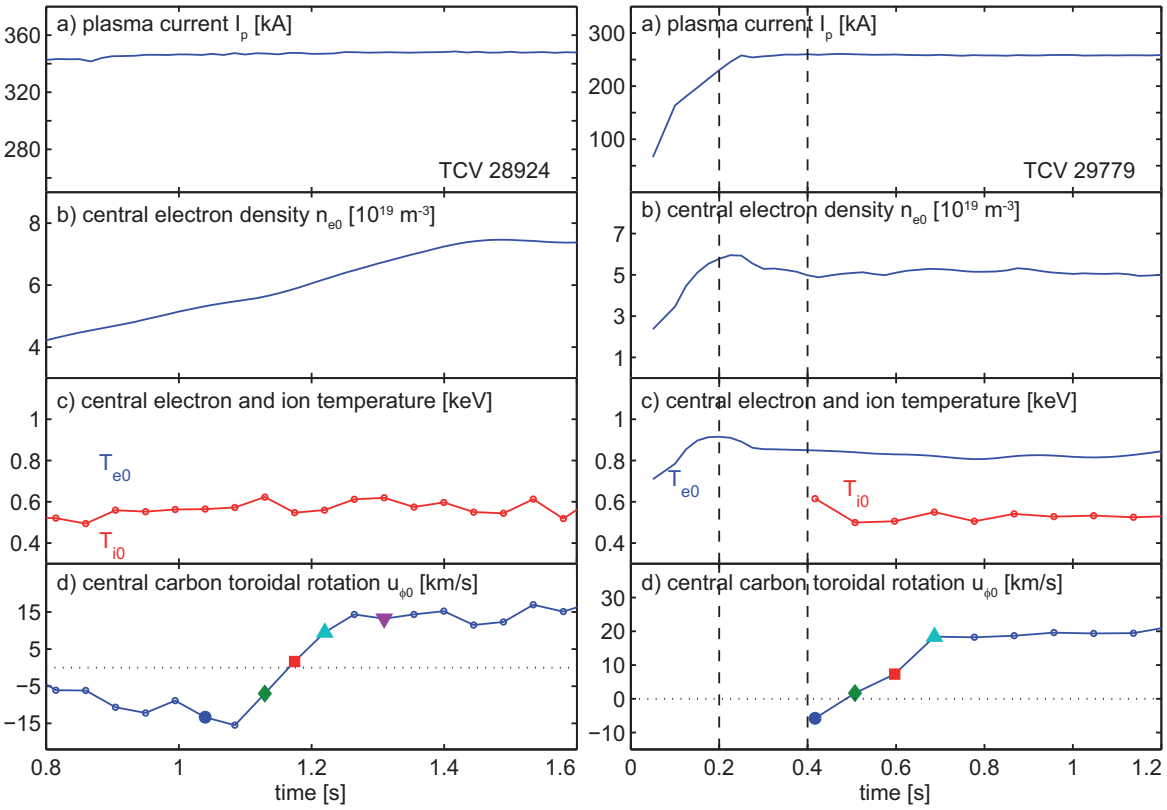

Figure 7.3: Temporal evolution of the main plasma parameters for of a limited (TCV 28924, left) and a diverted (TCV 29779, right) discharge. In the limited discharge the reversal of u_ϕ is obtained in a density ramp at constant plasma current. In the diverted discharge u_ϕ reversal appears in the evolution towards the stationary profile, that follows the divertor formation. Profiles of u_ϕ at the times indicated by shaped markers are shown in Fig. 7.4.

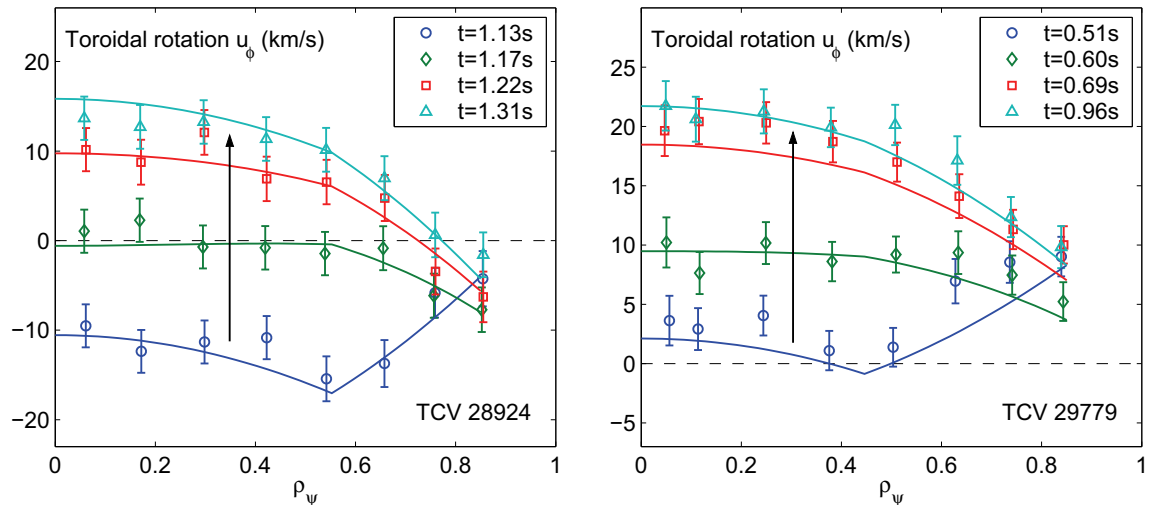

Figure 7.4: Evolution of u_ϕ profile across rotation reversal in two TCV discharges in limited (a) and diverted (b) configuration. The corresponding time traces of main parameters are shown in Fig. 7.3. Solid curves show the evolution of u_ϕ profile simulated assuming anomalous diffusivity and neglecting convective transport (TCV 28924,29779).

evolving from counter negative values to the stationary positive rotation of $u_\phi = 20$ km/s in the core. This evolution corresponds actually to a reversal of the rotation profile, as visible in Fig. 7.4.

The first profile measures the toroidal rotation at the end of the divertor formation, peaked in the counter direction, with high co current rotation in the peripheral region. The reversal to the co current peaking profile takes approximately 300 ms.

For both limited and diverted cases the core rotation reversal is accompanied by a counter current acceleration in the peripheral region, suggesting the presence of a momentum transfer from the peripheral region to the core (Fig. 7.4).

To estimate the toroidal momentum diffusivity, u_ϕ evolutions across the reversal have been reproduced within a predictive cylindrical 1-D transport model. In the model, ad hoc expressions for the toroidal momentum flux are assumed, in which toroidal momentum flux includes only contributions from viscosity and intrinsic torque, i.e. convective pinch, and external source are neglected. We restrict the simulation to the region $\rho_\psi < 0.85$. At the radius $\rho_\psi = 0.85$ a proper boundary condition has to be defined.

Some drastic simplifying assumptions allow to obtain the optimized solution, solving a certain degree of arbitrariness inherent to the procedure. The main elements of the model are the following:

- Toroidal momentum diffusivity χ_ϕ is assumed constant over the whole radius and during the evolution.
- Convective pinch is neglected.
- Constant $C_\phi = C_\phi^{ST} > 0$ (inward) for $\rho_\psi < \rho_{\rm inv}$, to reproduce the sawtooth bulge effect, coherently with observation exposed in chapter 8.
- Constant $C_\phi = C_\phi^{co,cnt}$ in the gradient region $\rho_{\rm inv} < \rho_\psi < 0.85$, positive (negative) for co (counter) current rotation regime. At this stage we consider this an acceptable simplification in the spirit of getting the zero order approximated values.
- Boundary condition at $\rho_\psi = 0.85$, on the out flux of momentum expressed as a friction force $\Gamma(0.85) = -\nu(u_{\phi,85} - \bar{u}_{\phi,85})$, where $\bar{u}_{\phi,85}$ is the asymptotic value of the boundary rotation, i.e. the value of the final relaxed profile. With this formulation, $u_{\phi,85}$ is free to vary across the reversal, and will recover the final experimental value $\bar{u}_{\phi,85}$ on a timescale $\tau \propto 1/\nu$. This parameter will estimate the rate of loss of momentum across the boundary surface.

Fig. 7.4 compares the evolution of u_ϕ profiles across the reversal from the model, with the CXRS04 experimental profiles. The dynamic of the inversion is reproduced with reasonable accuracy within the simplifying hypothesis of the model. The optimized choices of parameters used in the model are summarized in Table 7.1. The absolute values of the coefficients χ_ϕ and C_ϕ are comparable for the two cases shown. This is natural, as the stationary u_ϕ is reached in a similar time scale, and the final ∇u_ϕ is also similar.

Configuration	χ_ϕ m^2/s	$\chi_\phi/\chi_\phi^{neo}$	C_ϕ m/s	ν m/s
limited	0.3	150	0.2	6
diverted	0.2	100	0.15	4

Table 7.1: Values of parameters used to model u_ϕ reversal phenomena in limited (TCV 28424) and diverted (TCV 29779) discharges. In the model the convective component was neglected (see Fig. 7.2).

The resulting diffusive rates can be compared with the neoclassical prediction $\chi_\phi^{\rm neo} \approx 0.14\,\epsilon^2\,\nu_{ii}\,\rho_L^2$ [46], where ϵ is the aspect ratio, ν_{ii} is the ion-ion collision frequency and ρ_L the ion Larmor radius.

In the intermediate region we have $\chi_\phi^{neo} \approx 0.002$ m^2/s, two order of magnitude lower than what found in the present analysis. This indicates that for TCV Ohmic plasmas the toroidal momentum diffusivity, or radial viscosity, is dominated by an anomalous component.

It is important to notice that the abrupt sign change of C_ϕ in the gradient region, reproduces correctly the dynamic of counter acceleration in the peripheral region. Furthermore the non pinch flux sustains a finite stationary gradient at $\rho_\psi = 0.7$ in the limited discharge, where u_ϕ profile crosses zero.

The recent CXRS09 measurements provide a better radial resolution and allow to address the problem under a slightly different approach. We consider, as before, the case of negligible external sources and convective transport (no pinch). In these hypotheses, the relaxed u_ϕ stationary profile is determined by $\nabla u_\phi = v_{th} C_\phi / \chi_\phi$. The latter expression can be used to determine the non diffusive component C_ϕ as a function of χ_ϕ in the relaxed state.

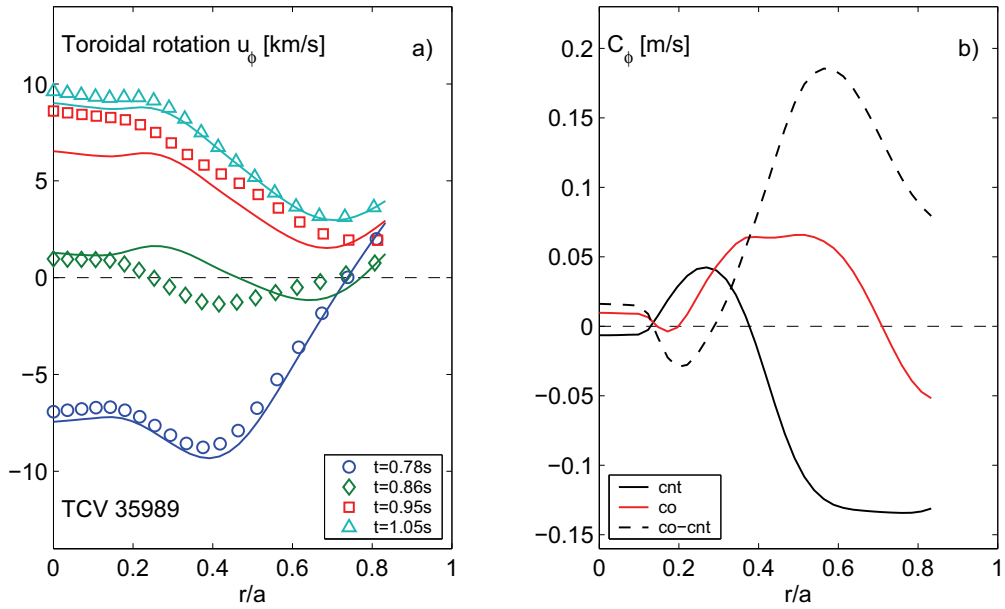

Figure 7.5: a) Evolution of u_ϕ profile simulated with intrinsic torque derived from the gradient (solid curves) compared to profiles fitted on experimental data (TCV 35989). The profiles for C_ϕ assumed for the initial and final states are plotted in (b). The evolution was reproduced assuming $\chi_\phi = 0.15$ m^2/s.

In Fig. 7.5, we plot the results of this type of modeling, for the case of a u_ϕ reversal in a density ramp limited discharge, measured with the CXRS09 diagnostic. The value of the viscosity is assumed constant over the minor radius, and two profiles of C_ϕ for the counter and co current rotation regimes are deduced from the expression $C_\phi = \frac{1}{v_{th}} \frac{du_\phi}{dr} \chi_\phi$, evaluated at first and last simulation times. The profile of the intrinsic torque C_ϕ, is plotted in the right graph, showing that the variation of the torque at the reversal is most pronounced around mid radius. At $\rho_\psi \approx 0.3$ a similar sawtooth effect is found for both rotation regimes. The timescale of the inversion implies $\chi_\phi = 0.15$ m^2/s, which is consistent with former results.

This simple analysis does not determine accurately the diffusivity profile. Nevertheless, when applied on several examples, it tends to provide values of the same order of magnitude.

The toroidal rotation reversal in limited configuration (see chapter 4) takes place with peripheral toroidal rotation close to zero, often slightly negative. This suggest the possibility of interpreting the rotation inversion as driven by the change of the boundary condition, passing from negative

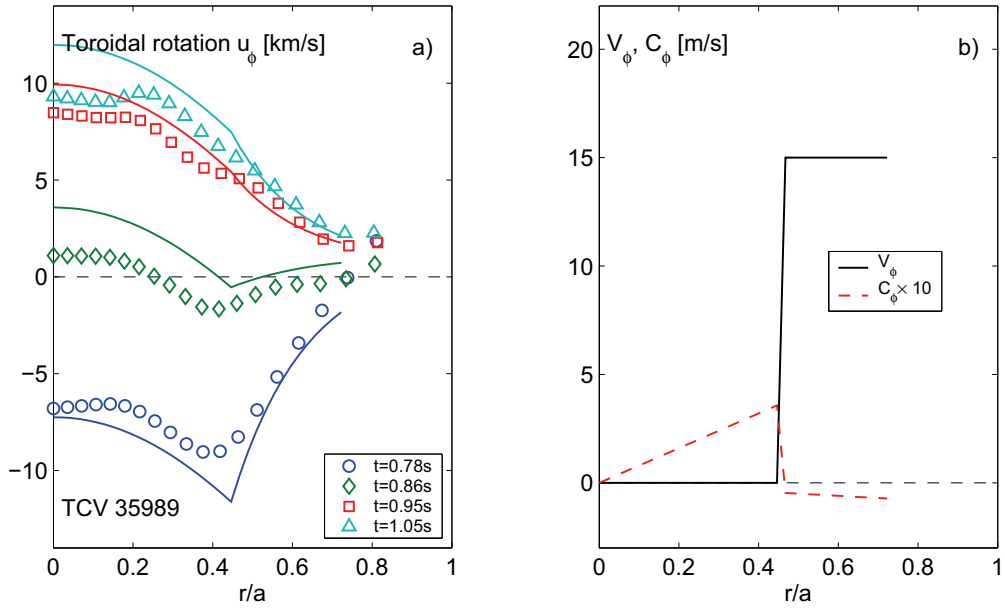

Figure 7.6: a) Evolution of u_ϕ profile simulated with dominant pinch non diffusive flux compared to profiles fitted on experimental data (TCV 35989). The profiles for V_ϕ and C_ϕ assumed are plotted in (b). The C_ϕ component is required to account for the stronger u_ϕ gradient in the counter current regime.

to positive, associated with a strong inward pinch. In fact, an eventual change in sign of the velocity at the boundary condition (e.g. $\rho_\psi \approx 0.9$) would translate in a reversal of the momentum flux $\Gamma_\phi = V_\phi u_\phi$ induced by the pinch (e.g. from inward to outward). For a dominant pinch transport the stationary gradient $\nabla u_\phi = V_\phi u_\phi / \chi_\phi$ changes sign as u_ϕ. For several aspects the results presented so far indicate a minor role of the convective pinch. Nevertheless, we consider here this hypothesis of a dominant pinch to clarify the possible role of the elements at play. With this spirit, we modeled TCV 35989 discharge, assuming the non diffusive flux has a dominant pinch part. Moreover, the boundary condition is defined prescribing $u_\phi(t)$ at $\rho_\psi = 0.85$, which evolves smoothly from -2 to 2 km/s during the simulation, with the zero value taken at t=0.8 s.

The results are shown in Fig. 7.6, together with the values of the optimized non diffusive transport coefficients. A satisfactory agreement is found with $\chi_\phi = 0.6$ m^2/s. Notice that a negative intrinsic torque in counter current direction had to be included to the non diffusive flux, to reproduce the difference in gradient, that distinguishes the co and counter rotation regime (see also Fig. 8.1). A pinch value of the order of $V_\phi = -15$ m/s is required in the gradient region to account for the peaking of the u_ϕ profile.

We stress again that, even if the picture of dominant pinch is capable of reproducing the dynamic of rotation reversals in limited configuration (characterized by low peripheral rotation), general observations rather suggest a combination of non diffusive fluxes, in which pinch is not dominant, and therefore is not the leading term in driving the reversal. In fact:

- Cases are observed in which, due to specific combinations of plasma parameters, also the limited inversion occurs at u_ϕ substantially lower than zero $u_\phi \lesssim -5$ km/s.

- The convective pinch term alone cannot account for the counter current acceleration, which is observed at the u_ϕ reversal, in edge measurements and passive measurements.

- In lower current discharges, when $u_\phi \approx 0$ km/s in the peripheral region, co current rotation should be regularly observed.

7.4 Comparison with neoclassical predictions

In the frame of the neoclassical theory, the toroidal rotation profile, or equivalently the radial electric field, can be determined by imposing the zero radial momentum flux condition. The problem has been addressed several times in the past decades, with rather controversial results [47, 120–122]. Recent treatments pointed out the existence, in the frame of neoclassical theory, of a component of radial momentum flux that is independent on both the rotation velocity or its radial gradient [39,46,48]. In the transport matrix formulation, this corresponds to an off-diagonal element that couples plasma flow with gradient of density and temperature. A momentum flux of this kind may generate a stationary finite rotation gradient even in case of small or null rotation, and is then a candidate to explain TCV observations.

The expression derived by Wong [46] for high collisionality regime is in strong qualitative and quantitative disagreement with TCV observations [45]. Here we consider another expression, originally proposed by Classen [39] in cylindrical approximation, later extended by Wong to general configurations [46], and more recently confirmed by Catto [47]. In the simplest formulation (cylindrical geometry, pure plasma) the neoclassical non diffusive momentum flux is:

$$\Gamma_\phi = \frac{0.107kq^2}{\chi_\phi}\frac{T_\mathrm{i}}{eB_\theta}\left(\frac{\partial \ln T_\mathrm{i}}{\partial r}\right)^2 \tag{7.4.1}$$

where q is the safety factor, χ_ϕ the radial viscosity and k a constant that depends on the collisional regime, and has been calculated for banana ($k_B P = 1.17$) and Pfirsch-Schlüter ($k_{PS} = -1.83$) regimes. At steady state, in absence of momentum sources, this momentum flux originates a u_ϕ gradient, that is sustained by the ion temperature gradient:

$$\frac{\partial u_\phi}{\partial r} = 0.107kq^2\frac{T_\mathrm{i}}{eB_\theta}\left(\frac{\partial \ln T_\mathrm{i}}{\partial r}\right)^2 = 0.107k\frac{q^2}{eB_\theta R}\frac{\partial T_\mathrm{i}}{\partial r}\frac{R}{L_{T_\mathrm{i}}} \tag{7.4.2}$$

The predicted u_ϕ profile follows by spatial integration with u_ϕ boundary condition. Notice that in this formulation the gradient of u_ϕ can be compared with the experimental one, independently on the absolute value of the velocity itself. The neoclassical stationary ∇u_ϕ has strong dependencies on T_i and I_p (via B_θ and q), that are coherent with the general trends observed in TCV. Remarkably, k factor takes opposite signs in different collisional regimes, which implies that the sign of the gradient may reverse following a change of collisionality. With the adopted conventions, a negative u_ϕ gradient is predicted for banana (PS) regime, while a positive one is predicted for PS regimes. These correspond respectively to a u_ϕ profile peaking in the counter and co current direction.

It would be tempting to relate the TCV u_ϕ observations to a change in collisionality regime, in particular for reversal in limited discharges 5. However, the rotation gradient predicted by neoclassical theory is much lower than the one observed in TCV: in Fig. 7.7 the neoclassical ∇u_ϕ profile calculated following Eq. 7.4.2, for banana and PS collisional regime, are compared with the experimental one. Left plot corresponds to a low density discharge, right plot to high density. It is clear that in the intermediate region ($\rho_\psi \approx 0.65$) the experimental ∇u_ϕ largely exceeds the neoclassical prediction in all cases, so that the effect of neoclassical contribution can only account for minor correction to the u_ϕ profile, hence, neoclassical arguments are not sufficient to explain the spontaneous rotation profile reversal.

7.5 Comparison with turbulent transport predictions

Motivated by the multiple evidences of intrinsic plasma rotation and in an attempt of explaining the observed level of momentum transport, the theory of turbulent transport has undergone new

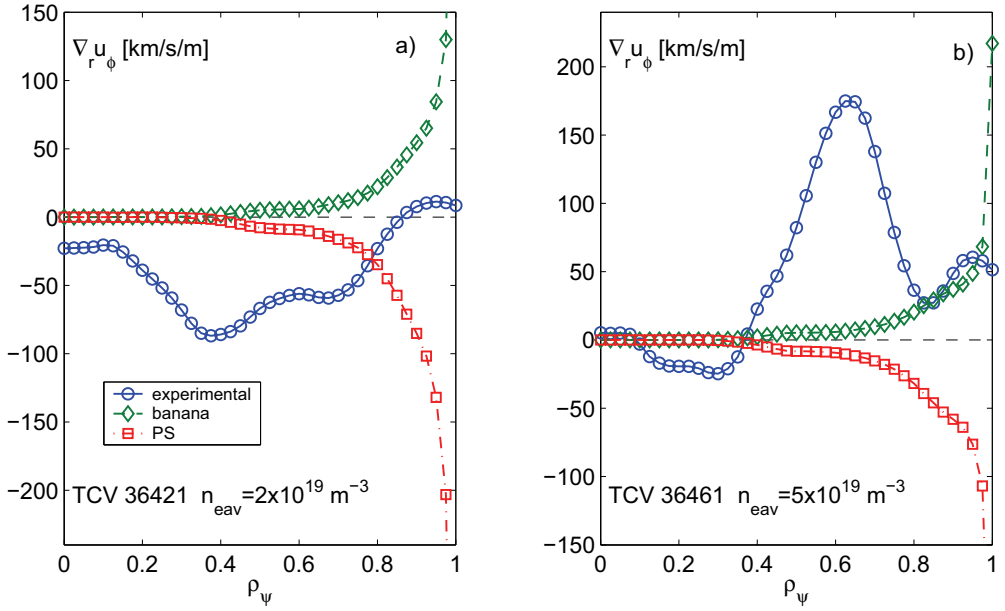

Figure 7.7: Experimental profiles of ∇u_ϕ compared with neoclassical predictions for collisional banana and collisional PS regime. The analysis is shown for for two discharges in diverted configuration at $I_p \approx 250$ kA: TCV 36421, low n_e co current rotation regime (a); TCV 36461 high n_e counter current rotation regime (b).

developments. In particular, several contributions to the radial flux of momentum have recently been identified. Turbulent transport can generate a diffusive flux (diagonal part - flux proportional to the background rotation gradient), a convective flux (pinch part - flux proportional to the background rotation) or a residual stress (equivalent to a local source - flux neither proportional to the background rotation, nor to its gradient). A brief review of some of these terms is presented in section 3.5.

The comparison between the turbulent momentum transport models and the experiments is not straightforward. First of all, it is difficult to isolate and study the effect of one physic mechanism from the others. Furthermore, predictions presented in the original works are often limited to simplified scenarios (no shape effect, no collisions) and not always suited for comparison with experiments in the sense that some elements of the model are not accessible to experimental measurements (e.g. $\langle k_{||} \rangle$, that provides the amount of symmetry breaking in [56]). Finally, recent theories are not yet implemented in predictive transport simulation codes.

During this thesis, a first step in theory-experiment comparison was undertaken considering the convective transport due to the Coriolis drift velocity [51, 53, 54]. This general mechanism for momentum transport is related to the background plasma rotation and does not require specifically steep gradients of temperature or density, and it could therefore be relevant in TCV L-mode plasmas. The general properties of the Coriolis pinch are sketched in [54] by means of a simple analytical fluid model. The Coriolis pinch is typically directed inward and thus predicts a peaking of the rotation profile in the direction of the plasma rotation for a large range of plasma conditions.

The effect of Coriolis pinch in TCV scenarios has been addressed in collaboration with Dr. Camenen by means of gyro-kinetic simulations with the GKW [123] code, that is used and developed at CFSA[(1)] to study turbulent energy, particle and momentum transport. GKW solves the gyro-kinetic equation for the perturbed distribution function over a flux-tube domain (local approximation) for an arbitrary number of species. The gyro-kinetic equation is formulated in the rotating

(1) Centre for Fusion, Space and Astrophysics, Department of Physics, University of Warwick

u_ϕ	$\nabla u_\phi/ut$	T_e	T_i	n_e	ν_{eff}	q	R/L_{n_e}	R/L_{T_e}	R/L_{T_i}	T_e/T_i
km/s		eV	eV	10^{19} m^{-3}						
-21	-15	470	370	2.55	1.1	1.5	-4.7	-11.5	-8.7	1.3

Table 7.2: Main plasma parameters of plasma discharge TCV 27502, taken at the radial position considered in GKW simulations, $\rho_\psi = 0.55$.

frame and consequently includes the Coriolis drift term that leads to a convective momentum transport.

For the comparison between experiments and gyro-kinetic predictions including Coriolis pinch, a stationary discharge in L-mode has been selected (TCV 27502) at $n_{e,av} = 2\times10^{19}$ m^{-3}, $I_p = 250$ kA $q_e \approx 8.8$. In this discharge, the rotation profile is counter current across the whole minor radius and the sawtooth inversion radius is relative small ($\rho_{inv} \approx 0.3$). The high central toroidal rotation $u_\phi \approx 43$ km/s, enhances the effect of an eventual radial convective flux $\Gamma_\phi^{pinch} = V_\phi u_\phi$.

Linear simulations have been performed taking as an input the experimental data for the profiles of T_e, n_e, T_i, averaged over a stationary time window and evaluated at $\rho_\psi = 0.55$. The magnetic equilibrium has been reconstructed by the LIUQE code, routinely used in TCV. Note that the simulations were linear and did not allow to compute the absolute value of χ_ϕ and V_ϕ as no saturation mechanism was included (the saturated amplitude of the turbulent mode is only obtained in non-linear simulations). Nevertheless, the ratio V_ϕ/χ_ϕ can still be estimated since the phase relations between momentum and electrostatic potential perturbations are usually quite similar in non-linear and linear simulations [124]. It should also be noted that the simulations did not include global effects which are known to affect the transport of momentum [125] and could be of importance in TCV due to the rather low magnetic field. This comparison shall therefore be seen as a first attempt to check whether the magnitude of the Coriolis pinch is somehow related to what is observed in the experiments.

In steady state, in the absence of sources and considering only convective momentum transport $V_\phi/\chi_\phi = \nabla u_\phi/u_\phi$, a direct comparison with the experimental normalized gradient is possible.

In Fig. 7.8a, the linear growth rate spectrum of the turbulent modes, which develop under the experimental plasma conditions, is shown as a function of the poloidal wave vector normalized to the ion Larmor radius. For each different mode the normalized gradient of rotation can be calculated (Fig. 7.8b), by computing the ratio $RV_\phi/\chi_\phi = (\Gamma_\phi(u' = 0, u = 0.1)/0.1)/(\Gamma_\phi(u' = 1, u = 0)/1)$. The predicted normalised gradient is typically between -2 and -3, which has to be compared with the experimental value of $\nabla u_\phi/u_\phi \approx -15$.

Although the simulation does not include all the effects known to affect momentum transport (for instance it neglects the effect of the $E \times B$ shear, global effects), it shows that, in a TCV relevant case, the Coriolis convective flux has the good sign, and that it can constitute a sizable fraction of the observed momentum flux. However, it can not alone explain the observed rotation peaking.

To assess the dependence of the Coriolis pinch on some plasma parameters, a set of linear simulations has been performed, varying separately the normalized density gradient R/L_{n_e} (at normalized ion temperature gradient $R/L_{T_i} = 12$) and the electron to ion temperature ratio T_e/T_i (at $R/L_{n_e} = 5$). The resulting normalized toroidal rotation gradient (considering $k_\theta \rho_i = 0.15$) is shown in the bottom graphs of Fig. 7.8. A strong effect of normalized density gradient is observed, with the peaking of u_ϕ increasing strongly with R/L_{n_e}. Conversely, a weak dependence on T_e/T_i is predicted. On the other hand, the Coriolis pinch appears sensitive to R/L_{T_i}, when $T_e/T_i \lesssim 1$, that is absent when $T_e/T_i \gg 1$ and that may induce a change of sign of the convective flux. This

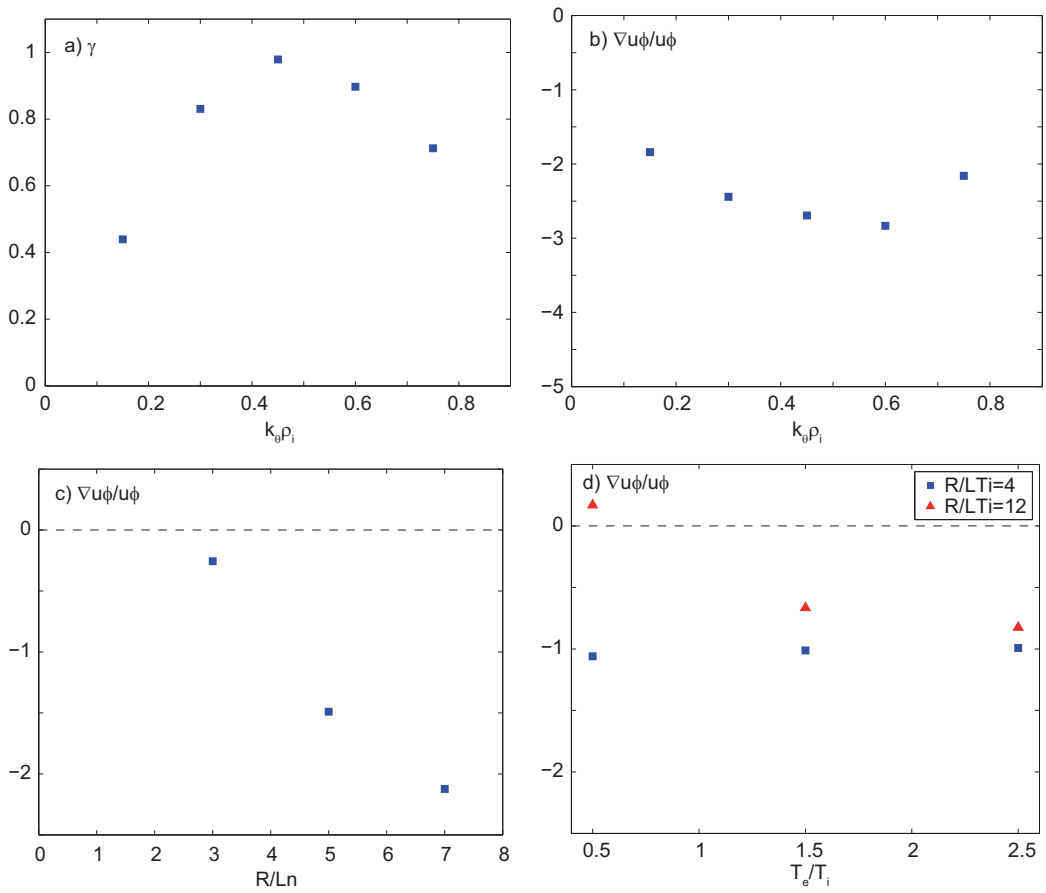

Figure 7.8: Top graphs: results of linear GKW simulation estimating the effect of the Coriolis momentum pinch, on the base of limited Ohmic discharge (TCV 27502): (a) growth rates γ of turbulent modes considered and (b) the resulting normalized toroidal rotation gradient $\nabla u_\phi/u_\phi$, as a function of normalized poloidal wave vector $k_\theta \rho_i$. Bottom graphs: dependence of the $\nabla u_\phi/u_\phi$ predicted by GKW simulations, varying separately the normalized density gradient (c) and the T_e/T_i ratio (d).

behavior might be pointed out experimentally in future investigations, by comparing Ohmic and EC heated discharges.

7.6 Conclusions

In this chapter, we considered the collected experimental observations in TCV Ohmic plasmas, in order to provide a phenomenological characterization of toroidal momentum transport. In the absence of momentum sources, the rotation profile is sustained by the balance of radial fluxes of toroidal momentum, which differ from the originating mechanisms and dependencies on plasma parameters. In particular our scope was to evaluate the role of the viscous, convective and residual stress components of the radial flux of toroidal momentum.

The existence of a finite residual stress flux $\Gamma_\phi = v_{th} C_\phi$ (non-diffusive momentum flux, not proportional to u_ϕ or its gradient ∇u_ϕ) has been demonstrated and quantified, considering stationary TCV Ohmic discharges in diverted configuration, where a finite gradient ∇u_ϕ was measured in the presence of null rotation. This momentum flux component has also been identified in other tokamak devices [116, 126]. At the same time, in TCV, the comparison of u_ϕ and ∇u_ϕ on an extended database of diverted discharges, suggests a minor role of the convective component of momentum transport, represented by the pinch velocity V_ϕ, marking a difference with larger toka-

maks, where with the high externally induced rotation, the convection becomes important or dominant [63, 116, 118, 119].

To estimate the experimental radial momentum diffusivity, spontaneous evolutions of toroidal momentum profile, observed in case of toroidal rotation reversals, have been modeled. The model considered a simplified predictive scheme, with *ad hoc* expression for radial momentum diffusivity, residual stress or pinch term. The radial momentum diffusivity is found of the order of $\chi_\phi \sim 0.2$ m^2/s, that is two orders of magnitude larger than neoclassical value. In the hypothesis of negligible convective momentum flux, the value of the residual stress coefficient C_ϕ has also been estimated, $C_\phi \approx 0.05, -0.1$ m^{-1} respectively in the co or counter rotation regime.

Concerning the physical mechanisms that may originate such radial momentum fluxes, neoclassical transport has been considered first. Even if formally capable to contribute to C_ϕ fluxes, that eventually change sign with plasma parameters [39], we showed that it can only give a small contribution to the spontaneous rotation.

A comparison with turbulent momentum transport theory has been undertaken, addressing the role of the Coriolis pinch, by means of linear gyro-kinetic simulations with the GKW core, on realistic experimental scenario. The preliminary results indicate that the Coriolis pinch contributes to the gradient in a minor but sizable part, but it cannot alone explain the rotation behavior in TCV Ohmic L-mode.

Chapter 8

Sawtooth effect

The relationship between plasma rotation and sawtooth instability has been experimentally addressed in several tokamak devices. Former studies were principally focused on the study of the background rotation effect on sawtooth properties (stability, amplitude and period), with the aim of identifying a possible tool to control the sawtooth itself in fusion devices. Notable examples are the works in TEXTOR [127], JET [128] and MAST [97], where the rotation was modulated by strong torque of auxiliary heating Neutral Beam Injectors and the sawtooth properties monitored. In such type of studies the strong applied torques mask the effect of sawtooth itself on rotation profile. In the TCV case, where intrinsic rotation is addressed, this effect becomes relevant.

A robust observation, common to all scenarios considered in this work, is that inside the sawtooth inversion radius, the toroidal rotation profile results flattened, or slightly bulged in the co current direction. Because the typical integration times for the standard operation of the CXRS diagnostic exceed the typical sawtooth period for TCV Ohmic plasmas, the observations reported so far only give information about the time averaged effect.

In this chapter we report the results of specific experiments, that allowed to study the evolution of core plasma rotation in time scales shorter that the sawtooth period. The chapter describes in detail the experimental strategy, the analysis method and the experimental results. Finally, the possible role of momentum transport and toroidal electric field at the sawtooth crash will be preliminarily addressed.

8.1 Sawtooth effect on average toroidal velocity

In both limited and diverted configuration the toroidal rotation profile inside the inversion radius appears determined by the sawtooth. In the counter current rotation regime u_ϕ profile tends to be hollow inside the inversion radius so that the maximum of rotation is approximately determined by the inversion radius position (see chapter 4). The role of inversion radius has also been confirmed by experiments where ECH was used to squeeze the inversion radius, with the result of a peaking of u_ϕ profile [45].

Conversely, in the co current rotation regime u_ϕ inside $\rho_{\rm inv}$ is flat or slightly peaking in the co current direction. This observation, suggested by the first CXRS04 measurements [81,95] was then confirmed with the upgraded CXRS09, taking advantage of the available higher radial resolution. Fig. 8.1 shows the stationary u_ϕ profile measured with CXRS09 in limited plasma discharges at $I_{\rm p} = 340$ kA. Profiles correspond to four values of $n_{\rm e,av}$ across the density threshold for the u_ϕ reversal. The position of the sawtooth inversion radius is also indicated. The bulge in co current direction is clearly present in both rotation regimes.

To quantify the sawtooth effect on toroidal rotation profile, we define $\Delta u_{\phi,ST} = u_\phi(0) - u_\phi(\rho_{\rm inv})$

the difference between the core rotation and the rotation at $\rho_{\rm inv}$, where we consider normalized to the current direction. With this definition $\Delta u_{\phi,ST}$ is positive for u_ϕ profiles in the figure, with values of $\Delta u_{\phi,ST} \approx 5 \div 7$ km/s.

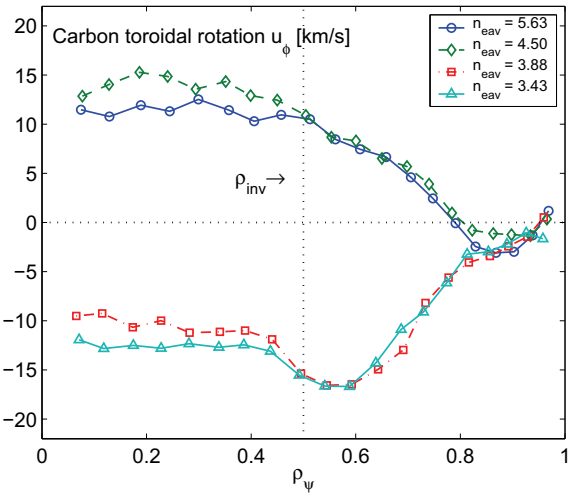

Figure 8.1: Rotation profiles for co and counter rotation regimes in Ohmic limited L-mode, measured with CXRS09 diagnostic. The core rotation profile is bulged in the positive (co current) direction. The approximate position of the sawtooth inversion radius ($\rho_{\rm inv} \approx 0.5$) is indicated by a vertical dotted line.

It is somehow natural to expect that sawtooth crash affects the rotation profile in a way similar to $T_{\rm e}$ and $n_{\rm e}$. For the latter quantities radial profiles are typically flattened by the redistribution of energy and particles that goes with the magnetic reconnection underlying the crash. On the other hand, the fact that the $\Delta u_{\phi,ST} > 0$ is generally observed (bulge in the co current direction) suggests that a torque of some sort is excerpted in the plasma core.

Addressing this effect involves both momentum transport and magnetic reconnection issues. A key point is question whether $\Delta u_{\phi,ST}$ is built *at* the sawtooth crash, hence related to magnetic reconnection, or *in between* crashes, hence related to slower momentum transport mechanisms.

An experimental answer to this question is not straightforward in TCV, as the typical exposure times required for the measurement of rotation with CXRS is of the order of 30 ms, while in Ohmic TCV plasmas sawtooth period is of the order of $\tau_{\rm ST} \approx 6$ ms or lower. Nevertheless, during this thesis work, an experimental scenario has been developed allowing to shed a light on the sawtooth effect on the intrinsic rotation profile, by measuring the evolution of intrinsic plasma rotation in between sawtooth crashes.

8.2 Experimental scenario and diagnostic setup

The experimental strategy that allowed to measure the inter crash evolution of toroidal plasma rotation was based on the following elements:

- Plasma discharge with an extended sawtooth period and large $\rho_{\rm inv}$ to maximize the effect of the sawtooth.
- Ad hoc setup of CXRS09 CCD detector to reduce of the exposure time down to 2 ms.
- Coherent averaging analysis to counteract the lack of CX active signal that follows the short integration times.

8.2.1 Target plasma discharge

A target discharge (TCV 35944, $n_{\mathrm{e,av}} \approx 1.4 \times 10^{19}\,\mathrm{m}^{-3}$,$I_{\mathrm{p}} \approx -260$ kA) was developed featuring strong sawtooth activity (large amplitude and inversion radius to maximize the impact on rotation), and sawtooth period τ_{ST} the longest as possible. The time traces of some relevant plasma parameters are shown in Fig. 8.2. The extension of τ_{ST} was obtained, by modulating the sawtooth period by means of localized Electron Cyclotron Current Drive (ECCD) deposition. In fact, τ_{ST}, that in TCV Ohmic plasmas typically lower than 7 ms, can be extended to tens of milliseconds by deposition of co current ECCD localized outside the $q = 1$ surface [129, 130].

The ECCD deposition scheme was chosen on the base of ray-tracing calculations from the code TORAY-GA [131], in order to maximize the localization of the current drive. The EC beam was launched from the equatorial plane, in the counter current direction[(1)]. The resonance layer was shifted on the inboard radius, by decreasing the toroidal magnetic field to $B_\phi = 1.2$ T, with the effect of reduction of q_e, hence a larger sawtooth inversion radius. At a plasma current $I_{\mathrm{p}} = -260$ kA, with $n_{\mathrm{e,av}} \approx 1.5{\times}10^{19}\,\mathrm{m}^{-3}$, $q_e = 2.7$ was obtained, with a $q = 1$ surface located at $\rho_\psi \approx 0.6$.

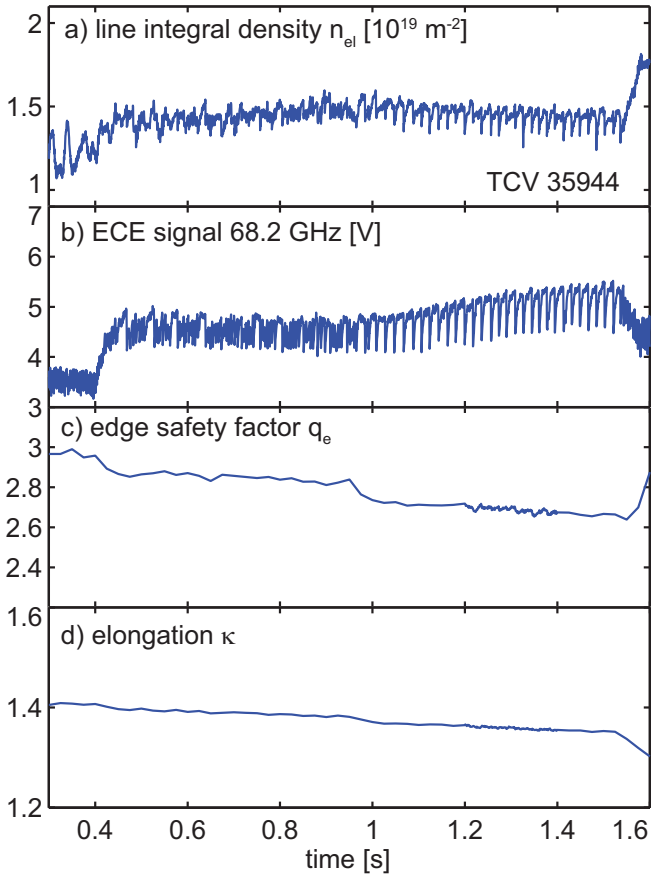

Figure 8.2: Main traces of TCV 35944 discharge. In the second part of the discharge a quasi stationary phase with $\tau_{ST} \approx 15$ ms was obtained ($1.1 < t < 1.5$ s).

The power and current density deposition profiles calculated with TORAY-GA are represented in Fig. 8.3. The ECCD deposition was localized outside the $q = 1$ surface, indicated in the graphs by a vertical line. During the experiments the radial location of the current drive deposition was

(1) This launching configuration, due the clockwise direction of B_ϕ and I_{p} used in this experiments, corresponds to co current directed current drive.

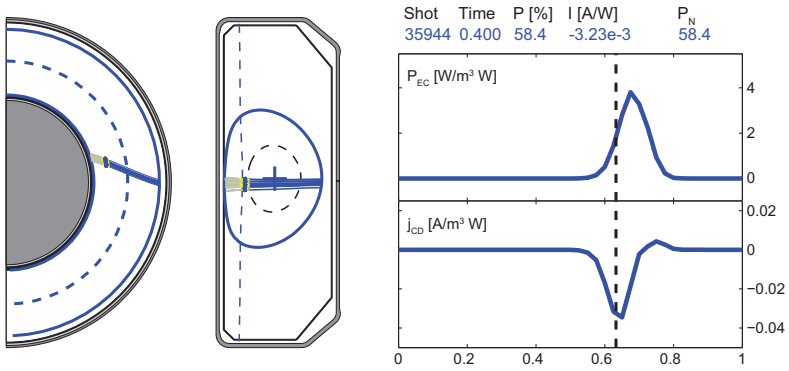

Figure 8.3: Current drive deposition scheme, reconstructed by the ray tracing core TORAY. The EC beam couples to the plasma just outside $q = 1$ surface, at the HFS. The EC driven current was negative, that is in the co current direction.

tuned, by sweeping the launcher toroidal injection angle. This operation has the principal effect of varying the electron heating and current drive efficiency, inducing small changes of safety factor profile.

Figure 8.2 shows some relevant traces from TCV 35944. Following an initial sweep, after 1.1 s the toroidal injection angle is maintained. Sawtooth periods τ_{ST} of the order of 10-15 ms are obtained, between $t = 1 \div 1.55$ s, in a quasi stationary phase lasting more than 400 ms.

8.2.2 CXRS acquisition setup

The fast toroidal rotation measurements were obtained with the LFS view of CXRS09 diagnostic. In standard operation mode the CCD detector of CXRS09 diagnostic is programmed to acquire 20 spectra for each time frame. Each spectrum results from the vertical bin of CCD rows corresponding to 20 Regions Of Interest (ROI) of the CCD surface. The standard exposure time of $10 \div 50$ ms permits to read out the 20 spectra with the maximum allowed spectral range (512 pixels, ≈ 65 Å). In order to reduce the exposure time to 2 ms and resolve timescales of the order of $\tau_{ST} \approx 10$ ms, the setup of CCD acquisition and read out has been optimized with the following actions:

- The acquired spectral range has been reduced to from 512 to 100 pixels (≈ 13 Å).
- The number of regions of interest to read out has been decreased from 20 to 4. This implies loss of radial coverage.
- To increase the spectral signal, the regions of interest have been vertically extended, so that each acquired spectrum results from the on-chip binning of CCD regions illuminated by 3,4 chords (Fig. 8.4). This implies a direct loss spatial resolution, as each acquired spectrum will result from the light coming from different radial locations in the plasma.
- The CCD is run in *double node read out* mode: with this option two separate nodes read out the left and right part of the CCD horizontal register.
- The stagnation time between read out of subsequent spectra, was decreased from 100 to 40 μs, with acceptable increase of read out noise.

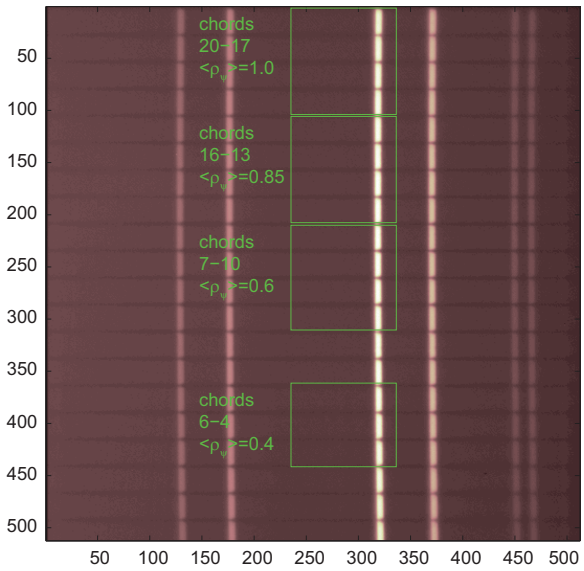

Figure 8.4: The CCD lecture scheme for fast CXRS acquisition mode is illustrated on a full frame acquisition of Neon light calibration spectrum: 4 spectra are read out. The average ρ_ψ is indicated for each.

With the present configuration, the resulting total read out time was 1.65 ms per frame. During experiments, the exposure time was set to 2 ms.

Alternative configurations are equally possible, varying the extension and number of ROI. E.g. limiting the read out to one ROI only, read out times down to 1 ms can be obtained. Nevertheless, the limiting factor then becomes the frame transfer time, that for the e2v 57-10 CCD detector is ≈ 300 μs. If the actual exposure time becomes comparable with the frame transfer time, the signal may be polluted by effect of smearing. For such measurements a mechanical shutter would be needed.

8.2.3 Coherent averaging

The reduction of the integration time of a factor of 15 or more (passing from 30 to 2 ms) implies a consequent reduction of CX spectral signal, that is only partially compensated by the on-chip binning of contiguous spectra. To counteract this problem, a coherent average analysis was adopted, taking advantage of the periodicity of the sawtooth.

CXRS fast measurements are grouped in ensembles of coherent spectra, sorted out following the time elapsed from the latest sawtooth crash t_{ca}. The spectral analysis will be then performed on data averaged within the ensembles. The final results will provide the evolution of rotation for the *average* sawtooth.

Coherent averaging has been widely applied in the plasma diagnostic domain [132, 133], but to our knowledge, it has never been implemented before for active CX measurements.

The fact that the 2 ms exposure time is comparable to the timescale of the phenomenon to be observed, imposes strict constraints to the measurement procedure. In fact, the continuous acquisition of a sequence of sawteeth, in coherent average spirit corresponds to a randomized sampling of the *average* sawtooth. In this case, measurements will be inevitably overlapping, smoothing out the dynamic that has to be resolved.

To overcome this difficulty, an external trigger system was designed and programmed, which provides a sequence of trig signals starting at the sawtooth crash. This way, the post crash phase

is sampled regularly, and CXRS frames can be sorted in ensembles following $t_{ca} = 1, 2, 3, ...$ ms, without overlap of exposure windows.

To attain this, a system for real time detection of sawtooth crashes was built, illustrated in Fig. 8.5. The raw signal coming from a central chord of camera 1 of XTOMO diagnostic (observing trough the plasma core), is digitalized by means of a d-tACQ196 acquisition card [134]. Within the same device, a real time analysis of the digital signal is performed, based on an algorithm of crash detection, which was programmed and tuned on the expected experimental waveforms. After each detected crash a sequence of pulses is provided at the d-tACQ output which are used as external trigger for the CXRS detector. Fig. 8.6 shows an example of real time generation of CXRS triggers, comparing the input SXR raw trace with the analog output of the CCD (parametric of the CCD read out phases).

An important element of CXRS09 measurements is a reliable distinction of the component of the spectrum induced by the DNBI (active) from the background component (passive). In standard operation, the background component is determined from the pulsed modulation of DNBI (see chapter 2). As the minimal duration of a DNBI pulse is ≈ 5 ms, this procedure is not applicable to fast CXRS measurements. Conversely, DNBI pulses of 15 ms were used during the experiment (larger than exposure time), with alternate ON and OFF phases, independently from the CXRS acquisition. A posteriori, an approximately equal number of beam ON and beam OFF spectra is expected, which will be treated separately in the analysis.

The CXRS09 data analysis, based on coherent averaging, was performed on a discharge time window characterized by small variation of plasma and sawtooth parameters. The main steps are summarized here:

1. Acquired spectra are sorted out in ensembles following t_{ca}, the time elapsed from the latest sawtooth crash. For the cases presented here $t_{ca} = 1, 2, 3...$ ms. DNBI ON spectra and DNBI OFF spectra are grouped in separate ensembles.

2. For each time t_{ca}, the average spectrum is calculated over the corresponding ensemble. DNBI ON spectra and the DNBI OFF spectra are considered separately.

3. For each time t_{ca}, the average DNBI OFF spectrum is subtracted from the average DNBI ON spectrum. At this point an *average* CX *active* spectrum is available for each t_{ca}.

4. Standard CXRS spectral analysis is performed on averaged active spectra, to obtain T_i and u_ϕ profiles as function of t_{ca}. A key aspect in this phase is to take into account properly of the instrumental function and calibration spectra, corresponding to the fast CCD read out scheme.

8.3 Experimental results

The main results were obtained on two TCV discharges (TCV 35944, 35946), with similar plasma parameters but different sawtooth periods. First of all, we consider the stationary part of the discharge TCV 35944 where the sawtooth period was stabilized to $\tau_\mathrm{ST} \approx 17$ ms. In Fig. 8.7 the reference SXR signal during the sawteeth selected for the coherent average analysis are plotted, indicating the reproducibility of the phenomenon in the selected time window. An increase of τ_ST from 15 to 20 ms, is visible due to the slow drift of q_e along the discharge.

In Fig. 8.8 some example of experimental spectra are illustrated. Top plots show the selected spectra for two acquired channels, corresponding to the first time window after the sawtooth crash

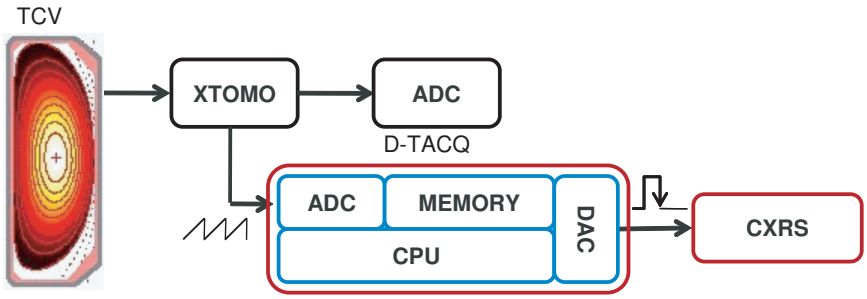

Figure 8.5: Schematic of the real time trigger system. The raw analog signal of a central chord of the XTOMO diagnostic, is the input of a d-tACQ acquisition card. The signal is digitalized and then processed in real time by a sawtooth crash detector algorithm. When a sawtooth crash is detected, TTL signal is generated and sent to the CXRS CCD detector.

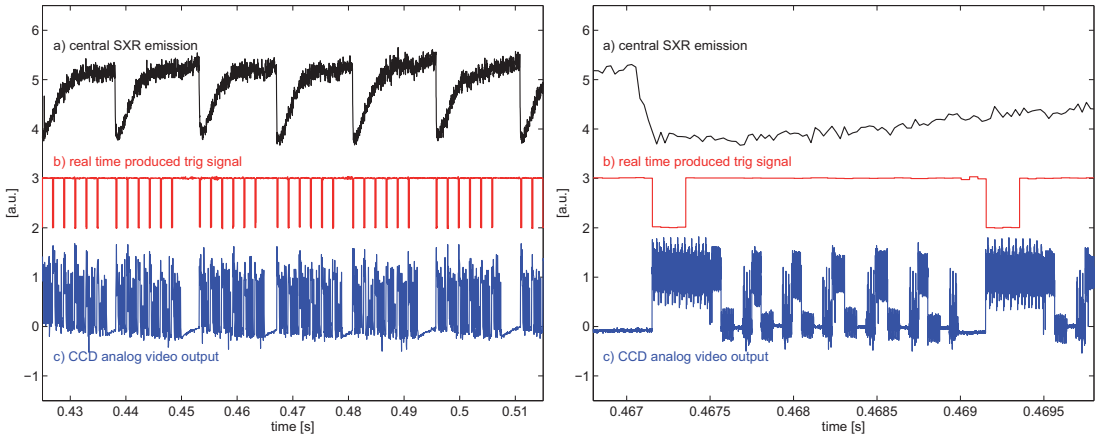

Figure 8.6: Example of real time CXRS09 trig on sawtooth crash. Left graph compares the raw SXR signal (a), the trig sequence generated by the d-tACQ card (b), and the CCD analog video output (c). In this case 6 frames are acquired after each sawtooth crash. For each frame 6 regions of interest are read out, as visible in the zoomed view (Right graph).

($t_{ca} = 1$ ms). Beam ON and OFF spectra are plotted in the same graphs. Owning to the on chip binning, the signal level is sufficiently high. Within a given ensemble, the spectra appear to be similar within the noise level, as requested for reliable coherent averaging. For channel 1 only, the average DNBI ON and OFF spectra are shown on bottom plots, together with the average active spectra calculated by subtraction. The last graph compares the active spectra for two selected times, $t_{ca} = 1$ ms (first measurement after the crash), and $t_{ca} = 11$ ms: a Doppler shift is apparent.

To estimate the convergence of the coherent averaging, the spectral analysis has been performed for several subset of active spectra, with an increasing number of elements. An example is provided in Fig. 8.9, where toroidal rotation u_ϕ at $t_{ca} = 1$ ms, for two channels is shown. In the graph, each point corresponds to u_ϕ calculated considering a different subset of active spectra. When a small number of spectra is considered in the analysis, different subsets lead to different results. With increasing number of spectra we observe a convergence towards the value calculated on the whole set. The spread of velocities calculated on half of the available active spectra, represents a reasonable estimate of the uncertainty introduced by the analysis. In this case we obtain ± 1 km/s, which is of the same order of other error sources inherent to the CXRS measurement (e.g. wavelength calibration).

We now turn on the final results, that are shown Fig. 8.10 for TCV 35944. In the top graph a sawtooth trace is presented as time reference. The rotation evolution in three regions along

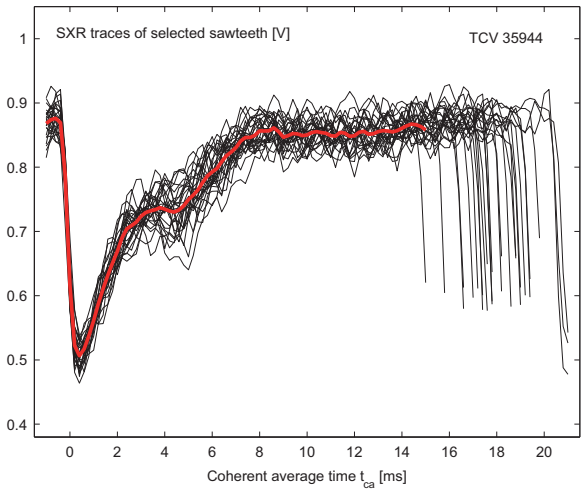

Figure 8.7: SXR traces for sawteeth selected for the coherent average analysis. The average trace, superimposed in red provides some indication of a partial reconnection at $t_{ca} = 5$ ms (TCV 35944).

the plasma minor radius is presented in the second graph. The core measurement shows a strong evolution of the u_ϕ in between sawtooth crashes. Just after the crash, $t_{ca} = 1$ ms, the plasma core rotates at $+4$ km/s, in the co current direction. Then it accelerates in the counter current direction, until the u_ϕ saturates at -5.5 km/s, at $t_{ca} = 9$ ms. Then the value remains approximately constant, until the last measurement at $t_{ca} = 13$ ms, suggesting that a relaxed stated has been reached. For $t_{ca} > 13$ ms the lack of statistics prevented a reliable coherent average analysis. Comparing the last measurement with the first, a differential $\Delta u_{\phi,crash} \approx 9.5$ km/s in the co current direction is found at the sawtooth crash. This is coherent with the average effect observed and well outside the uncertainty of the measurement.

Considering the more external measurements, we see a less pronounced evolution. This is visible in the sequence of radial profiles shown in the bottom graph, where the core evolution is visible on a profile that changes little for $\rho_\psi \geq \rho_{\rm inv} \approx 0.6$. Notice that the final developed profile is, in the diagnosed region, rather flat, with a slightly co current u_ϕ in the region close to the edge. This is somehow coherent with measurements in $q_e < 3$ discharges, where a rather flat profile was observed for $\rho_\psi > \rho_{\rm inv}$ together with a co current edge rotation (see e.g. the lowest q_e discharges in Fig. 4.3). However, this may also result from the loss of spatial resolution due to the on-chip binning, or an effect of smearing, hard to quantify , which affects more the upper part of the CCD, hence the peripheral channels.

The measurements of TCV 35944 have been confirmed by the ones on TCV 35946, where with with EC injection at lower toroidal angle, $\tau_{\rm ST} \approx 10$ ms has been obtained for a time window of 400 ms. Indeed the u_ϕ core trace evolves similarly to what observed in TCV 35944 discharge in both absolute values and timescale. Because of the shorter $\tau_{\rm ST}$, the last CXRS measurement falls before the stationary u_ϕ is attained. Conversely, a larger number of sawteeth has been sampled, so that the measurements are more accurate.

8.4 Discussion

The experimental evidence of the fast time resolved CXRS measurements in between sawteeth crashes demonstrates that, at the crash the plasma core accelerates in the co current direction; then the core rotation profile tends to relax to a counter current directed rotation, in a time scale of ≈ 10 ms. The co current bulge observed inside the inversion radius in in standard CXRS

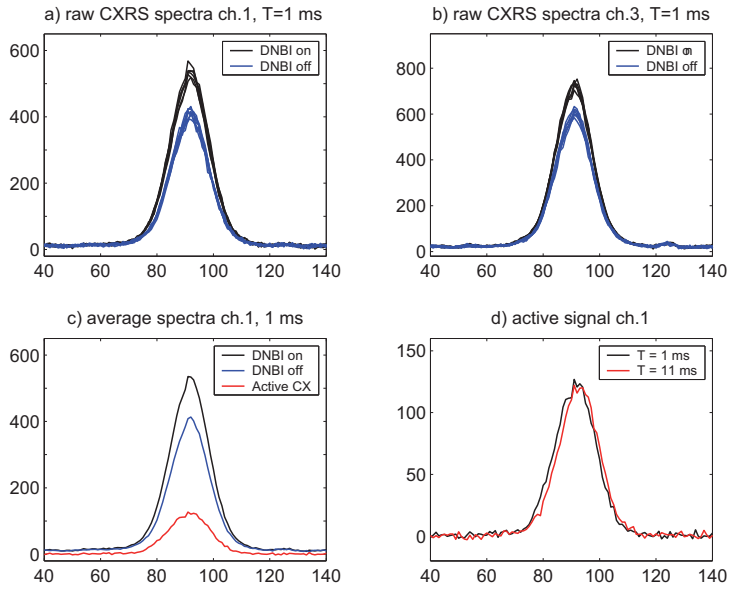

Figure 8.8: Top graphs: CXRS spectra selected for coherent averaging analysis of channel 1 (a) and 3 (b), for the first frame after sawtooth crash (TCV 35944). Bottom graphs: average spectra for channel 1 (c), and comparison of two active spectra separated by 10 ms (d). The Doppler shift indicating a change in rotation is visible (d). The abscissae axis represent the horizontal axis of the CCD detector.

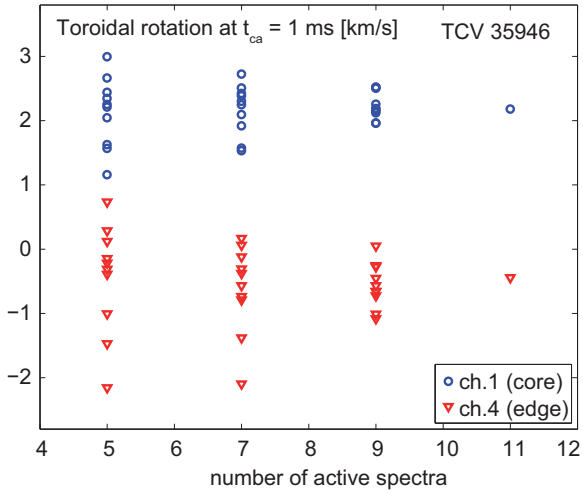

Figure 8.9: Convergence of coherent average results, for the toroidal rotation measured by two CXRS channels at $t_{ca} = 1$ ms. Each point represents the rotation calculated considering a different subset of spectra in the total coherent ensemble, as a function of the number of DNBI ON spectra selected (TCV 35944).

measurement would be the results of such dynamic, integrated over several cycles.

The effect is clear and robust, so it is expected to be related to a common physical mechanism. In a first interpretational step, the redistribution of momentum due to magnetic reconnection and an acceleration induced by reconnection toroidal electric field, have been considered. The following sections, report some preliminary study to address the possible role of these two mechanism.

8.4.1 Momentum redistribution during magnetic reconnection

In [135] the evolution of T_e in TCV plasmas under sawtooth activity and in presence of ECH, was described according to the theoretical model in [136]. Within this model, the description of the

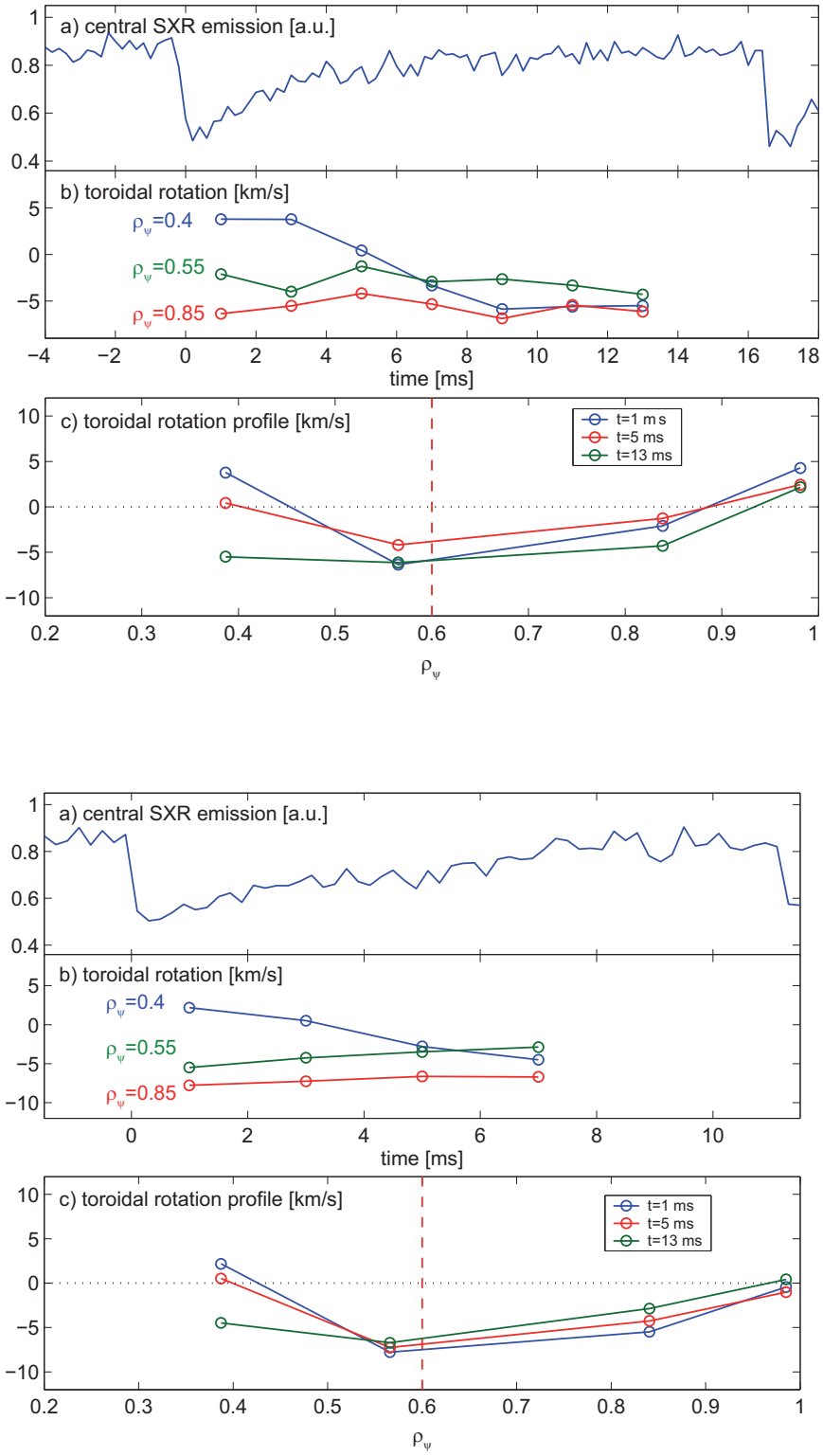

Figure 8.10: Results of fast CXRS measurement for TCV (35944) (top graphs) and TCV (35946) (bottom graphs). For each discharge, a reference SXR trace is shown in (a); the evolution of u_ϕ before the following sawtooth crash is shown in (b) for three radial channels. The radial profile at three reference times is represented in (c).

sawtooth crash is based on the Kadomtsev [137] theory of full or partial reconnection, in which topological constraints combined with particle and thermal energy conservation, are invoked to

determine the relaxed post-crash T_e profile, as a function of the pre-crash profile.

The model can easily be extended to include toroidal momentum and velocity. The mixing rules for toroidal rotation profiles are derived observing the formal correspondence between thermal energy $p_e = n_e T_e$ and toroidal momentum $p_\phi = m_i n_i u_\phi$ [135]. For the detailed derivations we refer to [135]. Interestingly, in the cited reference it was found that, following the degree of peaking of the pre crash T_e profile, the post-crash radial profile may result hollow (*hot ring*), flat or slightly peaking.

To estimate the impact of this effect on plasma rotation in TCV Ohmic discharges, the reconnection model was implemented in the ASTRA transport code [138], including the mixing rules for toroidal rotation profile. A set of simulations has then been performed on a reference Ohmic plasma (TCV 35928), assuming different test u_ϕ profiles, calculated from expression:

$$u_\phi(r) = u_{\phi 0}\left(1 - \frac{r^2}{a^2}\right)^\alpha \tag{8.4.1}$$

where $u_{\phi 0}$ defines the amplitude and direction of the toroidal rotation and α the peaking of the profile. In the transport simulation, sawtooth was modeled to obtain the experimental sawtooth period ($\tau_{ST} \approx 5$ ms). Fig. 8.11 shows the result of a relaxation of u_ϕ profile calculated assuming total magnetic reconnection, for a strongly ($\alpha = 3$) and weakly ($\alpha = 0.5$) peaking profiles, for the pre-crash u_ϕ. The relaxed rotation profile is hollow, with the effect especially evident in the peaking u_ϕ case, in qualitative agreement with TCV observations. For the lower peaking case, the effect is similar but less pronounced.

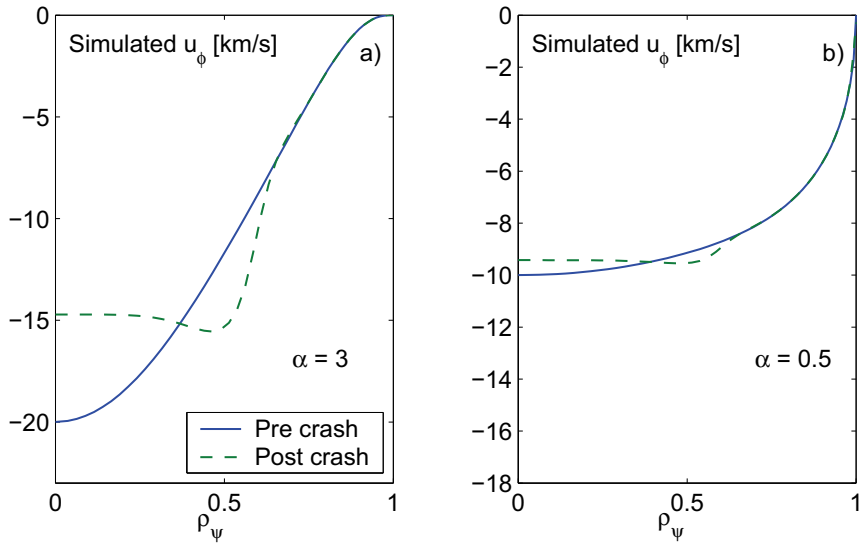

Figure 8.11: Effect of the total magnetic reconnection calculated by ASTRA, for two test u_ϕ profiles: peaked (a) and flattened (b). The after crash rotation profile is hollow.

It must be stressed, that this effect depends only on the peaking degree of the pre-crash u_ϕ profile, and returns the same results for opposite peaking direction. For similar peaking in opposite direction, as it is the case for TCV rotation reversals, the relaxed rotation profile is hollow in the core. In other words the transport of momentum related to the magnetic reconnection, in this model, can not alone explain the fact that is $\Delta u_{\phi,ST}$ is always observed in the co counter direction, independently on the rotation regime.

8.4.2 Toroidal electric field

To account for the fact that under the sawtooth activity, core u_ϕ profile always bulges in the co current direction, the role of strong toroidal electric field that develops the during the magnetic reconnection (sawtooth collapse) has been considered. In fact, the relaxation of the current density profile at the sawtooth crash, implies a variation of the poloidal magnetic flux ψ, that corresponds to a toroidal electric field E_ϕ in the direction of the plasma current.

The flows induced by a static parallel electric field have been addressed extensively in the past, with the aim of clarify the role of the inductive electric field on plasma toroidal rotation. This contribution has been evaluated for TCV Ohmic discharges [45] and it results small compared to the measured velocities. Nevertheless, the transient parallel electric field that develops at the reconnection is much higher than the inductive one, and can have strong accelerating effect on plasma particles. Good examples are the observed acceleration of electrons [16,139] and ions [140] to suprathermal energies, during magnetic reconnection events, related to toroidal electric fields of the order of tens of V/m. The theoretical modeling also supports the role of E_ϕ in these measurements [141]. The effect of the transient reconnection E_ϕ on bulk ions and impurities populations, has not been directly addressed specifically in the frame of tokamak research.

In general, the evolution of ion velocity over a non stationary E_ϕ event is the result of the interplay between electric force and friction forces within electrons, ions and impurities. The correct evaluation is complicated as the timescale for the reconnection can be smaller than the ion-ion collision time but larger than the electron ion collision time.

To clarify the elements at play, we estimated the electric field that develops at the sawtooth crash in the experiments presented in this chapter. This is done evaluating the poloidal flux variation before and after the crash. In TCV, the poloidal flux is not measured directly. A rough evaluation from experimental data set can be made as in [139], estimating the safety factor q variation from the knowledge of q_e and the radial position of $q = 1$ surface: $E_\phi \approx 10$ V/m was found in the core plasma across the sawtooth crash. To estimate $\Delta\psi$ with better accuracy, we applied a different strategy: the sawtooth crash has been simulated with the model [142] by means of the transport code ASTRA [138], with plasma parameters from TCV 35944.

In Fig. 8.12 the variation of poloidal flux,, at the sawtooth crash $\Delta\psi = \psi_{pre} - \psi_{post}$ is shown, along the minor radius ρ_ψ. This variation takes place on a time interval of time interval of $\Delta t \approx 100$ μs.

Over a sawtooth crash, the poloidal flux ψ diminishes in the core and increases in a region localized around $\rho_\psi = 0.6$ (a). For more external radii ψ is unchanged, coherently with a flattening of the core current density profile. The toroidal electric field engendered by this magnetic flux variation is plotted in graph (b), indicating that a co current directed force is exerted on ions in the central region.

The velocity that a free ion would acquire under such force is proportional to $\Delta\psi$ and does not depend on Δt:

$$\frac{\Delta u_\phi}{\Delta t} = \frac{qE}{m} = -\frac{1}{2\pi R}\frac{q}{m}\frac{\Delta\psi(R)}{\Delta t} \tag{8.4.2}$$

$$\Delta u_\phi = -\frac{1}{2\pi R}\frac{q}{m}\Delta\psi(R) \tag{8.4.3}$$

where q and m are the charge and mass of the particle, and R is the major radius. This free ion velocity increment depends on the q/m ratio, hence is the same for deuterium and carbon species. Bottom graph in Fig. 8.12 shows Δu_ϕ induced on plasma ions by the $\Delta\psi$ on top graph. Remarkably the free ion Δu_ϕ is comparable with the toroidal rotation excursion measured by CXRS fast acquisition in the same discharge, with values somehow higher than that observed experimentally (16 km/s to compare with the 9 km/s measured).

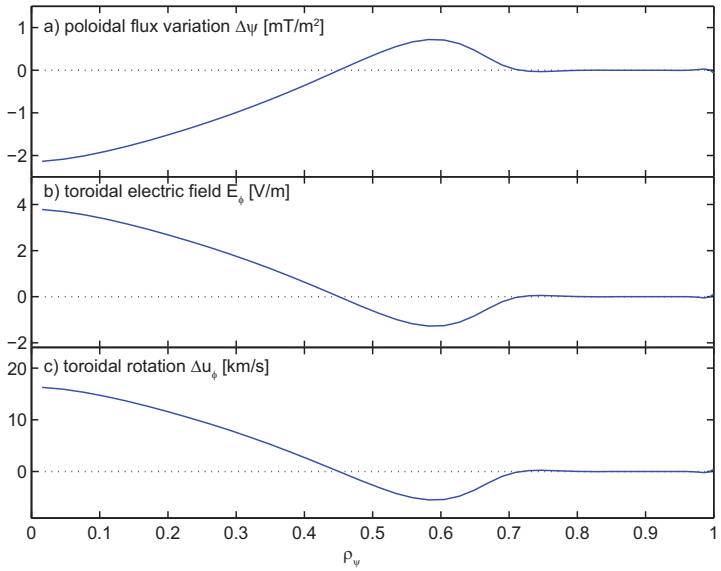

Figure 8.12: a) Poloidal flux variation at the sawtooth crash, simulated with ASTRA transport code [138] assuming total magnetic reconnection at the sawtooth crash (TCV 35944). b) Resulting toroidal electric field E_ϕ. c) Free ion acceleration induced by E_ϕ.

Of course the free ion acceleration is a drastic approximation of the problem. For example, it neglects friction forces and viscosity, that indeed may change radically the picture, e.g. predicting opposite direction acceleration for main ions and impurities in response to an applied electric field [38, 141].

However, friction effects are at play on timescales longer than ion-ion collision time τ_{ii} and the ion electron slowing down time τ_s:

$$\tau_s = \frac{3(2\pi)^{3/2}\epsilon_0^2 m_i T_e^{3/2}}{n_e e^4 m_e^{1/2} ln\Gamma} = \left(\frac{m_i}{m_e}\right)^{1/2}\left(\frac{T_e}{T_i}\right)^{3/2}\tau_{ii} \approx 60\tau_{ii} \tag{8.4.4}$$

While they have to be taken into account when addressing the stationary inductive E_ϕ effect [38, 141] or long lasting magnetic ($\tau_{ST} < \tau_{ii}$) reconnection events [140], they may have a less important role in the cases addressed here. In fact, for TCV Ohmic plasmas the ion-ion collision time τ_{ii} in the plasma core range typically between 0.2 to 1 ms. In particular for TCV 35944 $\tau_{ii} \approx 0.7$ ms, which is an order of magnitude longer than the sawtooth crash $\Delta t_{crash} \leq 100\ \mu s$.

A further strong approximation is also that the dynamic of development of E_ϕ is not spatially resolved. In fact, the reconnection electric field develops, in reality, in a more localized region (current sheet) where the reconnection takes place, whose extension has not been determined in this work.

These preliminary considerations, that in no way constitute a physical explanation of the phenomenon, suggest that the toroidal electric field may play an important role in accounting for the asymmetry of the of sawtooth effect on toroidal rotation u_ϕ.

8.5 Conclusions

The question of the effect of sawtooth on the toroidal rotation profile has been experimentally addressed, in an experimental scenario that permitted the measurement of the evolution of toroidal plasma rotation in between sawtooth crashes.

The experiments required the development of a new technique of active CXRS measurement, combining fast spectra acquisition with coherent average analysis methods. The optimization of the read out parameters of the CCD detector allowed to acquire four spectral channels with exposure times of 2 ms. A key point for the measurement was the possibility of synchronizing the CXRS acquisition with the sawtooth crashes. A real time triggering system, based on the observation of SXR radiation from the core, has been developed for this scope.

The measurements were performed on discharges specifically designed to maximize the effect of sawtooth. In particular the sawtooth period was extended up to 15 ms employing co current ECCD localized in the proximity, but outside, the $q = 1$ resonant surface.

The results indicate that at the sawtooth crash the plasma rotation increases abruptly in the co current direction. After the crash the core rotation increases counter current towards a saturated value, that in the present discharges was attained after 10 ms.

With preliminary investigations, the role of the momentum transport and toroidal electric field developed during a reconnection event as the sawtooth crash has been considered. Both elements appear likely to have a role in the phenomenon.

These experiments open the route to a more detailed study of fast dynamics of plasma rotation. Experimental activity on Edge Localized Modes relaxations in H-mode are already planned, with the diagnostic set up for fast acquisition triggered on D_α raw signal from photodiode.

Chapter 9

Conclusions and perspectives

This thesis, carried out at the *Centre de Recherches en Physique des Plasmas*, was devoted to the experimental study of rotation of plasmas magnetically confined in the TCV tokamak. The work is based on measurements from the CXRS diagnostic. In combination with a low power Diagnostic Neutral Beam, the CXRS diagnostic provides time and space resolved measurements of ion density, temperature and velocity, from analysis of spectroscopic emission of intrinsic carbon impurity.

The TCV CXRS diagnostic was first constructed as the thesis project of Dr. Bosshard [23]. Since the start of this work, the diagnostic was optimized for the measurement of plasma rotation and was upgraded to extend the measurement capabilities. In particular, the following operations were performed:

- An automated wavelength calibration system was installed. The nominal wavelength of the observed carbon CVI($n = 8 \rightarrow 7$) line, used for the calculation of Doppler shift, was determined experimentally by perpendicular observation of the passive emission. Viable measurement of rotation are obtained with uncertainties less than 1 km/s.

- A High Field Side (HFS) CXRS view, measuring the toroidal rotation across the inboard plasma radius and a VERtical (VER) view, for the observation of the plasma edge and the measurement of the poloidal velocity, were installed.

- The horizontal observation systems were modified to increase the radial resolution from 16 to 40 local measurements and to extend the radial coverage to the plasma edge. The Low Field Side (LFS) and HFS views have been equipped with new CCD back illuminated detectors, increasing the quantum efficiency to $\approx 85\%$, extending the measurable range of plasma density.

- A new measurement technique was developed and implemented for the measurement of periodical phenomena faster than the CXRS standard exposure time (e.g. sawteeth or Edge Localized Modes). The CXRS input trigger is constructed in real time from the observation of a plasma trace (e.g. SXR emission).

At the time of writing, the CXRS09 diagnostic consists of three independent systems, each capable of providing 40 local measurements of toroidal/poloidal rotation at a sampling rate of 60-150 ms, in most of TCV scenarios.

The CXRS diagnostic in TCV works in combination with a "pencil" Diagnostic Neutral Beam that induces only minor perturbations in the plasma. In particular, for most of the TCV scenarios,

the applied torque does not affect significantly the rotational state of the plasma, so that the so called intrinsic rotation of the plasma can be measured.

During this thesis the CXRS-DNBI tandem was employed for the first systematic study of plasma rotation in TCV. Although probably only the first step of a longer term research, the Ohmically heated discharges in low confinement mode (L-mode) were addressed. Some general features of the plasma rotation in TCV Ohmically heated discharges are listed here:

- Even in absence of externally applied torque, the plasma column accelerates to toroidal velocities $u_\phi \lesssim 50$ km/s, that is a significant fraction of the sound speed and of the order of the main ion diamagnetic speed.

- The toroidal rotation profile is sensitive to the plasma parameters. Spontaneous reversals of u_ϕ profile may take place as plasma parameters are dynamically varied, as with density or current ramps.

- Observation of poloidal rotation $u_\theta \sim 2$ km/s is coherent in amplitude and direction with predictions of neoclassical theory. A sharp peak of $u_\theta \approx 6$ km/s, localized near the plasma edge, was observed for limited magnetic configurations.

- Measurements of u_ϕ on the High Field Side midplane indicates that the carbon angular velocity $\omega_\phi = u_\phi/R$ is a flux surface quantity only to first approximation. The deviations from the rigid rotor approximation were explained by assuming poloidal velocity of the same order as that measured.

- The radial electric field E_r, estimated from the force balance equation, indicate that $E_r \lesssim 3$ kV/m in the peripheral plasma region and close to zero at the plasma edge. In the plasma core, positive or negative values are found, following the direction of toroidal plasma rotation.

- Plasma velocity contains a dominant $E \times B$ component, with the diamagnetic component increasing strongly in the edge proximity.

More specifically, in the experimental approach, the scenario of Ohmic plasmas in limited magnetic configurations was addressed first and then extended to diverted configurations. Surprisingly, modification of the magnetic topology in the boundary region has a substantial effect up to the core region. A rich phenomenology was encountered that was summarized using a practical description of the rotation profile in three radial regions.

Peripheral region ($0.85 < \rho_\psi < 1$). In limited plasmas, u_ϕ in the plasma periphery is observed to be close to zero for a large range of plasma parameters (no-slip boundary condition). This effect is possibly caused by a momentum sink constituted by the neutral particles in the plasma boundary. Conversely, in diverted configurations, the peripheral toroidal velocity varies strongly with n_e and I_p and is also sensitive to the direction of the ion $\vec{B} \times \nabla B$ drift, suggesting a relation with parallel fluxes present in the Scrape-Off Layer region. Comparison between measurements of CXRS09 and Reciprocating Mach probe, in the edge region ($\rho_\psi \approx 1$), indicate a strong coupling between the edge toroidal rotation and the SOL parallel particle fluxes.

Intermediate or gradient region ($\rho_\mathrm{inv} < \rho_\psi < 0.85$). In this region, extending inside the plasma and up to the sawtooth inversion radius, the plasma rotation increases monotonically with a gradient approximately proportional to ion temperature gradient [45]. However, following the plasma conditions, positive or negative gradient has been observed. This property, more than the rotation value itself, characterizes the co and counter rotation regimes observed in TCV Ohmic L-mode discharges. The transition between the two regimes was observed and induced by tailoring

the plasma parameters (n_e, I_p, Electron Cyclotron Heating deposition, magnetic configuration). In limited configurations, co current directed rotation in observed in high density and high current discharges ($n_{e,av} > 4{\times}10^{19}\,m^{-3}$, $q_e \approx 3$). The opposite dependence on density is found in diverted discharges, where co and counter current rotation regimes are observed respectively at low and high n_e. An underlying physics mechanism has not been identified.

Core or sawtooth region ($0 < \rho_\psi < \rho_{inv}$). In this region, the toroidal rotation profile, in all configurations and in both co and counter rotation regimes, is found to be "bulged" in the co current direction. The effect of the sawtooth crash on the toroidal rotation profile was investigated in dedicated experiments employing fast CXRS measurements to measure the central rotation evolution between sawtooth crashes. The results indicate a substantial (+9 km/s) co current acceleration at the core plasma, at the sawtooth crash. A complete model of the process has not yet been developed. Among the physical mechanisms that may play a role, two aspects were preliminarily considered, which are intrinsic to the magnetic reconnection occurring at the sawtooth crash: the redistribution of toroidal momentum inside the sawtooth mixing radius and the development of a strong toroidal electric field. With the support of the transport simulations based on the standard Kadomtsev model [135, 137], both effects were addressed separately and could be relevant in the comprehension of the phenomenon.

Applying multivariate regressions to stationary rotation measurements, phenomenological scaling laws have been formulated that describe the toroidal rotation profile from knowledge of some operational parameters. For example, the increment of rotation in the intermediate region in diverted configuration was found to be roughly proportional to the product $n_e T_i$, suggesting a role of stored ion energy for the drive of plasma spontaneous rotation .

In the absence of external torques or strong internal momentum sinks, the spontaneous peaking of the rotation profile results from the equilibrium between diffusive (radial viscosity) and non diffusive (convection, residual stress) components of momentum flux. From the analysis of toroidal rotation in stationary and transient phases, a characterization of momentum transport was attempted. A remarkable result is the existence of a residual stress component that sustains a substantial stationary rotation gradient over null background rotation. Conversely, the analysis suggests a minor role for the convective (*pinch*) component. This was supported by preliminary gyro-kinetic simulations with the GKW code using TCV relevant simulation parameters that included the turbulent Coriolis convective pinch. Neoclassical predictions were shown to be in quantitative and qualitative disagreement with the experimental observations.

During this thesis, the combination of TCV's flexibility, with the possibility of measuring plasma rotation with high spatial resolution without affecting the momentum balance of the plasma, opened a new experimental domain. Despite the extraordinarily rich amount of data collected, many questions remain unanswered, in particular, the key question of what is the mechanism or the combination of mechanisms that causes the spontaneous rotation. Several theoretical models have been recently proposed, often invoking the turbulent part momentum transport. However, a direct theory-experiment comparison is not straight forward and, in view of the range of theoretical models, to some extent premature.

An important contribution of this thesis is to have shown that the spontaneous rotation of a tokamak plasma is the result of a combination of effects, covering a vast range of plasma physics domains: edge physics, magneto hydrodynamic, neoclassical and turbulent transport, magnetic reconnection. This complexity requires a combined approach to the problem. In particular, some

effort should be devoted to the integration of neoclassical effects, important in the peripheral/edge region, and turbulent transport effects, mostly relevant in the gradient region.

From the experimental point of view, an important step forward will be the simultaneous CXRS and fluctuations measurements. A Phase Contrast Imaging diagnostic is at present in the commissioning phase on TCV. The CXRS09 diagnostic will be upgraded with CCD detectors with increased sensitivity that permit considerably faster acquisition rates. The direct study of plasma rotation evolution on a faster time scale are bound to provide greater insight on momentum transport dynamics.

Studies will, in the future, start to address more complex scenarios as High confinement mode plasmas, ECH dominated regimes, for which only preliminary measurements have been obtained to date.

Bibliography

[1] URL: http://www.iter.org

[2] R. J. Goldston and P. H. Rutherford, ***Introduction to Plasma Physics***. Institute of Physics Publishing, Bristol and Philadelphia, 1995.

[3] T. J. Dolan, ***Fusion Research Principles, Experiments and Technology***. Pergamon Press, 1982.

[4] A. H. Boozer, **"Physics of magnetically confined plasmas**," *Rev. Mod. Phys.*, vol. 76, no. 4, pp. 1071–1141, Jan 2005.

[5] J. Wesson, ***Tokamaks***, ser. International series of monograph in physics. Oxford, UK: Oxford University Press, 2004.

[6] R. A. Pitts, J. P. Coad, D. P. Coster, G. Federici, W. Fundamenski, J. Horacek, K. Krieger, A. Kukushkin, J. Likonen, G. F. Matthews, M. Rubel, J. D. Strachan, and J.-E. contributors, **"Material erosion and migration in tokamaks**," *Plasma Physics and Controlled Fusion*, vol. 47, no. 12B, pp. B303–B322, 2005. URL: http://stacks.iop.org/0741-3335/47/B303

[7] F. Hofmann, J. B. Lister, W. Anton, S. Barry, R. Behn, S. Bernel, G. Besson, F. Buhlmann, R. Chavan, M. Corboz, M. J. Dutch, B. P. Duval, D. Fasel, A. Favre, S. Franke, A. Heym, A. Hirt, C. Hollenstein, P. Isoz, B. Joye, X. Llobet, J.-C. Magnin, B. Marletaz, P. Marmillod, Y. Martin, J.-M. Mayor, J.-M. Moret, C. Nieswand, P.-J. Paris, A. Perez, Z. A. Pietrzyk, R. A. Pitts, A. Pochelon, R. Rage, O. Sauter, G. Tonetti, M. Q. Tran, F. Troyon, D. J. Ward, and H. Weisen, **"Creation and control of variably shaped plasmas in TCV**," *Plasma Physics and Controlled Fusion*, vol. 36, no. 12B, pp. B277–B287, December 1994. URL: http://dx.doi.org/10.1088/0741-3335/36/12B/023

[8] O. Sauter, C. Angioni, S. Coda, P. Gomez, T. P. Goodman, M. A. Henderson, F. Hofmann, J.-P. Hogge, J.-M. Moret, P. Nikkola, Z. A. Pietrzyk, H. Weisen, S. Alberti, K. Appert, J. Bakos, R. Behn, P. Blanchard, P. Bosshard, R. Chavan, I. Condrea, A. Degeling, B. P. Duval, D. Fasel, J.-Y. Favez, A. Favre, I. Furno, R. R. Kayruthdinov, P. Lavanchy, J. B. Lister, X. Llobet, V. E. Lukash, P. Gorgerat, P.-F. Isoz, B. Joye, J.-C. Magnin, A. Manini, B. Marlétaz, P. Marmillod, Y. R. Martin, A. Martynov, J.-M. Mayor, E. Minardi, J. Mlynar, P. J. Paris, A. Perez, Y. Peysson, V. Piffl, R. A. Pitts, A. Pochelon, H. Reimerdes, J. H. Rommers, E. Scavino, A. Sushkov, G. Tonetti, M. Q. Tran, and A. Zabolotsky, **"Steady-state fully noninductive operation with electron cyclotron current drive and current profile control in the tokamak [a-grave] configuration variable (TCV)**," *The 42nd annual meeting of the division of plasma physics of the American Physical Society and the 10th international congress on plasma physics*, vol. 8, no. 5, pp. 2199–2207, 2001. URL: http://link.aip.org/link/?PHP/8/2199/1

[9] F. Hofmann and G. Tonetti, **"Tokamak equilibrium reconstruction using Faraday-rotation measurements**," *Nuclear Fusion*, vol. 28, no. 10, pp. 1871–1878, October 1988.

[10] J.-M. Moret, F. Buhlmann, D. Fasel, F. Hofmann, and G. Tonetti, **"Magnetic measurements on the TCV Tokamak**," *Review of Scientific Instruments*, vol. 69, no. 6, pp. 2333–2348, June 1998, tCV Magnetics.

[11] I. H. Hutchinson, ***Principles of Plasma Diagnostics***. Cambridge: Cambridge Univ. Press, 1987.

[12] R. Behn, S. Franke, and Z. A. Pietrzyk, **"The Thomson Scattering diagnostic on the TCV tokamak**," in *Proceedings of the 21th EPS conference on Controlled Fusion and Plasma Physics*, Montpellier, France, 1994.

[13] E. P. Bertin, ***Principles and Practice of X-Ray Spectrometric Analysis***. Plenum Press, 1978.

[14] Y. Camenen, **"Etude du tranport d'énergie thermique dans les plasmas du Tokamak à Configuration Variable au moyen de chauffage électronique cyclotronique**," Ph.D. dissertation, Ecole Polytechnique Fédérale de Lausanne, thesis EPFL n.3618, 2006.

[15] I. Furno, **"Fast transient transport phenomena measured by soft x-ray emission in TCV tokamak plasmas**," Ph.D. dissertation, Ecole Polytechnique Fédérale de Lausanne, thesis EPFL n.2434, 2001.

[16] C. Schlatter, **"Turbulent ion heating in TCV tokamak plasmas**," Ph.D. dissertation, Ecole Polytechnique Fédérale de Lausanne, thesis EPFL n.4479, 2009.

[17] M. Mironov, **"DOUBLE-TCV: Simulation of CX fluxes emitted by tokamak plasma**," A.F.Ioffe Phisico-Technical Intitute, St. Petersburg, Russian Federation, Tech. Rep., 2006.

[18] J. Horacek, **"Measurement of edge electrostatic turbulence in the TCV tokamak plasma boundary**," Ph.D. dissertation, Ecole Polytechnique Fédérale de Lausanne, thèse EPFL n.3524, 2006.

[19] E. Doyle, W. Houlberg, Y. Kamada, V. Mukhovatov, T. Osborne, A. Polevoi, G. Bateman, J. Connor, J. Cordey, T. Fujita, X. Garbet, T. Hahm, L. Horton, A. Hubbard, F. Imbeaux, F. Jenko, J. Kinsey, Y. Kishimoto, J. Li, T. Luce, Y. Martin, M. Ossipenko, V. Parail, A. Peeters, T. Rhodes, J. Rice, C. Roach, V. Rozhansky, F. Ryter, G. Saibene, R. Sartori, A. Sips, J. Snipes, M. Sugihara, E. Synakowski, H. Takenaga, T. Takizuka, K. Thomsen, M. Wade, H. Wilson, I. T. P. T. Group, I. C. Database, M. T. Group, I. Pedestal, and E. T. Group, **"Chapter 2: Plasma confinement and transport**," *Nuclear Fusion*, vol. 47, no. 6, pp. S18–S127, 2007. URL: http://stacks.iop.org/0029-5515/47/S18

[20] J. Rice, A. Ince-Cushman, J. deGrassie, L.-G. Eriksson, Y. Sakamoto, A. Scarabosio, A. Bortolon, K. Burrell, B. Duval, C. Fenzi-Bonizec, M. Greenwald, R. Groebner, G. Hoang, Y. Koide, E. Marmar, A. Pochelon, and Y. Podpaly, **"Inter-machine comparison of intrinsic toroidal rotation in tokamaks**," *Nuclear Fusion*, vol. 47, no. 11, pp. 1618–1624, 2007. URL: http://stacks.iop.org/0029-5515/47/1618

[21] P. de Vries, M.-D. Hua, D. McDonald, C. Giroud, M. Janvier, M. Johnson, T. Tala, K.-D. Zastrow, and J. E. Contributors, **"Scaling of rotation and momentum confinement in JET plasmas**," *Nuclear Fusion*, vol. 48, no. 6, p. 065006 (18pp), 2008. URL: http://stacks.iop.org/0029-5515/48/065006

[22] R. J. Fonck, D. S. Darrow, and K. P. Jaehnig, **"Determination of plasma-ion velocity distribution via charge-exchange recombination spectroscopy**," *Physical Review A*, vol. 29, no. 6, pp. 3288–3309, Jun 1984.

[23] P. Bosshard, **"Confinement ionique dans le tokamak TCV mesuré pas spectroscopie d'échange de charge**," Ph.D. dissertation, Ecole Polytechnique Fédérale de Lausanne, thèse EPFL n.2723, 2003.

[24] A. Zabolotsky, M. Bernard, V.Piffl, H. Weisen, A. Bortolon, B. Duval, and A. Karpushov, **"Carbon transport in TCV**," in *Proceedings of the 33rd EPS Conference on Plasma Physics, Rome, Italy, June 19–23, 2006*, ser. Europhysics Conference Abstracts (ECA), F. D. Marco and G. Vlad, Eds., vol. 30I, no. P-1.145. European Physical Society (EPS), 2006, contributed poster. URL: http://epsppd.epfl.ch/Roma/pdf/P1_145.pdf

[25] H. P. Summers, **"Atomic Data and Analysis Structure Manual**," JET, Tech. Rep. JET-IR (94) 06, 1994, from Paolo's thesis.

[26] M. von Hellermann, P. Breger, J. Frieling, R. Konig, W. Mandl, A. Maas, and H. P. Summers, **"Analytical approximation of cross-section effects on charge exchange spectra observed in hot fusion plasmas**," *Plasma Physics and Controlled Fusion*, vol. 37, no. 2, pp. 71–94, 1995. URL: http://stacks.iop.org/0741-3335/37/71

[27] R. C. Isler, **"An overview of charge-exchange spectroscopy as a plasma diagnostic**," *Plasma Physics and Controlled Fusion*, vol. 36, no. 2, pp. 171–208, 1994. URL: http://stacks.iop.org/0741-3335/36/171

[28] N. C. Hawkes, **"Experimental Studies of ion Pressure, Impurity Flows and their Influence on Trasport in te JET Tokamak**," Ph.D. dissertation, Imperial College of Science, Technology and Medicine, London, 1995.

[29] R. E. Bell and E. J. Synakowski, **"New understanding of poloidal rotation measurements in a Tokamak plasma**," *ATOMIC PROCESSES IN PLASMAS: Twelfth Topical Conference*, vol. 547, no. 1, pp. 39–52, 2000. URL: http://link.aip.org/link/?APC/547/39/1

[30] W. M. Solomon, K. H. Burrell, P. Gohil, R. J. Groebner, and L. R. Baylor, **"Extraction of poloidal velocity from charge exchange recombination spectroscopy measurements**," *Review of Scientific Instruments*, vol. 75, no. 10, pp. 3481–3486, 2004. URL: http://link.aip.org/link/?RSI/75/3481/1

[31] A. N. Karpushov, G. F. Abdrashitov, I. I. Averboukh, P. Bosshard, I. Condrea, B. P. Duval, A. A. Ivanov, V. V. Kolmogorov, J. Mlynar, A. Perez, I. V. Shikhovtsev, A. N. Shukaev, and H. Weisen, **"Upgrade of the diagnostic neutral beam injector for the TCV tokamak**," *Fusion Engineering and Design*, vol. 66-68, pp. 899 – 904, 2003, 22nd Symposium on Fusion Technology. URL: http://dx.doi.org/10.1016/S0920-3796(03)00373-9

[32] A. N. Karpushov, Y. Andrebe, B. P. Duval, and A. Bortolon, **"The diagnostic neutral beam injector with arc-discharge plasma source on the TCV**

Tokamak," *Fusion Engineering and Design*, vol. 84, no. 2-6, pp. 993 – 997, 2009, proceeding of the 25th Symposium on Fusion Technology - (SOFT-25). URL: http://dx.doi.org/10.1016/j.fusengdes.2008.12.006

[33] **A. Karpushov**, private communication, 2009.

[34] F. L. Hinton and M. N. Rosenbluth, **"The mechanism for toroidal momentum input to Tokamak plasmas from neutral beams**," *Physics Letters A*, vol. 259, no. 3-4, pp. 267 – 275, 1999. URL: http://dx.doi.org/10.1016/S0375-9601(99)00453-3

[35] S. Hirschman and D. Sigmar, **"Neocalssical Transport of Impurities in Tokamak Plasmas**," *Nuclear Fusion*, vol. 21, no. 9, pp. 1079–1201, 1981.

[36] J. D. Callen, A. J. Cole, and C. C. Hegna, **"Toroidal flow and radial particle flux in tokamak plasmas**," *Physics of Plasmas*, vol. 16, no. 8, p. 082504, 2009. URL: http://link.aip.org/link/?PHP/16/082504/1

[37] R. D. Hazeltine, **"Rotation of a toroidally confined, collisional plasma**," *Physics of Fluids*, vol. 17, no. 5, pp. 961–968, 1974. URL: http://link.aip.org/link/?PFL/17/961/1

[38] Y. B. Kim, P. H. Diamond, and R. J. Groebner, **"Neoclassical poloidal and toroidal rotation in tokamaks**," *Physics of Fluids B: Plasma Physics*, vol. 3, no. 8, pp. 2050–2060, 1991. URL: http://link.aip.org/link/?PFB/3/2050/1

[39] H. A. Claassen, H. Gerhauser, A. Rogister, and C. Yarim, **"Neoclassical theory of rotation and electric field in high collisionality plasmas with steep gradients**," *Physics of Plasmas*, vol. 7, no. 9, pp. 3699–3706, 2000. URL: http://link.aip.org/link/?PHP/7/3699/1

[40] P. J. Catto, R. J. Hastie, I. H. Hutchinson, and P. Helander, **"Effect of the inductive electric field on ion flow in tokamaks**," *Physics of Plasmas*, vol. 8, no. 7, pp. 3334–3341, 2001. URL: http://link.aip.org/link/?PHP/8/3334/1

[41] T. S. Hahm, P. H. Diamond, O. D. Gurcan, and G. Rewoldt, **"Turbulent equipartition theory of toroidal momentum pinch**," *Physics of Plasmas*, vol. 15, no. 5, p. 055902, 2008. URL: http://link.aip.org/link/?PHP/15/055902/1

[42] P. Monier-Garbet, K. H. Burrell, F. Hinton, J. Kim, X. Garbet, and R. J. Groebner, **"Effect of Neutrals on Plasma Rotation in DIII-D**," *Nuclear Fusion*, vol. 37, no. 3, p. 403, 1997.

[43] A. Scarabosio, A. Bortolon, B. P. Duval, A. N. Karpushov, and A. Pochelon, **"Momentum transport and plasma rotation spin up in TCV**," in *Proceedings of the 32nd EPS Conference on Plasma Physics and Controlled Fusion combined with the 8th International Workshop on Fast Ignition of Fusion Targets, Tarragona, June 27– July 1, 2005*, ser. Europhysics Conference Abstracts, B. v. M. C. Hidalgo, Ed., vol. 29C, Asociación EURATOM-CIEMAT para Fusión, Madrid. Tarragona: The European Physical Society, 2005, pp. P–1.049. URL: http://epsppd.epfl.ch/Tarragona/pdf/P1_049.pdf

[44] D. Testa, C. Giroud, A. Fasoli, K.-D. Zastrow, and E.-J. Team, **"On the measurement of toroidal rotation for the impurity and the main ion species on the Joint European Torus**," *Physics of Plasmas*, vol. 9, no. 1, pp. 243–250, 2002. URL: http://link.aip.org/link/?PHP/9/243/1

[45] A. Scarabosio, A. Bortolon, B. P. Duval, A. Karpushov, and A. Pochelon, **"Toroidal plasma rotation in the TCV tokamak**," *Plasma Physics and Controlled Fusion*, vol. 48, no. 5, pp. 663–683, 2006. URL: http://stacks.iop.org/0741-3335/48/663

[46] S. K. Wong and V. S. Chan, **"The neoclassical angular momentum flux in the large aspect ratio limit**," *Physics of Plasmas*, vol. 12, no. 9, p. 092513, 2005. URL: http://link.aip.org/link/?PHP/12/092513/1

[47] P. J. Catto and A. N. Simakov, **"Evaluation of the neoclassical radial electric field in a collisional tokamak**," *Physics of Plasmas*, vol. 12, no. 1, p. 012501, 2005. URL: http://link.aip.org/link/?PHP/12/012501/1

[48] S. K. Wong and V. S. Chan, **"Fluid theory of radial angular momentum flux of plasmas in an axisymmetric magnetic field**," *Physics of Plasmas*, vol. 14, no. 11, p. 112505, 2007. URL: http://link.aip.org/link/?PHP/14/112505/1

[49] A. Scarabosio, **"Stability and toroidal rotation properties of highly shaped plasmas in the TCV tokamak**," Ph.D. dissertation, Ecole Polytechnique Fédérale de Lausanne, thesis EPFL n.3609, 2006.

[50] T. H. Stix, **"Decay of poloidal rotation in a tokamak plasma**," *Physics of Fluids*, vol. 16, no. 8, pp. 1260–1267, 1973. URL: http://link.aip.org/link/?PFL/16/1260/1

[51] A. G. Peeters, D. Strintzi, Y. Camenen, C. Angioni, F. J. Casson, W. A. Hornsby, and A. P. Snodin, **"Influence of the centrifugal force and parallel dynamics on the toroidal momentum transport due to small scale turbulence in a tokamak**," *Physics of Plasmas*, vol. 16, no. 4, p. 042310, 2009. URL: http://link.aip.org/link/?PHP/16/042310/1

[52] B. Coppi, **"Accretion theory of 'spontaneous' rotation in toroidal plasmas**," *Nuclear Fusion*, vol. 42, no. 1, pp. 1–4, 2002. URL: http://stacks.iop.org/0029-5515/42/1

[53] T. S. Hahm, P. H. Diamond, O. D. Gurcan, and G. Rewoldt, **"Nonlinear gyrokinetic theory of toroidal momentum pinch**," *Physics of Plasmas*, vol. 14, no. 7, p. 072302, 2007. URL: http://link.aip.org/link/?PHP/14/072302/1

[54] A. G. Peeters, C. Angioni, and D. Strintzi, **"Toroidal Momentum Pinch Velocity due to the Coriolis Drift Effect on Small Scale Instabilities in a Toroidal Plasma**," *Physical Review Letters*, vol. 98, no. 26, p. 265003, 2007. URL: http://link.aps.org/abstract/PRL/v98/e265003

[55] R. R. Dominguez and G. M. Staebler, **"Anomalous momentum transport from drift wave turbulence**," *Physics of Fluids B: Plasma Physics*, vol. 5, no. 11, pp. 3876–3886, 1993. URL: http://link.aip.org/link/?PFB/5/3876/1

[56] O. D. Gürcan, P. H. Diamond, T. S. Hahm, and R. Singh, **"Intrinsic rotation and electric field shear**," *Physics of Plasmas*, vol. 14, no. 4, p. 042306, 2007. URL: http://link.aip.org/link/?PHP/14/042306/1

[57] F. J. Casson, A. G. Peeters, Y. Camenen, W. A. Hornsby, A. P. Snodin, D. Strintzi, and G. Szepesi, **"Anomalous parallel momentum transport due to E x B flow shear in a tokamak plasma**," *Physics of Plasmas*, vol. 16, no. 9, p. 092303, 2009. URL: http://link.aip.org/link/?PHP/16/092303/1

[58] Y. Camenen, A. G. Peeters, C. Angioni, F. J. Casson, W. A. Hornsby, A. P. Snodin, and D. Strintzi, **"Transport of Parallel Momentum Induced by Current-Symmetry Breaking in Toroidal Plasmas**," *Physical Review Letters*, vol. 102, no. 12, p. 125001, 2009. URL: http://link.aps.org/abstract/PRL/v102/e125001

[59] C. J. McDevitt, P. H. Diamond, O. D. Gürcan, and T. S. Hahm, **"A novel mechanism for exciting intrinsic toroidal rotation**," *Physics of Plasmas*, vol. 16, no. 5, p. 052302, 2009. URL: http://link.aip.org/link/?PHP/16/052302/1

[60] F. L. Hinton and S. K. Wong, **"Neoclassical ion transport in rotating axisymmetric plasmas**," *Physics of Fluids*, vol. 28, no. 10, pp. 3082–3098, 1985. URL: http://link.aip.org/link/?PFL/28/3082/1

[61] J. deGrassie, D. Baker, K. Burrell, P. Gohil, C. Greenfield, R. Groebner, and D. Thomas, **"Toroidal rotation in neutral beam heated discharges in DIII-D**," *Nuclear Fusion*, vol. 43, no. 2, pp. 142–156, 2003. URL: http://stacks.iop.org/0029-5515/43/142

[62] T. Tala, K. Crombe, P. C. de Vries, J. Ferreira, P. Mantica, A. G. Peeters, Y. Andrew, R. Budny, G. Corrigan, A. Eriksson, X. Garbet, C. Giroud, M.-D. Hua, H. Nordman, V. Naulin, M. F. F. Nave, V. Parail, K. Rantamaki, B. D. Scott, P. Strand, G. Tardini, A. Thyagaraja, J. Weiland, K.-D. Zastrow, and J.-E. Contributors, **"Toroidal and poloidal momentum transport studies in tokamaks**," *Plasma Physics and Controlled Fusion*, vol. 49, no. 12B, pp. B291–B302, 2007. URL: http://stacks.iop.org/0741-3335/49/B291

[63] G. Tardini, J. Ferreira, P. Mantica, A. Peeters, T. Tala, K. Zastrow, M. Brix, C. Giroud, G. Pereverzev, and J.-E. contributors, **"Angular momentum studies with NBI modulation in JET**," *Nuclear Fusion*, vol. 49, no. 8, p. 085010 (8pp), 2009. URL: http://stacks.iop.org/0029-5515/49/085010

[64] M. D. Bock, I. Classen, C. Busch, R. Jaspers, H. Koslowski, B. Unterberg, and the TEXTOR Team, **"The interaction between plasma rotation, stochastic fields and tearing mode excitation by external perturbation fields**," *Nuclear Fusion*, vol. 48, no. 1, p. 015007 (16pp), 2008. URL: http://stacks.iop.org/0029-5515/48/015007

[65] H. R. Wilson, J. W. Connor, R. J. Hastie, and C. C. Hegna, **"Threshold for neoclassical magnetic islands in a low collision frequency tokamak**," *Physics of Plasmas*, vol. 3, no. 1, pp. 248–265, 1996. URL: http://link.aip.org/link/?PHP/3/248/1

[66] A. Thyagaraja and F. A. Haas, **"A two-fluid interpretation of low frequency modes in Tokamaks**," *Plasma Physics*, vol. 25, no. 5, pp. 459–485, 1983. URL: http://stacks.iop.org/0032-1028/25/459

[67] R. Fitzpatrick, P. G. Watson, and F. L. Waelbroeck, **"Two-fluid magnetic island dynamics in slab geometry: Determination of the island phase velocity**," *Physics of Plasmas*, vol. 12, no. 8, p. 082510, 2005. URL: http://link.aip.org/link/?PHP/12/082510/1

[68] F. L. Waelbroeck, **"Natural Velocity of Magnetic Islands**," *Physical Review Letters*, vol. 95, no. 3, p. 035002, Jul 2005.

[69] E. Lazzaro, **"Symmetry breaking and self-consistent rotation of magnetic islands in neoclassical viscous regimes**," *Physics of Plasmas*, vol. 16, no. 9, p. 092504, 2009. URL: http://link.aip.org/link/?PHP/16/092504/1

[70] F. Waelbroeck, **"Theory and observations of magnetic islands**," *Nuclear Fusion*, vol. 49, no. 10, p. 104025 (15pp), 2009. URL: http://stacks.iop.org/0029-5515/49/104025

[71] R. J. L. Haye, C. C. Petty, E. J. Strait, F. L. Waelbroeck, and H. R. Wilson, **"Propagation of magnetic islands in the E[sub r] = 0 frame of co-injected neutral beam driven discharges in the DIII-D tokamak**," *Physics of Plasmas*, vol. 10, no. 9, pp. 3644–3648, 2003. URL: http://link.aip.org/link/?PHP/10/3644/1

[72] A. Scarabosio, A. Bortolon, B. P. Duval, and A. Pochelon, **"Comparison of MHD-mode and Plasma Rotation Frequencies in TCV Ohmic and ECH Discharges**," in *Proceedings of the 33rd EPS Conference on Plasma Physics, Rome, Italy, June 19–23, 2006*, ser. Europhysics Conference Abstracts (ECA), F. D. Marco and G. Vlad, Eds., vol. 30I, no. P-1.151. European Physical Society (EPS), 2006, contributed poster. URL: http://epsppd.epfl.ch/Roma/pdf/P1_151.pdf

[73] A. Garofalo, G. Jackson, R. L. Haye, M. Okabayashi, H. Reimerdes, E. Strait, J. Ferron, R. Groebner, Y. In, M. Lanctot, G. Matsunaga, G. Navratil, W. Solomon, H. Takahashi, M. Takechi, A. Turnbull, and the DIII-D Team, **"Stability and control of resistive wall modes in high beta, low rotation DIII-D plasmas**," *Nuclear Fusion*, vol. 47, no. 9, pp. 1121–1130, 2007. URL: http://stacks.iop.org/0029-5515/47/1121

[74] A. Chankin and W. Kerner, **"Edge toroidal momentum and its effect on the scrape-off layer**," *Nuclear Fusion*, vol. 36, no. 5, pp. 563–9, 1996. URL: http://stacks.iop.org/0029-5515/36/563

[75] R. Pitts, J. Horacek, W. Fundamenski, O. Garcia, A. Nielsen, M. Wischmeier, V. Naulin, and J. J. Rasmussen, **"Parallel SOL flow on TCV**," *Journal of Nuclear Materials*, vol. 363-365, pp. 505 – 510, 2007, plasma-Surface Interactions-17. URL: http://dx.doi.org/10.1016/j.jnucmat.2006.12.065

[76] B. LaBombard, J. W. Hughes, N. Smick, A. Graf, K. Marr, R. McDermott, M. Reinke, M. Greenwald, B. Lipschultz, J. L. Terry, D. G. Whyte, S. J. Zweben, and Alcator C-Mod Team, **"Critical gradients and plasma flows in the edge plasma of Alcator C-Mod**," *Physics of Plasmas*, vol. 15, no. 5, p. 056106, 2008. URL: http://link.aip.org/link/?PHP/15/056106/1

[77] J. S. deGrassie, K. H. Burrell, L. R. Baylor, W. Houlberg, and J. Lohr, **"Toroidal rotation in DIII-D in electron cyclotron heating and Ohmic H-mode discharges**," *Physics of Plasmas*, vol. 11, no. 9, pp. 4323–4331, 2004. URL: http://link.aip.org/link/?PHP/11/4323/1

[78] J. Rice, A. Ince-Cushman, P. Bonoli, M. Greenwald, J. Hughes, R. Parker, M. Reinke, G. Wallace, C. Fiore, R. Granetz, A. Hubbard, J. Irby, E. Marmar, S. Shiraiwa, S. Wolfe, S. Wukitch, M. Bitter, K. Hill, and J. Wilson, **"Observations of counter-current toroidal rotation in Alcator C-Mod LHCD plasmas**," *Nuclear Fusion*, vol. 49, no. 2, p. 025004 (8pp), 2009. URL: http://stacks.iop.org/0029-5515/49/025004

[79] J. Rice, W. Lee, E. Marmar, P. Bonoli, R. Granetz, M. Greenwald, A. Hubbard, I. Hutchinson, J. Irby, Y. Lin, D. Mossessian, J. Snipes, S. Wolfe, and S. Wukitch, **"Observations of anomalous momentum transport in Alcator C-Mod plasmas with no momentum input**," *Nuclear Fusion*, vol. 44, no. 3, pp. 379–386, 2004. URL: http://stacks.iop.org/0029-5515/44/379

[80] J. Rice, A. Hubbard, J. Hughes, M. Greenwald, B. LaBombard, J. Irby, Y. Lin, E. Marmar, D. Mossessian, S. Wolfe, and S. Wukitch, **"The dependence of core rotation on magnetic configuration and the relation to the H-mode power threshold in Alcator C-Mod plasmas with no momentum input**," *Nuclear Fusion*, vol. 45, no. 4, pp. 251–257, 2005. URL: http://stacks.iop.org/0029-5515/45/251

[81] A. Bortolon, B. P. Duval, A. Pochelon, and A. Scarabosio, **"Observation of Spontaneous Toroidal Rotation Inversion in Ohmically Heated Tokamak Plasmas**," *Physical Review Letters*, vol. 97, no. 23, p. 235003, 2006. URL: http://link.aps.org/abstract/PRL/v97/e235003

[82] R. E. Bell and R. Feder, **"Measurement of poloidal velocity on NSTX**," *Proceedings of the 50th Annual Meeting of the Division of Plasma Physics, November 17–21, Dallas, Texas*, vol. 53, no. 14, November 2008. URL: http://meetings.aps.org/link/BAPS.2008.DPP.NP6.119

[83] A. R. Field, J. McCone, N. J. Conway, M. Dunstan, S. Newton, and M. Wisse, **"Comparison of measured poloidal rotation in MAST spherical tokamak plasmas with neo-classical predictions**," *Plasma Physics and Controlled Fusion*, vol. 51, no. 10, p. 105002 (17pp), 2009. URL: http://stacks.iop.org/0741-3335/51/105002

[84] W. M. Solomon, K. H. Burrell, R. Andre, L. R. Baylor, R. Budny, P. Gohil, R. J. Groebner, C. T. Holcomb, W. A. Houlberg, and M. R. Wade, **"Experimental test of the neoclassical theory of impurity poloidal rotation in tokamaks**," *Physics of Plasmas*, vol. 13, no. 5, p. 056116, 2006. URL: http://link.aip.org/link/?PHP/13/056116/1

[85] K. Crombé, Y. Andrew, M. Brix, C. Giroud, S. Hacquin, A. Murari, M. F. F. Nave, J. Ongena, V. Parail, G. V. Oost, I. Voitsekhovitch, and K.-D. Zastrow, **"Poloidal Rotation Dynamics, Radial Electric Field, and Neoclassical Theory in the Jet Internal-Transport-Barrier Region**," *Physical Review Letters*, vol. 95, no. 15, p. 155003, October 2005. URL: http://dx.doi.org/10.1103/PhysRevLett.95.155003

[86] A. Bortolon, B. P. Duval, A. N. Karpushov, A. Scarabosio, and A. Pochelon, **"Toroidal Rotation Observation in Ohmic TCV Discharges**," in *Proceedings of the 32nd EPS Conference on Plasma Physics and Controlled Fusion combined with the 8th International Workshop on Fast Ignition of Fusion Targets, Tarragona, June 27– July 1, 2005*, ser. Europhysics Conference Abstracts, B. v. M. C. Hidalgo, Ed., vol. 29C, Asociación EURATOM-CIEMAT para Fusión, Madrid. Tarragona: The European Physical Society, 2005, pp. P–4.098. URL: http://epsppd.epfl.ch/Tarragona/pdf/P4_098.pdf

[87] B. Duval, A. Bortolon, A. Karpushov, A. Pochelon, O. Sauter, and G.Turri, **"Effect of Sawteeth on the Spontaneous TCV Plasma Rotation**," in *Proceedings of the 35rd EPS Conference on Plasma Physics, Hersonissos, Grece, June 9 – 13 June, 2008*, ser. Europhysics Conference Abstracts (ECA), P. Lalousis and S. Moustaizis, Eds., vol. 32D, no. P-2.020. European Physical Society (EPS), 2008, contributed poster. URL: http://epsppd.epfl.ch/Hersonissos/pdf/P2_020.pdf

[88] K. H. Burrell, **"Effects of E x B velocity shear and magnetic shear on turbulence and transport in magnetic confinement devices**," *Physics of Plasmas*, vol. 4, no. 5, pp. 1499–1518, 1997. URL: http://link.aip.org/link/?PHP/4/1499/1

[89] R. M. McDermott, B. Lipschultz, J. W. Hughes, P. J. Catto, A. E. Hubbard, I. H. Hutchinson, R. S. Granetz, M. Greenwald, B. LaBombard, K. Marr, M. L. Reinke, J. E. Rice, D. Whyte, and A. C.-M. Team, **"Edge radial electric field structure and its connections to H-mode confinement in Alcator C-Mod plasmas**," *Physics of Plasmas*, vol. 16, no. 5, p. 056103, 2009. URL: http://link.aip.org/link/?PHP/16/056103/1

[90] K. H. Burrell, W. P. West, E. J. Doyle, M. E. Austin, J. S. deGrassie, P. Gohil, C. M. Greenfield, R. J. Groebner, R. Jayakumar, D. H. Kaplan, L. L. Lao, A. W. Leonard, M. A. Makowski, G. R. McKee, W. M. Solomon, D. M. Thomas, T. L. Rhodes, M. R. Wade, G. Wang, J. G. Watkins, and L. Zeng, **"Edge radial electric field structure in quiescent H-mode plasmas in the DIII-D tokamak**," *Plasma Physics and Controlled Fusion*, vol. 46, no. 5A, pp. A165–A178, 2004. URL: http://stacks.iop.org/0741-3335/46/A165

[91] J. Schirmer, G. Conway, H. Zohm, W. Suttrop, and the ASDEX Upgrade Team, **"The radial electric field and its associated shear in the ASDEX Upgrade tokamak**," *Nuclear Fusion*, vol. 46, no. 9, pp. S780–S791, 2006. URL: http://stacks.iop.org/0029-5515/46/S780

[92] C. S. Chang and S. Ku, **"Spontaneous rotation sources in a quiescent tokamak edge plasma**," *Physics of Plasmas*, vol. 15, no. 6, p. 062510, 2008. URL: http://link.aip.org/link/?PHP/15/062510/1

[93] R. P. Seraydarian, K. H. Burrell, and R. J. Groebner, **"Multichordal visible/near-UV spectroscopy on the DIII-D tokamak**," *Review of Scientific Instruments*, vol. 59, no. 8, pp. 1530–1532, 1988. URL: http://link.aip.org/link/?RSI/59/1530/1

[94] M. Tunklev, P. Breger, K. Gunther, M. von Hellermann, R. Konig, M. O'Mullane, and K.-D. Zastrow, **"Modelling of passive charge exchange emission and neutral background density deduction in JET**," *Plasma Physics and Controlled Fusion*, vol. 41, no. 8, pp. 985–1004, 1999. URL: http://stacks.iop.org/0741-3335/41/985

[95] B. P. Duval, A. Bortolon, A. Karpushov, R. A. Pitts, A. Pochelon, O. Sauter, A. Scarabosio, G. Turri, and the TCV Team, **"Spontaneous L-mode plasma rotation scaling in the TCV tokamak**," *Physics of Plasmas*, vol. 15, no. 5, p. 056113, 2008. URL: http://link.aip.org/link/?PHP/15/056113/1

[96] B. Duval, B. Joye, and B. Marchal, **"Behaviour of plasma rotation and radial electric field with density ramp rate in an ohmically heated tokamak**," *Nuclear Fusion*, vol. 32, no. 8, pp. 1405–19, 1992. URL: http://stacks.iop.org/0029-5515/32/1405

[97] I. Chapman, T. Hender, S. Saarelma, S. Sharapov, R. Akers, N. Conway, and the MAST Team, **"The effect of toroidal plasma rotation on sawteeth in MAST**," *Nuclear Fusion*, vol. 46, no. 12, pp. 1009–1016, 2006. URL: http://stacks.iop.org/0029-5515/46/1009

[98] C. Angioni, A. G. Peeters, G. V. Pereverzev, F. Ryter, and G. T. A. U. Team, **"Theory-based modeling of particle transport in ASDEX Upgrade H-mode plasmas, density peaking, anomalous pinch and collisionality**," *Physics of Plasmas*, vol. 10, no. 8, pp. 3225–3239, 2003. URL: http://link.aip.org/link/?PHP/10/3225/1

[99] Y. Camenen, A. Pochelon, A. Bottino, S. Coda, F. Ryter, O. Sauter, R. Behn, T. P. Goodman, M. A. Henderson, A. N. Karpushov, L. Porte, and G. Zhuang, **"Electron heat transport in shaped TCV L-mode plasmas**," *Plasma Physics and Controlled Fusion*, vol. 47, no. 11, pp. 1971–1987, November 2005. URL: http://dx.doi.org/10.1088/0741-3335/47/11/007

[100] H. Reimerdes, A. M. Garofalo, M. Okabayashi, E. J. Strait, R. Betti, M. S. Chu, B. Hu, Y. In, G. L. Jackson, R. J. L. Haye, M. J. Lanctot, Y. Q. Liu, G. A. Navratil, W. M. Solomon, H. Takahashi, R. J. Groebner, and the DIII-D team, **"Resistive wall mode stabilization in slowly rotating high beta plasmas**," *Plasma Physics and Controlled Fusion*, vol. 49, no. 12B, pp. B349–B358, 2007. URL: http://stacks.iop.org/0741-3335/49/B349

[101] M. Murakami, G. H. Neilson, H. C. Howe, T. C. Jernigan, S. C. Bates, C. E. Bush, R. J. Colchin, J. L. Dunlap, P. H. Edmonds, K. W. Hill, R. C. Isler, H. E. Ketterer, P. W. King, D. W. McNeill, J. T. Mihalczo, R. V. Neidigh, V. K. Pare, M. J. Saltmarsh, J. B. Wilgen, and B. Zurro, **"Plasma Confinement Studies in the ISX-A Tokamak**," *Physical Review Letters*, vol. 42, no. 10, pp. 655–658, March 1979. URL: http://link.aps.org/doi/10.1103/PhysRevLett.42.655

[102] C. Angioni, A. G. Peeters, G. V. Pereverzev, F. Ryter, and G. Tardini, **"Density Peaking, Anomalous Pinch, and Collisionality in Tokamak Plasmas**," *Physical Review Letters*, vol. 90, no. 20, p. 205003, May 2003.

[103] F. Ryter, C. Angioni, A. G. Peeters, F. Leuterer, H.-U. Fahrbach, and W. Suttrop, **"Experimental Study of Trapped-Electron-Mode Properties in Tokamaks: Threshold and Stabilization by Collisions**," *Physical Review Letters*, vol. 95, no. 8, p. 085001, Aug 2005.

[104] A. Ince-Cushman, J. E. Rice, M. Bitter, M. L. Reinke, K. W. Hill, M. F. Gu, E. Eikenberry, C. Broennimann, S. Scott, Y. Podpaly, S. G. Lee, and E. S. Marmar, **"Spatially resolved high resolution x-ray spectroscopy for magnetically confined fusion plasmas (invited)**," vol. 79, no. 10, p. 10E302, 2008. URL: http://link.aip.org/link/?RSI/79/10E302/1

[105] K. W. Hill, M. L. Bitter, S. D. Scott, A. Ince-Cushman, M. Reinke, J. E. Rice, P. Beiersdorfer, M.-F. Gu, S. G. Lee, C. Broennimann, and E. F. Eikenberry, **"A spatially resolving x-ray crystal spectrometer for measurement of ion-temperature and rotation-velocity profiles on the Alcator C-Mod tokamak**," *Review of Scientific Instruments*, vol. 79, no. 10, p. 10E320, 2008. URL: http://link.aip.org/link/?RSI/79/10E320/1

[106] H. Reimerdes, A. M. Garofalo, G. L. Jackson, M. Okabayashi, E. J. Strait, M. S. Chu, Y. In, R. J. L. Haye, M. J. Lanctot, Y. Q. Liu, G. A. Navratil, W. M. Solomon, H. Takahashi, and R. J. Groebner, **"Reduced Critical Rotation for Resistive-Wall Mode Stabilization in a Near-Axisymmetric Configuration**," *Physical Review Letters*, vol. 98, no. 5, p. 055001, 2007. URL: http://link.aps.org/abstract/PRL/v98/e055001

[107] M. Takechi, G. Matsunaga, N. Aiba, T. Fujita, T. Ozeki, Y. Koide, Y. Sakamoto, G. Kurita, A. Isayama, and Y. K. J.-. team, **"Identification of a Low Plasma-Rotation Threshold for Stabilization of the Resistive-Wall Mode**," *Physical Review Letters*, vol. 98, no. 5, p. 055002, 2007. URL: http://link.aps.org/abstract/PRL/v98/e055002

[108] P. Mantica, D. Strintzi, T. Tala, C. Giroud, T. Johnson, H. Leggate, E. Lerche, T. Loarer, A. G. Peeters, A. Salmi, S. Sharapov, D. V. Eester, P. C. de Vries, L. Zabeo, and K.-D. Zastrow, **"Experimental Study of the Ion Critical-Gradient Length and Stiffness Level and the Impact of Rotation in the JET Tokamak**," *Physical Review Letters*, vol. 102, no. 17, p. 175002, 2009. URL: http://link.aps.org/abstract/PRL/v102/e175002

[109] B. LaBombard, J. Rice, A. Hubbard, J. Hughes, M. Greenwald, J. Irby, Y. Lin, B. Lipschultz, E. Marmar, C. Pitcher, N. Smick, S. Wolfe, S. Wukitch, and the Alcator Group, **"Transport-driven Scrape-Off-Layer flows and the boundary conditions imposed at the magnetic separatrix in a tokamak plasma**," *Nuclear Fusion*, vol. 44, no. 10, pp. 1047–1066, 2004. URL: http://stacks.iop.org/0029-5515/44/1047

[110] B. LaBombard, J. E. Rice, A. E. Hubbard, J. W. Hughes, M. Greenwald, R. S. Granetz, J. H. Irby, Y. Lin, B. Lipschultz, E. S. Marmar, K. Marr, D. Mossessian, R. Parker, W. Rowan, N. Smick, J. A. Snipes, J. L. Terry, S. M. Wolfe, and S. J. W. A. C.-M. Team, **"Transport-driven scrape-off layer flows and the x-point dependence of the L-H power threshold in Alcator C-Mod**," *Physics of Plasmas*, vol. 12, no. 5, p. 056111, 2005. URL: http://link.aip.org/link/?PHP/12/056111/1

[111] C. Angioni, L. Carraro, T. Dannert, N. Dubuit, R. Dux, C. Fuchs, X. Garbet, L. Garzotti, C. Giroud, R. Guirlet, F. Jenko, O. J. W. F. Kardaun, L. Lauro-Taroni, P. Mantica, M. Maslov, V. Naulin, R. Neu, A. G. Peeters, G. Pereverzev, M. E. Puiatti, T. Pütterich, J. Stober, M. Valovič, M. Valisa, H. Weisen, and A. Z. A. U. T. J. E. Contributors, **"Particle and impurity transport in the Axial Symmetric Divertor Experiment Upgrade and the Joint European Torus, experimental observations and theoretical understanding**," *Physics of Plasmas*, vol. 14, no. 5, p. 055905, 2007. URL: http://link.aip.org/link/?PHP/14/055905/1

[112] I. H. Hutchinson, J. E. Rice, R. S. Granetz, and J. A. Snipes, **"Self-Acceleration of a Tokamak Plasma during Ohmic H Mode**," *Physical Review Letters*, vol. 84, no. 15, pp. 3330–3333, Apr 2000.

[113] J. Rice, R. Boivin, P. Bonoli, J. Goetz, R. Granetz, M. Greenwald, I. Hutchinson, E. Marmar, G. Schilling, J. Snipes, S. Wolfe, S. Wukitch, C. Fiore, J. Irby, D. Mossessian, and M. Porkolab, **"Observations of impurity toroidal rotation suppression with ITB formation in ICRF and ohmic H mode Alcator C-Mod plasmas**," *Nuclear Fusion*, vol. 41, no. 3, pp. 277–284, 2001. URL: http://stacks.iop.org/0029-5515/41/277

[114] Y. Camenen, A. G. Peeters, C. Angioni, F. J. Casson, W. A. Hornsby, A. P. Snodin, and D. Strintzi, **"Intrinsic rotation driven by the electrostatic turbulence in up-down asymmetric toroidal plasmas**," *Physics of Plasmas*, vol. 16, no. 6, p. 062501, 2009. URL: http://link.aip.org/link/?PHP/16/062501/1

[115] S. Kaye, W. Solomon, R. Bell, B. LeBlanc, F. Levinton, J. Menard, G. Rewoldt, S. Sabbagh, W. Wang, and H. Yuh, **"Momentum transport in electron-dominated NSTX spherical torus plasmas**," *Nuclear Fusion*, vol. 49, no. 4, p. 045010 (7pp), 2009. URL: http://stacks.iop.org/0029-5515/49/045010

[116] W. Solomon, K. Burrell, A. Garofalo, A. Cole, R. Budny, J. deGrassie, W. Heidbrink, G. Jackson, M. Lanctot, R. Nazikian, H. Reimerdes, E. Strait, M. V. Zeeland, and the DIII-D Rotation Physics Task Force, **"Advances in understanding the generation and evolution of the toroidal rotation profile on DIII-D**," *Nuclear Fusion*, vol. 49, no. 8, p. 085005 (11pp), 2009. URL: http://stacks.iop.org/0029-5515/49/085005

[117] P. C. de Vries, K. M. Rantamaki, C. Giroud, E. Asp, G. Corrigan, A. Eriksson, M. de Greef, I. Jenkins, H. C. M. Knoops, P. Mantica, H. Nordman, P. Strand, T. Tala, J. Weiland, K.-D. Zastrow, and J. E. Contributors, **"Plasma rotation and momentum transport**

studies at JET," *Plasma Physics and Controlled Fusion*, vol. 48, no. 12, pp. 1693–1708, 2006. URL: http://stacks.iop.org/0741-3335/48/1693

[118] T. Tala, K.-D. Zastrow, J. Ferreira, P. Mantica, V. Naulin, A. G. Peeters, G. Tardini, M. Brix, G. Corrigan, C. Giroud, and D. Strintzi, **"Evidence of Inward Toroidal Momentum Convection in the JET Tokamak**," *Physical Review Letters*, vol. 102, no. 7, p. 075001, 2009. URL: http://link.aps.org/abstract/PRL/v102/e075001

[119] M. Yoshida, Y. Kamada, H. Takenaga, Y. Sakamoto, H. Urano, N. Oyama, G. Matsunaga, and the JT-60 Team, **"Role of Pressure Gradient on Intrinsic Toroidal Rotation in Tokamak Plasmas**," *Physical Review Letters*, vol. 100, no. 10, p. 105002, 2008. URL: http://link.aps.org/abstract/PRL/v100/e105002

[120] M. N. Rosenbluth, P. H. Rutherford, J. B. Taylor, E. A. Frieman, and L. M. Kovrishnikh, **"Plasma Physics and Controlled Nuclear Fusion Researc**," *Vienna: IAEA*, vol. 1, p. 495, 1971.

[121] K. T. Tsang and E. A. Frieman, **"Toroidal plasma rotation in axisymmetric and slightly nonaxisymmetric systems**," *Physics of Fluids*, vol. 19, no. 5, pp. 747–756, 1976. URL: http://link.aip.org/link/?PFL/19/747/1

[122] R. D. Hazeltine and M. N. Rosenbluth, **"Effect of Field Asymmetry on Neoclassical Transport in a Tokamak**," *Physics of Fluids*, vol. 15, no. 12, pp. 2211–2217, 1972. URL: http://link.aip.org/link/?PFL/15/2211/1

[123] A. G. Peeters and D. Strintzi, **"The effect of a uniform radial electric field on the toroidal ion temperature gradient mode**," *Physics of Plasmas*, vol. 11, no. 8, pp. 3748–3751, 2004, gKW. URL: http://link.aip.org/link/?PHP/11/3748/1

[124] T. Dannert and F. Jenko, **"Gyrokinetic simulation of collisionless trapped-electron mode turbulence**," *Physics of Plasmas*, vol. 12, no. 7, p. 072309, 2005. URL: http://link.aip.org/link/?PHP/12/072309/1

[125] A. G. Peeters, C. Angioni, A. Bottino, A. Kallenbach, B. Kurzan, C. F. Maggi, W. Suttrop, and the ASDEX Upgrade team, **"Toroidal momentum transport**," *Plasma Physics and Controlled Fusion*, vol. 48, no. 12B, pp. B413–B420, 2006. URL: http://stacks.iop.org/0741-3335/48/B413

[126] M. Yoshida, Y. Sakamoto, H. Takenaga, S. Ide, N. Oyama, T. Kobayashi, Y. Kamada, and the JT-60 Team, **"Rotation Drive and Momentum Transport with Electron Cyclotron Heating in Tokamak Plasmas**," *Physical Review Letters*, vol. 103, no. 6, p. 065003, 2009. URL: http://link.aps.org/abstract/PRL/v103/e065003

[127] I. Chapman, S. Pinches, H. Koslowski, Y. Liang, A. Kramer-Flecken, the TEXTOR Team, and M. de Bock, **"Sawtooth stability in neutral beam heated plasmas in TEXTOR**," *Nuclear Fusion*, vol. 48, no. 3, p. 035004 (9pp), 2008. URL: http://stacks.iop.org/0029-5515/48/035004

[128] M. F. F. Nave, H. R. Koslowski, S. Coda, J. Graves, M. Brix, R. Buttery, C. Challis, C. Giroud, M. Stamp, and P. de Vries, **"Exploring a small sawtooth regime in Joint European Torus plasmas with counterinjected neutral beams**," *Physics of Plasmas*, vol. 13, no. 1, p. 014503, 2006. URL: http://link.aip.org/link/?PHP/13/014503/1

[129] C. Angioni, T. Goodman, M. Henderson, and O. Sauter, **"Effects of localized electron heating and current drive on the sawtooth period**," *Nuclear Fusion*, vol. 43, no. 6, pp. 455–468, 2003. URL: http://stacks.iop.org/0029-5515/43/455

[130] J. I. Paley, F. Felici, S. Coda, T. P. Goodman, F. Piras, and the TCV Team, **"Real time control of the sawtooth period using EC launchers**," *Plasma Physics and Controlled Fusion*, vol. 51, no. 5, p. 055010 (9pp), 2009. URL: http://stacks.iop.org/0741-3335/51/055010

[131] K. Matsuda, **"Ray tracing study of the electron cyclotron current drive in DIII-D using 60 GHz**," *Plasma Science, IEEE Transaction*, vol. 17(1), pp. 6–11, 1989.

[132] R. Pitts, S. Alberti, P. Blanchard, J. Horacek, H. Reimerdes, and P. Stangeby, **"ELM driven divertor target currents on TCV**," *Nuclear Fusion*, vol. 43, no. 10, pp. 1145–1166, 2003. URL: http://stacks.iop.org/0029-5515/43/1145

[133] R. Behn, A. Alfier, S. Y. Medvedev, G. Zhuang, R. Pasqualotto, P. Nielsen, Y. Martin, and the TCV team, **"Edge profiles of electron temperature and density during ELMy H-mode in ohmically heated TCV plasmas**," *Plasma Physics and Controlled Fusion*, vol. 49, no. 8, pp. 1289–1308, 2007. URL: http://stacks.iop.org/0741-3335/49/1289

[134] URL: http://www.d-tacq.com

[135] I. Furno, C. Angioni, F. Porcelli, H. Weisen, R. Behn, T. Goodman, M. Henderson, Z. Pietrzyk, A. Pochelon, H. Reimerdes, and E. Rossi, **"Understanding sawtooth activity during intense electron cyclotron heating experiments on TCV**," *Nuclear Fusion*, vol. 41, no. 4, pp. 403–420, 2001. URL: http://stacks.iop.org/0029-5515/41/403

[136] F. Porcelli, D. Boucher, and M. N. Rosenbluth, **"Model for the sawtooth period and amplitude**," *Plasma Physics and Controlled Fusion*, vol. 38, no. 12, pp. 2163–2186, 1996. URL: http://stacks.iop.org/0741-3335/38/2163

[137] B. B. Kadomtsev, **"Disruptive instability in tokamaks**," *Sov. J. Plasma Physics*, vol. 1, no. 5, pp. 389–391, September–October 1975, (english translation of Fiz. Plazmy 1, 710–715, 1975).

[138] G. V. Pereverzev, P. N. Yushmanov, and A. Y. Dnestrovskii, **"ASTRA An Automatic System for Transport Analysis in a Tokamak**," Max-Planck-Institut fuer Plasmaphysik (MPP), Garching, Germany, IPP-Report 5/42, 1991.

[139] I. Klimanov, A. Fasoli, T. P. Goodman, and the TCV team, **"Generation of suprathermal electrons during sawtooth crashes in a tokamak plasma**," *Plasma Physics and Controlled Fusion*, vol. 49, no. 3, pp. L1–L6, 2007. URL: http://stacks.iop.org/0741-3335/49/L1

[140] P. Helander, L.-G. Eriksson, R. J. Akers, C. Byrom, C. G. Gimblett, and M. R. Tournianski, **"Ion Acceleration during Reconnection in MAST**," *Physical Review Letters*, vol. 89, no. 23, p. 235002, Nov 2002.

[141] P. Helander, **"On ion flow caused by the inductive electric field in a tokamak**," *Physics of Plasmas*, vol. 8, no. 10, pp. 4700–4703, 2001. URL: http://link.aip.org/link/?PHP/8/4700/1

[142] F. Porcelli, E. Rossi, G. Cima, and A. Wootton, **"Macroscopic Magnetic Islands and Plasma Energy Transport**," *Physical Review Letters*, vol. 82, no. 7, pp. 1458–1461, Feb 1999.

Acknowledgements

This thesis work could not be accomplished without the contribution of many people, that I want to acknowledge here.

First of all I want to thank Basil Duval, my thesis director, who always firmly supported me in work and life, during my years at CRPP.

I am particulary grateful to Alexander Karpushov and Yanis Andrebe for their generous and tireless help with the diagnostic implementation and operation. I thank Paolo Bosshard, who first built the magical toy I enjoyed playing with, and Andrea Scarabosio, with whom I moved my first steps in the puzzling world of plasma rotation. Thanks very much also to Lucia Federspiel, who already began to take care of the CXRS diagnostic with dedication and enthusiasm: you will not be lacking in results.

I am obliged to Stefano Coda, Ivo Furno, Richard Pitts, Antoine Pochelon, Olivier Sauter, Henri Weisen and many other senior colleagues who contributed to my research path with helpful discussions and supported me in the practice of experimental research.

I thank all colleagues whose everyday effort permits TCV to exist and work, in particular Xavier Llobet and Pascal Conti.

I am thankful to the CRPP direction, in particular to Prof. Minh Quang Tran, Prof. Kurt Appert and Prof. Ambrogio Fasoli, who welcomed me at CRPP and gave me the opportunity to work in such a great environment. I also thank Prof. Piero Martin who first introduced me to the fusion research and supported me in many occasions.

I finally want to thank all my young colleagues: office mates, apéro addicted, physique numérique gang, etc. They all enriched my permanence at CRPP in many ways and some of them became sincere friends.

Dedico questa tesi a Gianni e Ida, i miei genitori. Un gran ringraziamento va a tutta la mia famiglia e ai miei amici italiani, che mi sono stati vicini in questi anni di lontananza. Un grazie di cuore alla famiglia di Valentina, per tutto, la straordinaria figlia in primis.

L'ultimo e primo pensiero va a Vale, che dal primo all'ultimo momento mi ha sostenuto in questa avventura elvetica, che piú di chiunque altro crede in me e che sarà mia amata compagna e complice delle prossime peripezie della vita.

This work was partially supported by the Swiss National Science Foundation.

Curriculum Vitae

Education

Since 2004/04: Ecole Polytechnique Fédérale de Lausanne (EPFL), Switzerland: Ph.D. thesis at Centre de Recherches en Physique des Plasmas (Dr. B.P. Duval): "Plasma rotation and momentum transport studies in the TCV Tokamak, based on Charge Exchange Spectroscopy measurements".

2003/12: Post-Master course in Thermonuclear Plasma Engineering at Consorzio RFX / Università di Padova (Italy). Main projects: 1) Analysis of JET impurity seeding experiments (Argon, Carbon, Molybdenum), by means of simulation of spectroscopic emission (Dr. M. Valisa); 2) Determination of the entire set of atomic ionization and recombination coefficients for the simulation of Zirconium transport in JET plasmas discharges (Prof. M. Mattioli, EURATOM Association, Cadarache).

2002/12: Master degree thesis at Università di Padova (Prof. P. Martin, Dr. M.E. Puiatti): "Analisi del trasporto di impurità nei regimi di confinamento migliorato con iniezione di Argon nell'esperimento JET" (Impurity transport analysis in improved confinement regimes with Argon injection in the JET experiment).

Research collaborations

2-5 December 2008: Plasma Science and Fusion Center (PSFC), Massachusetts Institute of Technology, Cambridge, Massachusetts, US. Data reduction and analysis of Alcator C-mod plasma discharges featuring spontaneous reversal of toroidal rotation (ITPA Joint Experiment TC-9).

1-4 April 2008 Centre for Fusion, Space and Astrophysics (CFSA) Department of Physics, University of Warwick Coventry, CV4 7AL, UK. Collaboration with Prof. A. Peeters and Dr. Y. Camenen on the interpretation of TCV plasma rotation observations by means of gyrokinetic simulations including momentum pinch terms.

Selected refereed scientific publications

- A. Bortolon, B.P. Duval, A. Pochelon and A. Scarabosio, *Observation of spontaneous toroidal rotation inversion in ohmically heated Tokamak plasmas*, Physical Review Letters, 97 (2006), 235003.

- B.P. Duval, A. Bortolon, A. Karpushov, R.A. Pitts, A. Pochelon, O. Sauter, A. Scarabosio, G. Turri and the TCV Team, *Spontaneous plasma rotation scaling in the TCV Tokamak*, Phys. Plasmas 15 (2008), 056113.

- B.P. Duval, A. Bortolon, A. Karpushov, R.A. Pitts, A. Pochelon, A. Scarabosio and the TCV Team, *Bulk plasma rotation in the TCV tokamak in the absence of external momentum input*, Plasma Phys. Control. Fusion 49, No 12B (2007), B195-B209.

- A. Scarabosio, A. Bortolon, B.P. Duval, A. Karpushov and A. Pochelon, *Toroidal plasma rotation in the TCV tokamak*, Plasma Phys. Controlled Fusion 48 (2006), 663.

- M.E. Puiatti, M. Valisa, M. Mattioli, T. Bolzonella, A. Bortolon, I. Coffey, R. Dux, M. von Hellermann, P. Monier-Garbet, M.F.F. Nave, J. Ongena, and contributors to the EFDA-JET *Simulation of the time behaviour of impurities in JET Ar-seeded discharges and its relation with sawtoothing and RF heating*, Plasma Phys. Control. Fusion 45 No 12 (2003), 2011-2024.

Conferences and seminars

- *Intrinsic rotation and radial electric field in TCV plasmas*, 50$^{\text{th}}$ Annual Meeting of the Division of Plasma Physics, November 17-21, 2008, Dallas, Texas (poster contribution).

- *Bulk Plasma Rotation in the TCV Tokamak in the Absence of External Momentum Input*, 34$^{\text{th}}$ EPS Conference on Plasma Physics Warsaw, Poland July 2007 (invited talk presented by B.P. Duval).

- *Spontaneous plasma rotation scaling in the TCV Tokamak*, 49$^{\text{th}}$ Annual Meeting of the Division of Plasma Physics, November 16 2007, Orlando, Florida (invited talk presented by B.P. Duval).

- *Toroidal momentum transport in limited and diverted TCV Ohmic plasmas*, 12$^{\text{th}}$ US EU Transport Taskforce Workshop, San Diego, April 18 2007 (oral contribution).

- *Toroidal momentum transport in limited and diverted TCV Ohmic plasmas*, CDBM and Transport ITPA groups meeting, Lausanne (EPFL), Switzerland, May 8 2007 (oral contribution).

- A. Bortolon, B.P. Duval, A. Scarabosio, A. Karpushov and A. Pochelon, *Spontaneous plasma rotation in limited and diverted TCV ohmic discharges*, in Proceedings of the 33$^{\text{rd}}$ EPS Conference on Plasma Physics, Rome, 2006 (poster contribution), Europhys. Conf. Abstr. 30I (2006)., 1.154

- A. Bortolon, B.P. Duval, A. Karpushov, A. Scarabosio, A. Pochelon, *Toroidal Rotation Observation in Ohmic TCV Discharges*, in Proceedings of the 32$^{\text{nd}}$ EPS Conference on Plasma Phys. Tarragona, 2005 (poster contribution), Europhys. Conf. Abstr. Vol.29C (2005), P-4.098.

Selected contributed publications

- J.E. Rice, A. Ince-Cushman, J.S. deGrassie, L.-G. Eriksson, Y. Sakamoto, A. Scarabosio, A. Bortolon, K.H. Burrell, B.P. Duval, C. Fenzi-Bonizec, M.J. Greenwald, R.J. Groebner, G.T. Hoang, Y. Koide, E.S. Marmar, A. Pochelon and Y. Podpaly, *Inter-machine comparison of intrinsic toroidal rotation in tokamaks*, Nucl. Fusion 47 No 11 (2007), 1618-1624.

- Y. Camenen, A. Pochelon, R. Behn, A. Bottino, A. Bortolon, S. Coda, A. Karpushov, O. Sauter, G. Zhuang and the TCV team, *Impact of plasma triangularity and collisionality on electron heat transport in TCV L-mode plasmas*, Nucl. Fusion 47 No 7 (2007), 510-516.

- A. Scarabosio, A. Bortolon, B.P. Duval and A. Pochelon, *Comparison of MHD-mode and Plasma Rotation Frequencies in TCV Ohmic and ECH Discharges*, in Proceedings of the 33rd EPS Conference on Plasma Physics, Rome, 2006, Europhys. Conf. Abstr. 30I (2006), 1.151.

- L. Porte, S. Coda, S. Alberti, G. Arnoux, P. Blanchard, A. Bortolon, A. Fasoli, T.P. Goodman, Y. Klimanov, Y. Martin, M. Maslov, A. Scarabosio and H. Weisen, *Plasma dynamics with second and third-harmonic ECRH and access to quasi-stationary ELM-free H-mode on TCV*, Nucl. Fusion 47 No 8 (2007), 952-960.

Teaching

2006/10 - 2008/12: Assistant for *Physique Numerique* I and II course for Physics students at EPFL.

2004/10 - 2006/7: Assistant for Laboratory III course for Physics students at EPFL (plasma gun experiment).